Mathematical models for angiogenic, metabolic and apoptotic processes in tumours

by

Colin Phipps

A thesis
presented to the University of Waterloo
in fulfillment of the
thesis requirements for the degree of
Doctor of Philosophy
in
Applied Mathematics

Waterloo, Ontario, Canada, 2014

Author's Declaration

I hereby declare that I am the sole author of this thesis. This is a true copy of the thesis, including any required final revisions, as accepted by my examiners.

I understand that my thesis may be made electronically available to the public.

Abstract

This doctoral thesis outlines a body of research within the field of mathematical oncology that focusses on the inclusion of microenvironmental factors in mathematical models for solid tumour behaviour. These models primarily address tumour angiogenesis signalling, tumour metabolism and inducing apoptosis via novel treatment combinations.

After a brief introduction in Chapter 1, background material pertinent to cancer biology and treatment is provided in Chapter 2. This chapter details tumour angiogenesis, tumour metabolism and various cancer treatments. This is followed in Chapter 3 by a survey of mathematical models that directly influence my work including summaries of models for relevant tumour entities such as angiogenic growth factors, interstitial fluid pressure, tumour metabolism and acidosis. The progression of topics in these two preliminary chapters emulate the ordering of the original research presented in Chapters 4–6.

Chapter 4 presents an angiogenic growth factor (AGF) model used to study the impact of transport processes on tumour angiogenic behaviour. The study focusses on a coupled system of diffusion-convection-reaction equations that establish the role of convection in determining relative concentrations of proangiogenic and antiangiogenic growth factors, and hence the angiogenic behaviour, in solid tumours. The effect of various cancer treatments, such as chemotherapy and antiangiogenic drugs, that can alter tumour properties are considered through parameter analyses. The angiogenesis that results from angiogenic stimulation provides tumours with an oxygen and nutrient supply required for metabolism.

Chapter 5 quantifies the benefit of metabolic symbiosis on tumour ATP production. A diffusion-reaction model of cell metabolism in the hypoxic tissue surrounding a leaky tumour blood vessel is developed that includes both lactate and glucose fuelled respiration along with glycolysis. We can then study the energetic effects of cancer cells' metabolic behaviour, such as the Warburg effect and metabolic symbiosis. A model coupling these metabolic behaviours with acidosis is also analyzed that includes the effects of extracellular buffers. These models can be used to investigate metabolic inhibitor treatments by knocking out specific model parameters and buffering therapies.

While treatment effects are considered in the previous chapters via parameter alteration, Chapter 6 explicitly models concentrations of molecular inhibitors and chemotherapy nanoparticles. These treatments are coupled to a model for apoptotic protein expression to evaluate strategies for counteracting chemoresistance in triple-negative breast cancer. The protein model is then used to predict cell viability, which indicates the efficacy of schedules for treatment combinations. The model prediction of post-chemotherapy inhibitor outperforming pre-chemotherapy and simultaneous application is verified by further experiments.

Finally, a summary of the contributions to the field of mathematical oncology and suggested future directions are indicated in the final chapter.

Acknowledgements

Firstly, I would like to thank my supervisor Dr. Mohammad Kohandel for his research guidance and scientific insight. The other professors in the Applied Mathematics Biomedical Research Group were also integral to my graduate studies: I thank Dr. Siv Sivaloganathan (also on my thesis defence committee) for his advice and support and Dr. Giuseppe Tenti for his wisdom and notes on biophysics and continuum mechanics. I also owe a debt of gratitude to the other members of my Ph.D. committee for their time and useful feedback: Dr. Matthew Scott (Applied Mathematics, University of Waterloo), Dr. Maud Gorbet (internal-external: Systems Design Engineering, University of Waterloo) and Dr. Philip K. Maini (external examiner: Oxford University). I acknowledge my many research colleagues who were integral to my success, especially Dr. Hamid Molavian, Dr. (Venkata) Satya Manem, Dr. Gibin Powathil and Dr. Kathleen Wilkie. Many of these projects could not be accomplished without wonderful collaborators including Dr. Ambarish Pandey, Dr. Aaron Goldman and Dr. Shiladitya Sengupta. Finally, thanks to my friends and my very supportive family for their love and support.

Dedication

This thesis is dedicated to my mother, Diana (1955–1995).

Table of Contents

List of Tables

List of Figures

List of Acronyms

AGF angiogenic growth factor

ADP adenosine diphosphate

AMP adenosine monophosphate

ATP adenosine triphosphate

CAC citric acid cycle

DCM directed cell movement

DNA deoxyribonucleic acid

ECM extracellular matrix

EPR enhanced permeability and retention

FGF fibroblast growth factor

HIF hypoxia-inducible factor

IFP interstitial fluid pressure

IFV interstitial fluid velocity

LDH lactate dehydrogenase

mAb monoclonal antibody

MTD maximum-tolerated dose

NAD nicotinamide adenine dinucleotide

NP nanoparticle

ODE ordinary differential equation

PDE partial differential equation

PI3K phosphatidylinositol-4,5-bisphosphate 3-kinase

pH power of hydrogen

ROS reactive oxygen species

SACN self-assembling cis-platinum nanoparticles

TNBC triple negative breast cancer

TSP thrombospondin

VEGF vascular endothelial growth factor

XIAP X-linked inhibitor of apoptosis protein

Chapter 1

Introduction

This doctoral thesis outlines my body of research within the field of mathematical oncology, an area that utilizes mathematical tools to address problems in cancer research. The overarching goal is to develop mathematical models that provide insight into cancer processes with a focus on cancer treatment, which fosters collaboration with clinicians and leads to meaningful contributions in the medical community. Repeated calls to bridge the gap between the fields of experimental and mathematical oncology [6, 7] have been met with many success collaborative efforts and my research has been strongly enriched and occasionally guided by direct collaboration with biologists and clinicians [8]. Mathematical oncology encompasses the modelling of many cancer processes, including genetic mutational events, tumour growth, cell signalling, among many others; for an overview, see [9]. These models can occur on multiple length scales, ranging from molecular modelling all the way up to tissue modelling, and can even address problems on multiple scales, referred to as multiscale models [10]. These models can be developed within numerous mathematical frameworks ranging from continuous partial differential equations (PDEs) to discrete models [11], and can be combinations of these methodologies, termed hybrid models [12]. The models that I use will be formulated as PDEs on the microscale (single blood vessel) or on the macroscale (whole tumour) and then analyzed in steady state, thus reducing their complexity to ordinary differential equations (ODEs) in Chapters 4 and 5, or be formulated as strictly time-dependent ODEs in Chapter 6.

From a public health perspective, encouraging non-medical scientists to research cancer, and indeed other diseases, is becoming a favourable and increasingly common phenomenon amongst mathematicians, computer scientists, physicists, statisticians, chemists and, un-

surprisingly, biologists. This serves as a boon to cancer research as cancer continues to be a global threat that is one of the leading causes of death in both the developed and developing world, causing an estimated 7.6 millions deaths in 2008 [13]. In Canada the incidence rate for all cancers has increased by 0.9% per year in males and 0.8% in females, however, the mortality rates dropped 0.3% for males and 0.2% for females over the same time period [14]. Some of the seemingly bloated rates of incidence can be explained by improved screening methods and diagnosis, while the decrease in mortality can be attributed to improved treatments and earlier detection [14]. Mathematical oncology has much to contribute to the further improvement of cancer treatments, including the optimization of treatment scheduling and dosages, especially in the complex scenarios encountered when considering combinations of multiple treatment modalities. This can be achieved by predicting tumour progression, cell signalling, metabolic and angiogenic behaviours as well as cancer cell evolution, all of which can be addressed with mathematical models and have crucial bearing on the efficacy of cancer treatments.

My research focusses on the incorporation of microenvironmental factors unique to cancerous tissues into mathematical models that govern tumour behaviour. To facilitate the discussion of these medically motivated models, a brief background of cancer biology and treatment is provided in Chapter 2. This contains pertinent information on tumour angiogenesis, tumour metabolism and various therapies. This is followed by a survey of mathematical models that directly influence my work in Chapter 3. This chapter contains summaries of models for relevant tumour entities such as angiogenic growth factors, interstitial fluid pressure, tumour metabolism and acidosis. The progression through these two preliminary background chapters mirror the sequence of original research content in Chapters 4–6.

Chapter 4 presents an angiogenic growth factor (AGF) model to study the impact of transport processes on tumour angiogenic behaviour. The study focusses on a coupled system of diffusion-convection-reaction equations that elucidate the role of convective fluid flow on local imbalances of proangiogenic and antiangiogenic factors in solid tumours. These cell signalling factors promote or suppress angiogenesis and hence have a significant influence on determining a tumour's oxygen and nutrient supply. The effect of various cancer treatments, such as chemotherapy and antiangiogenic drugs, that can alter tumour properties are considered through parameter analyses.

Chapter 5 investigates a diffusion-reaction model of cell metabolism in the hypoxic tissue surrounding a leaky tumour blood vessel. The model includes both lactate and glu-

cose fuelled respiration along with glycolysis, to study the effects of cancer cells' metabolic behaviour, such as the Warburg effect and metabolic symbiosis, on ATP production. A model coupling metabolic behaviour and acidosis is also analyzed that includes the effects of extracellular buffer and blood vessel properties. These models can be used to investigate metabolic inhibitor treatments by knocking out specific model parameters.

While effects of treatment are included in the previous models by altering model parameters, Chapter 6 explicitly studies drug concentrations in a data-driven study of combinations of molecular inhibitors and chemotherapy nanoparticles. A model for apoptotic protein expression is coupled to models for nanoparticle release in an acidic microenvironment and cellular treatment concentrations to investigate counteracting chemoresistance in triple-negative breast cancer. These protein expressions are then used in a cell viability model in an attempt to predict the optimal scheduling of nanoparticles in combination with a molecular inhibitor. The model prediction of post-chemotherapy inhibitor performing better than pre-chemotherapy or simultaneous application is verified by further experiments.

The major contributions to the field of mathematical oncology include the following, contained in Chapters 4, 5 and 6 respectively:

(i) Establishing the role of convective transport in angiogenesis signalling: This model is used to classify angiogenic tumour behaviours and to predict the effects of various treatments via physiological parameter changes. This finding is generalizable to other cell signalling pathways in tumours.

(ii) Metabolism model that includes lactate-fuelled and glucose-fuelled respiration along with oxygen-repressible glycolysis: This was the first model to spatially consider the optimal ATP production in a tumour on the microscale and could be used to analyze metabolic inhibitors.

(iii) The optimal sequence of chemotherapy nanoparticles and molecular inhibitors: Utilizing nanoparticle release models in conjunction with protein expression models can yield cell viability estimates for treatment optimization. This contribution has the most significant medical and clinical relevance.

Chapter 2

Biological and Medical Background

2.1 Cancer

Cancer is the result of genetic mutations that accumulate through the generations of a cell's progeny. These mutations lead to abnormal cells, typically characterized by unregulated proliferation, that are detrimental to an organism's survival. A cell population is considered cancerous when these mutations lead to their uncontrolled proliferation and intrusion into nearby tissues. In humans these cancer cells can interfere with the normal functioning of the body and if left untreated can metastasize to other tissues and lead to death. While some forms of cancer do not form a solid mass, such as leukaemia (cancer of the blood/bone marrow), our focus will be on solid tumours that possess most or all of the following capabilities: avoidance of apoptosis (the natural cell death trigger), self-sufficient growth signalling, antigrowth signal insensitivity and unlimited replicative potential [15]. Along with these traits, solid tumours promote angiogenesis, the growth of new vessels from pre-existing vessels. They facilitate this by upregulating the production of proangiogenic growth factors and developing insensitivity to antiangiogenic growth factors, leading to tumour vasculature [16] (see Section 2.1.1). In light of recent evidence it has become increasingly clear that cancer cells also reprogram their energy metabolism pathways and can evade the immune system [17]. Most lethal is their invasive nature, a result of decreased cell-cell adhesion due to disruption of the normal production of integrins that tether cells to the extracellular matrix (ECM). In addition, they can often degrade the surrounding ECM in order to facilitate their movement within the tissue. The invasiveness of cancer cells poses

a threat to the viability of normal cell populations as they become crowded and attempt to create space by triggering their own death or those of surrounding normal cells. The normal cells are also deprived of oxygen and nutrients as these invaders use their resources to fuel their movements and proliferation. This invasion is often not limited to those tissues that are directly adjacent to the tumour. Tumour cells often metastasize, making their way into blood vessels or the lymphatic system, using the vasculature for transport to other parts of the body. This process is very complex and includes the original event of entering the vasculature, the process of eventually extravasating into tissue, adapting to this new microenvironment and finally the development of another cancer cell colony that could lead to a secondary tumour. Pioneering attempts by cancer cells commonly fail, but the ones that do succeed will themselves have the potential to colonize further.

Each of these cancer cell traits must be taken into consideration when attempting to treat a tumour (and when attempting to model their behaviour). Their ability to avoid apoptosis and senescence implies that natural cell death is relatively rare and must therefore be triggered (directly or indirectly) by an agent. Their accelerated proliferation can be exploited by using drugs that target rapidly dividing cells. The promotion of angiogenesis can be countered by antiangiogenic agents that target endothelial cells or inhibit proangiogenic factors. The invasive nature of cancer implies that in many tissues, the surrounding area must also be treated in case cancer cells have migrated to these areas. While metastasis continues to be the most consistent indicator of negative prognosis, this is countered primarily by expedient treatment and early detection efforts.

2.1.1 Tumour angiogenesis

Ever since the extremely important connection between angiogenesis and tumour growth was established in [16], the field of oncology has been revitalized by the advent of antiangiogenic treatments. When a tumour begins to form, the survival of the cell colony is completely dependent on the diffusion of oxygen and nutrients in its immediate vicinity. However, after it reaches a certain size, approximately 2–3 mm in diameter, the center of this cell cluster can no longer be sustained by the inadequate amount of oxygen attainable via simple diffusion, a condition known as hypoxia. In response to this, the effected cells begin to release hypoxia-inducible factors (HIFs). These HIFs are responsible for triggering the production of proangiogenic factors in nearby cells, most prominently (and heavily-studied) among them being those in the vascular endothelial growth factor (VEGF)

family. These factors initiate signalling cascades that begin the complex process of tumour vascularization. Typically there is a balance between the action of proangiogenic and antiangiogenic factors which leads to vessel maintenance in normal tissues. However, the increased proangiogenic factor production in tumours disrupts the delicate balance between angiogenic inducers and inhibitors [18].

These processes are very effective in causing blood vessels to sprout from nearby existing vasculature, however, the development of the vessels is hasty and unregulated. The balance between proangiogenic and antiangiogenic factors is disrupted to the point that vessel construction and network structure are sacrificed. Tumour vasculature is often highly tortuous and inefficiently assembled, with the vessels typically exhibiting large fenestrations and poor pericyte coverage (pericytes are cells that wrap around endothelial cells and regulate blood flow among many other vessel processes) [19]. These factors lead to both spatially and temporally heterogeneous blood flow. The vessel leakiness results in compromised nutrient and oxygen delivery and contributes to high interstitial fluid pressure (IFP). The cancer cells that originally triggered the angiogenic switch rarely see the benefit of their efforts since these incoming vessels usually penetrate only the tumour rim, leaving the bulk of the tumour with an inadequate oxygen supply. As a result, regions near the center of a tumour often develop into a necrotic core and the hypoxic cells that surround this core maintain constant angiogenic signalling. As the tumour grows, the very dense blood vessels and tumour cells become compacted leading to restricted blood flow and collapsed blood vessels.

2.1.2 Cell metabolism

Cell metabolism can be broadly lumped into two categories, those that are catabolic, breaking down molecules to derive energy, and those that are anabolic, constructing molecules using this energy. Anabolic processes, such as cellular proliferation and motility, are primarily fuelled by adenosine triphosphate (ATP) whilst catabolic processes, such as glycolysis and cellular respiration, are primarily employed to manufacture ATP. Thus ATP is the fundamental carrier of chemical energy in cells. In what follows we will focus on catabolism, specifically the consumption of glucose and the subsequent generation of ATP molecules. While anabolism is certainly central to cancer research as it is responsible for cell growth, division and movement, the models that comprise the bulk of this thesis are concerned with processes that occur on a much faster time scale than tumour growth, and

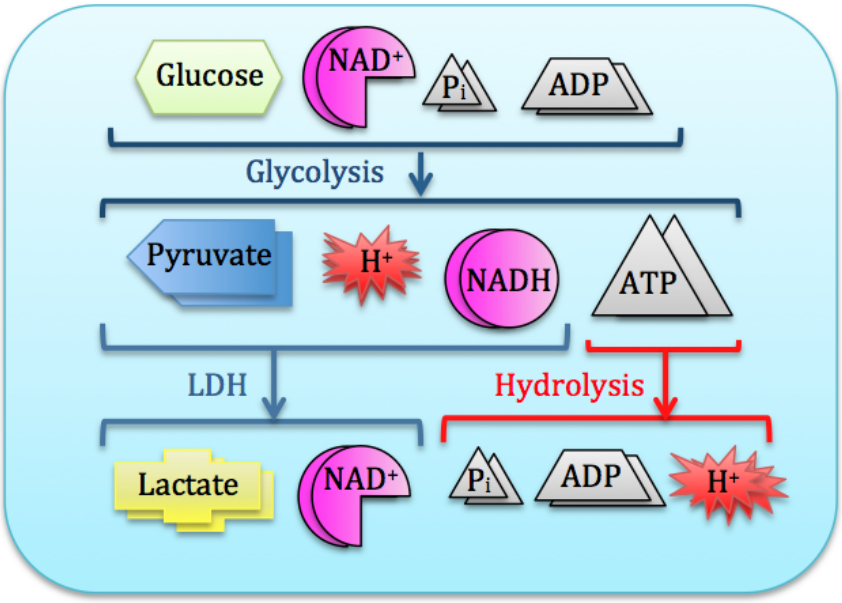

Figure 2.1: A simplified view of glycolysis. The top row contains the molecules required for the ten constitutive steps of glycolysis that convert glucose to pyruvate; see C.5 for the intermediary steps and enzymes. Glycolysis yields two ATP and one NADH. If respiration cannot proceed due to hypoxia, or glucose upregulation then the pyruvate is converted to lactate by lactate dehydrogenase (LDH). Once the ATP is consumed the net reaction is: glucose$\rightarrow$2 lactate+2H^+.

thus we generally assume static tumour tissues. As such we will only consider anabolism via the inclusion of ATP hydrolysis in the cytosol.

Before relating how genetic mutations and the tumour microenvironment affect cancer cell metabolism, we will present a highly simplified view of normal cell respiration including glycolysis, the citric acid cycle (CAC) and the electron transport chain (ETC). As mentioned above, the primary goal of these processes is to produce ATP, either directly via substrate-level phosphorylation or indirectly via the reduction of cofactors, specifically nicotinamide adenine dinucleotide (NAD) and coenzyme Q_{10} (Q), that will be used by the ETC to fuel ATP synthesis.

In normal adequately oxygenated tissues the primary source of ATP is the process of cellular respiration. The complete conversion of glucose to carbon dioxide and water has an ideal yield of approximately 29 ATP [20] (my calculations, which are the result of the

reactions contained in C.4, purport that this theoretical yield is an overestimate). The preliminary stage of cellular respiration is glycolysis, the conversion of glucose to pyruvate. This process consists of ten enzyme-catalysed steps (given in C.5) and directly produces two ATP and two reduced NAD (NADH). In hypoxic conditions this pyruvate is converted into lactate by the enzyme lactate dehydrogenase (LDH) to regenerate the essential oxidized cofactor NAD^+. This process, including ATP hydrolysis, which regenerates adenosine diphosphate (ADP) and phosphate (P_i), is shown in Figure 2.1. The net reaction for glycolysis is then: glucose$\rightarrow$2 lactate+2 H^+.

In oxygenated conditions the pyruvate is transported across the inner mitochondrial matrix and the malate-aspartate shuttle enables the NADH in the cytosol to reduce a NAD^+ in the mitochondrion. The pyruvate is decarboxylated and then enters the citric acid cycle. The citric acid cycle directly generates 1 more ATP per pyruvate (2 per glucose). One pyruvate molecule's pathway can also produce four NADH and one reduced Q (QH_2). A pictorial summary of this process is provided in Figure 2.2 and the details are found in C.5.

The primary energy payoff is a result of cofactor oxidization that enables the electron transport chain (ETC) to establish a proton gradient across the inner mitochondrial matrix. Ten H^+ are deposited in the intermembrane space per NADH, and 6 per QH_2. ATP synthase then utilizes the electrochemical gradient across the mitochondrial matrix to drive the phosphorylation of ADP at a cost ratio of 10 H^+ for 3 ATP [21]. The simplified version of the reactions involved with the ETC are given in C.5 and the net effect on intermembrane space protons is shown in Figure 2.3.

The summary given above is a highly simplified version of metabolic biochemistry. A more in-depth view of the reactions is given in C.4 where the impacts of transport across the cell membrane and the inner mitochondrial membrane are detailed along with summary reactions of the above processes.

2.1.3 Tumour metabolism and acidosis

The metabolic scenario described above corresponds to the case of a tissue that has access to sufficient nutrients and oxygen. There are a number of factors, including increased metabolic requirements to support uncontrolled proliferation, tumour blood vessel properties and acidosis that compound to create a much altered metabolic landscape in tumours.

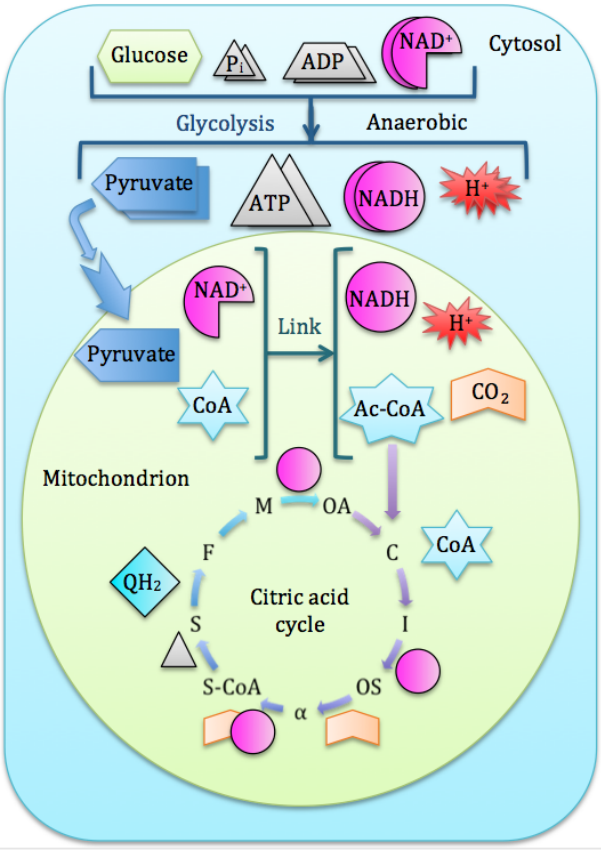

Figure 2.2: The components of cellular respiration excluding the electron transport chain are presented here. The first step is the conversion of glucose to pyruvate via glycolysis followed by transport of the pyruvate into the mitochondrion. The pyruvate is decarboxylated to acetyl-CoA, reducing a NAD and fuelling the CAC. The CAC intermediaries are denoted with their first letter. One full 'revolution' of the CAC directly produces three more NADH, one ATP and one reduced Q (QH_2).

The inefficient structure of the tumour vasculature network is directly responsible for high interstitial fluid pressure and the lack of oxygen and nutrients that most tumours experience. In addition to releasing HIFs that trigger tumour angiogenesis, tumour cells can also alter their metabolic pathways. Typically, in the presence of sufficient oxygen, cells prefer to use respiration to produce energy. However, in the tumour microenvironment there are typically regions experiencing hypoxia or anoxia, leaving them unable to perform aerobic respiration. Instead, they must rely on the consumption of glucose via the process

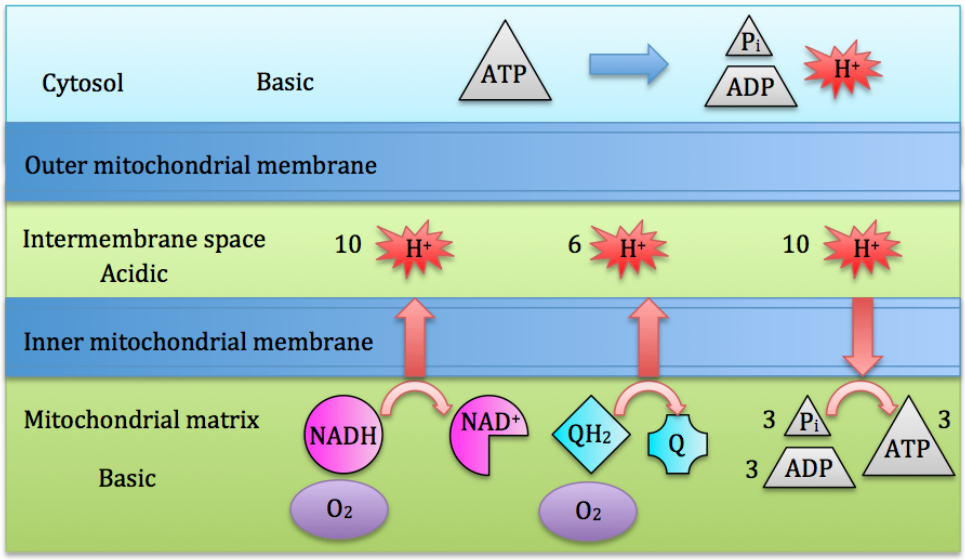

Figure 2.3: Ten H^+ are deposited in the intermembrane space per NADH, and 6 per QH_2. ATP synthase then utilizes the electrochemical gradient across the mitochondrial matrix to drive the phosphorylation of ADP at a ratio of 10 H^+ per 3 ATP [21]. ATP generated in the mitochondrion can be consumed by cellular processes in the cytosol. The acidic statuses of mitochondrion components are also shown.

of glycolysis for their energy needs. The drawback of utilizing predominantly glycolysis is the resulting acidification of the microenvironment. The net byproducts produced by this metabolism are more acidic than those from respiration. The issue is compounded by the fact that even in the presence of sufficient oxygen, cancer cells continue to rely on glycolysis as their primary metabolism. There is still no consensus as to the cause of this phenomenon, known as the Warburg effect [22], although by not requiring oxygen, it could give tumour cells a proliferative advantage [23]. The resulting acidosis from upregulated glycolysis is considered to be a key factor in the invasiveness and metastatic activity of cancer cells as they try to escape the toxic microenvironment [24].

Some very interesting experimental results, reported in [5] show that cancer cell metabolism and acidosis may be more complicated than originally suspected. They took measurements of pH and oxygen concentration around single microvessels, the first time this had been done, to give average radial profiles of these quantities. Perhaps surprisingly, there was a plateau observed in the pH measurements, located approximately 100 to 170 μm away

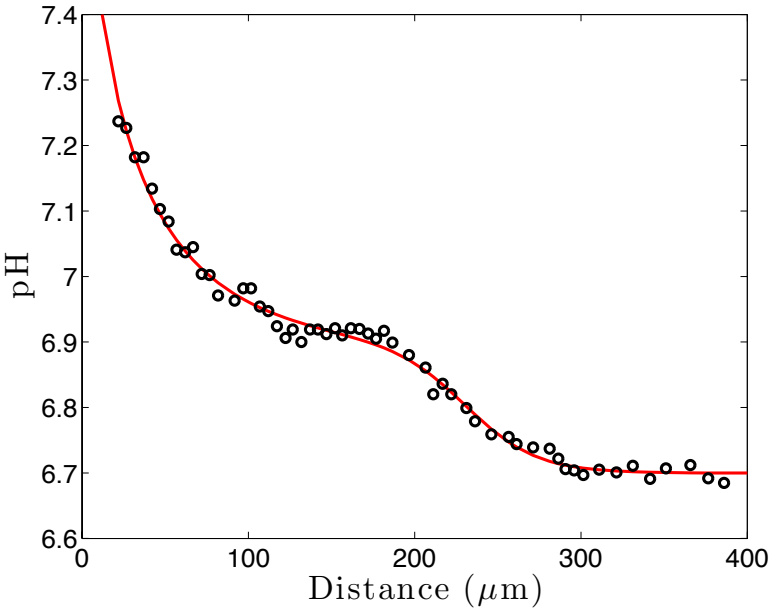

Figure 2.4: The average pH profile surrounding a single microvessel [5]. The smooth curve is a simple functional fit to the data.

from the vessel as can be seen in Figure 2.4. It was surmised to be a consequence of the tumour cells performing respiration even in anoxic conditions or a lack of glucose preventing glycolysis. An alternative explanation of this is provided by a mathematical model [25] and will be revisited in Sections 3.4.2 and Chapter 5.

There is also an emerging metabolic story in tumours of a symbiosis existing between lactate-producing glycolytic cells and lactate-consuming respiratory cells whereby lactate is converted back into pyruvate via LDH and fed into respiration. This has been observed since the 80s [26] but rekindled interest due to successful cancer treatment that blocked lactate transport [27]. The phenomenon of metabolic symbiosis (and the effects of metabolic inhibition) will also be investigated in Chaper 5.

2.2 Cancer treatments

Prior to the seminal work of Folkman [16], and the subsequent development and integration of antiangiogenic therapy into mainstream clinical use, the focus in oncology had always

been on surgical techniques and cytotoxic therapies aimed at *directly* removing or killing cancer cells. Here, I will omit discussions of two very important and common treatment strategies, surgery and radiotherapy, and focus on those that will be the topic of the mathematical modelling to follow: chemotherapy, antiangiogenic agents and molecular inhibitors. Drug delivery vehicles such as nanoparticles, and treatment combinations will also be discussed.

2.2.1 Chemotherapy

Chemotherapy involves the administration of drugs that directly kill cancer cells. Unfortunately, this cytotoxicity is rarely specific to tumour cells alone leading to the death of normal cells as well. Most often, these drugs damage the DNA or inhibit microtubule formation which kills rapidly dividing cells. This results in a wide array of side effects that limit both the size of the dosage and the frequency of administrations. Initially, chemotherapy agents were used primarily on those tumours that were beyond the physical limitations of the surgical and radiotherapy techniques of the time. However, they are now frequently used, targeting many different cellular pathways. For example, one of the more commonly used agents, doxorubicin, discovered and shown to have anti-tumour effects by DiMarco et al. [28], induces apoptosis by essentially wedging itself between the two DNA strands (intercalation) inhibiting transcription and replication. The chemotherapy drug that will be of most interest to us here, is cisplatin, a platinum-containing drug that is capable of binding to DNA bases and can cause crosslinking of DNA strands [29]. When the cell attempts to repair this DNA damage, apoptosis is triggered once it is deemed impossible. This cell-killing mechanism is widely effective and thus used in the treatment of testicular, ovarian, cervical, lung and breast cancer among others [30, 31, 32].

The combination of chemotherapy agents with other treatments presented a major leap forward in oncology, starting with adjuvant therapy, the administration of chemotherapy agents after surgery to kill the remaining cells. The next step was combination chemotherapy which employed different cytotoxic agents administered concurrently. These met with success in certain forms of leukaemia and lymphoma and these types of drug cocktails are still researched extensively today. Today, chemotherapy is often combined with antiangiogenic agents, that target tumour vasculature, and molecular inhibitors, that can prevent chemoresistance, leading to questions of optimal scheduling; the latter case will be addressed in Chapter 6. Also of concern in chemotherapy research is the efficient delivery of

chemotherapy agents and their ability to preferentially target cancer cells. These concerns will be described shortly when drug delivery vehicles are introduced.

2.2.2 Antiangiogenic agents

In recent years the focus of cancer treatments has shifted, with the realization that tumours are dependent on angiogenesis for sustained growth and metastasis, to the development of antiangiogenic treatments. Originally, the rationale was that destroying all tumour vasculature would starve the tumour of essential nutrients and oxygen leading to tumour cell death. When endothelial cell killing drugs such as combretastatin were first injected into a tumour, the antiangiogenic effects were deemed to be significant and fast-acting [33], yet the majority of tumour cells remained unaffected. This outcome is due to a number of factors but most importantly, many types of cancer cells can survive under hypoxic conditions until vasculature is re-established. Not only does the tumour survive, it also leaves the source of angiogenic signalling intact ensuring the recurrence of tumour angiogenesis. Moreover, with no functioning vasculature in the tumour, the delivery of chemotherapy drugs to the tumour is highly compromised, severely reducing treatment efficacy [34]. An alternative to this approach, coined vascular normalization [35], involves applying enough antiangiogenic drugs to prune underdeveloped or unnecessary vessels and remodel the network. This would theoretically lead to a more regular blood vessel structure that could provide a means of effectively delivering chemotherapy drugs in a more homogeneous fashion to the tumour. While this could also lead to the improved delivery of oxygen and nutrients to the tumour, this effect would hopefully be inconsequential. Some successes have been documented [36], but the main limitation remains: this state of normalized vasculature lasts for a brief period of time, referred to as the normalization window, followed by either a return to an irregular, dense system or, on the other hand, an overkill of the endothelial cells.

While the efficacy of antiangiogenic treatment strategies remains far from established, there have been a number of different angiogenic mechanisms successfully exploited for antiangiogenic treatments. There are many types of drugs which target endothelial cell proliferation in various ways, some similar to regular chemotherapy drugs. While not specifically antiangiogenic, standard chemotherapy agents have been shown to have antiangiogenic effects even before they begin to kill tumour cells [37]. There are a few that do attack endothelial cells directly such as combretastatin, angiostatin and endostatin.

Combretastatin disrupts the cytoskeletal structure of the endothelial cells causing them to change into a balloon-shape resulting in vasculature breakdown [38]. Others inhibit the migration or adhesion of endothelial cells. The other key area of antiangiogenic therapy are those that indirectly target the endothelial cells by instead targeting various signalling integrins and factors.

Naturally, due to its large role in tumour angiogenesis and consistent overexpression by cancer cells, VEGF is a prime target of antiangiogenic therapy. The two most common ways to prevent the angiogenic action of VEGF are by blocking its receptors or directly inhibiting it. In the former case, a small molecule which blocks tyrosine kinase receptors is administered, preventing the binding of VEGF. Two of these drugs are now commercially available, sunitinib (Sutent) and sorafenib (Nexavar) while there are a handful more in clinical trials. The side effects of these treatments are rarely serious but due to their nonspecific receptor targeting there is a wide array of possible side effects. Factor inhibiting agents were the first type of anti-VEGF drug developed and the monoclonal antibody bevacizumab was the first anti-angiogenesis drug to be successfully combined with chemotherapy in a Phase III trial [39] and has now been used in various clinical scenarios [40]. Bevacizumab recognizes all of the VEGF isoforms and has widespread clinical applications. The most serious side effects include the impairment of wound healing and the suspension of the body's natural blood vessel maintenance which has made the research focus turn toward drug localization. Large fenestrations in the tumour vasculature lead to some natural targeting of the areas around the tumour but drug delivery vehicles (see Section 2.3) will improve targeting capabilities. Both forms of anti-VEGF treatments are now primarily used in combination with chemotherapy drugs or radiotherapy.

Other forms of antiangiogenic treatment have been proposed, some even the result of mathematical models that show a specific mechanism to be a worthwhile target. For instance, the blockade of the coupling between VEGFR-2 and its co-receptor NRP1 was shown to be a good strategy in [41] yet such an inhibitor has not yet been developed.

Various aspects of antiangiogenic drug treatments will be investigated in Chapter 4 including the augmentation of antiangiogenic factors and the inhibition of proangiogenic factors.

2.2.3 Molecular inhibitors

With ever-increasing knowledge of cell signalling pathways, automated molecular discovery algorithms and the emergence of systems biology, the list of potential cellular targets and corresponding potential cancer treatments grows by the day. However, there is still hope that the very potent cytotoxic agents already developed can be made to be more effective by overcoming their main drawbacks: side effects and resistance. The side effects can be reduced by improved targeting and delivery techniques which will be described below. Chemoresistance on the other hand can be counteracted by targeting specific molecules of signalling networks that elicit an anti-apoptotic response [42]. Here, we will discuss a specific instance of this phenomenon that will be the focus of the study in Chapter 6.

In previous studies, a chemotherapy drug described above, cisplatin, has been shown to upregulate PI3K signalling, which can reduce the cytotoxic effects of cisplatin and thus cause the cells to display chemoresistance [43]. This suggests the application of a PI3K inhibitor in combination with cisplatin could increase the anti-tumour effect. The question of the scheduling of molecular inhibitors with chemotherapy is the primary concern of Chapter 6.

2.2.4 Other treatments

While some of the most popular forms of treatment have been outlined, there are many others which will not be included in the mathematical models to follow but those with potential for significant clinical benefits could be considered in future modelling attempts. Various hormonal therapies have gained prominence across genders since breast and prostate cancers rely heavily on specific hormones for tumour growth. Immunotherapy is a treatment that relies on the patient's immune system to fight the cancer. This can be achieved by giving monoclonal antibodies that can identify antigens specific to the tumour cells. In fact, the antiangiogenic drug bevacizumab can be thought of as a form of immunotherapy against tumour vasculature. The developing field of radioimmunotherapy which uses radioactively conjugated antibodies to target tumour antigens holds promise in treating radio-sensitive tumours (such as lymphomas [44]). Along with gene therapy and photodynamic therapy, there are countless other biological mechanisms that are targeted by current cancer treatments and as more viable targets are found, additional molecules will be fashioned to exploit them.

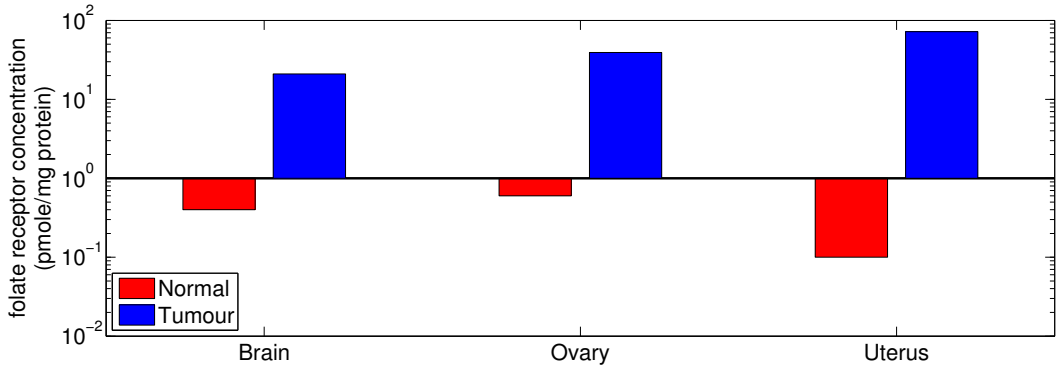

Figure 2.5: Comparing the levels of folate receptors on the cell membrane of normal tissues with medium or high grade tumours. Adapted from [48] using data from [49].

2.3 Drug delivery vehicles

By administering drugs in nanoparticles, many advantages over direct administrations of free agents have been observed [45]. Improved tumour cell specificity can be achieved by natural and engineered tumour targeting, longer circulation times are obtained by avoiding the immune system and slowly eroding layers lead to sustained drug release.

Natural tumour targeting is exhibited by most nanoparticles larger than 100 nm since the typical pore size in normal blood vessels is approximately 50 nm while the size of tumour vasculature pores can be upwards of 500 nm. Due to their size, the nanoparticles cannot escape the tight gap junctions of normal blood vessels leading to their extravasation primarily in the tumour vicinity. Once they exit the blood vessel, they are trapped in the tumour tissue. This increases the efficiency of the contained agents and decreases the severity of side effects in the normal tissue. Exploitation of this natural targeting process, known as the enhanced permeability and retention (EPR) effect and coined in [46], is a critical consideration for reducing side effects and successful delivery of therapeutics to tumours [47].

In addition to this natural targeting, nanoparticles also enable bioengineered attempts at increasing cancer cell targeting capabilities. Most commonly, a ligand is attached to the nanoparticle surface whose corresponding receptor is overexpressed on the cancer cell membrane. The prime example of this technique is folate targeting since folate receptors are overexpressed on the cell membrane of many different cancers. Due to the comparatively

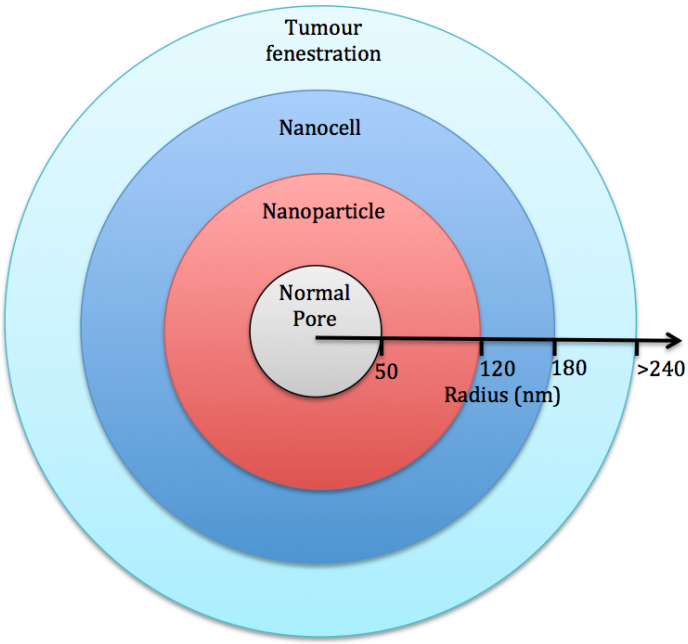

Figure 2.6: Approximate sizes of nanocell and nanoparticle core in relation to normal and tumour pores. Data from [53].

low concentration of folate receptors on most types of healthy cells, this was identified as a possible marker that could be targeted, see Figure 2.5. By attaching folic acid to both liposomal [50] and polymer nanoparticle surfaces, these nanoparticles would be preferentially taken up by the tumour cells, leaving normal cells mostly unaffected [51].Many other cell surface receptors have been exploited for cancer treatment targeting. Tumour vasculature has also been targeted, commonly using the $\alpha_v\beta_3$ integrin as a target for antiangiogenic therapies [52].

The immune system is a large obstacle to overcome for successful drug delivery. As soon as a foreign substance is detected in our bloodstream, our immune system tags them for removal (opsonization) and then macrophages remove them. Therefore, the drug delivery system must attempt to avoid this natural process. By attaching certain polymers to the surface of the nanoparticle envelope, the tagging proteins are prevented from binding to the nanoparticle. A concern that must be kept in mind is that in order to successfully target cancer cells via receptor-ligand binding, the density of these polymers cannot be so high as to interfere with this process.

Nanoparticles are typically either lipid-based or polymer-based. Lipid-based nanoparticles can be lumped into two categories based on the number of phospholipid layers they contain: single-layered micelles and double-layered liposomes. Micelles are good for carrying hydrophobic agents and are relatively straightforward to create. However, they have relatively short release times since after injection they are rapidly dissolved to below the minimum micelle concentration. Liposomes have the advantage of being able to carry both hydrophobic and hydrophilic drug in a single delivery vehicle and have longer circulation times due to the increased stability of the structure. They can also fuse with other lipid bilayers such as the cell membrane, aiding in drug delivery. The main disadvantage of these lipid-based vehicles is their surfaces are not easily modifiable for targeting or immune system avoidance [45].

Polymer-based nanoparticles, usually forming a nanocapsule or nanosphere, are typically upwards of 100 nm in diameter in order to take advantage of the EPR effect. The major advantage of polymer-based nanoparticles over lipid-based nanoparticles is their stable surface structure. This allows for various surface modifications that can dissuade the immune system and preferentially target cancer cells as described above. However, as we shall discuss below, a combination of lipid and polymer-based delivery may be advantageous.

Nanocells

Pioneered by Shiladitya Sengupta at the labs of MIT, nanocells are delivery vehicles that have the ability to trap different agents in separate layers of lipids and polymers. Nanocells can target cancer cells, in much the same way as nanoparticles, by attaching ligands corresponding to overexpressed receptors to their surface. They are approximately 150 nm in diameter, allowing them to take advantage of the EPR effect. Initial trials were reported in [53] and used a nanoparticle core (nanocore) loaded with doxorubicin (chemotherapy) inside of a lipid envelope containing the antiangiogenic drug combretastatin. The nanoparticles were heterogeneous in size, so they were filtered and only those between 80–120 nm were covered in lipids to form nanocells; see Figure 2.6 for the comparative average (desired) sizes of the nanoparticle and the nanocell complete with lipid layer. This delivery vehicle enables the controlled temporal release of two separate drugs in a single administration. First, the outer lipid-bound antiangiogenic agents are released and destroy or prune the surrounding vasculature. The chemotherapy nanoparticles are now captured inside the

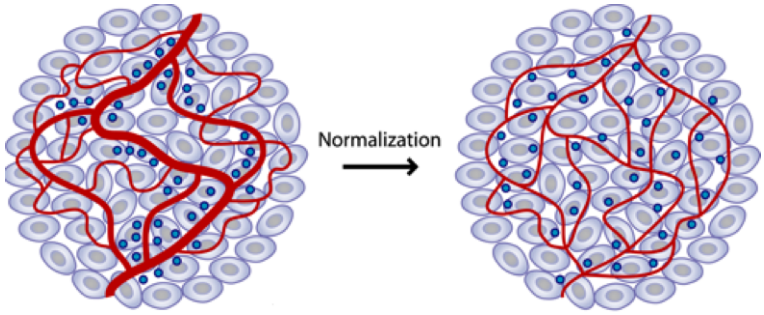

Figure 2.7: The antiangiogenic agent in nanocells leads to tumour vasculature normalization and the trapping of chemotherapy agents in the tumour [55].

tumour, liberating cytotoxic agents as they erode (this process is illustrated in Figure 2.7). This research area has 'taken off' with many centers investigating the concept of a nanocell with recent attempts at improving folate-targeted nanocells reported in [54].

2.4 Treatment strategies and combinations

The maximum-tolerated dose (MTD) method was a popular treatment technique amongst oncologists during the 1950's and 60's. Since typical chemotherapy drugs have serious side effects due to their toxicity to normal cells as well as cancer cells, there is an upper limit on the drug dosage that can be administered to an individual in a single administration without risking the patient's life. This amount is referred to as the MTD and anything above this amount is potentially lethal. The MTD requires a break of weeks between administrations allowing the patient to recover from the treatment and effected healthy cells to repair. Unfortunately this also gives the cancer cells time to reproduce. While this method has fallen out of favour, the MTD is still often explored during experiments and considered at certain points during a patient's treatment.

The metronomic technique, coined in [56], is different from MTD in both the scheduling and dosage of treatments. Dosages much lower than the MTD are used and thus less recovery time is needed between treatments. These treatments are applied more frequently, even daily and have been shown to cause less side effects and improved tumour response. This technique has been shown to provide increased antiangiogenic effects (reviewed in [57]) since the tumour vasculature does not have time to repair during breaks in treatment [58]. These two extremes of cancer treatment scheduling can be viewed as a spectrum with

continuous low dose at one end of the spectrum and an infrequent MTD at the opposite end.

A more complicated question than individual drug dosing is how to schedule the treatments of multiple methodologies to optimize the anti-tumour effect. My Master's thesis [59] focussed primarily on the optimal scheduling of antiangiogenic drugs and chemotherapy, using a mathematical model to predict the benefits of tumour vessel normalization. Here, we will not look at this specific combination but instead at a combination of cisplatin-nanoparticles and the molecular inhibitor described above (PI3K inhibitor) that has been demonstrated to aid in overcoming chemoresistance.

2.5 Summary

The understanding of cancer biology has expanded exponentially over the past couple of decades; historically one of the largest threats to life with no known cure, advanced treatment techniques greatly improve chances of survival. The discovery of the importance of tumour angiogenesis led to the development of antiangiogenic treatments which in combination with traditional chemotherapy agents have improved clinical outcomes. Improved targeting and increased circulation time of these agents have been achieved due to drug delivery vehicles such as nanoparticles. The surface of nanoparticles can be manipulated to target specific cancer cell receptors and to degrade in a controlled way. The recent advent of nanocells that have the aforementioned advantages along with the ability to carry multiple agents could be the next leap forward for efficient delivery and tumour eradication. The diagrammatic summary contained in Figure 2.8 and explained below will outline the topics that will be of importance in this thesis. These areas span a wide breadth of cancer research but still comprise only a minute niche of the field.

A diagram containing the most relevant interactions and causal relationships between tumour microenvironmental factors, treatment effects, treatment targets and tumour behaviour is presented in Figure 2.8. The entries contained in the leftmost column, with the exception of cell survival, are not explicitly included in the models that follow but are the tumour responses to the tumour traits and microenvironmental conditions listed in the second column. These omitted phenomena include tumour invasion in response to hypoxic or acidic conditions, metastases enabled by tumour blood vessels and cellular proliferation fuelled by metabolism. The tumour properties in the second column include

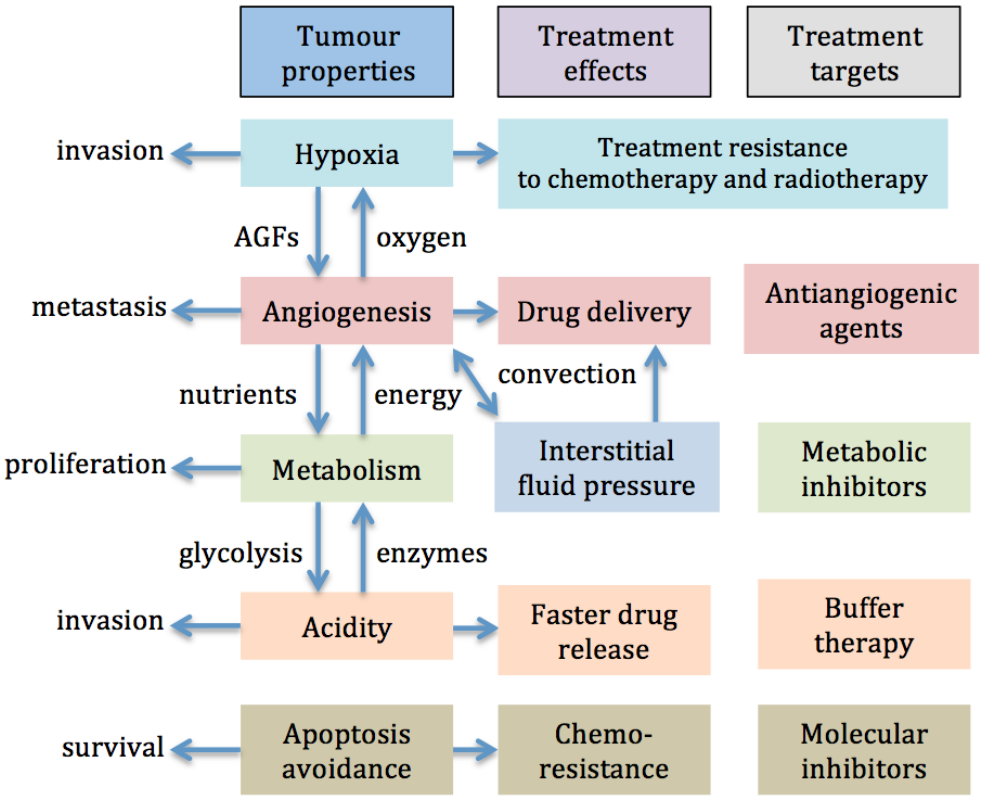

Figure 2.8: Interactions and relationships between the major components of cancer biology and treatments that are the focus of the models contained in this thesis. The leftmost column are tumour responses to microenvironmental factors that, with the exception of cell survival, are not the focus of the models to follow. Tumour properties are linked as follows: Hypoxia leads to **AGF** production that initiates angiogenesis; angiogenesis provides **oxygen** to the tumour; this angiogenesis also provides **nutrients** for cell metabolism, which produces **energy** for angiogenesis and cell proliferation. Tumour metabolism is predominantly **glycolysis** which acidifies the environment; this acidity can impede metabolic **enzymes**. Cancer cells can also avoid apoptosis by ignoring apoptotic signals. These properties affect the outcome of cancer therapies. Hypoxia decreases the efficacy of chemotherapy and radiotherapy; angiogenesis enables drug delivery while the leaky walls of tumour vessels lead to **convection** of drugs and AGFs; acidity causes rapid drug release from delivery vehicles; pro-survival signalling also increases chemoresistance. These properties can be exploited by therapies: angiogenesis is targeted by antiangiogenic agents, metabolic inhibitors can halt ATP production, buffer therapies could normalize acidity, and molecular inhibitors can overcome chemoresistance.

the most substantial links between them. Hypoxic microenvironmental conditions lead to AGF production (via HIFs) that initiates angiogenesis. The resulting angiogenesis provides oxygen to some cells but hypoxic populations typically remain at all times. Angiogenesis also provides nutrients for cell metabolism, which produces energy for angiogenesis, cell proliferation and many other cellular processes. Tumour metabolism relies predominantly on glycolysis, a process which acidifies the environment. The resulting acidosis can reduce enzyme functionality and further alter metabolic pathways (e.g. increased reliance on glutaminolysis). In addition to these interconnected properties cancer cells can also avoid apoptosis by ignoring anti-growth signals and producing pro-survival signals. This cell survival is typically the result of genetic mutations (as is much of the altered cell metabolism).

The aforementioned tumour characteristics also affect the outcome of cancer therapies and are shown in Figure 2.8 under 'Treatment effects'. Hypoxia decreases the efficacy of chemotherapy (since these cells proliferate less) and radiotherapy. Angiogenesis enables drug delivery and the blood vessel structure enables the EPR effect. These leaky walls of tumour vessels lead to elevated interstitial fluid pressure. The resulting pressure gradient leads to convective flow that can dramatically impair drug delivery and alter AGF concentrations. Acidity promotes more rapid drug release from delivery vehicles due to accelerated erosion. Upregulated pro-survival signalling, and other cellular adaptations, result in decreased chemotherapy efficacy, known as chemoresistance. However, all of these properties can be exploited as shown in the rightmost column under 'Treatment targets'. Tumour angiogenesis suggests the application of antiangiogenic agents to eradicate vessels or normalize the vessels. Metabolic inhibitors could be applied to impede glycolysis or respiration while buffer therapies could normalize acidity, thus reducing invasion. Finally, molecular inhibitors could be applied to encourage cell apoptosis to occur upon administration of cytotoxic agents.

Our attention will now turn to modelling the entities that affect the tumour microenvironment and cancer treatments described above. Previous models will be reviewed in the next chapter in order to lay the foundation for the mathematical models contained in the original research discussed in Chapters 4–6.

Chapter 3

Mathematical Modelling Background

The development of mathematical models that accurately predict tumour growth has been an ongoing field of research for over fifty years. The first models were simple ordinary differential equations (ODEs) typically borrowed from ecology. The parameters in the models were estimated from limited experimental data. The evolution of these model systems exhibits ever-increasing complexity as more aspects of the tumour microenvironment and the effects of cancer treatments are included. Mathematical models can be simplified by assuming spatial homogeneity and symmetry, strict time-dependence, which does not take into account spatial effects, or steady state. These models are now complemented by ones with more complex formalisms that include tumour heterogeneity, a defining characteristic that determines, among many others, local growth rates [60], metabolic behaviours and treatment response. For continuous spatio-temporal models, we use partial differential equations (PDEs) that have enabled modellers to simulate heterogeneity by adding tumour vasculature, growth factor concentrations, and drug distributions [59]. Tumour metabolic behaviour and the resulting acidosis have also been modelled, whereby the tumour growth and invasive capability are linked by the development of hypoxia resistant and acidity resistant populations of cancer cells [24, 61]. Efforts continue to develop spatial models that include accurate tumour vasculature and concentrations of metabolites, signalling factors and various treatment types. Developing a model of this type has been the focus of my previous work while the focus of this thesis is the development of three interconnected mathematical models spanning the processes of angiogenesis, metabolism and chemoresistance.

The predominant mathematical oncology models that have guided my work will be pre-

sented in this chapter. First, a mathematical model of interstitial fluid pressure and velocity developed by Jain et al. [62] will be considered on both the microscale ($\sim 10^{-4}$ m=100 μm) and the macroscale ($\sim 10^{-2}$ m=1 cm). This model is critical to developing models for the convective transport of solutes including AGFs. General solute transport equations including convection, diffusion and ion migration are also developed on these spatial scales. We will then formulate specific applications of these equations. The first application, modelling of angiogenic growth factors (AGFs), will be outlined, where diffusion-reaction equations are used to predict angiogenic activity. This model will be extended in Chapter 4 to include the well-established and prevalent convective transport in solid tumours. We will then turn our attention to models of tumour metabolism including the work of Casciari et al. [3, 4], which links metabolism and acidity on the macroscale and Molavian et al. [25], which does this on the microscale. Other models of cell metabolism that contribute to the development of functional forms for metabolite consumption, e.g. [63, 64, 65] will also be touched upon. These will all contribute to the modelling contained in Chapter 5, which consider metabolite consumption on the microscale and their effect on acidosis. The novel nanoparticle release, protein expression and cell viability model contained in Chapter 6 remain independent of the mathematical background given below.

3.1 Interstitial fluid pressure

Based on studies of fluid and molecule movement in tumours through interstitial space [66] and through the blood vessel wall [19], a series of papers developed models for fluid and macromolecule transport ([67, 68, 69, 70]) and were used to explain various phenomenon such as the heterogenous distribution of monoclonal antibodies (mAbs) in tumours [62]. The fluid transport models are rigorously derived in [71] and a simplified formulation will be outlined here for predicting IFP. This will be followed in the next section by its effect on macromolecule distribution. This will be needed to formulate the PDEs for macromolecules, such as AGFs and large metabolites.

3.1.1 Microscopic pressure

We adapt the derivation from [71] to calculate the pressure profile in the interstitial matrix surrounding a single blood vessel. The radial distance under consideration is restricted to

some value Ω known as the penetration depth; small enough to ensure limited interactions with neighbouring vessels but large enough to ensure that this local pressure profile, p, approaches the average macroscopic pressure p^* at this distance. We assume this vessel is a rigid cylinder of constant radius ω with negligible changes in the local axial pressure gradient. It is also assumed that this vessel experiences constant vascular pressure p_v (mmHg), the vessel wall has constant hydraulic conductivity L_p (cm/mmHg-s) while the blood plasma has constant osmotic pressure π_v and the osmotic reflection coefficient for plasma proteins is σ_v (the fraction of solute filtered through a membrane if there is zero concentration difference with high filtration rate). This vessel is surrounded by tissue which is treated as a homogeneous poroelastic medium with constant hydraulic conductivity K (cm^2/mmHg-s) and osmotic pressure π_i.

We consider the interstitial fluid on a length scale such that the assumption of it being a continuous entity is appropriate. From the conservation of mass equation, once can derive the formula

$$\frac{\partial \rho}{\partial t} = -\nabla \cdot \mathbf{J}$$

where $\mathbf{J}$ is the mass flux and ρ is the density of the fluid. The flux of the fluid is given by $\mathbf{J} = \rho \mathbf{v}$ where $\mathbf{v}$ is the interstitial fluid velocity. This give a differential equation

$$\frac{\partial \rho}{\partial t} + \nabla \cdot (\rho \mathbf{v}) = 0,$$

referred to as the continuity equation for fluids. Expanding the second term using the product rule gives:

$$\frac{\partial \rho}{\partial t} + \nabla \rho \cdot \mathbf{v} = -\rho \nabla \cdot \mathbf{v}. \tag{3.1}$$

For incompressible flow, it is assumed that ρ is constant within an infinitesimal volume dV that moves at the velocity $\mathbf{v}$ of the fluid. This is equivalent to assuming that the material derivative of the fluid, denoted $D\rho/Dt$, and given by

$$\frac{D\rho}{Dt} = \frac{\partial \rho}{\partial t} + \nabla \rho \cdot \mathbf{v},$$

is equal to zero. This expression can be identified as the left-hand side of (3.1). Putting this together with the fact that $D\rho/Dt = 0$ for incompressible flow, we must have

$$\nabla \cdot \mathbf{v} = 0. \tag{3.2}$$

It should be noted that (3.2) can also be reached by making a stronger assumption: that the fluid itself is homogeneous and incompressible, and thus of constant density. This would mean $\frac{\partial \rho}{\partial t} = 0$ and $\nabla \rho = 0$ in (3.1) giving (3.2) without discussion of the material derivative. The relationship between these two derivations can be summarized by noting that homogeneous, incompressible fluids always lead to an incompressible flow while those fluids undergoing incompressible flow are not necessarily incompressible.

For the geometry we are currently considering, a rigid cylinder with axial and angular symmetry, the interstitial fluid velocity (IFV) in the interstitial space is given by $\mathbf{v} = (u(r), 0, 0)$. Thus, (3.2) becomes

$$\frac{d}{dr}(ru) = 0.$$

where u is interstitial fluid velocity in the radial direction. The IFV of this fluid is related to the IFP by Darcy's Law in a porous medium [72]:

$$u = -K\frac{dp}{dr}. \tag{3.3}$$

Substituting this into the continuity equation gives

$$\frac{d}{dr}\left(r\frac{dp}{dr}\right) = 0. \tag{3.4}$$

Before moving on, we should note that the above derivation of (3.4) corresponds to incompressible fluid flow, however it ignores the fact that tissue is in fact comprised of multiple non-fluid phases, most notably the extracellular matrix and various cell types, whose behaviours are not strictly fluid and are better treated as deformable solids. Many physical models of tumour tissues consider biphasic [73] or even triphasic (separate compartment for vasculature) [74]. These problems can be addressed using mixture theory, which fundamentally assumes that the phases simultaneously exist at each point in space, among other simplifying assumptions which make the equations tractable (e.g. complete saturation, small deformations, etc.). However, despite the complexity invoked by considering multiple phases, if one assumes that the fluid exchange between phases is small [75], that the fluid is experiencing incompressible flow and that the solid is incompressible, then one once again obtains (3.2), see Appendix A for a brief derivation.

For the boundary condition at the vessel wall, we must balance the IFV with the fluid velocity across the vessel wall J_f/S, where J_f is the flux across the vessel wall and S is

the surface area of the vessel wall. This fluid flux was observed to be proportional to the difference between the hydrostatic pressure change, $\Delta p = p_v - p$, and the osmotic pressure change, $\Delta\pi = \pi_v - \pi_i$, across the vessel wall by Starling [76]. This was later altered to account for the vessel permeability of those molecules that contribute to maintaining the osmotic pressure difference, predominantly albumin, via the osmotic reflection coefficient σ_v, which is set to one if the vessel wall is completely impermeable to plasma proteins, and approaches zero as the vessel becomes leakier [77]. Thus, the net fluid loss from a single vessel, J_f (mL/s), is then given by Starling's Law

$$J_f = L_p S[p_v - p - \sigma_v(\pi_v - \pi_i)]. \tag{3.5}$$

This gives us the boundary condition,

$$-K\frac{dp}{dr} = L_p(p_e - p) \qquad \text{at } r = \omega \tag{3.6}$$

where p_e is the effective pressure, $p_e = p_v - \sigma_v(\pi_v - \pi_i)$. The other boundary condition ensures that the macroscopic pressure is reached as we move far away from the vessel

$$p = p^* \qquad \text{at } r = \Omega. \tag{3.7}$$

With these boundary conditions, (3.4) can be solved for p from which the IFV u can be obtained via Darcy's Law (3.3). Before solving we will nondimensionalize the problem as described below.

Nondimensionalizing (3.4) and the corresponding boundary conditions by setting $p = p_e\tilde{p}$ and $r = \omega\tilde{r}$ and rescaling $p^* = p_e\tilde{p^*}$ and $\Omega = \omega\tilde{r}_0$ gives the identical nondimensional equivalent of (3.4) and the boundary conditions

$$\begin{aligned} \frac{d\tilde{p}}{dr} &= -\alpha(1-\tilde{p}) && \text{at } \tilde{r} = 1 \\ \tilde{p} &= \tilde{p}^* && \text{at } \tilde{r} = \tilde{r}_0, \end{aligned}$$

where the nondimensional parameter α is given by $\alpha = L_p\omega/K$. Solving (3.4) yields the solution $\tilde{p}(\tilde{r}) = A\ln\tilde{r} + B$ where A and B are constants. Using the boundary conditions

to solve for the constants yields

$$A = -\alpha\left(\frac{1-\tilde{p}^*}{1+\alpha\ln\tilde{r}_0}\right) \text{ and } B = \frac{\tilde{p}^*+\alpha\ln\tilde{r}_0}{1+\alpha\ln\tilde{r}_0}.$$

With some algebraic manipulation, once can find that

$$\tilde{p}(\tilde{r}) = \frac{\alpha(1-\tilde{p}^*)}{1+\alpha\ln(\tilde{r}_0)}\ln\left(\frac{\tilde{r}_0}{\tilde{r}}\right)+\tilde{p}^*. \tag{3.8}$$

Applying Darcy's Law, and nondimensionalizing the IFV by the characteristic velocity of Kp_e/ω gives

$$\tilde{u}(\tilde{r}) = \frac{\alpha(1-\tilde{p}^*)}{1+\alpha\ln(\tilde{r}_0)}\frac{1}{\tilde{r}}. \tag{3.9}$$

This implies that the fluid velocity at the vessel wall is

$$\tilde{u}(1) = \frac{\alpha(1-\tilde{p}^*)}{1+\alpha\ln(\Omega)}.$$

3.1.2 Macroscopic pressure

Similar to the derivation above, we will now consider an entire spherical tumour of radius R embedded in a host tissue, both of which are considered to be homogeneous and poroelastic media. The average flow across the vessel wall is again given by Starling's Law (3.5) where now the parameters correspond to average values in the entirety of the tissue rather than corresponding to any one specific vessel. In normal tissues, the excess fluid flux by normal vessels J_f would be counteracted by absorption by the lymphatic system. However, in tumours the fluid can either leak toward the core of the tumour, or toward the periphery [62]. Inward flow would lead to increased IFP until the effective pressure, $p_e = p_v - \sigma_v(\pi_v - \pi_i)$, is reached at which point $J_f = 0$. Outward flow would lead to excess fluid entering the interstitium. The interstitial velocity of this fluid, u, is related to the IFP by Darcy's Law (3.3) where now r is the macroscopic distance from the tumour core.

Considering the conservation of mass between the fluid filtered from the vessels with the fluid moving toward the periphery gives

$$\frac{1}{r^2}\frac{d(r^2u)}{dr} = \frac{J_f}{V}. \tag{3.10}$$

Substituting equations Darcy's Law (3.3) and Starling's Law (3.5) into (3.10) yields

$$\frac{1}{r^2}\frac{d}{dr}\left(r^2\frac{dp}{dr}\right) = -\frac{L_p}{K}\frac{S}{V}[p_v - p - \sigma_v(\pi_v - \pi_i)], \tag{3.11}$$

which is typically rewritten as

$$\frac{1}{r^2}\frac{d}{dr}\left(r^2\frac{dp}{dr}\right) = -\frac{\alpha^2}{R^2}(p_e - p), \tag{3.12}$$

where

$$\alpha = R\sqrt{\frac{L_p S}{KV}}$$

is a nondimensional parameter that measures the ratio of the flow resistance in the interstitial space to the resistance in the microvessel wall. With appropriate boundary conditions (3.12) can also be solved analytically. Below we will present a different derivation than that typically found in the literature [67, 2] since the nondimensionalization implicitly assumes the same effective pressure in both tumour and host tissues, involves a far-field boundary condition that fixes the pressure at some value or shifts the solutions by this far-field pressure. Here, we assume far-field zero flux conditions and include the generalization to nonzero effective pressures in the host tissue for the embedded tumour case.

Isolated

Considering the case of an isolated tumour, we can nondimensionalize (3.12) by setting $p = p_e\tilde{p}$ and $r = R\tilde{r}$, which gives

$$\frac{1}{\tilde{r}^2}\frac{d}{d\tilde{r}}\left(\tilde{r}^2\frac{d\tilde{p}}{d\tilde{r}}\right) = -\alpha^2(1 - \tilde{p}). \tag{3.13}$$

To achieve spherical symmetry at the tumour core a no-flux boundary condition is enforced

$$\left.\frac{d\tilde{p}}{d\tilde{r}}\right|_{\tilde{r}=0} = 0. \tag{3.14}$$

Note that the form of (3.13) is very similar to the diffusion-reaction equations that will be considered below for AGF concentrations (3.35) discussed in Section 3.3, so the derivation to follow will be referred to later.

To solve this system we will consider a Dirichlet boundary condition, where at the tumour boundary, we set the pressure to the pressure found in the host tissue, $\tilde{p_h}$ and hence take $\tilde{p}(1) = \tilde{p}_h$.

The nondimensional equation for the equation (3.13) can be transformed into a modified Bessel function in $z(u)$ of order $n = 1/2$ via the substitutions $u = \alpha\tilde{r}$, $z = \sqrt{\tilde{r}}(p-1)$ [78]. This modified Bessel function is

$$u^2\frac{d^2z}{du^2} + u\frac{dz}{du} - z\left(\frac{1}{4} + u^2\right) = 0,$$

which has the general solution

$$z(u) = C_1 I_{1/2}(u) + C_2 K_{1/2}(u),$$

where I_n and K_n are the modified Bessel functions of the first and second kind, respectively. For $n = 1/2$, these functions reduce to the elementary functions:

$$I_{1/2}(u) = \sqrt{\frac{2}{\pi u}}\sinh(u), \quad K_{1/2}(u) = \sqrt{\frac{\pi}{2u}}e^{-u}.$$

Thus, reverting back to our original variables, the solution of (3.35) is of the form

$$\tilde{p}(\tilde{r}) = A\frac{\sinh(\alpha\tilde{r})}{\tilde{r}} + B\frac{e^{-\alpha\tilde{r}}}{\tilde{r}} + 1, \qquad 0 \le \tilde{r} \le 1, \tag{3.15}$$

where the constants A and B will be determined by enforcing boundary conditions.

Considering boundary conditions, the symmetry condition at the tumour core (3.14) can only hold if $B = 0$ eliminating the second term in the general solution. Enforcing the tumour boundary condition gives $A = (\tilde{p}_h - 1)/\sinh(\alpha)$ and so the solution is

$$\tilde{p}(\tilde{r}) = 1 - \frac{1-\tilde{p}_h}{\sinh(\alpha)}\frac{\sinh(\alpha\tilde{r})}{\tilde{r}}.$$

If $\tilde{p}_h$ is set to zero, then the solution typically found in the literature (e.g. [2]) is recaptured.

Applying Darcy's Law and nondimensionalizing u by again setting $u = Kp_e\tilde{u}/R$ gives

$$\tilde{u}(\tilde{r}) = \frac{1-\tilde{p}_h}{\sinh(\alpha)}\left(\frac{\alpha\tilde{r}\cosh(\alpha\tilde{r}) - \sinh(\alpha\tilde{r})}{\tilde{r}^2}\right).$$

Embedded

We now consider the case of a tumour embedded in host tissue. This boils down to the consideration of an infinite spatial domain instead of the finite one considered for the isolated case, where the various parameters change value at the tumour boundary. We differentiate between tumour and host tissue parameters with subscripts (or superscripts for effective pressures) t and h, i.e.

$$\alpha = \begin{cases} \alpha_t, & 0 \leq r \leq R, \\ \alpha_h, & r > R. \end{cases}$$

We will once again nondimensionalize (3.12) by setting $p = p_e^t \, \tilde{p}$ and $r = R\tilde{r}$, to obtain the equation

$$\frac{1}{\tilde{r}^2} \frac{d}{d\tilde{r}} \left(\tilde{r}^2 \frac{d\tilde{p}}{d\tilde{r}} \right) = \begin{cases} \alpha_t^2 (\tilde{p} - 1), & 0 \leq \tilde{r} \leq 1, \\ \alpha_h^2 (\tilde{p} - \hat{p}_e), & 1 < \tilde{r} < \infty, \end{cases} \tag{3.16}$$

where $\hat{p}_e = p_e^h / p_e^t$.

The boundary conditions for this case, in addition to the symmetry condition (3.14), are:

$$\begin{aligned} \tilde{p}|_{\tilde{r}=1^-} &= \tilde{p}|_{\tilde{r}=1^+}, \\ -K_t \frac{d\tilde{p}}{d\tilde{r}}\bigg|_{\tilde{r}=1^-} &= -K_h \frac{d\tilde{p}}{d\tilde{r}}\bigg|_{\tilde{r}=1^+}, \\ \lim_{\tilde{r}\to\infty} \frac{d\tilde{p}}{d\tilde{r}} &= 0. \end{aligned}$$

Performing an analogous procedure to the one outlined above, the nondimensional equation for the system (3.16) can once again be transformed into a modified Bessel function. Thus, reverting back to our original variables, solutions to (3.35) are of the form

$$\tilde{p}(r) = \begin{cases} A_t \dfrac{\sinh(\alpha_t \, \tilde{r})}{\tilde{r}} + B_t \dfrac{e^{-\alpha_t \, \tilde{r}}}{\tilde{r}} + 1, & 0 \leq \tilde{r} \leq 1, \\ A_h \dfrac{\sinh(\alpha_h \, \tilde{r})}{\tilde{r}} + B_h \dfrac{e^{-\alpha_h \, \tilde{r}}}{\tilde{r}} + \hat{p}_e, & 1 < \tilde{r} < \infty, \end{cases} \tag{3.17}$$

where the constants A_e and B_e, $e = t, h$ will be determined by enforcing the boundary

conditions above.

The tumour core and far-field conditions immediately yield $B_t = 0$ and $A_h = 0$ respectively. Enforcing the conditions at the tumour boundary yields two equations for the unknowns A_t and B_h, which can be solved to give

$$A_t = \frac{(\hat{p}_e - 1)(1 + \alpha_h)}{(1 + \alpha_h - K)\sinh(\alpha_t) + K\alpha_t \cosh(\alpha_t)},$$
$$B_h = \frac{(\hat{p}_e - 1)K[\sinh(\alpha_t) - \alpha_t \cosh(\alpha_t)]e^{\alpha_h}}{(1 + \alpha_h - K)\sinh(\alpha_t) + K\alpha_t \cosh(\alpha_t)},$$

where the relative hydraulic permeability K is given by K_t/K_h; for simplicity we typically assume $K \approx 1$. This gives the analytical solution,

$$\tilde{p}(\tilde{r}) = \begin{cases} 1 - \dfrac{(1 - \hat{p}_e)(1 + \alpha_h)}{\phi + \theta}\dfrac{\sinh(\alpha_t \tilde{r})}{\tilde{r}}, & 0 \le \tilde{r} \le 1 \\ \hat{p}_e + \dfrac{(1 - \hat{p}_e)\theta}{\phi + \theta}\dfrac{e^{-\alpha_h(\tilde{r}-1)}}{\tilde{r}}, & \tilde{r} > 1 \end{cases} \tag{3.18}$$

where $\theta = K[\alpha_t \cosh(\alpha_t) - \sinh(\alpha_t)]$ and $\phi = (1 + \alpha_h)\sinh(\alpha_t)$. A typical solution in the literature corresponds to the case where $\hat{p}_e = 0$, i.e. $p_e^t \gg p_e^h$. The nondimensional interstitial fluid velocity is then given by

$$\tilde{u}(\tilde{r}) = \begin{cases} \dfrac{(1 - \hat{p}_e)(\alpha_h + 1)}{\phi + \theta}\dfrac{[\alpha_t \tilde{r}\cosh(\alpha_t \tilde{r}) - \sinh(\alpha_t \tilde{r})]}{\tilde{r}^2}, & 0 \le \tilde{r} \le 1 \\ \dfrac{(1 - \hat{p}_e)\theta}{K(\phi + \theta)}\dfrac{(\alpha_h r + 1)e^{-\alpha_h(\tilde{r}-1)}}{\tilde{r}^2}, & \tilde{r} > 1. \end{cases} \tag{3.19}$$

The nondimensional pressure and velocity profiles are given in Figure 3.1. As the parameter α_t increases, the pressure reduction at the tumour rim becomes more drastic, it also leads to higher IFP inside the tumour. Equivalently, as α_t increases, the interstitial fluid velocity reaches a higher and sharper peak at the tumour rim. Note that the parameter choices for α_t inside the tumour of 2, 6, and 14 correspond roughly to parameters associated with normal tissue, normalized tumour tissue, and nonnormalized tumour tissue, respectively [2]; the choice for α_h outside the tumour remains a constant value of 2 in Figures 3.1a and 3.1b [2].

These analytical solutions were first presented in [62] but were not experimentally

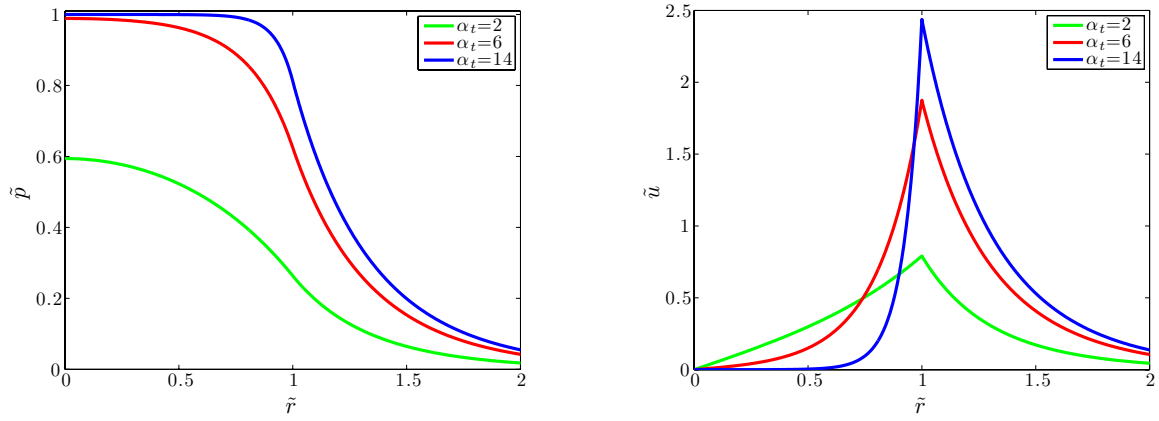

(a) Nondimensional interstitial fluid pressure. (b) Nondimensional interstitial fluid velocity.

Figure 3.1: The effect of changing the parameter α on IFP and IFV in an embedded tumour. These analytical solutions are given in (3.18) and (3.18) respectively and are from a model developed and analytically solved by Baxter and Jain [62, 67].

confirmed until direct measurements of interstitial fluid pressure were made in [79]. It was found that indeed the isolated tumour solution fit the IFP data of various tumours, including mammary adenocarcinoma using the parameter values of $\alpha^2 = 1210$ and $p_e = 10.2$ mmHg [79, Figure 8], which was in good agreement with the estimated parameters from [62].

3.2 General solute transport equations

Considering the conservation of mass equation for concentrations of a solute in solution X, results in the continuity equation,

$$\frac{\partial X}{\partial t} = -\nabla \cdot J_X + P_X \tag{3.20}$$

where J_X is the flux of the solute and P_X is the production rate (related to source and sink densities). This solute flux through the interstitium is governed by some combination of transport processes, including diffusion, convection and charge migration, each of which we will address below. Letting J_d be the diffusive flux, J_c be the convective flux and J_i be the charge migratory flux, we seek an expression for J_X of the form $J_X = J_d + J_c + J_i$,

where depending on the relative contributions of each process, in specific scenarios one or more of these fluxes can be omitted for simplicity.

Diffusion is driven by thermal energy which results in the random movement of molecules. The macroscopic effect of this random movement is the movement of molecules down their concentration gradient, i.e. in the direction of $-\nabla X$. This can be intuitively understood as the movement from areas of higher concentration to those of lower concentrations. The diffusive flux is assumed to be proportional to $-\nabla X$, known as Fick's Law, with proportionality constant, called the diffusion coefficient D_X. In a biological context this constant is more accurately referred to as the interstitial effective diffusion coefficient and we will typically assume that it is constant throughout each tissue.

Convection is the transport of molecules in the direction of a bulk fluid flow. In tissue this flow is typically due to leaky blood vessels. The convective flux is proportional to the product of the concentration and the interstitial fluid velocity u with proportionality constant r_X known as the retardation factor, the ratio of solute velocity to fluid velocity. Thus the convective flux is given by $J_c = r_X u$, where analytical solutions for the IFV u have already been derived in cylindrical (microscopic) and spherical (macroscopic) geometries above.

Finally, the flux due to the electric potential ϕ is proportional to the product of the concentration and the ion migration velocity v_X. The derivation of a functional form for v_X is more in depth so we will address this in the next section. Taking all of the previous form for fluxes into consideration this gives the total interstitial flux as

$$J_X = -D_X \nabla X + (r_X u + v_X) X. \tag{3.21}$$

We will now address v_X before explicitly writing down the corresponding microscopic and macroscopic tumour equations.

3.2.1 Charge migration

For charged particles, we must calculate a form for the velocity v_X, here we will adapt a derivation from [3] to include convection and diffusion.

The force F (N) exerted on a unit charge within an electric field $\mathbf{E}$ (N/C) is given by $F = q\mathbf{E}$ where $q \approx 1.602 \times 10^{-19}$ C is the elementary charge. The force exerted on an

ion with valence z_X is then $F_X = q_X\mathbf{E}$, where $q_X = z_X q$ is the charge of the particle. The velocity of ion migration is then this force divided by a frictional coefficient f_X (kg/s) giving

$$v_X = \frac{q_X}{f_X}\mathbf{E};$$

f_X (kg/s) is sometimes called the Stokes drag coefficient and is related to the commonly used parameter electrical mobility $\mu_X = q_X/f_X$. Before simplifying this expression, note that the ionic current, J_{ion} associated with this velocity is

$$J_{ion} = \frac{q_X X}{f_X}\mathbf{E},$$

which is Ohm's Law with conductivity $\sigma = q_X X/f_X$.

Assuming a quasi-steady state, there is no magnetic contribution to the electric field and $\mathbf{E} = -\nabla\phi$ where ϕ (V) is the electric potential, which gives

$$v_X = -\frac{q_X}{f_X}\nabla\phi.$$

The Stokes-Einstein equation gives the relationship between the diffusion coefficient D_X and the drag coefficient f_X (for low Reynolds number) as

$$D_X = \frac{k_B T}{f_X},$$

where $k_B \approx 1.380 \times 10^{-23}$ J/K and T(K) is the absolute temperature. Thus,

$$v_X = -D_X\frac{q_X}{k_B T}\nabla\phi,$$

or using different universal constants

$$v_X = -D_X\frac{z_X F}{RT}\nabla\phi,$$

since Faraday's constant, $F = qN_A \approx 96485$C/mol and the gas constant $R = k_B N_A \approx 8.314$ J/K/mol, where the Avogadro constant $N_A \approx 6.022 \times 10^{23}$ /mol, share the same ratio as

q/k_B. The flux granted by the ionic current is then

$$J_{ion} = -D_X \frac{z_X F}{RT} X \nabla \phi. \tag{3.22}$$

If a system is comprised of multiple species X with charges z_X, then the charge density of the system is

$$Q = F \sum_X z_X X,$$

while the total charge flux is

$$I = F \sum_X z_X J_X$$

where J_X is given in (3.21). When $Q = 0$ this represents electroneutrality in the system; this is a commonly justified modelling assumption. A stronger simplifying assumption, is the condition that there is no net current, equivalent to $I = 0$, gives

$$\sum_X z_X \left(-D_X \nabla X + r_X u X - D_X X \frac{z_X F}{RT} \nabla \phi \right) = 0,$$

or

$$\nabla \phi = \frac{RT}{F} \frac{\sum_X z_X (-D_X \nabla X + r_X u X)}{\sum_X D_X z_X^2 X}.$$

This expression for the electric field can now be substituted back into (3.22) and subsequently into (4.2) to give

$$\frac{\partial X}{\partial t} = -\nabla \cdot \left(r_X u X - D_X \left(\nabla X + z_X X \frac{\sum_Y z_Y (-D_Y \nabla Y + r_Y u Y)}{\sum_Y D_Y z_Y^2 Y} \right) \right). \tag{3.23}$$

If transport is diffusion-dominated, implying the contribution of convection is relatively negligible, we can write

$$\frac{\partial X}{\partial t} = -D_X \left(\nabla^2 X - z_X \nabla \cdot \left(X \frac{S_{1,1}}{S_{2,0}} \right) \right), \tag{3.24}$$

where $S_{i,j} = \sum_X D_x z_X^i \nabla^j X$, and we define $\nabla^0 X = X$. Distributing the divergence over

the ionic flux gives the tractable form

$$\frac{\partial X}{\partial t} = -D_X\left(\nabla^2 X - \frac{z_X S_{1,1}}{S_{2,0}}\left(X\left(\frac{S_{1,2}}{S_{1,1}} - \frac{S_{2,1}}{S_{2,0}}\right) + \nabla X\right)\right). \tag{3.25}$$

This previous equation, or the more general (3.23), could be adapted for microscopic and macroscopic applications, but to simplify the equations in what follows, we will limit the discussion to uncharged particles and thus take $v_X = 0$ (since $z_X = 0$).

3.2.2 Microscopic solute transport

Making similar assumptions on the blood vessel and interstitial space as was done when deriving equations for microscopic pressure in Section 3.1.1, we arrive at the equation

$$\frac{\partial X}{\partial t} = \frac{D_X}{r}\frac{\partial}{\partial r}\left(r\frac{\partial X}{\partial r}\right) - \frac{1}{r}\frac{\partial}{\partial r}r(r_X u + v_X)X + P_X. \tag{3.26}$$

Further, noting that the fluid is assumed to be incompressible, (3.26) simplifies to

$$\frac{\partial X}{\partial t} = \frac{D_X}{r}\frac{\partial}{\partial r}\left(r\frac{\partial X}{\partial r}\right) - r_X u\frac{\partial X}{\partial r} + P_X, \tag{3.27}$$

for an uncharged molecule; the case of $v_X > 0$ would require the use of (3.25).

Following the process above, we determine the vessel boundary condition by considering the transport of solute molecules J_s due to extravasation from blood vessels. There are many variations on the formula for this transport, such as the Kedem-Katchalsky equation [77], but the most useful to us is written as a sum of its diffusive and convective parts. This diffusion is proportional to the difference between the plasma concentration V_X and the interstitial concentration X, and convection is proportional to the fluid leakage J_f in (3.5). Known as the Patlak equation [80], it gives the rate of solute transport as,

$$J_s = \mu_X S(V_X - X)\frac{\mathrm{Pe}_X}{e^{\mathrm{Pe}_X} - 1} + J_f(1 - \sigma_X)V_X, \tag{3.28}$$

where Pe_X is the Peclet number defined by

$$\mathrm{Pe}_X = \frac{J_f(1-\sigma_X)}{\mu_X S},$$

μ_X is the vascular permeability coefficient and σ_X is the osmotic reflection coefficient for the solute. For large molecules the first term can be ignored since they do not diffuse very much, instead their primary means of movement is convection while the opposite is true for small molecules dominated by diffusion. Now, balancing the solute extravasation from blood vessels in (3.28) with the solute moving in the interstitial space (3.21) gives the boundary condition at the vessel wall for a microscopic model:

$$r_f u X - D_X \frac{dX}{dr} = \mu(V_X - X)\frac{\mathrm{Pe}_X}{e^{\mathrm{Pe}_X}-1} + \frac{J_f}{S}(1-\sigma_X)V_X \quad \text{at } r = \omega. \tag{3.29}$$

We also require the concentrations to reach a steady state as we move away from the vessel and take

$$\frac{dX}{dr} = 0 \quad \text{at } r = \Omega, \tag{3.30}$$

where Ω is the penetration depth [71], a distance far enough from the microvessel to justify the assumption that the system has reached steady state but close enough to ensure minimal contributions from other nearby vessels.

3.2.3 Macroscopic solute transport

As in the above discussion on interstitial fluid pressure, this can be readily expanded into a macroscopic convection-diffusion equation for the entire tumour by taking the blood vessels as an averaged source term giving,

$$\frac{\partial X}{\partial t} = \frac{D_X}{r^2}\frac{\partial}{\partial r}\left(r^2\frac{\partial X}{\partial r}\right) - \frac{1}{r^2}\frac{\partial}{\partial r}[r^2(r_X u + v_X)X] + P_X + \frac{J_s}{V}. \tag{3.31}$$

Once again assuming that interstitial fluid is incompressible and the particle is uncharged yields

$$\frac{\partial X}{\partial t} = \frac{D}{r^2}\frac{\partial}{\partial r}\left(r^2\frac{\partial X}{\partial r}\right) - r_X u\frac{\partial X}{\partial r} + P_X + \frac{J_s}{V}. \tag{3.32}$$

The boundary conditions ensure continuity of concentrations and equality of fluxes at the tumour boundary. The above equation can be useful when considering the extravasation of drug delivery vehicles from tumour vasculature and the release of the agents contained therein and could be easily expanded to a non-radially symmetric case.

3.3 Angiogenic growth factor model

This section will outline a model developed by Ramanujan et al. [1] that considers the concentrations of proangiogenic and antiangiogenic growth factors in a solid spherical tumour of radius R. This will be followed by consideration of measures of angiogenic activity, essentially functions that summarize whether angiogenic activity is being locally stimulated or suppressed. The notation used in this section is consistent with the simplified notation used in my work [81], i.e. instead of c_e^f to denote the concentration of factor f (proangiogenic: +, antiangiogenic: -) in environment e (malignant: m, host: h) [1], we will use f_j for concentration of factor j (proangiogenic: p, antiangiogenic a) where it is understood that for $0 < r < R$ we are inside the tumour and for $R > 0$ we are in the host tissue; when necessary tumour (t) and host (h) parameters are differentiated with the appropriate superscript.

Following [1] for this preliminary modelling, let f_j denote the concentration of factor j where the factor can either be considered to be proangiogenic $(j = p)$ or antiangiogenic $(j = a)$. This tumour is assumed to be a homogeneous sphere of radius R. Proangiogenic growth factors are those responsible for encouraging and stimulating angiogenesis while antiangiogenic growth factors are those that discourage or counteract vascularization. The factors are assumed to be produced at constant rates g_j, degrade exponentially at rates k_j and diffuse with diffusion constants D_j, $j = p, a$, all of which can differ between tumour (superscript t) and host (superscript h) tissues. These assumptions lead to the PDEs

$$\frac{\partial f_j}{\partial t} = D_j \nabla^2 f_j - k_j f_j + g_j, \quad j = p, a. \tag{3.33}$$

Now by making a pseudo-steady-state assumption, it is assumed that local changes in factor concentration are relatively small, i.e. $\partial f_j / \partial t = 0$, compared to the cellular responses such

as proliferation. Assuming spherical symmetry, solutions of the equation

$$D_j \frac{1}{r^2}\frac{\partial}{\partial r}\left(r^2 \frac{\partial f_j}{\partial r}\right) - k_j f_j + g_j = 0 \tag{3.34}$$

with suitable boundary conditions can be derived. First we nondimensionalize (3.34), which is not only a useful process for parameter reduction in this case, but also crucial to subsequently defining angiogenic activity. This can be achieved by setting $r = R\tilde{r}$, $f_j = f_j^s \tilde{f}_j$, and by defining the rescaled parameters $\kappa_j = \sqrt{k_j R^2/D_j}$ and $\gamma_j = g_j R^2/D_j f_j^s$ where

$$f_j^s := \lim_{r\to\infty} f_j(r) = \frac{g_j^h}{k_j^h}$$

is the steady state factor concentration in host tissue. This process yields the equations

$$\frac{1}{\tilde{r}^2}\frac{d}{d\tilde{r}}\left(\tilde{r}^2 \frac{d\widetilde{f}_j}{d\tilde{r}}\right) - (\kappa_j)^2 \widetilde{f}_j + \gamma_j = 0. \tag{3.35}$$

Note that the derivatives are no longer denoted as partial derivatives to reinforce that the concentration $\widetilde{f}_j$ is a function of the single variable $\tilde{r}$ with no time dependence and that $\gamma_j^h = (\kappa_j^h)^2$. To be explicit about the spatial dependence and since the solutions to follow require their consideration, we could rewrite (3.35) as

$$\frac{1}{\tilde{r}^2}\frac{d}{d\tilde{r}}\left(\tilde{r}^2 \frac{d\widetilde{f}_j}{d\tilde{r}}\right) = \begin{cases} (\kappa_j^t)^2 \widetilde{f}_j - \gamma_j^t, & 0 \le \tilde{r} \le 1, \\ (\kappa_j^h)^2 (\widetilde{f}_j - 1), & 1 < \tilde{r} < \infty. \end{cases} \tag{3.36}$$

Solutions to (3.35) with appropriate boundary conditions can be found and the details are presented below since only partial ([82]) or erroneous ([1, 59]) solutions in this context exist in the literature. The solution process is very similar to the process whereby the analytical pressure solution in an embedded tumour geometry was derived above in Section 3.1.2.

The nondimensional equation for the system (3.35) can be transformed into a modified Bessel function in $z(u)$ of order $n = 1/2$ via the substitutions $u = \kappa_j \tilde{r}$, $z = \sqrt{\tilde{r}}(\tilde{f}_j - \gamma_j/\kappa_j^2)$ [78]. This modified Bessel function is

$$u^2 \frac{d^2 z}{du^2} + u\frac{dz}{du} - z\left(\frac{1}{4} + u^2\right) = 0,$$

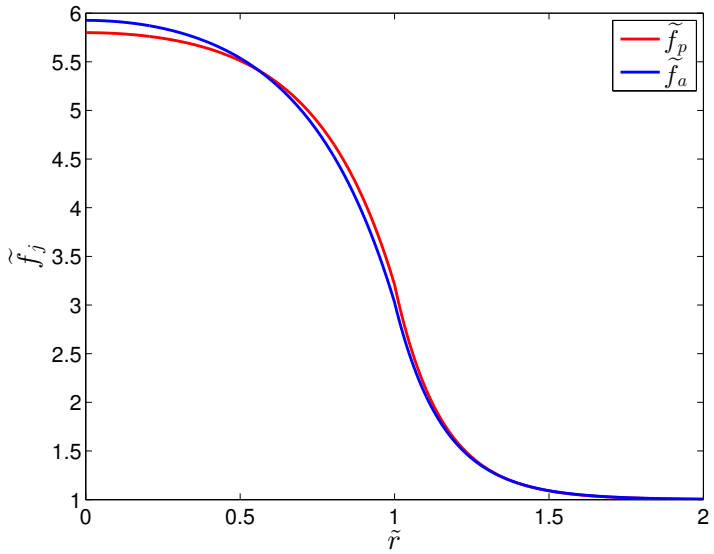

Figure 3.2: The nondimensional concentrations of antiangiogenic, $\widetilde{f}_a$, and proangiogenic, $\widetilde{f}_p$, growth factors [1]. At the tumour core $\widetilde{f}_p > \widetilde{f}_a$, at the rim ($\tilde{r} = 1$) $\widetilde{f}_p < \widetilde{f}_a$ and in the host tissue they are approximately equal.

which has the general solution

$$z(u) = C_1 I_{1/2}(u) + C_2 K_{1/2}(u),$$

where I_n and K_n are the modified Bessel functions of the first and second kind, respectively. For $n = 1/2$, these functions reduce to the elementary functions:

$$I_{1/2}(u) = \sqrt{\frac{2}{\pi u}}\sinh(u), \quad K_{1/2}(u) = \sqrt{\frac{\pi}{2u}}e^{-u}.$$

Thus, reverting back to our original variables, solutions to (3.35) are of the form

$$\widetilde{f}_j(r) = \begin{cases} A_j^t \dfrac{\sinh(\kappa_j^t\,\tilde{r})}{\tilde{r}} + B_j^t \dfrac{e^{-\kappa_j^t\,\tilde{r}}}{\tilde{r}} + \Omega_j, & 0 \le \tilde{r} \le 1, \\ A_j^h \dfrac{\sinh(\kappa_j^h\,\tilde{r})}{\tilde{r}} + B_j^h \dfrac{e^{-\kappa_j^h\,\tilde{r}}}{\tilde{r}} + 1, & 1 < \tilde{r} < \infty, \end{cases} \tag{3.37}$$

where $\Omega_j = \gamma_j^t/(\kappa_j^t)^2$ and the constants A_j^e and B_j^e $(j = p, a;\ e = t, h)$ will be determined by enforcing boundary conditions.

Considering boundary conditions, we require symmetry at the tumour core, continuity of concentrations and fluxes at that the tumour boundary, and the concentrations approach steady state value as we move into the host tissue. These correspond to the following conditions:

$$\begin{aligned} \left.\frac{d\widetilde{f}_j}{d\tilde{r}}\right|_{\tilde{r}=0} &= 0, \\ \left.\widetilde{f}_j\right|_{\tilde{r}=1^-} &= \left.\widetilde{f}_j\right|_{\tilde{r}=1^+}, \\ -D_j^t \left.\frac{d\widetilde{f}_j}{d\tilde{r}}\right|_{\tilde{r}=1^-} &= -D_j^h \left.\frac{d\widetilde{f}_j}{d\tilde{r}}\right|_{\tilde{r}=1^+}, \\ \lim_{\tilde{r}\to\infty} \frac{d\widetilde{f}_j}{d\tilde{r}} &= 0. \end{aligned}$$

The first (tumour core) and last (far-field) conditions immediately yield $B_j^t = 0$ and $A_j^h = 0$. This gives the factor concentrations $f_j(0) = A_j^m \kappa_j^m + \Omega_j$ at the tumour core and

$\widetilde{f}_j = 1$ as $\tilde{r} \to \infty$. Enforcing the conditions at the tumour boundary yields two equations for the unknowns A_j^t and B_j^h, which can be solved to give

$$A_j^t = \frac{(1-\Omega_j)(1+\kappa_j^h)}{(1+\kappa_j^h-\beta_j)\sinh(\kappa_j^t)+\beta_j\kappa_j^t\cosh(\kappa_j^t)},$$
$$B_j^h = \frac{(1-\Omega_j)\beta_j[\sinh(\kappa_j^t)-\kappa_j^t\cosh(\kappa_j^t)]e^{\kappa_j^h}}{(1+\kappa_j^h-\beta_j)\sinh(\kappa_j^t)+\beta_j\kappa_j^t\cosh(\kappa_j^t)},$$

where $\beta_j = D_j^t/D_j^h$. Thus, the final solution is given by

$$\widetilde{f}_j = \begin{cases} \Omega_j - \dfrac{(\Omega_j-1)(\kappa_j^h+1)}{\theta_j+\phi_j}\dfrac{\sinh(\kappa_j^t\tilde{r})}{\tilde{r}}, & 0 \le \tilde{r} \le 1 \\ 1 + \dfrac{(\Omega_j-1)\theta_j}{\theta_j+\phi_j}\dfrac{e^{-\kappa_j^h(\tilde{r}-1)}}{\tilde{r}}, & 1 < \tilde{r} < \infty, \end{cases} \tag{3.38}$$

where $\theta_j = \beta_j[\kappa_j^t\cosh(\kappa_j^t) - \sinh(\kappa_j^t)]$ and $\phi_j = (1+\kappa_j^h)\sinh(\kappa_j^t)$. This solution is analogous to the solution form of IFP in an embedded tumour (3.16). A plot of the solutions using the parameters from [1], given in Table B.1 for your reference, is shown in Figure 3.2.

Angiogenic growth factor models have been used in my previous work [59], where it is assumed that these angiogenic factors slide along the tumour cell density gradient toward the periphery. The equation for these factors was given by

$$\frac{\partial f_j}{\partial t} = D_j\nabla^2 f_j - k_j f_j + g_j + P_j n + \gamma_j \nabla\cdot(f_j\nabla n), \tag{3.39}$$

where n is tumour cell density and P_j is the rate of production by tumour cells. The last term is a proxy for the omission of a model for interstitial fluid pressure which is typically required in order to add convective transport. This directed movement term is a convenient addition to the equation but could be made more precise by adding a true convection term as will be done in Chapter 4. However, this modelling will not be coupled to tumour growth in what follows.

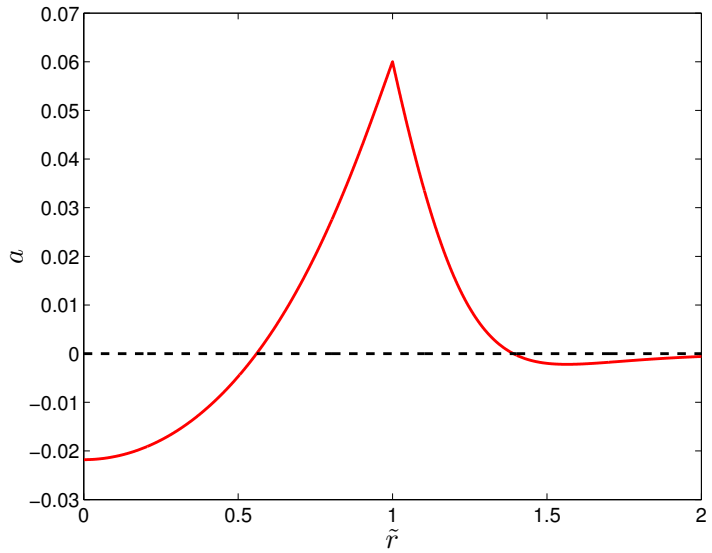

Figure 3.3: Areas of angiogenic suppression near the tumour core ($r = 0$) fall below the dashed line while areas of stimulation near the rim ($r = 1$) are above the line. The measure a depicted here corresponds to the AGF concentrations from Figure 3.2 [1].

3.3.1 Angiogenic activity

The balance between proangiogenic and antiangiogenic factors is the primary determinant of whether angiogenesis is suppressed or initiated. This was represented in [82] by the parameter a defined by

$$a = \begin{cases} \dfrac{\widetilde{f}_p}{\widetilde{f}_a} - 1 & \widetilde{f}_p > \widetilde{f}_a \\ 1 - \dfrac{\widetilde{f}_a}{\widetilde{f}_p} & \widetilde{f}_p < \widetilde{f}_a \end{cases} \tag{3.40}$$

where $\widetilde{f}_p$ and $\widetilde{f}_a$ correspond to the *nondimensional* concentrations of proangiogenic and antiangiogenic factors respectively. This definition makes a an indicator of angiogenic activity where $a > 0$ corresponds to angiogenesis being initiated, $a = 0$ when angiogenesis is stable and $a < 0$ implies vessels are regressing. This measure of angiogenic activity has been incorporated into blood vessel development models based on the previous observations [82]. A typical scenario of an angiogenic activity radial profile displaying angiogenic repression at the tumour core and angiogenic stimulation around the rim is shown in Figure 3.3.

3.4 Models for cancer cell metabolism and pH

We will now briefly review a model developed for tumour cell metabolism and acidity in an entire tumour [3] before showing how this model was adapted to model metabolic and acidity on the microscale. This will be followed by a more general discussion of consumption rates for glucose, oxygen and other metabolites that are present in the literature. Finally, we will present many of the estimated parameters for diffusion coefficients, vessel concentrations and metabolic parameters for cancerous tissues that appear in the literature.

3.4.1 Macroscopic tumour model

Following a model developed by Casciari et al. [3], a model to describe the concentrations of the major players in the metabolic pathways of respiration and glycolysis, along with a pH buffering system, will be outlined here.

Respiration requires oxygen (O_2) and glucose ($C_6H_{12}O_6$) molecules to produce a total of approximately 29 ATP molecules [20], with carbon dioxide (CO_2) and water (H_2O) as the only byproducts. Denoting glucose by G, the simplified chemical reaction is

$$\mathrm{G} + 6\mathrm{O}_2 \rightarrow 6\mathrm{CO}_2 + 6\mathrm{H}_2\mathrm{O}. \tag{3.41}$$

In hypoxic and anoxic conditions, cells must partially or exclusively rely on metabolic pathways, such as glycolysis, that do not require oxygen. In glycolysis, a single glucose molecule yields 2 ATP with the byproducts of the anion lactate ($C_3H_5O_3^-$) and a single hydrogen ion (H^+). Denoting lactate by L^-, we consider the net reaction to be

$$\mathrm{G} \rightarrow 2\mathrm{L}^- + 2\mathrm{H}^+. \tag{3.42}$$

The accumulation of these hydrogen ions in a solid tumour is one of the primary causes of tumour acidosis, quantified by the usual measure of acidity, pH. The precise definition and measurement techniques of pH will not be addressed here, and are rarely discussed in mathematical models that consider tumour acidosis, e.g. [3], [83]. Suffice it to say, in the tumour microenvironment we will calculate pH with the approximate relationship

$$\mathrm{pH} = -\log_{10}(H), \tag{3.43}$$

where H denotes the concentration of hydrogen ions measured in mol/L, a unit which we will denote with M, the commonly used molar concentration. A seemingly pedantic point of clarification in this approximation is that we must normalize H with a standard state H_0 (M). This eliminates the units of concentration allowing the application of the logarithm to this dimensionless value. In practice, this standard state is always set to $H_0 = 1$ M thus recovering the approximation above, although other non-arbitrary choices for this state could yield more biochemically relevant measures of acidity.

In addition to the chemical species in the metabolic pathways in (3.41) and (3.42), they included the primary biological buffering system due to bicarbonate, whereby bicarbonate (HCO_3^-) neutralizes a hydrogen ion by combining into carbonic acid (H_2CO_3) which rapidly disassociates into water and carbon dioxide. This reaction is reversible and summarized by

$$CO_2 + H_2O \underset{k_r}{\overset{k_f}{\rightleftharpoons}} HCO_3^- + H^+, \tag{3.44}$$

where k_f and k_r are the forward and reverse rate (taken to be $k_r = 58$ /mM/s and $k_f = 7.4\times10^{-7}$ /s [84]). In order to ensure charge neutrality, chloride ions (Cl^-) and sodium cations (Na^+) must be included in the model, however, they do not play an active role in the production or consumption rates of the other molecules, so they are considered extraneous and are not explicitly considered in what follows. The presence of water molecules in (3.41) and (3.44) is also non-consequential to the modelling since they comprise the bulk of the fluid in the cytosol and interstitial fluid.

We denote the concentrations of H^+, lactate$^-$, bicarbonate$^-$, CO_2, glucose and oxygen in the extracellular space by $X = H$, L, B, C, G, O, respectively, and in the intracellular space by X^*; their consumption rates are denoted by Q_X, and when appropriate their production rate is denoted by $P_X = -Q_X$. These extracellular concentrations are modelled by conservation equations of the form

$$\frac{\partial X}{\partial t} + \nabla \cdot J_X + Q_X = 0,$$

where J_X is the flux of species X. Assuming this flux is given by Fick's law $J_X = -D_X \nabla X$, where D_X is the constant diffusion coefficient, gives

$$\frac{\partial X}{\partial t} - D_X \nabla^2 X + Q_X = 0. \tag{3.45}$$

Steady state solutions in a spherical tumour are sought and so (3.45) becomes

$$D_X \frac{1}{r^2}\frac{\partial}{\partial r}\left(r^2 \frac{\partial X}{\partial t}\right) = Q_X. \tag{3.46}$$

The boundary condition to ensure symmetry at the tumour core is:

$$\left.\frac{dX}{dr}\right|_{r=0} = 0$$

while at the tumour rim, we must have equality of the flux inside the tumour and outside. Inside the tumour,we have $J_X = -D_X dX/dr$ while just outside the flux will be assumed to be a linear function of the concentration difference between the medium outside the tumour X_o and at the tumour rim $X(R^-)$ giving the boundary condition

$$D_X \frac{dX}{dr} = \mu_X\big(X_o - X(R^-)\big).$$

The consumption rates of glucose and oxygen are empirically formulated and will be addressed below but relationships between the production rates of the molecules involved in cell metabolism can be gleamed. Since CO_2 and H^+ are present in the buffering reaction along with a metabolic pathway, it will be convenient to denote the production of CO_2 by respiration alone by P_Y and the production of H^+ by glycolysis alone by P_Z. It is immediately clear from reaction 3.41 that $P_Y = Q_O$ and from 3.42 that $P_Z = -Q_L$. Considering both reactions, it can be observed that the consumption of glucose is given by $Q_G = \frac{1}{6}P_Y + \frac{1}{2}P_Z$. Putting these three observations together yields, $Q_L = \frac{1}{3}Q_O - 2Q_G$, a relation between the three production rates that are not explicitly involved in the buffering reaction 3.44.

The following production rates follow from the metabolic and buffering reactions above:

$$P_C = k_r(\epsilon BH + (1-\epsilon)B^*H^*) - k_f(\epsilon C + (1-\epsilon)C^*) + Q_O, \tag{3.47}$$
$$P_B = k_f(\epsilon C + (1-\epsilon)C^*) - k_r(\epsilon BH + (1-\epsilon)B^*H^*), \tag{3.48}$$
$$P_H = k_f(\epsilon C + (1-\epsilon)C^*) - k_r(\epsilon BH + (1-\epsilon)B^*H^*) - Q_L, \tag{3.49}$$

where ϵ denotes the volume fraction of extracellular space and $1-\epsilon$ is the volume fraction of the intracellular space. The only species that will be assumed to have the same extracellular

and intracellular concentrations, are oxygen and CO_2 which can freely diffuse across the cell membrane whereas the others have to rely on the action of cell membrane transporters and other forms of active transport.

We now present a modified argument (modified from [3]) for eliminating the product B^*H^* in (3.47)-(3.49) to obtain a system with extracellular concentrations only. We utilize the assumption $C = C^*$ to perform this crucial simplification of the model. We use X_C to denote the left hand side of (3.46) for CO_2, the total mass transport in the radial direction per unit volume of tumour. Considering only the extracellular transport, the following equation must be satisfied

$$\beta X_C = -k_f \epsilon C + k_r \epsilon BH$$

where β is the fraction of transport that occurs outside the cells. Since it has already been assumed that $C = C^*$, this implies that $\beta = \epsilon$ and therefore,

$$X_C = -k_f C + k_r BH. \tag{3.50}$$

Now, considering just the intracellular production of CO_2, we must also have

$$\gamma X_C = Q_O - k_f(1-\epsilon)C^* + k_r(1-\epsilon)B^*H^*$$

where $\gamma = 1 - \epsilon$ is the fraction of transport that occurs through the cells and once again $C = C^*$. This gives

$$X_C = \frac{Q_O}{1-\epsilon} - k_f C + k_r B^* H^*. \tag{3.51}$$

Equating (3.50) and (3.51) yields

$$B^*H^* = BH - \frac{Q_O}{k_r(1-\epsilon)} \tag{3.52}$$

which upon substituting into (3.47)-(3.49) yields

$$P_C = k_r BH - k_f C, \tag{3.53}$$
$$P_B = k_f C - k_r BH + Q_O, \tag{3.54}$$
$$P_H = k_f C - k_r BH - Q_L + Q_O. \tag{3.55}$$

The issue of what functional forms to utilize for glucose and oxygen consumption was

broached in [4] and applied in [3] in tandem with the buffering model described above. They suggest a simple form for glucose and oxygen production rates given by

$$Q_O = \left(A_O + \frac{B_O}{G}\right)\left(\frac{O}{k_O + O}\right)$$
$$Q_G = \left(A_G + \frac{B_G}{O}\right)\left(\frac{G}{k_G + G}\right).$$

They also present a more complicated version that incorporates the decreasing consumption of oxygen and glucose in the presence of hydrogen ions due to the acidic breakdown of proteins critical to metabolism:

$$Q_O = \left(A_O + \frac{B_O}{GH^n}\right)\left(\frac{O}{k_O + O}\right)$$
$$Q_G = \left(A_G + \frac{B_G}{O}\right)\frac{1}{H^m}\left(\frac{G}{k_G + G}\right)$$

where n and m are phenomenological constants. Other possible functional forms for these consumption rates will be addressed below.

3.4.2 Microvessel model

Microvessel scale models of coupled glucose and oxygen concentrations exist in the literature [85], but do not analyze the implications for tumour acidity. Of note, they proposed oxygen and glucose consumption rates of the form:

$$Q_O = K_O \frac{OG}{(k_O + O)(k_G + G)}$$
$$Q_G = K_G \frac{OG}{(k_O + O)(k_G + G)} - K_{Gly}\frac{G}{k_{Gly} + G}$$

where K_O and K_G are the maximum consumption rates than can be achieved by respiration while K_{Gly} is the maximum rate of glycolysis. These consumption rates will make an appearance in the next section where we discuss the development of these functional forms.

In [25], a mathematical model was developed to describe the concentrations of various molecules important to cell metabolism in order to study pH profiles in a two-dimensional

region outside of a single microvessel. This corresponds with the experimental setup used in [5], a transparent dorsal window chamber implanted in a mouse. This was partly undertaken to explain the observed pH plateau in [5] and to incorporate the role of an alternative metabolic pathway, glutaminolysis.

Diffusion-reaction equations were used to describe concentrations of the major players in respiration and glycolysis: H^+, Cl^-, Na^+, lactate$^-$, bicarbonate$^-$, CO_2, glucose and oxygen, given by (3.45) where the consumption rate of species X, Q_X, is a function of the other chemical species (provided in Table B.4, detailed below). We are not concerned with the time evolution of these concentrations, and so assume that all species have reached steady state by setting $\partial X/\partial t = 0$. Thus, we must solve the equations:

$$D_i \frac{d^2X}{dr^2} = Q_X, \tag{3.56}$$

similar to (3.46) except now we are using a Cartesian Laplacian rather than a spherical one. Since we are considering a single micro vessel rather than an entire tumour, the boundary conditions must change as well. The boundary condition at the vessel wall must ensure that the diffusive flux in the interstitial space outside of the vessel is equal to the fluid flux across the vessel wall:

$$-D_X \frac{dX}{dr} = \mu_X(V_X - X). \tag{3.57}$$

We also use a far field assumption that as r grows large the system approaches steady state.

The production rates of bicarbonate, hydrogen ions and carbon dioxide are from [3] and are given in (3.53)-(3.55). The glucose and oxygen consumption rates for this model are given by $Q_G = K_G G/(G + k_G) f_1(O)$ and $Q_O = R Q_G O/(O + k_O) f_2(O)$ respectively, where $0 \leq R \leq 6$ is the ratio of respiration to glycolysis and the functions f_1 and f_2 are given by

$$f_i(O) = 1 - a_i O^{0.02} \exp(-100(O - 0.01)^4), \quad i = 1, 2,$$

where $a_1 = 2/3$ and $a_2 = 1/2$. These consumption rates are depicted in (the inset) of Figure 3.4. These forms of the consumption rates assume that respiration is the dominant metabolism near the vessel (in well-oxygenated regions), glycolysis and oxygen are both reduced at intermediary distances (in hypoxic regions) and glycolysis is dominant distant from the vessel (in anoxic regions).

First, the coupled system of oxygen and glucose can be solved. Using these we can then

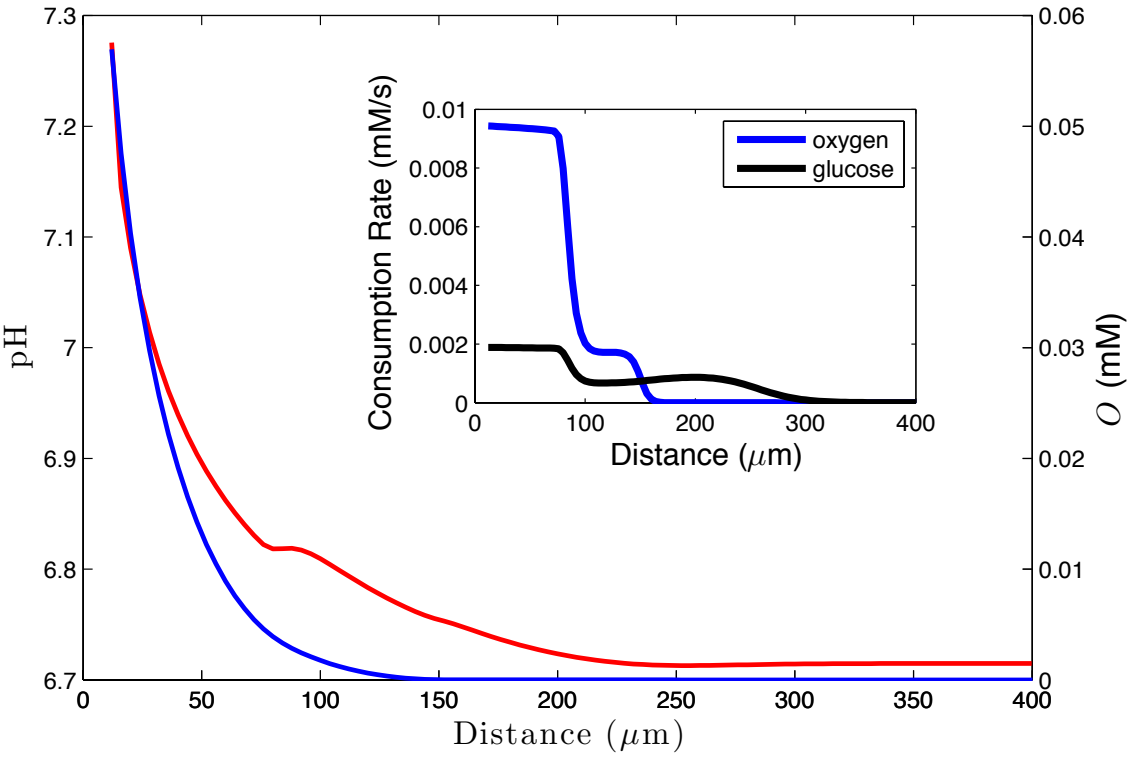

Figure 3.4: Profiles of pH (red) and oxygen concentration (blue) in the tissue surrounding a single microvessel with the base case of parameters [25]. Inset: glucose and oxygen consumption rates.

solve for the system governing bicarbonate, carbon dioxide and hydrogen ions. Finally, acidity is determined using the relation pH$=-\log_{10}(H)$. As can be seen in Figure 3.4 these assumptions produce a pH plateau experimentally observed in [5] (see Figure 2.4). We delay a discussion of any results gleamed from this paper as they will be expanded upon in Chapter 5. Here, in order to build upon previous work, we will outline the nondimensionalization and numerical methods used to solve the system outlined above. Nondimensionalizing X by setting $x = X/V_X$ and formally nondimensionalizing space by dividing the spatial variable r by a characteristic length 1μm (but not changing its notation), gives the equations

$$\frac{d^2x}{dr^2} = Q_x, \tag{3.58}$$

where $Q_x = Q_X/(D_X V_X)$ and the boundary conditions are

$$-\frac{d\tilde{x}}{dr} = \mu_x(1-x), \quad \text{at } r = \omega \tag{3.59}$$

where $\mu_x = \mu_X l/D_X$ and

$$\frac{dx}{dr} = 0, \quad \text{at } r = \Omega. \tag{3.60}$$

Nondimensionalization is a useful process for computational and analytical reasons. When attempting to understand model behaviour and performing sensitivity analyses, it is usually enlightening and convenient to consider nondimensional groups of parameters rather than individual parameters. Additionally, computational and numerical methods could be rescued from errors by scaling variables by a characteristic value.

3.4.3 Metabolite consumption rates

The most straightforward place to start our discussion about proposing functional forms for consumption rates is with consideration of the oxygen consumption rate, In models that do not include lactate-fuelled respiration, oxygen is consumed at six times the rate of glucose-fuelled respiration, i.e. $Q_O = 6k_O$, see (C.34). Assuming for now that there is sufficient glucose to ensure that this rate is not glucose-limited, i.e. independent of G, then a reasonable starting point, would be to require that (i) $Q_O = 0$ when $O = 0$ and (ii) Q_O is bounded and approaches some constant value, say B_O, as O grows large. The simplest form for this rate would be some constant rate $Q_O = B_O$ for $O > 0$. This supposition forms the basis of the Krogh model [86] whose work with Erlang helped form the foundation for the

disciplinary nature of the field of mathematical biology. This model is limited by the fact that once all the oxygen is consumed the solutions dip into negative concentration values unless the spatial domain is truncated when $O = 0$, or if the consumption rate is piecewise defined so that no consumption occurs once the oxygen supply is depleted. The simplest form for a continuous function that satisfies the aforementioned conditions is given by a Michaelis-Menten formulation, which has been rigorously formulated for certain enzyme kinetics, and is given by

$$k_O(O) = B_O \frac{O}{O + K_O},$$

where K_O is the concentration at which the consumption is half the maximum rate, i.e. $k_O(K_O) = B_O/2$. This was first proposed and analyzed in the context of oxygen consumption by Blum [87]; he also analyzed constant (the correct solution in this case was derived later [88]) and linear consumption rates. The latter will be neglected here due to its unbounded nature although it could be used as an approximation to the Michaelis-Menten rate for small oxygen concentrations (only applicable in hypoxic conditions).

One generalization of a Michaelis-Menten function is the Hill equation,

$$k_O(O) = B_O \frac{O^n}{O^n + K_O^n},$$

where $n > 0$ is the Hill coefficient which recaptures Michaelis-Menten kinetics when $n = 1$. This form can also be derived in a biological context to describe cooperative (or noncooperative) binding, but here we mention it only because of its sigmoidal properties. A sample of these functions is shown in Figure 3.5 showing that as n increases, the function exhibits more switch-like behaviour. Using these functions with larger values of n than unity can have numerical advantages for low concentrations as their derivatives are equal to $1/K_O^n$ as the concentration approaches zero. So for large n, the derivative at the origin approaches zero.

The Michaelis-Menten formulation formed the basis of more complicated versions that included dependencies on other species concentrations. For instance, if the rate is limited by glucose availability then the maximal rate B_O should also show some dependance on G. An appropriate form for k_O that continues to satisfy the minimal requirements above was proposed by Kirkpatrick et al. [85] and is given by

$$k_O(O, G) = B_O \frac{G}{G + \Gamma_G} \frac{O}{O + K_O}.$$

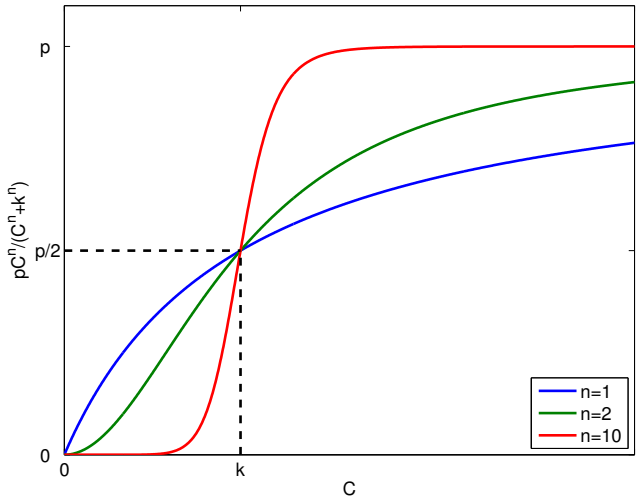

Figure 3.5: Michaelis-Menten function ($n = 1$) and Hill functions ($n = 2, 10$) of concentration C with maximum rate p and half-maximal concentration k. As the exponent n increases the function becomes more switch-like.

In [4], a seemingly opposite approach was taken with the maximal rate approaching a constant as G increases, but approaching infinity as G approaches zero

$$k_O(O, G) = B_O \left(1 + \frac{A_O}{G}\right) \frac{O}{O + K_O}.$$

This functional form captures the so-called Crabtree effect, which is the observation that oxygen consumption will actually decrease as glucose increases, as cells tend to rely more on glycolysis in hyperglycaemic conditions. However this form certainly does not hold for small glucose values, as the rate rapidly increases. When they attempted to implement this form numerically, they had to modify the expression for low glucose values, so that when $G < 0.27$ mM,

$$k_O(O, G) = \alpha_O(1 - \beta_O G^2) \frac{G^2}{G^2 + \Gamma_G^2} \frac{O^2}{O^2 + K_O^2},$$

forced to use both a Hill coefficient of 2, and bounding the maximal rate. While more complicated forms for oxygen consumption certainly exist, we will hold off their discussion

since they must be broached in tandem with glucose, lactate or pyruvate consumption rates.

Similarly for our discussion of glucose consumption Q_G, as a starting point for proposing a functional form, we require as a bare minimum that $Q_G = 0$ when $G = 0$ and that Q_G is bounded and preferably approaches some constant value, say B_G, as G grows large. The simplest form for this is once again given by a Michealis-Menten formulation,

$$Q_G(G) = B_G \frac{G}{G + K_G}.$$

This formalism for glucose consumption has been used in previous tumour spheroid models [65, 63, 89] that similarly consider diffusion-reaction equations albeit in a larger spherical tissue with boundary conditions appropriate for that scenario. Unfortunately this form does not account for the Pasteur effect, i.e. the decreased glucose consumption as oxygen increases, or conversely the increased glucose consumption as oxygen decreases. The latter interpretation can be understood by the cell's adaptation to the lower ATP yield of glycolysis experienced by hypoxic cells. This could be achieved by making the maximal achievable consumption rate, previously denoted by B_G, a decreasing function of O. This one again was attempted in [4] by introducing a variable maximum rate which we will denote by $B_G(O)$, which gives a consumption rate of

$$Q_G(G, O) = B_G(O)Q_G(G) = B_G \left(1 + \frac{A_G}{O}\right) \frac{G}{G + K_G},$$

where B_G is the consumption rate at high oxygen concentrations and A_G determines the inhibitory sensitivity to oxygen. This expression cannot be applied globally since $B_G(O) \to \infty$ as $O \to 0$, so in [3] they modify the expression and use $B_G(O) = B_G(1 - A_O O^2)$ and similarly switch to a Hill coefficient of 2 for $O < 0.01$ mM. In [25], a complicated form of $B_G(O)$ was proposed, namely,

$$B_G(O) = 1 - \tfrac{2}{3} O^{0.02} \exp(-100(O - 0.01)^4).$$

Its main drawbacks are the introduction of many parameters, a very sharp upward spike for low oxygen values and lower glucose consumption values for hypoxic conditions. However, it is a bounded functional form that can be easily interpreted as a maximal rate. This glucose consumption rate was coupled to oxygen consumption with the form $Q_O = RQ_G O/(O +$

$k_O)f(O)$, where $0 \leq R \leq 6$ is the ratio of respiration to glycolysis [25] and the functions f is very similar to the form of $B_G(O)$ given above and is given

$$f(O) = 1 - \tfrac{1}{2}O^{0.02}\exp(-100(O-0.01)^4).$$

These forms of the consumption rates ensure that respiration is the dominant metabolism near the vessel (in well-oxygenated regions), glycolysis and respiration are both active yet reduced at intermediary distances (in hypoxic regions) and glycolysis is dominant distant from the vessel (in anoxic regions). The consumption rates above include a total of 14 parameters and manage to produce a pH plateau.

Another tactic for proposing glucose consumption rates is to formally separate the two processes of respiration (in the presence of oxygen) and glycolysis (ending in lactate production) by proposing functions for the glycolytic rate k_G and the respiration rate k_O and taking their sum, giving $Q_G = k_O + k_G$. This is the approach taken in [85], where

$$Q_G = B_O \frac{G}{G+\Gamma_G}\frac{O}{O+K_O} + B_G\frac{G}{G+K_G}.$$

This is also the approach taken in [90], discussed below, where the phenomenon of metabolic symbiosis was included in their model. The lactate produced by glycolytic cells can be consumed during respiration by cells with access to oxygen. This is captured via a competition term, where lactate inhibits glucose consumption via respiration and vice versa,

$$Q_G = B_O \frac{\alpha_G G}{\alpha_G G + \alpha_L L + \Gamma_G} + B_G\frac{G}{G+K_G}.$$

In addition to glucose and oxygen, lactate consumption is also a key consideration since it can be used as fuel for cells performing respiration. In [65], the transmembrane transport of glucose, oxygen and lactate are given by Michaelis-Menten rates $Q_{X,m}$ (the m subscript denotes transmembrane rates),

$$Q_{X,m} = B_X\frac{X}{X+K_X}$$

and serve as the maxima for the corresponding metabolic rates. The model is more complicated than this but was criticized in [63] for a lack of lactate production when lactate concentrations drop to zero in normoxic conditions. To remedy this Bertuzzi et al. formu-

lated a series of models originating in [63], and being revised in[89] that propose forms for glucose, lactate and pyruvate consumption

$$
\begin{aligned}
Q_G &= B_G \frac{G}{K_G + G}, \\
Q_P &= -2Q_G + B_P \frac{P}{K_p + P} \frac{O}{K_O + O} + \phi, \\
Q_L &= -\phi - h(L - L^*),
\end{aligned}
$$

where B_P is the maximal rate of oxidative phosphorylation, ϕ is the rate of interconversion between lactate and pyruvate, and h is the rate constant for lactate transmembrane transport which is proportional to the difference between extracellular and intracellular concentration $(L - L^*)$. This uses the facts that pyruvate is produced at twice the glycolytic rate, consumed in the presence of oxygen, and that pyruvate and lactate are reversibly interchanged by the enzyme lactate dehydrogenase (LDH). They derive their oxygen consumption based on the intracellular equations for pyruvate and lactate which ends up being the solution to a quadratic equation. This approach differs from those above because they consider glycolysis and respiration to be inextricably linked processes, instead of two distinct fates of glucose. This requires the introduction of pyruvate, but since its intracellular concentration can be found in steady state, it is readily eliminated. However, their functional form for Q_G leaves something to be desired since hypoxic conditions are often prevalent in tumours and cells compensate for the lowered rate of respiration (and thus ATP production) by dramatically increasing their glycolytic flux. This approach also leads to a very complicated function form for Q_O which will not be reproduced here.

A key step was taken by Mendoza-Juez et al. [90] when they explicitly included the symbiotic nature of glycolytic and respiration fuelled cells (without including pyruvate). They used ODEs of the form $dX/dt = -Q_X$ where their functional forms for glucose and lactate consumption by respiration assume that glucose inhibits lactate consumption and vice versa and are given by

$$
\begin{aligned}
Q_G &= B_O \frac{\alpha_G G}{\alpha_G G + \alpha_L L + N_*} + B_G \frac{G}{G + G_*} \\
Q_L &= B_L \frac{\alpha_L L}{\alpha_G G + \alpha_L L + M_*} - 2B_G \frac{G}{G + G_*},
\end{aligned}
$$

where B_X, $X = O, L, G$ have been redefined from [90] for simplicity and comparison, by

$B_O = \beta_o P_o$, $B_G = \beta_g P_g$, $B_L = \beta_L P_o$ to absorb the aerobic and glycolytic cell population proportions, denoted by P_o and P_g respectively. Equations that govern these population proportions are omitted but it should be noted that they switch metabolism when lactate reaches a threshold level L_*. These equations were extended to include oxygen concentrations and spatial effects (by including diffusion), but were not investigated [90]. These proposed rates are

$$\begin{aligned}
Q_G &= B_O \frac{\alpha_G G}{\alpha_G G + \alpha_L L + \Gamma_G} \frac{O}{O + K_O} + B_G \frac{G}{G + K_G}, \\
Q_L &= B_L \frac{\alpha_L L}{\alpha_G G + \alpha_L L + \Gamma_L} \frac{O}{O + K_O} - 2B_G \frac{G}{G + K_G}, \\
Q_O &= 6B_O \frac{\alpha_G G}{\alpha_G G + \alpha_L L + \Gamma_G} \frac{O}{O + K_O} + 3B_L \frac{\alpha_L L}{\alpha_G G + \alpha_L L + \Gamma_L} \frac{O}{O + K_O}.
\end{aligned}$$

As summarized above, the issue of what functional forms to utilize for glucose and oxygen consumption was broached in [4] and applied in [3] in tandem with a bicarbonate buffering model. In [4] they suggest a simple form for glucose and oxygen production rates given by

$$\begin{aligned}
Q_O &= \left(A_O + \frac{B_O}{G} \right) \left(\frac{O}{O + K_O} \right) \\
Q_G &= \left(A_G + \frac{B_G}{O} \right) \left(\frac{G}{G + K_G} \right).
\end{aligned}$$

The choice of modification from standard Michaelis-Menten kinetics is to compensate for a Pasteur-like and Crabtree-like effect explained above. They also present a more complicated version that incorporates the decreasing consumption of oxygen and glucose in the presence of hydrogen ions due to the acidic breakdown of proteins critical to metabolism:

$$\begin{aligned}
Q_O &= \left(A_O + \frac{B_O}{G H^n} \right) \left(\frac{O}{O + K_O} \right) \\
Q_G &= \left(A_G + \frac{B_G}{O} \right) \frac{1}{H^m} \left(\frac{G}{G + K_G} \right)
\end{aligned}$$

where n and m are phenomenological constants, and the choice of the pH dependencies are based on experimental observations. An equivalently generalized model could raise O and G to some powers in these consumption rates as well (as they were forced to do for

low concentrations).

3.4.4 Parameter estimation

Diffusion coefficients

There is no single study that has measured the apparent diffusion coefficients of all of the molecules of interest, which include but are not limited to glucose, lactate, oxygen, carbon dioxide, bicarbonate and hydronium, in the same type of tissue. In fact, our references for these parameter values have not measured any more than two of the diffusion parameters of interest. In general, these apparent diffusion coefficients may exhibit spatial-dependence due to changes in temperature, tissue properties and molecular concentrations but for simplicity, we will assume that they are constant in the tissue surrounding a blood vessel. As a starting point, we will consider these diffusion coefficients in water and then move to measurements in various normal and tumour tissues to observe their changes.

A detailed study on the estimation of the diffusion coefficients of dissolved carbon dioxide and bicarbonate was performed by R. Zeebe [91]; we will only use the functional fit to his simulation results, namely, $D_X^w = D_X^0[(T/T_X) - 1]^{p_X}$, where the applicable temperature range is $273 < T < 373$ and the parameters are given in Table 3.1. These functions give a reasonable fit to carbon dioxide diffusion coefficients [92, 93, 94], and bicarbonate diffusion coefficients [94, 95] in the literature. We will fix the temperature at a value slightly higher than body temperature (≈310 K) due to hyperthermia exhibited by many solid tumours [96]. Temperature differences can even differentiate between malignant and benign growths with malignant tumours, exhibiting a temperature more than 0.7 K higher than normal tissue [97]. We will take T=311 K which would yield D_C=2745 μm^2/s and D_B=1495 μm^2/s in water. Approximate diffusion coefficients of other molecules in water are given in Table 3.2.

X	D_X^0 (μm^2/s)	T_X	p_X
C	14 683.6	217.2056	1.9970
B	7015.8	204.0282	2.3942

Table 3.1: Parameter values for calculating diffusion coefficients of bicarbonate and carbon dioxide in water, adapted from [91].

Most mathematical models of tumour metabolism that include diffusive transport use values calculated in various tissues; some common choices are listed in Table 3.3. However, the self-consistency of these values is rather suspect. In some cases, the diffusion coefficients of uncharged molecules are not even inversely related to their molecular mass, i.e. some particle A with lower molecular weight than particle B ($M_A < M_B$) is assumed to have a lower diffusion coefficient than particle B ($D_A < D_B$). Here, we will ensure this does not occur by first taking a very loose assumption, by simply ensuring that $M_A < M_B$ implies $D_A > D_B$.

X	M_X (g/mol)	D_X^w (μm^2/s)	Reference
G	180.16	940	[98]
		925	[99], used in [100, 89]
L	89.07	1230	[101]
		1200	[75] used in [102, 89]
O	32.00	3240	interpolated [103]
B	61.02	1495	[91]
C	44.01	2745	[91]
H	1.01	>10 000	extrapolated [95]

Table 3.2: Molecular masses and diffusion coefficients D_X^w of molecules in water.

Diffusion coefficients vary depending on the tissue under study but the ratio between the diffusion coefficients of different species remains relatively constant. For two neutral molecules, A and B, with molecular weights M_A and M_B respectively, their diffusion coefficients satisfy the (very) approximate relation

$$\frac{D_X}{D_Y} = \left(\frac{M_Y}{M_X}\right)^n$$

where $n = 1/2$ in water and $n \approx 3/4$ for molecules in 37° tissue [75] (specifically $D_X = 17780/M_X^{3/4}$ μm^2/s, $32 < M < 69000$, [75]). The latter is used to estimate the lactate diffusion coefficient in [3] from the glucose diffusion coefficient measured in [105].

Vessel concentrations

Typical ranges for normal lactate, glucose and oxygen concentration in the blood are V_L: 0.5–2 mM, V_G: 4–6 mM, and V_O: 0.04–0.08 mM. The range of glucose to include extreme

hyperglycaemic and hypoglycaemic conditions that could arise locally in a tumour would encompass V_G: 1–10 mM; similarly, for oxygen, including severely hypoxic conditions would allow V_O: 0.01–0.08 mM.

As an example of tumour blood vessel concentrations, the experiments performed by [5] represent the first micrometer scale measurements of the partial pressure of oxygen (pO_2) and interstitial pH adjacent to tumour blood vessels. We will focus on their measurements of average pO_2 provided as functions of distance from a single blood vessel. In their experiment the individual measurements were taken from multiple blood vessels in 7 tumours. When averaged, these measurements were only considered up to a distance D/3 from the vessel, where D is the distance to the nearest neighbouring vessel, in order to ensure that the contribution was predominantly from the local effects of a single vessel. The corresponding average pO_2 profile gives even more information, specifically that certainly the oxygen concentration drops to zero well before the penetration depth, in fact here near anoxic conditions are encountered less than 200 μm away from the vessels, and the average partial pressure of oxygen in the tumour vessel is 13.5 mmHg [5]. Henry's Law relates this partial pressure, pO_2, to the molar concentration, O, via the solubility coefficient, S_O, i.e. $O = S_O pO_2$. At 37° C the solubility of oxygen of DS-carcinosarcoma in the rat kidney is $S_O = 1.05 \times 10^{-3}$ mM/mmHg [117]; this yields $V_O \approx 1.43 \times 10^{-2}$ mM.

Metabolic parameters

Parameters determining Michaelis-Menten consumption rates and half-maximal concentrations have been estimated in a number of tissues. Some representative values and their previous model usage are summarized in Table 3.4.

3.5 Summary

The mathematical models presented in this chapter will form the basis on which the models to follow will be built. The general solute transport equation derived in Section 3.2 are utilized in the models that consider the concentrations of specific entities in tumours. The models for interstitial fluid pressure and velocity, along with those that govern angiogenic growth factor concentrations in Sections 3.1.2 and 3.3 respectively will both be utilized to formulate the system in Chapter 4. Similarly the metabolic models developed in Section

3.4, especially the microscale model, and the consumption rates discussed have influenced the symbiosis model and the metabolism-acidity model presented in Chapter 5.

X	D_X (μm^2/s)	Medium
G	11.5	V79-171B tumour spheroid [104]*
	23–55	human cell spheroids [105], upper bound used in [106]
	42.1	EMT6/Ro tumour spheroid [104]*, used in [107]
	105	EMT6/Ro tumour spheroid [105], used in [64, 25]**,[108, 109, 65, 63, 89]
	126/139	rat brain (with/without glucose infusion) [110]
	150	9L rat brain tumours[99]
	362	Swabb relation [75]
	500	EMT6/Ro tumour spheroid [111], used in [85] (they cited [75])
	560	used in [112]
	700, 770	blood plasma [113], [114]
L	59	used in [107]
	176	rat brain [110]
	177	molecular weight correlation with D_G [105] [3], used in [65, 63, 89]
	350	used in [102]
	608	Swabb relation [75]
	820, 887	blood plasma [114], [113]
	900	[112]
O	1321	Swabb relation [75]
	1460	EMT6/Ro tumour spheroid [115] (25° C), used in [25]
	1500	used in [85]
	1650	used in [107]
	1690	V79-171B tumour spheroid [116]
	1750	DS-carcinosarcoma (rat kidney) [117], used in [108, 109]
	1820	EMT6/Ro tumour spheroid [116] (37° C), used in [3, 65, 64, 63, 89]
	1980	[112]
	2000	[118] used in [119, 120, 106, 121]
B	22	mammalian corneal epithelium (310 K) [122]
	140	100% hemolysate [123]
	150	mammalian corneal stroma (310 K) [122]
C	340	100% hemolysate [123]
H	190	mammalian corneal epithelium (310 K) [122]
	1180	mammalian corneal stroma (310 K) [122]

Table 3.3: Apparent diffusion coefficients reported in the literature for various molecules in tissues. Those for bicarbonate, carbon dioxide and hydrogen ions are sparsely reported whereas those for metabolites have been frequently measured in tumour tissues.
* value calculated using molecular weight correlation with inulin.
**value rounded to 110 as in the abstract of [105]

Parameter	Value	Reference
K_O	2×10^{-4}	used in [25]
K_O	4.640×10^{-3} mM	[3], used in [64, 65, 63, 89]
K_G	4.0×10^{-2} mM	[4] cites [99], used in [3, 64, 65, 63, 89]
K_G	5.0×10^{-2} mM	used in [25]
K_G	0.58 mM	9L rat brain tumours[99], cited by [4]
β_O	1.43916×10^{-2} mM/s	[3], used in [64]
β_G	0.04 mM/s	[3], used in [64]

Table 3.4: Parameters used in metabolic models.

Chapter 4

The Effect of Convective Transport on Angiogenic Activity

In this chapter, the effect of convective transport on angiogenic factors concentrations and consequently the overall angiogenic behaviour is investigated. The majority of results presented here are reported in [81]. This work shows that altering physiological parameters of a tumour, such as hydraulic conductivity of the tissue, vessel permeability and vascular pressure, all of which alter macromolecule transport, can alter the spatial distribution of angiogenic growth factors (AGF) concentrations. The imbalance between proangiogenic and antiangiogenic factors can subsequently suppress or initiate angiogenesis in a tumour.

While the process of tumour angiogenesis and interstitial fluid pressure were outlined in Chapter 2 and models for AGFs and interstitial fluid pressure (IFP) were given in Chapter 3, we will first give a brief introduction for the modelling to follow.

4.1 Introduction

The process of angiogenesis, the development of new blood vessels from preexisting vasculature, is governed by the net balance between proangiogenic and antiangiogenic growth factors [124]. Multiple regulatory factors are involved in this process, including the vascular endothelial growth factor (VEGF) family and its receptors, the fibroblast growth factor (FGF) family, angiostatin, and endostatin [124]. During tumour progression, this delicate

balance is heavily skewed in favour of angiogenesis at the tumour rim, resulting in an abnormal tumour vasculature and microenvironment [35, 125]. The tumour core remains relatively devoid of nutrient-providing blood vessels and thus maintain highly upregulated AGF production.

The tumour vascular network in solid tumours is spatially and temporally heterogeneous, resulting in a harsh microenvironment characterized by hypoxia, acidosis, and elevated interstitial fluid pressure. While all three of these traits play critical roles in the activity and upregulation of angiogenic growth factors, the relationships between these features and tumour angiogenesis are complex and not fully understood. The most prominent and widely studied AGF is VEGF, a potent proangiogenic agent that is independently upregulated by both hypoxia and acidosis [126]. While angiogenesis is commonly triggered as a result of hypoxia, it is also the case that acidic pH induces the production of several other angiogenic molecules including basic FGF [127] and nitric oxide [128]. Although the effects of hypoxia and acidosis on angiogenic factors have been investigated experimentally, the effects of elevated IFP are less clearly understood. Here, we seek to explore the effect of IFP gradients on proangiogenic and antiangiogenic factor concentrations, with a focus on extrapolating a tumour's spatial angiogenic tendency induced by the local imbalance of these factor concentrations.

Two compounding factors that contribute to elevated IFP in solid tumours are the increased permeability of blood vessels and the absence of functional lymphatics [125, 129]. It has been hypothesized that the normalization of tumour vessels, by the application of antiangiogenic therapies such as antibodies inhibiting VEGF or blocking VEGFR-2, would lead to lowered tumour IFP [35, 130]. Baxter and Jain [67] developed a mathematical model to study the transport of fluid and macromolecules in tumours. Recently, Jain et al. [2] revisited their model to investigate the effect of vascular normalization by antiangiogenic therapy on IFP, as well as to determine the parameters that could lead to a reduction of IFP.

In other work, Ramanujan et al. [1] used a mathematical framework to study the local imbalance of pro- and antiangiogenic factors. Their model contained production, diffusion, and degradation of these factors, and was used to explain focal necrosis and dormancy in tumours. The details of their work is contained in Section 3.3. Here, we expand and generalize their model to include the effect of interstitial convection on proangiogenic and antiangiogenic factor concentrations, which is supported by the fact that convection can contribute significantly to the transport of molecules of the typical size of AGFs (see

Table 4.1). It has also been noted that convection plays an important role, not only in determining local concentrations, but also in the functionality and activity of AGFs, particularly VEGF [131]. This effect is added via a convection term in the equations that govern the concentrations of AGFs (see following section). The mathematical model is then used to study the changes in a tumours angiogenic behaviour as a result of altering tissue or blood vessel properties (e.g. hydraulic conductivity of tissue, hydraulic permeability of vessels).

Molecule	Angiogenic category	Size (kDa)	Reference
$VEGF_{165}$ dimer	Proangiogenic	45	[132]
FGF family	Proangiogenic	17–34	[133]
TSP-1	Antiangiogenic	140	[134]
Angiostatin	Antiangiogenic	38	[135]
Endostatin	Antiangiogenic	20	[136]

Table 4.1: Molecular weights of common proangiogenic and antiangiogenic growth factors.

4.2 Mathematical model

4.2.1 Angiogenic growth factor model

We first assume that angiogenic growth factors can be considered to initiate either proangiogenic (stimulatory) or antiangiogenic (inhibitory) activity [1, 78]. Although some of these factors may behave in either a proangiogenic or antiangiogenic manner depending on the state of the system, we consider this effect to be negligible. While different cellular mechanisms and signaling cascades activated by specific (and possibly multiple) factors have greater effects on the level of angiogenic activity than others, we simply consider the pro- and antiangiogenic factor concentrations to be representative of the angiogenic effect enabled by these two categories. The proangiogenic (p) and antiangiogenic (a) factor concentrations will be denoted by f_p and f_a (μg/mm^3), respectively. These factors are assumed to diffuse with constant diffusion coefficients D_j (mm^2/s), $j = p, a$, to degrade under first-order kinetics with constant deactivation rates k_j (s^{-1}) and to be produced independently with constant production rates g_j (μg/mm^3/s). Since the aforementioned diffusion, deactivation, and production parameters are used to describe entire families of factors with

Parameter	Units	Host	Tumour	Normalized
R	mm	–	4	4
K	mm^2/s/mm Hg	2.5×10^{-5}	2.5×10^{-5}	2.5×10^{-5}
Angiogenic growth factors				
D_p	mm^2/s	4.0×10^{-5}	5.5×10^{-5}	5.5×10^{-5}
D_a	mm^2/s	3.25×10^{-5}	4.0×10^{-5}	4.0×10^{-5}
k_p	s^{-1}	2.0×10^{-4}	1.99×10^{-4}	1.99×10^{-4}
k_a	s^{-1}	1.5×10^{-4}	1.1×10^{-4}	1.1×10^{-4}
g_p	μg/mm^3/s	2.0×10^{-4}	12.0×10^{-4}	12.0×10^{-4}
g_a	μg/mm^3/s	1.5×10^{-4}	7.0×10^{-4}	7.0×10^{-4}
$\widetilde{k}_p$	–	80	57.9	57.9
$\widetilde{k}_a$	–	73.8	44	44
$\widetilde{g}_p$	–	80	349	349
$\widetilde{g}_a$	–	73.8	280	280
$\widetilde{K}_p$	–	12.5	9.1	9.1
$\widetilde{K}_a$	–	15.4	12.5	12.5
Interstitial fluid pressure				
L_p	mm/s/mm Hg	3.6×10^{-7}	1.86×10^{-5}	3.7×10^{-6}
$\Phi = S/V$	mm^{2}2/mm^3	17.4	16.5	15.2
p_v	mmHg	20	20	20
σ	–	0.91	8.7×10^{-5}	2.1×10^{-3}
π_v	mmHg	20	19.8	19.2
π_i	mmHg	10	17.3	15.1
p_e	mmHg	10.9	20	20
α	–	2	14	6

Table 4.2: AGF model parameters primarily from [1] and [2]. See Tables B.1 and B.2 for further information.

varying molecular weights and kinetic rates, they are assumed to be representative of their respective angiogenic categories. However, each of these parameters can differ in host and tumour tissue, both of which are assumed to be homogeneous and isotropic, so that when appropriate, we will distinguish between these values with superscripts for host (h) and tumour (t) tissues, explicitly, e.g.

$$D_j = \begin{cases} D_j^t, & 0 \leq r \leq R, \\ D_j^h, & r > R. \end{cases}$$

As indicated earlier, we also include the convection of these factors since interstitial fluid velocity (IFV) in the tumour plays a role in determining the concentration of macromolecules including AGFs in the tumour. Assuming the velocity of these molecules is equal to the interstitial fluid velocity u (mm/s) [75] (this is equivalent to setting the retardation coefficient to 1), we arrive at the equation

$$\frac{\partial f_j}{\partial t} = D_j \nabla^2 f_j - k_j f_j + g_j - \nabla \cdot (u f_j), \quad j = p, a, \tag{4.1}$$

where the IFV, u, is given by Darcy's Law $u = -K\nabla p$, where K (mm^2/s/mm Hg) is the hydraulic conductivity of the interstitium and p (mm Hg) is the IFP [62, 137]. The IFP is modelled utilizing Starling's Law; see Section 3.1.2 for the derivation, specifically (3.12). In addition, the analytical pressure solutions are given in Equation(3.18) and plotted in Figure 3.1a for a tumour embedded in host tissue.

By adding convection to this equation, we can study larger tumours since the model was previously restricted to those where convection was not a factor (usually those tumours with radii less than 2 mm). It is worthwhile reemphasizing that interstitial convection also plays a vital role in the activity of AGFs and the process of tumour angiogenesis [131]. Convective effects have been incorporated in previous models of drug distribution and other macromolecules in tumours [62, 67], and thus it seems natural to include it in this case. The parameters for the diffusion, production, and degradation of AGFs inside the host and tumour tissues are those assumed based on the conditions stated in Ramanujan et al. [1] and these are presented in Table 4.2.

To facilitate solving (4.1), we assume that the tumour is a sphere of radius R (mm), and since the dynamics of growth factor distribution occur on a much faster time scale than tumour growth, we consider the system to be in quasi-steady-state. This results in

the equation

$$\frac{D_j}{r^2}\frac{d}{dr}\left(r^2\frac{df_j}{dr}\right) - k_j f_j + g_j + \frac{K}{r^2}\frac{d}{dr}\left(r^2\frac{dp}{dr}f_j\right) = 0. \tag{4.2}$$

Equation (3.34) can be nondimensionalized by setting $\tilde{r} = r/R$ and $\widetilde{f}_j = f_j/f_j^s$ where $f_j^s = g_j^h/k_j^h$ is the steady-state AGF concentration in host tissue. Dividing by D_j eliminates the diffusion coefficient and gives the nondimensional parameters $\widetilde{k}_j = k_j R^2/D_j$, $\widetilde{g}_j = g_j R^2/(D_j f_j^s)$ and $\widetilde{K}_j = K p_e/D_j$ where p_e (mm Hg) is the effective pressure used to nondimensionalize the equation for pressure (the nondimensional pressure is defined to be $\tilde{p} = p/p_e$, refer to Equation (3.13)). This nondimensionalization yields the equation

$$\frac{1}{\tilde{r}^2}\frac{d}{d\tilde{r}}\left(\tilde{r}^2\frac{d\widetilde{f}_j}{d\tilde{r}}\right) - \widetilde{k}_j\widetilde{f}_j + \widetilde{g}_j + \frac{\widetilde{K}_j}{\tilde{r}^2}\frac{d}{d\tilde{r}}\left(\tilde{r}^2\frac{d\tilde{p}}{d\tilde{r}}\widetilde{f}_j\right) = 0. \tag{4.3}$$

This step is essential to the model since the nondimensional quantities are used to define a measure of angiogenic activity below in (4.4).

The nondimensional parameters in the tumour and host tissues are shown in the context of the model geometry in Figure 4.1 with tumour parameters shown inside the spherical tumour and host parameters outside. Note that in the host tissue, the normalization by the steady state factor concentrations simplifies the degradation rate so that $\tilde{g}_j^h = \tilde{k}_j^h$. The system has been reduced to a system with seven nondimensional parameters.

In the absence of the convection term, that is, eliminating the last term in (4.3), an analytical solution can be obtained with appropriate boundary conditions [1] (see Section 3.3). However, in this work, we also consider the scenario where diffusion and convection could play a significant role in factor transport, and hence we rely on numerical integration schemes to solve (4.3).

4.2.2 Angiogenic activity

While we are interested in the qualitative effects of IFP on AGF concentrations, we are not specifically interested in the quantitative concentrations of these two factor groups. The relationship between the proangiogenic and antiangiogenic forces is of greater importance, since the balance between these factors is the determinant of whether angiogenesis will be locally suppressed or initiated. Following Stoll et al. [82], we introduce a measure of

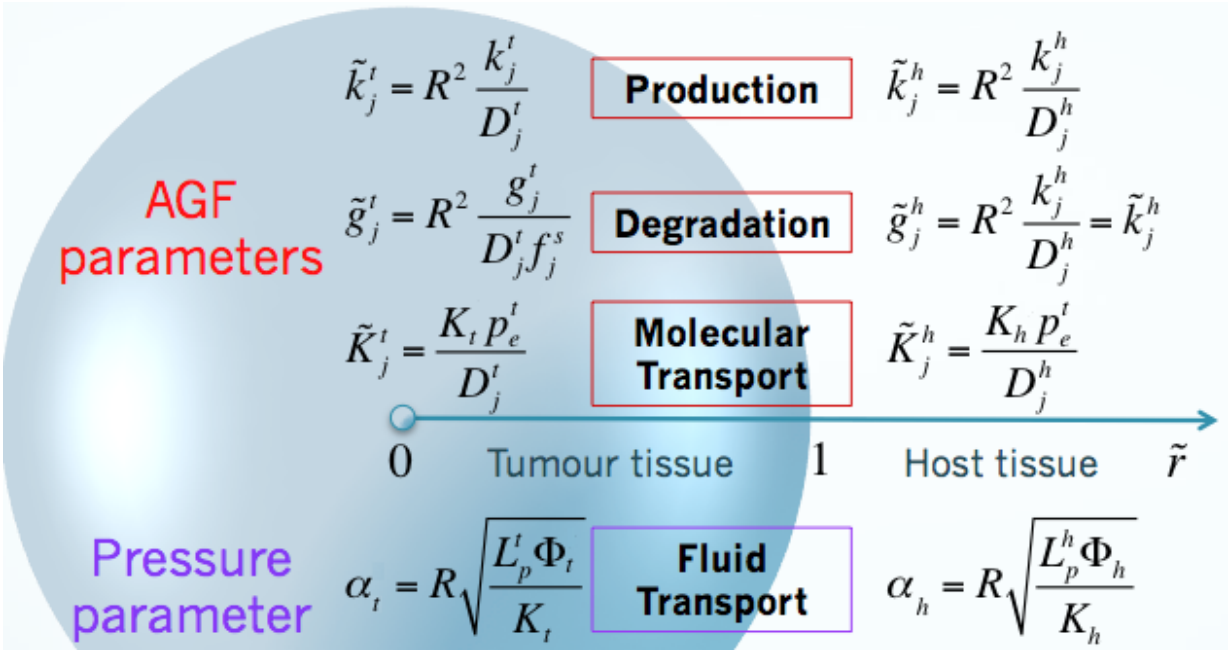

Figure 4.1: The nondimensional parameters in the tumour and host tissues are shown in the context of the model geometry. Tumour parameters are shown inside the spherical tumour while host parameters are shown outside. These parameters include the nondimensionalized production, degradation and transport parameters for AGFs and the nondimensional pressure parameter.

angiogenic activity a defined by

$$a = \begin{cases} \dfrac{\widetilde{f}_p}{\widetilde{f}_a} - 1, & \text{if } \widetilde{f}_p \geq \widetilde{f}_a, \\ 1 - \dfrac{\widetilde{f}_a}{\widetilde{f}_p}, & \text{if } \widetilde{f}_p < \widetilde{f}_a, \end{cases} \tag{4.4}$$

where $a > 0$ corresponds to angiogenesis being initiated, $a = 0$ indicates a stable vasculature network, and $a < 0$ implies that no angiogenesis is taking place, and vessels could be regressing. These scenarios are depicted in Figure 4.2 where the scale of AGFs can be tilted toward suppression or initiation of angiogeniesis. While other forms of this function for a are viable, we choose this form due to its symmetry and the apparent inclusion of the balance between these nondimensionalized factor concentrations.

A typical angiogenic activity scenario in a solid tumour maintains angiogenic repression at the tumour core where heightened levels of angiogenic inhibitors override the effect of elevated proangiogenic factor production. They also exhibit angiogenic stimulation near the tumour boundary where the angiogenic balance leans toward a proangiogenic tendency. This typically leads to the development of both an oxygen-deprived core consisting of hypoxic and necrotic cells along with a heavily vascularized and rapidly proliferating outer rim [138].

We use the angiogenic activity measure a to classify the model output into one of three cases: focal suppression, global suppression, and global angiogenesis [1]. The typical focally suppressive behaviour described above is characterized by a transition from negative to positive values of a as we move from the core to the rim part of the tumour. Global suppression and angiogenesis are defined by $a < 0$ and $a > 0$, respectively, everywhere inside the tumour (i.e., for all $r \in [0, R]$).

4.2.3 Parameters

Parameters governing AGF production, degradation and diffusion are taken from [1] while those that govern the pressure and therefore convection in the model are taken from [2, Table 3]; these are all given in Table 4.2. Those that differ between host (superscript h) and tumour (superscript t) tissues along with those for tumours whose vascular structure has been normalized using antiangiogenic agents are given in separate columns. While

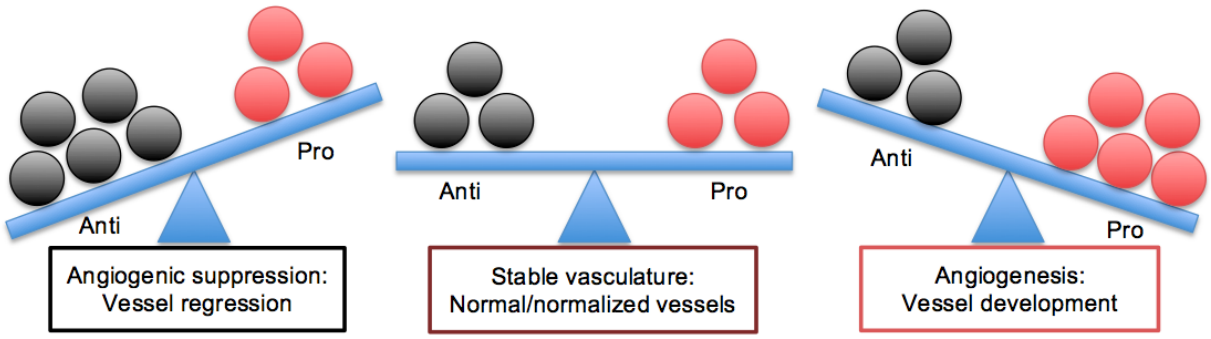

Figure 4.2: The balance between proangiogenic and antiangiogenic factors can be perturbed by the removal or addition of proangiogenic or antiangiogenic factors. If the angiogenic switch is thrown, the balance is tipped toward proanigiogenic factors, this corresponds to $a > 0$. If vessels are regressing, the balance is tipped toward antiangiogenic factors and $a < 0$. In normal tissues and normalized tumour tissues, the scale is balanced and $a = 0$.

the original table in [2]has a range for the vascular pressure p_v, we have set a base value of $p_v = 20$ mmHg for all tissues. This value is close to the mean value for the range of parameters in both normal and tumour tissues. Similarly, the ranges for surface area of blood vessel wall per unit volume $\Phi := S/V$ are replaced with values near the mean.

4.2.4 Solution method

We assume that the tumour is embedded in normal host tissue (e.g., in an organ) and consider the following boundary conditions. We ensure spherical symmetry at the core by imposing

$$\left.\frac{df_j}{dr}\right|_{r=0} = 0, \quad \text{and} \quad \left.\frac{dp}{dr}\right|_{r=0} = 0$$

and enforce continuity of factor concentrations and fluxes at the tumour boundary by setting

$$f_j(R^-) = f_j(R^+), \quad \text{and} \quad \left.-D_j^t\frac{df_j}{dr} + uf_j\right|_{r=R^-} = \left.-D_j^h\frac{df_j}{dr} + uf_j\right|_{r=R^+}$$

along with continuity of IFP and IFV by setting

$$p(R^-) = p(R^+), \quad \text{and} \quad u(R^-) = u(R^+).$$

The latter condition is equivalent to

$$-K_h \frac{dp}{dr}\bigg|_{r=R^-} = -K_t \frac{dp}{dr}\bigg|_{r=R^+},$$

where typically $K_h = K_t$ (based on [2, Table 3]). We also require that factor concentrations and the pressure reach steady state as we move away from the tumour and so impose

$$\lim_{r\to\infty} \frac{df_j}{dr} = 0, \quad \lim_{r\to\infty} \frac{dp}{dr} = 0.$$

This ensures that the factor concentration reaches steady state f_j^s and that $p(r) \to 0$ for large r (achieved by setting $p_e^h = 0$).

The analytical solution for nondimensionalized pressure, $\widetilde{p}$, can be obtained by solving (3.13). This along with the solution for nondimensional IFV, $\widetilde{u} = uR/(K_t p_e)$, was derived by Jain et al. [67] (see Section 3.1.2). The radial profile for $\widetilde{p}$ is then used to numerically solve for the factor concentrations in (4.3). Due to the non-linearity of (4.3), we could no longer rely on the analytical technique shown in 3.3, instead we had to develop a numerical scheme to approximate their solutions. The corresponding matrix inversion problem was performed using a second-order finite difference scheme in MATLAB [139].

4.3 Results

Interstitial pressure and velocity profiles are obtained from solving (3.13); these profiles can be viewed in Figures 3.1a and 3.1b, respectively. Most notably, as the parameter α_t increases, the pressure reduction at the tumour rim becomes more drastic and the IFP inside the tumour increases. Equivalently, as α_t increases, the interstitial fluid velocity reaches a higher and sharper peak at the tumour rim while remaining zero at the core.

We solve (4.3), with the boundary conditions given in the previous section and the analytical pressure profiles, to determine AGF concentrations and subsequently the imbalance factor in (4.4). First, we compare the results of our model with those of the model without

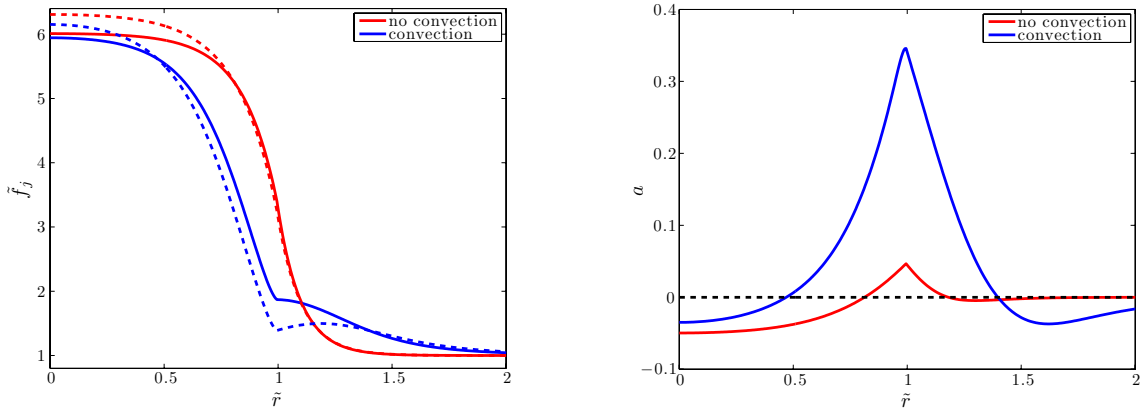

(a) Nondimensional AGF concentrations $\tilde{f}_j$.

(b) Angiogenic activity a.

Figure 4.3: Comparing 4.3a nondimensionalized proangiogenic (solid) and antiangiogenic (dashed) growth factor concentrations and 4.3b angiogenic activity for the model without convection ($u = 0$) and with convection ($\alpha_t = 14$, $\alpha_h = 2$). With the addition of convection, the area of angiogenic stimulation is larger and more pronounced

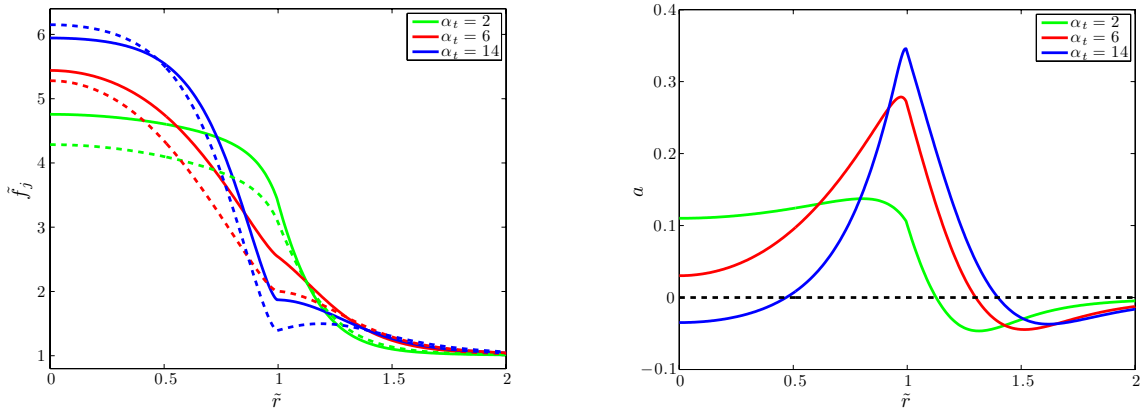

(a) Nondimensional AGF concentrations $\tilde{f}_j$.

(b) Angiogenic activity a.

Figure 4.4: Effect of varying the vascular hydraulic permeability, L_p (mm/s/mm Hg), in the tumour tissue on 4.4a AGF concentrations and 4.4b angiogenic activity. The values of α_t=2, 6, 14 correspond to L_p=3.6×10^{-7}, 3.7×10^{-6}, 1.86×10^{-5} mm/s/mm Hg. The parameter for host tissue was fixed at $\alpha_h = 2$. This changes the shape of the resulting pressure profile and thus the interstitial fluid velocity.

convection [1]; the only difference between the curves corresponding to no convection in Figure 4.3a and the original results of [1] is that we consider a tumour radius of 4mm (up from 2.5mm) in order to remain consistent with the parameter estimates from [2] that are used for the pressure model. For our model with convection, the angiogenic activity still reaches a maximum at the tumour boundary, and the region of angiogenic suppression persists at the tumour core. However, we now observe a higher peak of angiogenic tendency at the rim and a larger area of angiogenic stimulation, see Figure 4.3b. This is due to the larger difference between the proangiogenic and antiangiogenic growth factor concentrations near the boundary, a result of these factors being pushed out of the tumour core into the surrounding normal tissue as can be seen in Figure 4.3a. However, as we will see, the transition from a system without convection to a system with convection is not straightforward.

By changing the values of α_t, we can see the effect of varying only the contribution of the pressure profile on the model. This can be achieved by modifying L_p, Φ, or R. However, we wish to consider a fixed tumour radius and surface to volume ratio, so we will consider changes in α_t to correspond to changes in the values of L_p only. Note that we cannot analyze the contribution of IFP alone by modifying K since this would also change the value of the nondimensional convection parameter in (4.3). Similarly, we can look at the contribution of the nondimensional convection parameter alone by modifying p_e. Finally, we will consider the effect of changing the hydraulic conductivity K which simultaneously decreases α_t and increases $\widetilde{K}_j$ affecting the pressure profile and the rate of convection.

We consider first the effects of varying only the pressure parameter α_t (for fixed $\alpha_h = 2$), which, as stated above, we will assume is achieved by changing L_p, leaving the rest of the parameters fixed as in Table 4.2. As can be seen in Figures 4.4a and 4.4b, the results suggest that altering the pressure parameter leads to different angiogenic behaviour in the tumour. Indeed, the region of angiogenic suppression ($a < 0$) at the core is not conserved for all values of α_t between the cases of negligible convection ($\alpha_t \approx 0$) and non-normalized tumour tissue ($\alpha_t = 14$). Thus, the behaviour is more complicated than that observed by modifying the convection parameter via p_e or both pressure and convection parameters via K (see Figures 4.5a and 4.5b and the Discussion below). For values of α_t close to zero, there is a region of angiogenic suppression ($a < 0$) at the core and stimulation ($a > 0$) at the rim (similar to the no convection case in Figure 4.3b). For midrange values of α_t the tumour can experience global angiogenesis (i.e., $a > 0$ for all $r \in [0, R]$). That is, instead

of the proangiogenic and antiangiogenic concentrations balancing inside the tumour, the antiangiogenic factor concentration lies entirely below that of the proangiogenic factor concentration. Considering $\alpha_t = 2$, this assumes that the tumour tissue has the same value of L_p as normal tissue. Indeed, the angiogenic activity in this case remains constant inside the tumour due to a consistent difference between the two factor concentrations leading to global angiogenesis. For the parameters corresponding to normalized tumour tissue ($\alpha_t = 6$), we see an intermediate behaviour where global angiogenesis occurs, but the activity at the core is much lower than at the tumour rim. For high values of α_t (e.g., $\alpha_t = 14$), the core once again becomes a region of suppression but with higher levels of angiogenic activity occurring close to the tumour rim as previously observed in the convection case in Figure 4.3b. While different angiogenic profiles are obtained, it remains true that the angiogenic activity at the tumour rim increases with α_t.

As expected, fixing $\alpha_t = 14$ and increasing p_e, thereby increasing the convection of factors leads to higher concentrations outside the tumour (see Figure 4.5b) and larger concentration differences at the rim. This coincides with an increase of angiogenic activity at the tumour rim. For the parameters considered and a reasonable range of p_e, the tumour exhibits only focal suppression. Other activities can be achieved but require a modification of the AGF parameters (see the sensitivity analysis in Figures 4.6a–4.6c).

Finally, we consider varying K, an increase in this parameter value leads to decreased α_t and α_h along with increased values of the convection parameters $\widetilde{K}_j$. This essentially compounds the effects observed in Figures 4.4a, 4.4b and 4.5a leading to elevated levels of angiogenesis inside the tumour (from decreasing α_t) and at the tumour rim (from increasing p_e); refer to Figure 4.5b.

Following Ramanujan et al. [1], we performed a sensitivity analysis on AGF production; see Figures 4.6a–4.6c. We generalize their results by fixing one of the parameters of interest (α_t, p_e, and K) and analyze results over a large range of tumour production values ($\tilde{g}_p^t$ and $\tilde{g}_a^t$). Focal suppression occurs between lines of the same colour, global suppression occurs above this region (high $\tilde{g}_a^t$, low $\tilde{g}_p^t$), and global angiogenesis occurs above (low $\tilde{g}_a^t$, high $\tilde{g}_p^t$). The results indicate that focal suppression is observed only for a narrow sliver of the parameter space. This is realistic since one would assume that the behaviour is sensitive to the balance of these factors production rates. As expected, the behaviour is not as sensitive to varying the host production parameters as it is to tumour production (results are not shown).

Figure 4.6a shows how this sensitivity changes when varying α_t. As α_t increases, the

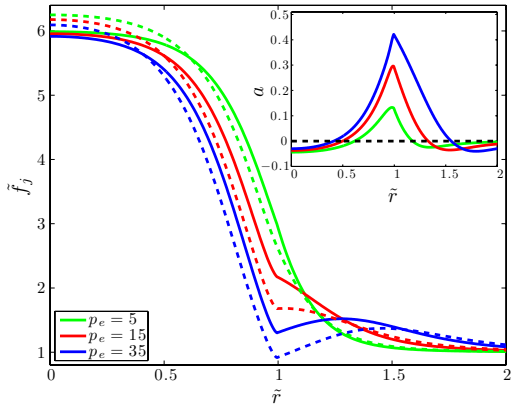

(a) The effect of varying p_e (mmHg) on nondimensional AGF concentrations $\tilde{f}_j$ and angiogenic activity a (inset) for fixed $L_p = 1.86 \times 10^{-5}$ mm/s/mm Hg. This alters the value of the convection parameters $\widetilde{K}_j$.

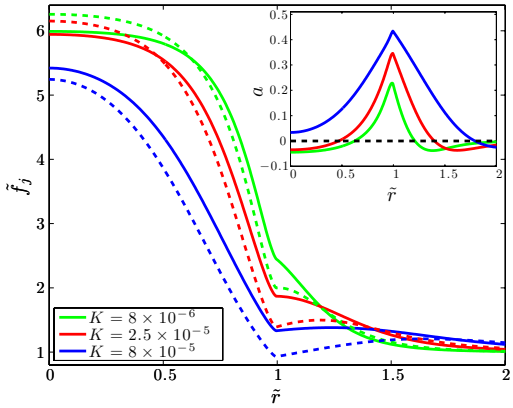

(b) The effect of increasing K (mm^2/s/mmHg) on nondimensional AGF concentrations $\tilde{f}_j$ and angiogenic activity a (inset) for fixed $L_p = 1.86 \times 10^{-5}$ mm/s/mm Hg and $p_e = 10.9$ mm Hg. This simultaneously decreases α_t and increases $\widetilde{K}_j$ leading to altered IFP and elevated convective transport.

Figure 4.5: Nondimensional AGF concentrations $\tilde{f}_j$ under parameter changes. Inset: Angiogenic activity a.

region of focal suppression widens from a very narrow region to encompass more of the parameter space above and below this region. For different values of p_e, we notice little movement in the boundary between focal suppression and global angiogenesis while the boundary between focal suppression and global suppression increases with p_e (see Figure 4.6b). Finally, for K, we see a combination of these effects; the region where focal suppression and peripheral stimulation occur is widening and drifting towards the top left corner of Figure 4.6c (high $\tilde{g}_a^t$, low $\tilde{g}_p^t$). Parameter values that correspond to focal suppression switch to values corresponding to globally angiogenic behaviour when the convection term is added. Also shown in these graphs are the precise points in parameter space corresponding to the tumour production values $\tilde{g}_p^t = 349$ and $\tilde{g}_p^t = 279$; this will be discussed further in the following section.

4.4 Discussion

α_t	$\tilde{g}_p^t = 349$ (no treatment)	$\tilde{g}_p^t = 279$
2	Global angiogenesis	Global suppression
6	Global angiogenesis	Focal suppression
14	Focal suppression	Focal suppression

Table 4.3: Angiogenic activity resulting from cytotoxic therapy (see Figure 4.7a).

We have presented a mathematical model to study the effects of interstitial convection on proangiogenic and antiangiogenic factor concentrations in tumour and surrounding host tissue, and from this determined the overall angiogenic activity of the tumour. The resulting AGF concentration profiles agree qualitatively with experimental observations that show the highest concentrations in the core of the tumour, decreasing as one approaches the tumour rim [126]. Also, the resulting angiogenic behaviours, including suppression at the tumour core and maximal angiogenic stimulation near the tumour rim, correspond with experimental observations such as tumour perfusion [140]. The imbalance between proangiogenic and antiangiogenic factors provides an empirical explanation for observed angiogenic activity and could be correlated with resulting tumour necrosis or growth. While the precise effects of IFP and factor convection on the angiogenic activity of tumours have not been experimentally verified, our results indicate that an IFP gradient could significantly influence suppression and stimulation of angiogenesis in a tumour.

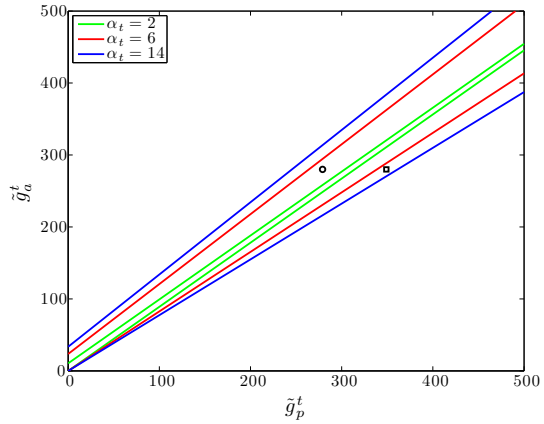

(a) The effect of changing the nondimensional pressure parameter α.

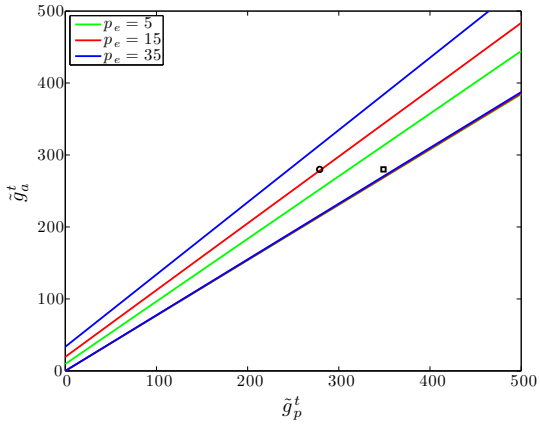

(b) The effect of changing the effective pressure p_e.

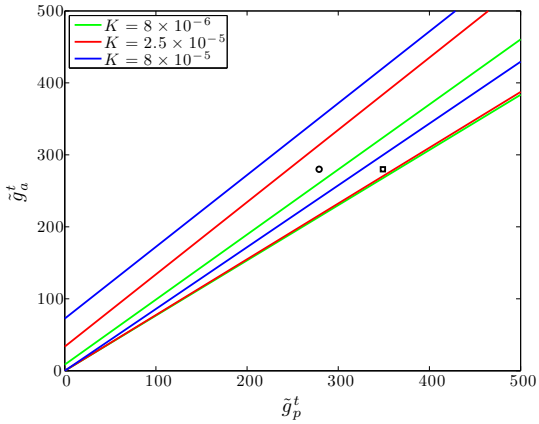

(c) The effect of changing the hydraulic conductivity of the interstitium K.

Figure 4.6: Sensitivity to AGF production parameters where focal suppression occurs between lines of the same color, global suppression occurs above this region (high $\tilde{g}_a^t$, low $\tilde{g}_p^t$) and global angiogenesis occurs above (low $\tilde{g}_a^t$, high $\tilde{g}_p^t$). The black square denotes parameters from Table 4.2 used for the tumour angiogenic factor production ($\tilde{g}_p^t = 349$) while the black circle indicates the lowered proangiogenic factor production used for chemotherapy ($\tilde{g}_p^t = 279$); resulting angiogenic activity profiles are shown in Figure 4.7a.

While not explicitly included, the effect of antiangiogenic treatments can be ascertained in this model since it has been shown that the value of α_t decreases when the vasculature is normalized due to the application of, for instance, anti-VEGFR-2 [130]. The value of α_t can decrease through any combination of decreasing Φ, L_p, or R, all of which could occur as a result of antiangiogenic therapy. Φ decreases as blood vessels are destroyed and/or remodelled due to the administration of an antiangiogenic drugs (in this case, there is less area of vessel wall per unit of tumour volume). The radius R decreases indirectly; as tumour vessels regress, tumour cells are deprived of oxygen and consequently become hypoxic or necrotic. Moreover, the vessel permeability L_p could decrease due to judicious application of antiangiogenic agents (vessel normalization, [35]). The pressure parameter α_t could also be decreased by increasing the hydraulic conductivity K, an effect that would be somewhat counterbalanced by the corresponding increase in the convection parameter (refer to Figure 4.5b). However, K could be increased by administering enzymes that degrade the extracellular matrix (ECM), which subsequently decreases the flow resistance in the interstitium [137]. Overall, strategies that lead to the reduction of the parameter α_t result in decreased IFP, which influences tumour angiogenesis activity. As shown in Figure 4.4b and discussed in the previous section, the changes in the interstitial fluid velocity from decreasing α_t reduces the angiogenic activity at the rim and produces a more constant level of angiogenic activity inside the tumour. On the other hand, one could also consider the administration of antiangiogenic agents by decreasing the concentration of proangiogenic factors through an increase of their degradation (or deactivation) constant (see Figure 4.7b). This increase in deactivation should take into account that most antiangiogenic treatments only affect a single factor or a family of growth factors.

One can consider the effect of cytotoxic therapies by noting that the application of either chemotherapy or radiotherapy reduces the number of tumour cells leading to less proangiogenic factor production (Figure 4.7a); this is achieved by lowering the parameter $\tilde{g}_p^t$. We considered the reduction of this production rate and the movement through parameter space is shown in the sensitivity diagrams (Figures 4.6a–4.6c). In Figure 4.7a, we can observe that the resulting angiogenic behaviour depends on the value of α_t as summarized in Table 4.3. The effect of cytotoxic therapies either on tumour cells or blood vessels could also reduce the pressure due to increased interstitial space; this could be included in our model by, for instance, increasing K (Figure 4.5b). The effects of cytotoxic treatments could also be included by reducing the tumour radius R. Combinations of antiangiogenic therapy and chemotherapy could be considered by performing the aforementioned param-

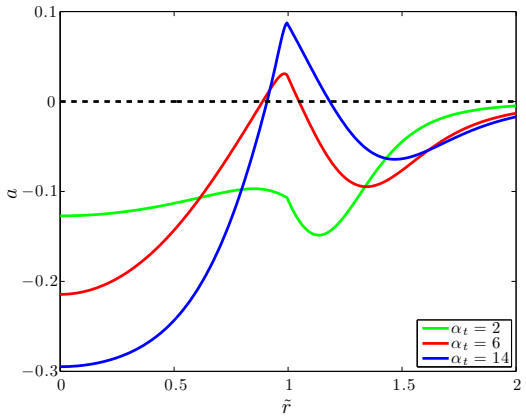

(a) Applying chemotherapy leads to cell death and hence decreased tumour proangiogenic production (from $\tilde{g}_p^t = 349$ to $\tilde{g}_p^t = 279$).

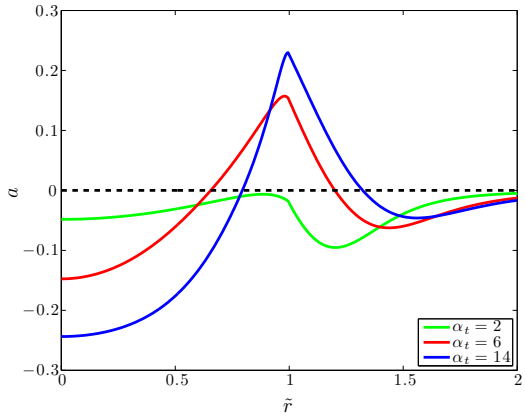

(b) Applying antiangiogenic therapy inactivates proangiogenic factors leading to increased tumour proangiogenic deactivation (from $\widetilde{k}_p^t = 58$ to $\widetilde{k}_p^t = 70$).

Figure 4.7: The effects of treatment on angiogenic behaviour of tumours.

eter changes simultaneously; these changes compound the effects leading to even further reduced angiogenic tendency.

Decreasing the IFP prior to or simultaneously with other therapies is an important concern in cancer treatment since the flow of interstitial fluid out of the tumour prevents drugs from penetrating the tumour bulk. While the various effects of antiangiogenic treatments (decreasing Φ, L_p, or R) or ECM-degrading enzymes (increasing K) all reduce α_t and hence pressure, there are other independent mechanisms that could also elicit reductions in pressure. For instance, reducing p_e would reduce IFP. This could be achieved by reducing the vascular pressure p_v, which can be readily accomplished by decreasing the resistance of blood. Clinically, decreasing the viscosity of the blood or normalizing the tumour vasculature would accomplish the goal of less resistance [137]. The effects of changing p_e are shown in Figure 4.5a as decreasing the effective pressure leads to diminishing levels of angiogenic activity at the rim.

4.5 Conclusions

By taking into consideration the different angiogenic behaviours exhibited by modifying any of the key parameters involved in the pressure model, we can establish an alternate (or more likely, complementary) mechanism for these changes. Whereas it was previously hypothesized [1] that the production, degradation, and diffusion of the AGFs were primarily responsible for the overall angiogenic behaviour, we have exhibited that changes in the tumour tissue physiology could also elicit these changes. The interplay between the two groups of parameters, those related to AGF properties that determine AGF concentrations and those corresponding to the tumour physiology that determine interstitial fluid pressure, should be further investigated with more detailed modelling and experimental work. We emphasize that it was never the goal of this work to quantitatively predict concentrations of specific AGFs or to model the process of angiogenesis but rather to emphasize the importance of tumour tissue properties and macromolecule convection on angiogenic behaviour.

One should note that there are limitations to our mathematical model, many of which have been mentioned during the model development. These include the existence of two distinct groups of AGFs, the specific functional form of our angiogenic activity measure and the distributed fluid source terms. Most prominent among these various assumptions are those of spherical symmetry and homogeneity of tissues and environment [1]. The other main limitation is the assumption of constant parameter values both inside the tumour and in the host tissue, or even the constant values assumed across this boundary. These assumptions make the modelling and computation tractable especially since physiological parameters as functions of radial distance are uncommon in the literature. However, our computational approach can readily be extended to include aspects of the heterogeneous tumour microenvironment upon availability of relevant experimental data. Finally, we propose that an experimental study measuring both interstitial fluid pressure and quantities associated with AGF concentrations or angiogenic activity (such as vessel density or perfusion) would help to validate our qualitative model predictions.

Chapter 5

Microvessel Models for Cell Metabolism and pH

This chapter analyzes microvessel models for cell metabolism and pH. Cell metabolism in a tumour is enabled by angiogenesis that brings the oxygen, glucose, and other metabolites necessary to cell survival. First, we will propose a model for metabolic symbiosis that includes glucose, lactate and oxygen concentrations in a tissue that utilizes glucose-fuelled and lactate-fuelled respiration along with glycolysis. The ATP production in tissue under various metabolic inhibitor treatments are considered and the importance of glycolysis shutdown is emphasized. A simpler version of this metabolic model that includes oxygen-fuelled respiration and glycolysis is coupled to a cellular buffering model that requires the addition of carbon dioxide, bicarbonate and H^+ to the model. The effects of hypoxia and cell permeability are observed in this context. We also show results for adding convective transport, which show that unlike the macroscopic model considered in the previous chapter, this is a diffusion-dominated system.

5.1 Introduction

The extensive metabolic requirements for cancer cell proliferation coupled with the harsh microenvironment in solid tumours culminates in a highly adaptive and complex network for cellular energy production. The genetically altered metabolic behaviour of cancer cells

has led to a number of emerging metabolic paradigms, in addition to those that are universally exhibited in both cancerous and normal cells. We will investigate this complex metabolic behaviour by formulating a minimal mathematical model that includes the essential metabolites of glucose, lactate and oxygen in the tissue surrounding a microvessel. This model will enable the quantification of various behaviours, such as the symbiotic relationship that exists between lactate-producing glycolytic cells and lactate-consuming respiratory cells, and the analysis of metabolic dependence on various physiological conditions such as hypoxia and induced metabolic inhibition. Metabolic inhibition including glycolytic inhibitors among many others targets could be very important for cancer treatment since an ATP deficit can induce apoptosis [141]. The key consideration for addressing this problem with mathematics is the formulation of nutrient consumption rates that encompass the various primary facets of cancer cell metabolism and their corresponding ATP yields.

In normal well-oxygenated tissues the primary source of ATP is the process of cellular respiration. The complete conversion of glucose to carbon dioxide and water has an ideal yield of at most 29 ATP [20] (although the reactions contained in C.4 suggest a yield as low as 24.25). The preliminary stage of cellular respiration is glycolysis, the conversion of glucose to pyruvate; this process directly produces 2 ATP. In hypoxic conditions this pyruvate is preferentially converted into lactate via the enzyme lactate dehydrogenase (LDH) to regenerate the essential cofactor NAD^+. In oxygenated conditions this pyruvate is transported across the inner mitochondrial matrix where it is decarboxylated and enters the citric acid cycle; the citric acid cycle directly generates 2 more ATP per glucose. The primary energy payoff is a result of cofactor oxidization that enables the electron transport chain to establish a proton gradient across the inner mitochondrial matrix. ATP synthase utilizes this electrochemical gradient to drive the phosphorylation of approximately 25 additional ATP per glucose molecule.

The aforementioned universal traits that cancer cells and normal cells share include cellular responses to various levels of oxygen, lactate or glucose. Examples include a Crabtree-like effect and a Pasteur-like effect [4]. The Crabtree-like effect is when oxygen consumption decreases as glucose concentration increases. This can be explained by an increasing reliance on glycolysis for ATP when hyperglycaemic conditions are encountered. The Pasteur-like effect is decreased glucose consumption as oxygen increases. This is due primarily to the inhibition of various metabolic steps by the presence of elevated ATP and other intermediaries. However, cancer cells are unique in that they preferentially utilize

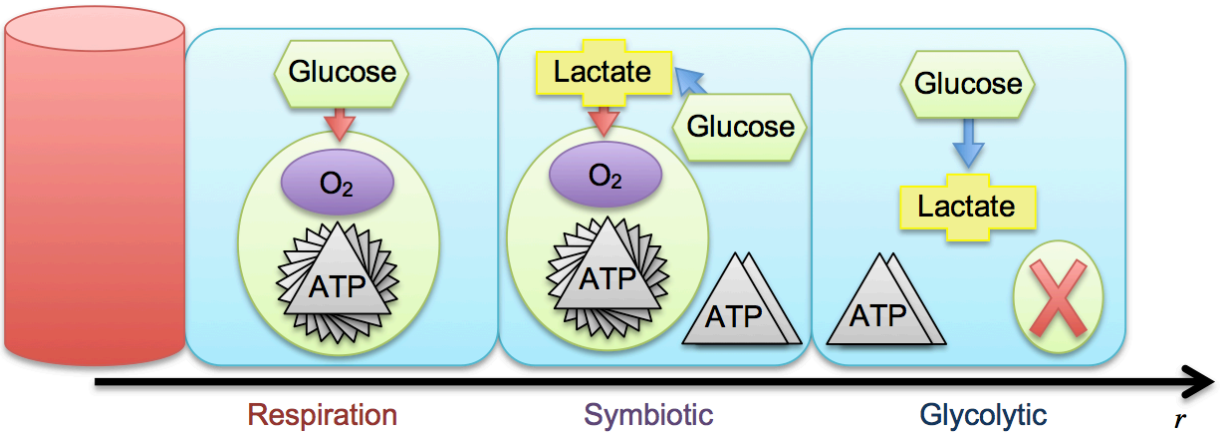

Figure 5.1: The spatial relationship between the cell populations in the model. When the glucose and oxygen concentrations are highest near the vessel wall, the cells preferentially utilize glucose-fuelled respiration. When the oxygen supply is depleted far from the vessel, the cells rely on glycolysis. The glycolytic cells produce large quantities of lactate which are consumed by cells at intermediary distances. These cells are participating in a behaviour that we will refer to as metabolic symbiosis.

glycolysis, even in the presence of oxygen, coined aerobic glycolysis. This phenomenon is generally referred to as the Warburg effect whereby cells rely primarily on glycolysis even in the presence of sufficient oxygen to perform respiration [22]. There is a perceived inefficiency of this metabolic strategy, namely the dramatically reduced ATP yield, just 2 per glucose instead of 29, however, it has the benefits of faster ATP production and it is likely that much of this glucose is being consumed for proliferative [23] (e.g. by the pentose phosphate pathway) purposes. In addition to the typical glycolytic phenotype exhibited in many cancers, there is also a developing story of a co-operative relationship existing between aerobic and anaerobic cancer cells. The lactate necessarily produced by glycolytic cells is being pushed back into the respiratory cycle by being converted into pyruvate (summarized in [142, 143]); this spatial relationship is shown in Figure 5.1. Lactate consumption has been observed *in vitro* in various models [144, 145] as well as *in vivo* as early as the early 80s [26]. However, a renewed interest in the topic was piqued when Sonveaux et al. [27] showed that reducing lactate uptake by cancer cells led to hypoxic cell death, a particularly difficult subpopulation to target using traditional methods.

Metabolic phenomena have been studied in great detail by mathematical models, but models of tumour metabolism rarely include the interaction of the transport mechanisms

of microvessels with the localized metabolic behaviour of cells. In the section to follow, we will develop a mathematical model that describes the concentrations of molecules that are important to cellular metabolism in the tissue around a single three-dimensional vessel that exhibits diffusion-dominated interstitial transport. We will then use this model to demonstrate how the properties of the tumour cell population, such as glucose, lactate and oxygen consumption rates, affect hypoxia and ATP production around a single vessel. The effects of metabolic inhibitors will be investigated by parameter changes that could be elicited by the application of glycolysis inhibitors, lactate dehydrogenase (LDH) inhibitors or respiratory inhibitors. We are interested in those metabolic inhibitors that could cripple the cells' ability to produce ATP. Furthermore, these micrometer scale predictions give an indication of local shifts in cell metabolism, which could aid in developing combination treatments that can simultaneously hinder multiple metabolic pathways in tumours. Our simulations show that treatments targeting glycolysis via glycolytic enzyme inhibition or LDH inhibition, which have been thoroughly investigated [146, 147, 148], could be the most successful metabolic suppression strategy.

5.2 Mathematical model

A model to describe the concentrations of the major players in the metabolic pathways of respiration and glycolysis, will be outlined here. Its origins lie in a metabolic model developed by Casciari et al. [3] that was subsequently applied on the microscale by [25]. The functional forms for the production rates are similar to those proposed by Mendoza et al. [90].

In hypoxic and anoxic conditions, cells must partially or exclusively rely on metabolic pathways, such as glycolysis, that do not require oxygen for ATP production. In glycolysis, the preliminary stage of respiration, a single glucose molecule ($C_6H_{12}O_6$) yields 2 ATP, which we will denote under the reaction arrow with a boxed ATP yield number, with the byproducts of lactate and a proton. Denoting glucose by G and lactate by $L^-(C_3H_5O_3^-)$, the net reaction is

$$\mathrm{G} \xrightarrow[\boxed{2}]{k_G} 2\mathrm{L}^- + 2\mathrm{H}^+, \tag{5.1}$$

where k_G (mM/s) is the rate of glucose consumption by glycolysis that results in lactate formation. The accumulation of these hydrogen ions in a solid tumour is a primary

contributor to tumour acidosis.

In the presence of oxygen (O_2), glycolysis is typically followed by the rest of the respiratory process with an ideal energy yield of approximately 29 ATP molecules with carbon dioxide (CO_2) and water (H_2O) as the only byproducts. The constituent reactions can be found in C.4 and the simplified summary reaction is

$$\mathrm{G} + 6\mathrm{O_2} \xrightarrow[\boxed{29}]{k_O} 6\mathrm{CO_2} + 6\mathrm{H_2O}, \tag{5.2}$$

where k_O is the rate of glucose consumption that results in cellular respiration.

To represent the metabolic symbiosis between cells primarily producing energy via glycolysis and those consuming lactate in well-oxygenated areas, we will link the above two reactions with the lactate-consuming net reaction

$$\mathrm{L^-} + \mathrm{H^+} + 3\mathrm{O_2} \xrightarrow[\boxed{13.5}]{k_L} 3\mathrm{CO_2} + 3\mathrm{H_2O}, \tag{5.3}$$

where k_L is the rate of lactate consumption. This summarizes the re-entry of lactate, via conversion to pyruvate, into aerobic respiration that yields 13.5 ATP per lactate molecule. The relationships between the summary reactions included in the model are given in Figure 5.2. For details on the omitted intermediary steps and derivations of these summary reactions and ATP yields, see C.4.

Under the strictest assumptions, the only chemical species required for a mathematical model are the three substrates required for the metabolic pathways in (5.1), (5.2) and (5.3). We denote the concentrations of oxygen, lactate$^-$ and glucose in the extracellular space by $X = O$, L, G, respectively, and their consumption rates per unit volume are denoted by Q_X. These extracellular concentrations are modelled by conservation equations of the form

$$\frac{\partial X}{\partial t} + \nabla \cdot J_X + Q_X = 0,$$

where J_X is the flux of species X. In general, the flux can be given as a sum of convective, migratory and diffusive elements. Due to the small molecular sizes of the molecules considered here, their transvascular and interstitial transport are diffusion-dominated. On larger spatial scales, convection becomes an important transport mechanism for large molecules

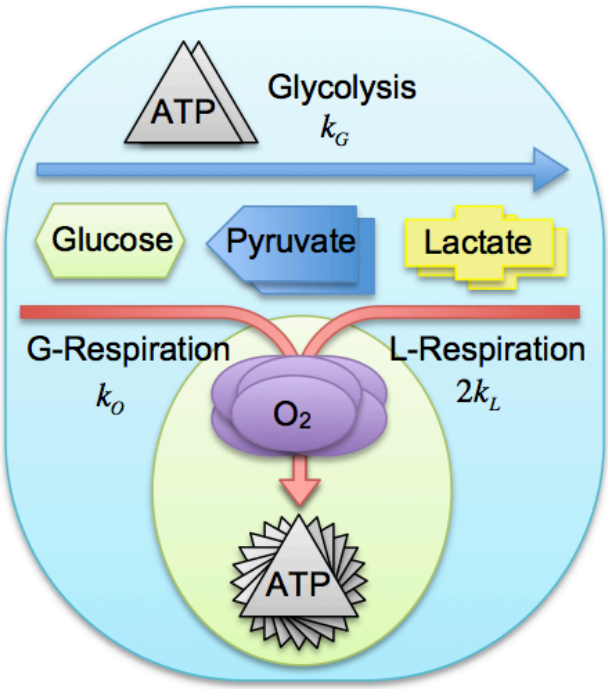

Figure 5.2: The summary reactions included in the metabolism model.

but since we are dealing only with the interstitial fluid pressure generated by a single microvessel, and the molecules are sufficiently small, convection is excluded here (as it was in [25]). The migration of charged particles due to the presence of an electric field will also be omitted since its contribution to the flux of lactate is minimal and requires the addition of other charged molecules (e.g. protons, sodium, chlorine, etc.) to the model in order to ensure electroneutrality. Assuming the simplified flux is given by Fick's law $J_X = -D_X \nabla X$, where D_X is an effective diffusion coefficient in the tissue and that all species have reached steady state, gives

$$D_X \nabla^2 X = Q_X. \tag{5.4}$$

In cylindrical coordinates, corresponding to the tissue outside of a vessel, the system of equations is

$$D_X \frac{1}{r}\frac{d}{dr}\left(r\frac{dX}{dr}\right) = Q_X, \qquad X = G, L, O, \tag{5.5}$$

where the consumption rates will be discussed below.

The appropriate boundary condition at the vessel wall must ensure that the diffusive flux in the interstitial space outside of the vessel is equal to the fluid flux across the vessel wall, however, a simplified version of this boundary condition can be used which corresponds to high vascular permeability, where the perivascular concentration and vessel concentration are assumed equal: $X(\omega^+) = V_X$. The far-field boundary condition at the penetration depth (r=Ω)

$$\left.\frac{dX}{dr}\right|_{r=\Omega} = 0, \tag{5.6}$$

assumes that there is zero flux of the molecular concentrations far from the vessel. See C.1 for further information on the boundary conditions.

The consumption rates of glucose, lactate and oxygen are empirically formulated functions of their concentrations that are capable of capturing the behaviour of multiple metabolic behaviour regimes. Many have been proposed in the literature, those provided in [65, 89] form a sample. The production rates given below are motivated by taking a minimalist approach to the choice of functional forms with fewer parameters than previous propositions [25] that encompass previous models ([90]) yet capture many metabolic regimes. Assuming that oxygen, glucose and lactate are present only in metabolic pathways, their consumption rates can be expressed in terms of the rates of the metabolic reactions (5.1), (5.2) and (5.3): k_O, k_G and k_L. Indeed, we have

$$\begin{aligned} Q_O =& 6k_O + 3k_L, \\ Q_L =& k_L - 2k_G, \\ Q_G =& k_O + k_G. \end{aligned}$$

These three observations together yield the equation,

$$Q_G = \tfrac{1}{6}Q_O - \tfrac{1}{2}Q_L, \tag{5.7}$$

a strict relationship between the three consumption rates. We will now proceed with formalizing these rates by formulating expressions for k_O, k_G and k_L in order to obtain the consumption rates. Note that an alternate approach could formulate expressions for only two of Q_O, Q_G and Q_L and then use (5.7) for the remaining consumption rate. The latter method is not plausible unless additional molecules are added to the model, specifically

pyruvate, the molecular hub of these rates.

To establish k_G, the rate of glycolysis that results in lactate production, above and beyond the rate required as the pyruvate-producing preliminary step of respiration, we must consider encompassing both normal cell behaviour and cancer cell behaviour. One of the noted key differences between these cell types is the well-known Warburg effect whereby cancer cells consume much more glucose, and preferentially utilize glycolysis even in the presence of sufficient oxygen for respiration, a process dubbed aerobic glycolysis. We propose the form

$$k_G = B_G \frac{G}{G + \Lambda_O O + K_G},$$

where B_G is the maximal rate, K_G is the half-maximal concentration (in the absence of oxygen) and Λ_O is a novel parameter that can inhibit superfluous glycolysis in the presence of sufficient oxygen to produce ATP. In cancer cells exhibiting the Warburg effect this parameter would be relatively small, as the glycolytic flux would be highly elevated regardless of oxygen concentration, while in normal cells or cancer cells that do not preferentially utilize aerobic glycolysis this parameter value would be relatively large, effectively inhibiting glycolysis until hypoxic conditions are encountered.

For glucose and lactate-fuelled respiration we use a basic Michaelis-Menten expression to express the dependence on oxygen concentration and a competitive expression to include the proportion that is glucose-fuelled and lactate-fuelled. These rates are

$$k_O = B_O \left(\frac{\Lambda_G G}{\Lambda_G G + \Lambda_L L + \Gamma_G} \right) \frac{O}{O + K_O}, \tag{5.8}$$

$$k_L = B_L \left(\frac{\Lambda_L L}{\Lambda_G G + \Lambda_L L + \Gamma_L} \right) \frac{O}{O + K_O}, \tag{5.9}$$

respectively. The Michaelis-Menten half-maximal concentration for oxygen is K_O, the maximal rates for glucose and lactate consuming cells are B_O and B_L respectively, the preference of cells to utilize glucose or lactate in respiration is parameterized by Λ_G and Λ_L, and to ensure that these expression are defined near $(L, G) = (0, 0)$, Γ_G and Γ_L are constants that correspond to half-maximal rates in the absence of the other fuel (these will be set to zero later but for generality are included here).

In summary, the consumption rates of the species in the model are:

$$Q_O = \left(6B_O \frac{\Lambda_G G}{\Lambda_G G + \Lambda_L L + \Gamma_G} + 3B_L \frac{\Lambda_L L}{\Lambda_G G + \Lambda_L L + \Gamma_L}\right) \frac{O}{O + K_O}, \tag{5.10}$$

$$Q_L = B_L \left(\frac{\Lambda_L L}{\Lambda_G G + \Lambda_L L + \Gamma_L}\right) \frac{O}{O + K_O} - 2B_G \frac{G}{G + \Lambda_O O + K_G}, \tag{5.11}$$

$$Q_G = B_O \left(\frac{\Lambda_G G}{\Lambda_G G + \Lambda_L L + \Gamma_G}\right) \frac{O}{O + K_O} + B_G \frac{G}{G + \Lambda_O O + K_G}. \tag{5.12}$$

Clearly these rates satisfy the aforementioned relation (5.7): $Q_G = Q_O/6 - Q_L/2$.

In order to utilize the model, we require estimates of the diffusion coefficients and vessel concentrations of the aforementioned molecular species along with the parameter values contained in the functional forms for oxygen consumption (respiration) and lactate production (glycolysis). The sheer volume of necessary parameters can be dramatically reduced by first nondimensionalizing the system. This is a useful process for computational and analytical reasons.

We can also rewrite the system of equations in a way more conducive to gaining some analytical traction and simpler parameter estimation. Since the production rates of oxygen, glucose and lactate satisfy the relation $Q_G = Q_O/6 - Q_L/2$, we can replace one of the equations for these individual species with this relation, which we will evolve into a simpler formula below. For concreteness we will omit the diffusion-reaction equation for glucose and retain the equations for oxygen and lactate in the nondimensionalization below.

Nondimensionalizing concentrations by their vessel concentration V_X, i.e. setting $X = V_X x$, and nondimensionalizing space by dividing the spatial variable r by a characteristic length of $\tilde{r} = 1$ μm (but not changing its notation), gives the nondimensional system:

$$\frac{1}{r}\frac{d}{dr}\left(r\frac{do}{dr}\right) = \left(6\beta_o \frac{g}{g + \lambda\ell + \gamma_g} + 3\frac{\beta_\ell \alpha_\ell}{\alpha_o}\frac{\ell}{g/\lambda + \ell + \gamma_\ell}\right)\frac{o}{o + \kappa_o}, \tag{5.13}$$

$$\frac{1}{r}\frac{d}{dr}\left(r\frac{d\ell}{dr}\right) = \beta_\ell \left(\frac{\ell}{g/\lambda + \ell + \gamma_\ell}\right)\frac{o}{o + \kappa_o} - \frac{2\beta_g}{\alpha_\ell}\frac{g}{g + \delta o + \kappa_g}, \tag{5.14}$$

$$\frac{1}{r}\frac{d}{dr}\left(r\frac{dg}{dr}\right) = \frac{\alpha_o}{6}\frac{1}{r}\frac{d}{dr}\left(r\frac{do}{dr}\right) - \frac{\alpha_\ell}{2}\frac{1}{r}\frac{d}{dr}\left(r\frac{d\ell}{dr}\right), \tag{5.15}$$

where $\alpha_x = d_x v_x$ ($d_x = D_X/D_G$, $v_x = V_X/V_G$), $\beta_x = B_X/(D_X V_X)$, $\lambda = \Lambda v_\ell$ ($\Lambda = \Lambda_L/\Lambda_G$), $\delta = \Lambda_O v_o$, $\kappa_x = K_X/V_X$ and $\gamma_x = \Gamma_X/(V_X \Lambda_X)$. In addition to these equations, we also

require the nondimensional version of the vessel boundary conditions, namely, $x(\rho) = 1$, where $\rho = \omega/\tilde{r}$; the far-field boundary condition is essentially the same:

$$\left.\frac{dx}{dr}\right|_{r=P} = 0, \tag{5.16}$$

where $P = \Omega/\tilde{r}$.

First, integrating (5.15) over (r, P) and enforcing the far-field boundary condition (5.16) gives

$$\frac{dg}{dr} = \frac{\alpha_o}{6}\frac{do}{dr} - \frac{\alpha_\ell}{2}\frac{d\ell}{dr}. \tag{5.17}$$

Now integrating the equations once more, this time over (ρ, r), and using the vessel boundary condition gives

$$g(r) = 1 - \frac{\alpha_o}{6}\big(1 - o(r)\big) + \frac{\alpha_\ell}{2}\big(1 - \ell(r)\big). \tag{5.18}$$

This expression for glucose enables a simpler system to solve numerically for $\ell(r)$ and $o(r)$. These solutions also hold in a Cartesian geometry, as was considered by Molvian et al. [25] to correspond to the geometry of window chambers used by Helm et al. [5]. See C.2 for additional details.

To calculate the ATP turnover rate, an analysis of the stoichometry of all the involved processes at physiological pH is required. For glycolysis, 2 ATP are produced while for the full process of respiration including glycolysis, approximately 29 ATP are produced [20], see C.4 for summary biochemical reactions. This ATP yield is less than the yield assumed by previous models, e.g. [65] assumed the classical 38, [25] assumed an intermediary 36, while [63] assumed 32; these are all more than the accepted ideal yield of approximately 29 [20]. While this accepted value will be used to generate the results that follow, I have also calculated a novel estimate of 24.25 ATP/glucose based on the reactions contained in C.4. The discrepancy arises from the uncertainty associated with the efficiency of ADP phosphorylation and processes such as ATP and pyruvate transport that effect the electrochemical gradient across the inner mitochondrial membrane. Most significantly, the multiple protonated states of phosphate, which is critical to intercellular buffering is included in the summary reaction for phosphate transport across the inner mitochondrial wall. The results calculated below have all been recalculated using this novel estimate in C.6.

In terms of the reaction rates for the processes considered here for glycolysis (k_G),

glucose-fuelled respiration (k_O) and lactate-fuelled respiration (k_L), the production rate of ATP P_{ATP} is given by:

$$P_{ATP} = 2k_G + 29k_O + 13.5k_L. \tag{5.19}$$

The total production rate in the tissue space is characterized by the normalized value

$$\Phi = \int_{\rho}^{P} P_{ATP} r dr. \tag{5.20}$$

The total production rate is the triple integral over a unit of tissue defined by a uniform cylindrical annulus of height Δz with inner radius ρ and outer radius P, so the parameter of interest is normalized by $2\pi\Delta z$. This value is used to indicate the relative contributions of the metabolic pathways.

5.2.1 Parameter estimation

There is no single study that has measured the apparent diffusion coefficients of oxygen, glucose and lactate in the same type of tissue. In general, these apparent diffusion coefficients may exhibit spatial-dependence due to changes in temperature, tissue properties and molecular concentrations but for simplicity, we have assumed that they are constant in the tissue surrounding a blood vessel. The diffusion coefficients will remain fixed for the simulations presented here and were chosen for consistency with previous modelling attempts (e.g. [64, 3, 25, 65, 63, 89]); they are given in Table 5.1 along with the other model parameters.

The base case for vessel concentrations considers a slightly hypoglycaemic condition of 2 mM since glucose consumption is highly upregulated in tumours. For reference, a normal fasting concentration of glucose is approximately 5 mM. It would be reasonable to consider hyperglycaemic conditions that could arise locally in a tumour but for simplicity we will neglect this consideration in the present study. For lactate we consider an elevated level of 2mM since cancer cells are performing increased glycolysis. If it is being consumed as the primary respiratory fuel, it could be lower. A normal resting level is 1 mM of lactate. The oxygen concentration will be taken to be consistent with the hypoxic conditions measured by Helmlinger et al. [5]. They found the average partial pressure of oxygen in the tumour vessel to be 13.5 mmHg [5]. Henry's Law relates this partial pressure to the molar concentration via a proportionality constant, known as the solubility coefficient, denoted by S_O

Parameter	Value	Units	Reference
ω	11.5	μm	[149]
Ω	401.5	μm	[25][a]
V_O	1.43×10^{-2}	mM	[5]
V_L	2	mM	[25]
V_G	2	mM	this work
D_O	1820	μm^2/s	[116]
D_L	177	μm^2/s	[3]
D_G	105	μm^2/s	[105]
K_O	2×10^{-4}	mM	[25]
K_G	5.0×10^{-2}	mM	[25]
B_O	2.32×10^{-4}	mM/s	this work[b]
B_L	4.63×10^{-4}	mM/s	this work[b]
B_G	2.8×10^{-3}	mM/s	this work[c]
Λ_O	4×10^{3}	-	this work
Λ	1	-	[90]
Γ_L	0	mM	this work
Γ_G	0	mM	this work

Table 5.1: Fixed parameter values for physiological, molecular and metabolic parameters for the 'base case' simulation.
[a] 401.5 is chosen for numerical convenience (400 was used in [25]). Evidence for steady state achieved at this distance is given in [5] where oxygen and pH have reached steady state.
[b] Numerical fit based on data from [5]. Details in C.3. These values satisfy $6B_O = 3B_L = p_O$.
[c] This maximum glucose consumption rate is assumed to be approximately $3 \times p_O$, the maximum oxygen consumption rate. This is similar to the relationship that exists between consumption rates in [4].

(mM/mmHg). At 37° C the solubility of oxygen of DS-carcinosarcoma in the rat kidney is $S_O = 1.05 \times 10^{-3}$ mM/mmHg [117]; this yields $V_O \approx 1.43 \times 10^{-2}$ mM.

The consumption and production rate parameters are typically varied over large ranges as is commonly done since these can vary widely depending on the tumour type, e.g. [90]. However, we will enforce one condition to remain consistent with the oxygen profiles in [5]. Performing a least squares fitting to this spatial data, the maximum oxygen consumption rate is approximately $p_O = 1.39 \times 10^{-3}$ mM/s, the details are outlined in C.3. We will

utilize this value to fix B_O and B_L, the maximum consumption rates of glucose-fuelled and lactate-fuelled respiration respectively. We will ensure $Q_O \leq p_O$ by taking $p_O = 6B_O = 3B_L$ which implies that the maximal oxygen consumption rate is the same regardless of whether lactate or glucose is the respiratory fuel. There are cancer cell lines, namely SiHa cervix cancer cells [27] and C6 glioma cells [150], which have been shown to temporally obey the relation $2B_O = B_L$ [90]; there are others where $B_O \approx B_L$ (e.g. WiDr colon cancer cells [27]) or $3B_O \approx B_L$ (e.g. LN18 and LN229 glioblastoma cells [151]) [90].

While the system given above is widely applicable, it can be argued that in the interest of further parameter reduction, the constants γ_g and γ_ℓ are superfluous in this scenario where ℓ never approaches zero. Thus, we will take $\gamma_g = \gamma_\ell = 0$. This reduces our nondimensional parameters to a total of 10.

5.3 Results and discussion

5.3.1 Base case

We will first examine how our model captures the behaviour of metabolic symbiosis in tumours. Using the parameters given in Table 5.1, we numerically solve the nondimensional system given by (5.13) and (5.14). The corresponding glucose concentration is found by using the explicit formula (5.18). The solutions for the nondimensional oxygen, lactate and glucose concentrations are given in Figure 5.3. The oxygen concentration decreases to anoxic values approximately 100 μm away from the vessel as expected. The glucose concentration also decreases as it is consumed by respiratory cells near the vessel and then predominantly consumed by glycolytic cells further from the vessel. The lactate concentration increases over double its vessel concentration as it is produced by glycolytic cells at a much higher rate than it is consumed by lactate-fuelled cells. These observations are complemented by consideration of their consumption rates shown in Figure 5.4. Oxygen is consumed for the first 150 μm outside of the vessel and as it decreases you can clearly see the glucose consumption rate ramp up in response to increased glycolytic activity. The lactate consumption rate is negative (implying production) everywhere except for directly adjacent to the vessel where there is very little glycolysis occurring. The positive contribution of lactate consumption to the total consumption rate is washed out as the glycolytic production rate is much higher. The energetic landscape of the base case considered here

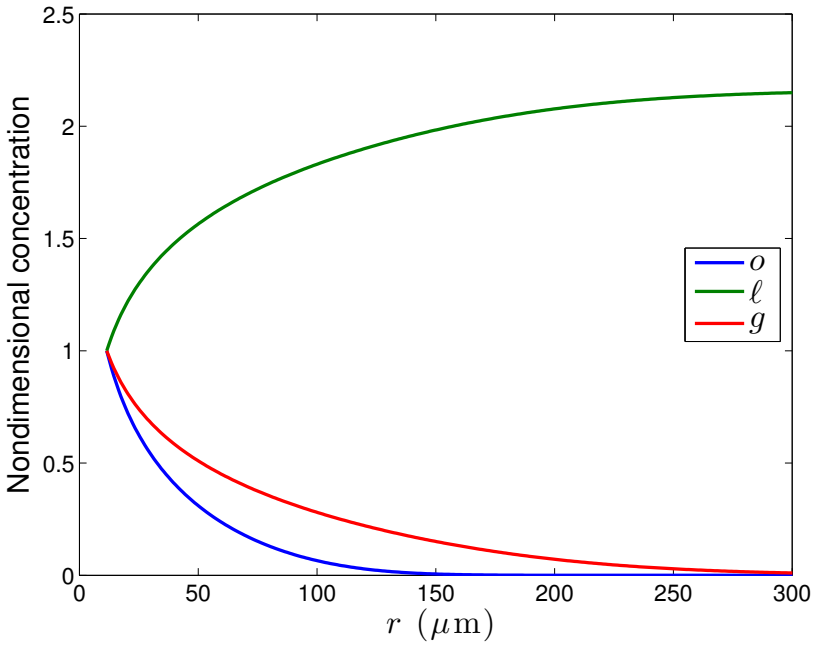

Figure 5.3: Solution to base case boundary value problem. Nondimensional oxygen and glucose concentrations decrease due to consumption. Lactate increases to almost double its vessel concentration since it is produced by glycolysis at a higher rate than it is consumed by respiration due to a limiting oxygen concentration. This image has been spatially truncated to 300 μm since the concentrations are approximately constant after this point.

are given in Figure 5.5 where the contributions of the three cell populations' metabolic pathways are given as areas under the total ATP turnover rate. Glycolysis dominates the total ATP production in hypoxic and anoxic regions while glucose-fuelled respiration occurs sparingly near the blood vessel. The lactate-fuelled cell population, sandwiched between these glucose consuming cells are utilizing the byproduct of the glycolytic cells while there is still sufficient oxygen. Before analyzing the effects of parameter changes we will note that the ATP production profile just described is a function of radial distance. When considering the total ATP turnover rate of the whole tissue, those regions further away from the vessel contribute much more than those close to the vessel. This is reflected in the first bar of the graph given in Figure 5.8 where the total amount of ATP turnover by respiratory cells is more accurately represented after integrating over the whole tissue.

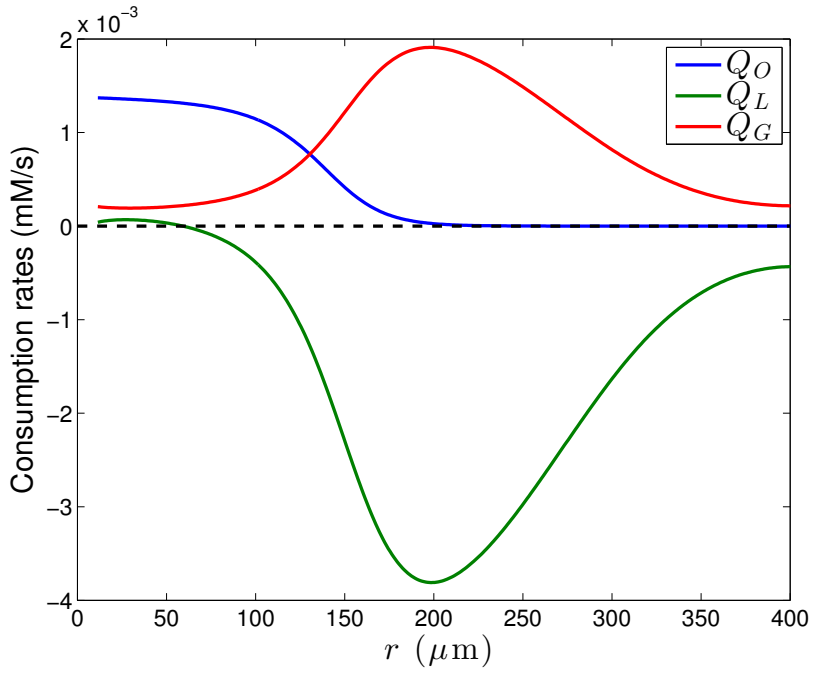

Figure 5.4: Consumption rates of oxygen, lactate and glucose for the concentrations given in Figure 5.3. The glucose and oxygen consumption rates are strictly positive while the consumption rate of lactate is predominantly negative. This indicates that even in regions where lactate is being consumed, it is being produced at a higher rate by glycolysis.

5.3.2 Warburg effect

In the base case considered above glycolysis is inhibited until the oxygen consumption drops to values that prevent the production of sufficient ATP to maintain cell survival. However, cancer cells will commonly utilize glycolysis as a primary energy source even when there is enough oxygen to ensure cell survival. In the model we characterize the cell's ability to hold off on utilizing glycolysis in oxygenated areas by the parameter Λ_O. Reducing it 400-fold from the base case above (from 4000 to 100) results in spatial ATP turnover rate as given in Figure 5.6. Cells near the vessel greedily consume the available resources leaving cells further from the vessel to die from insufficient ATP supply. The ATP production breakdown corresponds to the second bar in Figure 5.8 and is slightly higher than the whole tissue considered in the base case above.

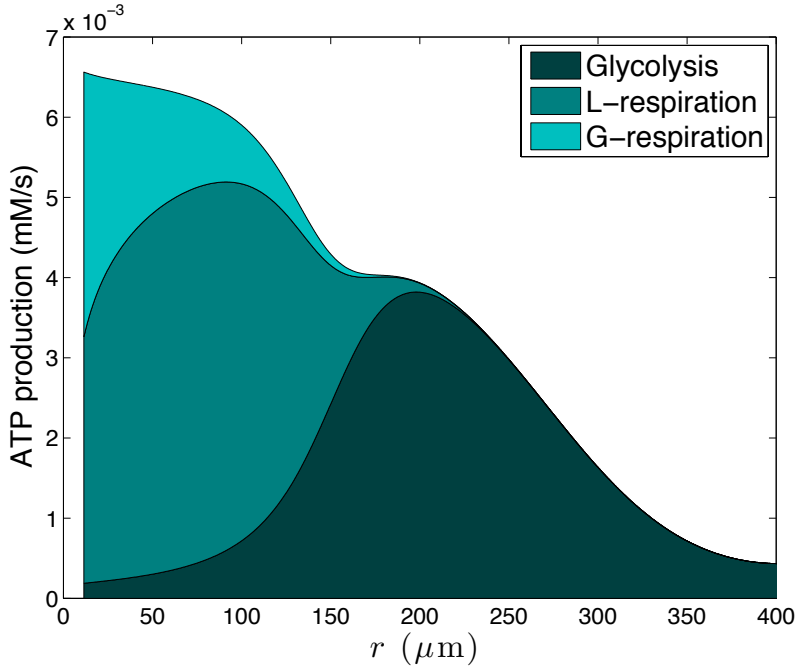

Figure 5.5: The base case for ATP turnover (consumption/production) rates corresponding to consumption rates given in Figure 5.4. The contributions of the pathways are bounded by the total ATP turnover rate P_{ATP}. Glycolysis dominates in hypoxic/anoxic regions while glucose-fuelled respiration occurs sparingly near the blood vessel. Lactate-fuelled cells are consuming the byproduct of the glycolytic cells where there is oxygen present.

5.3.3 Optimal metabolic behaviour

Instead of fixing all of the parameters to the values given in Table 5.1, we could leave some of the parameters free and optimize the amount of ATP generated from the given metabolites by imposing a maximum constraint on ATP production. For instance, setting all of the parameters initially to those given in Table 5.1, and then minimizing some function of $Z = P_{ATP} - \theta$ where θ is the maximum allowed ATP turnover rate. Allowing cells to alter their consumption rates β_o, β_g and β_ℓ, along with the glycolytic trigger parameter δ gives the results shown in Figure 5.7. In this simulation θ was set to 7×10^{-3} mM/s and the minimized function was $f(Z) = Z^2$. While there was still enough constraint that the system still exhibited a non-constant ATP turnover where it could, this reinforces the suggested optimal strategy of glucose-fuelled respiration near the vessel, glycolysis far from

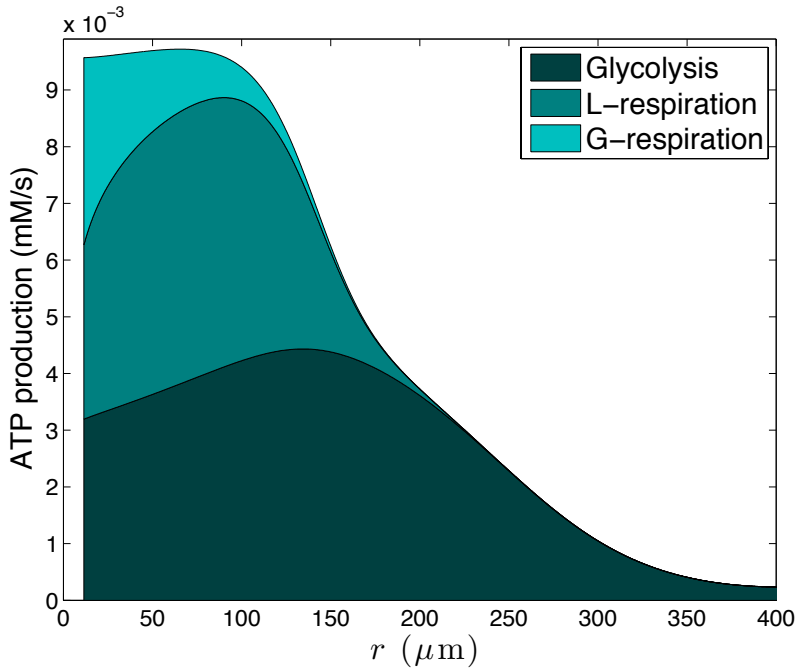

Figure 5.6: ATP turnover (consumption/production) rates for cells exhibiting the Warburg effect (differs from base case because $\Lambda_O = 100$ instead of 4000). The contributions of the pathways are bounded by the total ATP turnover rate P_{ATP}. Glycolysis is dominant in all regions of the tumour. Glucose-fuelled respiration occurs sparingly near the blood vessel. Lactate-fuelled cells are consuming the byproduct of the glycolytic cells where there is oxygen present.

the vessel and a lactate-consuming population in between these two.

5.3.4 Cancer treatment effects

The mathematical model presented here can give insight into the effects of blocking various metabolic pathways. The three metabolic pathways that we have considered, namely (i) glucose-fuelled respiration, (ii) lactate-fuelled respiration and (iii) glycolysis, could be inhibited by various agents, and the effects on ATP production will be outlined below.

Entirely knocking out lactate metabolism could be achieved by inhibiting lactate dehydrogenase (LDH) which is responsible for the reentry of lactate into respiratory pathways

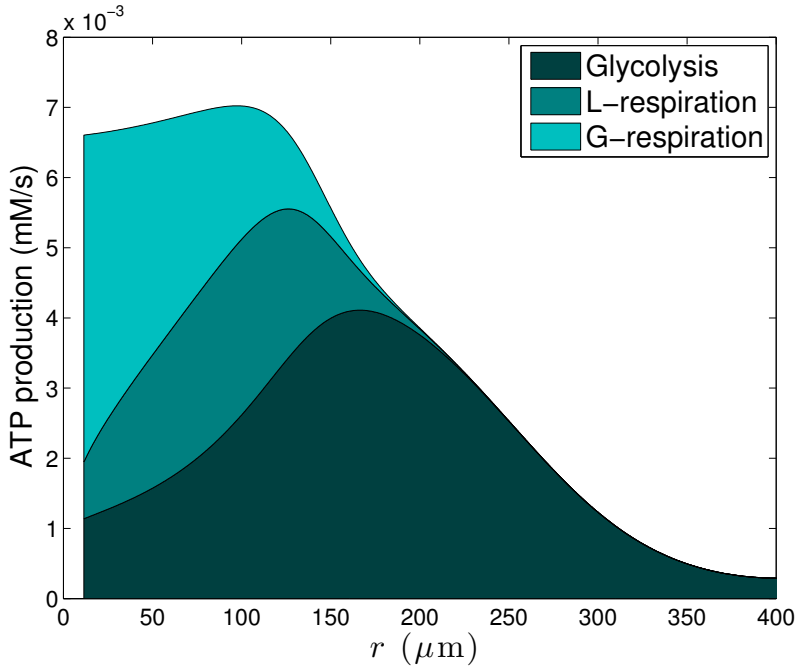

Figure 5.7: The optimal metabolic behaviour on the microscale given an ATP turnover maximum of $\theta = 7 \times 10^{-3}$ mM/s. This shows glucose-fuelled respiration near the vessel, glycolysis far from the vessel and a lactate-consuming population in between these two.

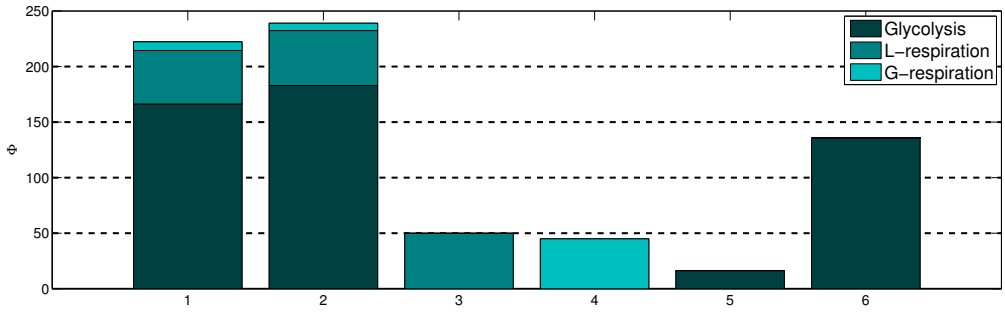

	1. base	2. W	3. Glyc	4. LDH	5. Resp	6. R-W
Λ_O	4000	100	N/A	N/A	4000	100
B_G	1	1	0	0	1	1
B_L	1	1	1	0	0	0
B_O	1	1	0	1	0	0

Figure 5.8: The ATP turnover contributions of the pathways are bounded by the total ATP turnover rate Φ in a unit annulus of tissue. This more accurately represents the total contribution of each cell population to metabolism. From left to right the bars denote the following cell populations: 1. **Base case**: Tissue that exhibits lactate consumption in hypoxic conditions with parameters in Table 5.1, see Figure 5.5. 2. **Warburg effect**: Tissue utilizing aerobic glycolysis, see Figure 5.6. 3. **Glycolytic knockdown**: Tissue experiencing complete glycolytic inhibition. 4. **LDH inhibitor**: Tissue experiencing complete LDH inhibition. 5. **Respiration knockdown**: Tissue experiencing mitochondrial inhibition with glycolysis repression by oxygen. 6. **Respiration knockdown and Warburg effect**: Mitochondrial inhibition with aerobic glycolysis. If either of the reactions which block glycolysis are knocked out, glycolysis (3) or LDH inhibitors (4), the total ATP produced is diminished ($\Phi < 50$). If on the other hand respiration is inhibited then either (i) if oxygen represses glycolysis there is minimal ATP production (5), or (ii) if glycolysis is independent of oxygen concentration there is an intermediary amount of ATP produced (6).

by converting it into pyruvate, see (C.15) for the reaction. Successful inhibition would concurrently prevent the conversion of pyruvate to lactate as well, a crucial step for regenerating NAD^+ in glycolytic cells. This has been shown to reduce ATP levels and consequently induce cell death in tumours [152]. The complete inhibition of lactate dehydrogenase would eliminate two of the three pathways considered here: lactate-fuelled respiration and glycolysis. Complete inhibition can be reflected in the model by setting

$B_L = 0$ and $B_G = 0$, leaving only glucose-fuelled respiration to produce ATP, a physiologically normal condition. However, the hypoxic and hypoglycaemic conditions considered here do not leave enough fuel for cell survival. This scenario corresponds to the third bar in Figure 5.8.

We could also target glucose transport into the cell, an intermediary of glycolysis or one of the critical enzymes responsible for converting glucose to pyruvate. This is distinct from the strategy noted above of inhibiting LDH which prevents the conversion of lactate to pyruvate and vice versa. This has also been noted as a prime target for cancer therapy [146, 147] and there are currently many potential targets [148]. Here we will consider the shutdown of glycolysis as preventing both glucose-fuelled respiration and glycolysis since both of these require glucose to be converted into pyruvate. However, it leaves the lactate-fuelled respiratory pathway intact. This could be considered in the model by taking $B_O = 0$ and $B_G = 0$. Similar to the case of LDH inhibition this leads to a significant decrease in ATP production as shown in the fourth bar of Figure 5.8.

The final scenario that we consider corresponds to full inhibition of respiration somewhere along the chain between pyruvate transport into the mitochondria and the electron transport chain. There are numerous potential targets in the mitochondria [153] and we will consider the complete shutdown of respiration by setting $B_L = 0$ and $B_O = 0$. This would result in negligible oxygen consumption and with our base case of $\Lambda_O = 400$ this would lead to repressed glycolysis in the tissue. This is likely a non-physiological scenario since glycolysis would attempt to compensate for a lack of ATP production but it would lead to heavily reduced ATP production. If glycolysis was able to compensate for the lack of respiration, represented in the model by reducing Λ_O to 100, then the tissue could still produce a significant amount of ATP. This indicates that in a hypoxic microenvironment, commonly found in tumour tissue, the complete inhibition of respiration would still allow the tumour energy supply to be maintained by glycolysis alone.

We could also consider the effects of theoretical single knockdowns in the model by setting one of the parameters to zero at a time (results not shown). Inhibiting just one of the respiratory pathways had negligible effect on the total ATP production (in both the base case and Warburg case) since the other fuel compensated. If glycolysis alone is inhibited, the respiration is split between lactate and glucose-fuelled and the total ATP is similar to the amount produced during LDH inhibition or glycolytic inhibition (bars 4 and 5 respectively).

5.4 A model for metabolism and acidity

Here we will utilize the model for interstitial fluid pressure formulated for a single vessel in [71] (see Section 3.1.1 for a summary) to add convective transport to a pH microvessel model [25] (see Section 3.4.2). This model assumed a two-dimensional region in Cartesian coordinates to correspond with the experimental setup in [5], namely transparent dorsal window chambers implanted in mice that contained human colon adenocarcinmoa. Firstly, we see if the predicted plateau is robust enough to occur in a more appropriate geometry corresponding to an *in vivo* tissue: a three-dimensional cylindrical vessel with diffusive and convective transvascular transport. We also want to consider effects that could be induced by cancer treatments, such as decreased vessel permeability and increased oxygen concentration by the application of antiangiogenic agents or increased ratio of respiration to glycolysis caused by glycolysis inhibitors.

Before adding convection we will first consider the model with glucose-fuelled respiration and glycolysis (production rates given in Table B.4) are the included metabolisms and they are coupled to the bicarbonate buffering system [3]. A diagram of the model is provided in Figure 5.9, showing the extracellular species included in the model and the direction of their diffusive transport. Also shown are the intracellular metabolism reactions and ATP yields.

Collecting the system of steady-state equations for the pertinent molecular species derived in Section 3.4.1, we have

$$D_O \frac{d^2O}{dr^2} = Q_O, \tag{5.21}$$

$$D_G \frac{d^2G}{dr^2} = Q_G, \tag{5.22}$$

$$D_L \frac{d^2L}{dr^2} = Q_L, \tag{5.23}$$

$$D_C \frac{d^2C}{dr^2} = -k_r BH + k_f C, \tag{5.24}$$

$$D_B \frac{d^2B}{dr^2} = k_r BH - k_f C - Q_O, \tag{5.25}$$

$$D_H \frac{d^2H}{dr^2} = k_r BH - k_f C - Q_O + Q_L, \tag{5.26}$$

where $Q_L = Q_O/3 - 2Q_G$, and Q_G and Q_O are empirical formulas relating the concentra-

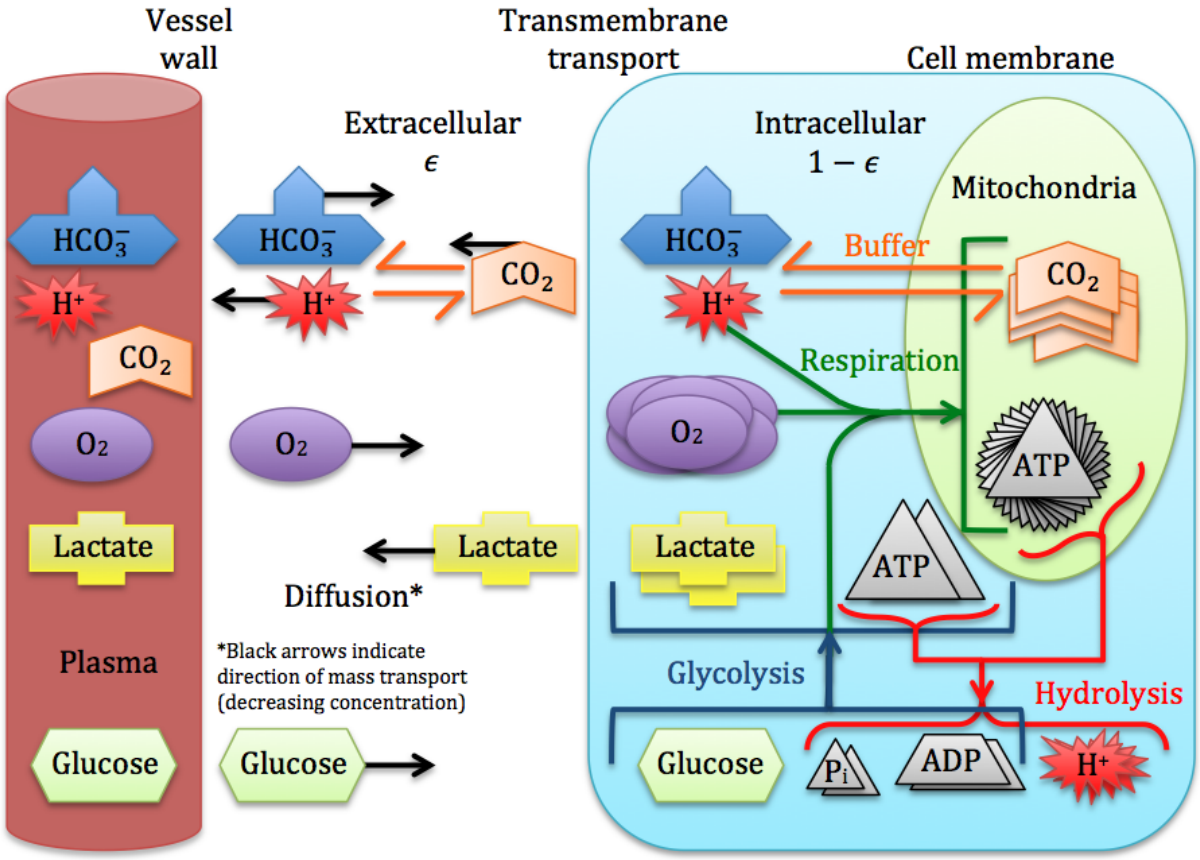

Figure 5.9: The metabolism and pH model diagram showing extracellular species direction of diffusive transport and buffering, along with the intracellular metabolism, ATP yields and buffering.

tions of glucose and oxygen (and possibly pH) to their consumption rates. The boundary condition at the vessel wall ($r = \omega$) is

$$-D_X \frac{dX}{dr}\bigg|_{r=\omega} = \mu_X(V_X - X_0), \tag{5.27}$$

where $X_0 = X(\omega)$ ensuring equality of fluxes at the interface between blood and tissue, while at the penetration depth ($r = \Omega$)

$$\frac{dX}{dr}\bigg|_{r=\Omega} = 0, \tag{5.28}$$

which assumes that the concentrations have reached a steady state equilibrium concentration.

5.4.1 Parameters

We require estimates of the diffusion coefficients, vessel concentrations, vessel permeabilities and buffering reaction rates of all the molecular species mentioned above along with functional forms and parameter values for oxygen consumption (respiration) and lactate production (glycolysis). The values for oxygen, glucose and lactate diffusion coefficients are provided above in Table 5.1. Those for the molecules necessary for including bicarbonate buffers along with vessel concentrations and permeabilities are found in Table B.5 and the metabolic parameters are found in Table B.4.

For blood vessel concentrations, we assume that the concentrations of the molecules involved in the primary buffering reaction (3.44) are in equilibrium and thus,

$$\frac{V_B V_H}{V_C} = \frac{k_f}{k_r} = K.$$

Based on a pK of 6.12 [154], this gives $K \approx 7.6 \times 10^{-4}$ mM. In normal vessels pH typically ranges from 7.35–7.45 with the higher end of this range usually occurring in arteries while the lower end is observed in veins. pH values above this range imply alkalosis has set in while values below this indicate acidosis, a characteristic commonly observed in tumour vessels, e.g. tumour pH near a microvessel of approximately 7.25 [5]. The vessel measurement corresponds to $V_H \approx 4 \times 10^{-5}$ mM, so we must have $V_B/V_C \approx 20$. Vessel

concentrations of bicarbonate typically lie in the range of 18–23 mM , and thus carbon dioxide lies in the range of 0.75–1.25 mM. As noted above these blood vessel observations along with these species diffusion coefficients are given in Table B.5.

5.4.2 Analytical observations

Before considering the effects of altering geometries and molecular transport, I will consider some analytical ramifications of the model in its present form.

I will know rewrite the system (5.21)-(5.26) in a way more conducive to eliminate one of the diffusion-reaction equations in a similar fashion to the three species system above. Since the consumption rates of oxygen, glucose and lactate satisfy the relation $Q_L = Q_O/3 - 2Q_G$, we can replace one of (5.21)-(5.23) with this relation; for simplicity we omit (5.22) since Q_L and/or Q_O are present in (5.25) and (5.26). Assuming that we know $O(r)$ and thus Q_O, along with $L(r)$ and thus Q_L, allows us to derive some useful relations in terms of these concentrations.

Adding (5.24) and (5.25) gives

$$D_C \frac{d^2C}{dr^2} + D_B \frac{d^2B}{dr^2} + D_O \frac{d^2O}{dr^2} = 0,$$

while subtracting (5.25) and (5.26) gives

$$D_B \frac{d^2B}{dr^2} - D_H \frac{d^2H}{dr^2} + D_L \frac{d^2L}{dr^2} = 0,$$

both useful relations since we can simply integrate over the spatial variable twice to eliminate derivatives in this equation. Finally, we retain (5.26) to close the system for reasons that will become evident in what follows. Nondimensionalizing concentrations by their vessel concentration V_X, i.e. setting $X = V_X x$ and formally nondimensionalizing space by dividing the spatial variable r by a characteristic length of 1 μm (but not changing its

notation), gives the non dimensional system:

$$\frac{d^2o}{dr^2} = Q_o, \tag{5.29}$$

$$\frac{d^2\ell}{dr^2} = Q_\ell, \tag{5.30}$$

$$\frac{d^2\ell}{dr^2} = \frac{\alpha^o_\ell}{3}\frac{d^2o}{dr^2} - 2\alpha^g_\ell\frac{d^2g}{dr^2}, \tag{5.31}$$

$$\frac{d^2b}{dr^2} = \alpha^h_b\frac{d^2h}{dr^2} - \alpha^\ell_b\frac{d^2\ell}{dr^2}, \tag{5.32}$$

$$\frac{d^2c}{dr^2} = -\alpha^b_c\frac{d^2b}{dr^2} - \alpha^o_c\frac{d^2o}{dr^2}, \tag{5.33}$$

$$\frac{d^2h}{dr^2} = \frac{k_rV_B}{D_H}bh - \frac{k_fV_C}{D_HV_H}c - \alpha^o_hQ_o + \alpha^\ell_hQ_\ell, \tag{5.34}$$

where $\alpha^y_x = d^y_x v^y_x$, $d^y_x = D_Y/D_X$, $v^y_x = V_Y/V_X$ and $Q_x = Q_X/(D_XV_X)$. In addition to this system, we also require the non dimensional version of the vessel boundary condition (5.27), namely,

$$-\frac{dx}{dr}\bigg|_{r=\omega} = \mu_x(1-x_0), \tag{5.35}$$

where $x_0 = x(\rho)$ and $\mu_x = \mu_X/D_X$; the far-field boundary condition is essentially the same:

$$\frac{dx}{dr}\bigg|_{r=\Omega} = 0. \tag{5.36}$$

First, integrating (5.31)-(5.33) over (r,Ω) and enforcing the far-field boundary condition (5.36) gives

$$\frac{d\ell}{dr} = \frac{\alpha^o_\ell}{3}\frac{do}{dr} - 2\alpha^g_\ell\frac{dg}{dr}, \tag{5.37}$$

$$\frac{db}{dr} = \alpha^h_b\frac{dh}{dr} - \alpha^\ell_b\frac{d\ell}{dr}, \tag{5.38}$$

$$\frac{dc}{dr} = \alpha^b_c\frac{db}{dr} - \alpha^o_c\frac{do}{dr}. \tag{5.39}$$

Before integrating again, it is worth noting that by applying (5.35) and rearranging the

previous equalities at $r = \omega$ yields

$$\ell_0 = 1 - \frac{\beta_\ell^o}{3}(1 - o_0) + 2\beta_\ell^g(1 - g_0), \tag{5.40}$$

$$b_0 = 1 - \beta_b^h(1 - h_0) + \beta_b^\ell(1 - \ell_0), \tag{5.41}$$

$$c_0 = 1 + \beta_c^b(1 - b_0) + \beta_c^o(1 - o_0). \tag{5.42}$$

where $\beta_x^y = \mu_x^y V_x^y$ and $\mu_x^y = \mu_Y/\mu_X$. Now integrating the equations once more, this time over (ω, r), gives

$$\ell(r) = \ell_0 - \frac{\alpha_\ell^o}{3}\big(o_0 - o(r)\big) + 2\alpha_\ell^g\big(g_0 - g(r)\big), \tag{5.43}$$

$$b(r) = b_0 + \alpha_b^h(h(r) - h_0) - \alpha_b^\ell(\ell(r) - \ell_0), \tag{5.44}$$

$$\begin{aligned} c(r) &= c_0 + \alpha_c^b\big(b_0 - b(r)\big) + \alpha_c^o\big(o_0 - o(r)\big) \\ &= c_0 - \alpha_c^h(h(r) - h_0) + \alpha_c^\ell(\ell(r) - \ell_0) + \alpha_c^o\big(o_0 - o(r)\big). \end{aligned} \tag{5.45}$$

As a consequence of (5.36), the steady state concentrations satisfy $h(\Omega)b(\Omega)/c(\Omega) = 1$. Thus in order to achieve a steady state concentration of $h(\Omega) = h_\infty$ we must have,

$$h_\infty = \frac{c_0 - \alpha_c^h(h_\infty - h_0) + \alpha_c^\ell(\ell_\infty - \ell_0) + \alpha_c^o o_0}{b_0 + \alpha_b^h(h_\infty - h_0) - \alpha_b^\ell(\ell_\infty - \ell_0)},$$

where $\ell_\infty = \ell_0 - \alpha_\ell^o o_0/3 + 2\alpha_\ell^g g_0$. This expression gives the far-field acidity for the system as a function of vessel concentrations and diffusion coefficients .

5.5 Convective transport in a metabolism model

Adding convective transport to (3.56) gives the equation

$$\frac{\partial X}{\partial t} = \frac{D_X}{r}\frac{\partial}{\partial r}\left(r\frac{\partial X}{\partial r}\right) - r_i\frac{1}{r}\frac{\partial}{\partial r}(ruX) + P_X. \tag{5.46}$$

where r_i is the retardation coefficient of species i. Typically, we assume that each solute travels at the same velocity as the fluid and thus take $r_i = 1$ [75]. Again, the production rates P_X are given in Table B.4 while the diffusion coefficients D_X are given in Table B.5. The analytical solution for IFV u is given in 3.9. Expanding the convection term and

noting that $du/dr = -u/r$ yields

$$\frac{D_X}{r}\frac{d}{dr}\left(r\frac{dX}{dr}\right) - r_i u\frac{dX}{dr} + P_X = 0.$$

The boundary condition at the blood vessel wall ensures the equality of the flux of solute through the vessel wall (3.28) with the flux through the interstitial space (3.21) giving

$$r_f uX - D_X\frac{dX}{dr} = \mu(V_X - X)\frac{\mathrm{Pe}_X}{e^{\mathrm{Pe}_X} - 1} + \frac{J_f}{S}(1-\sigma_i)V_X \quad \text{at } r = \omega. \tag{5.47}$$

We also require the concentrations to reach a steady state as we move away from the vessel and take

$$\frac{dX}{dr} = 0 \quad \text{at } r = \Omega, \tag{5.48}$$

where Ω is the penetration depth [71], a distance far enough from the microvessel to justify the assumption that the system has reached steady state but close enough to ensure minimal contributions from other nearby vessels. This is more practical than the 'far field' boundary condition in (3.60) [25] since numerically we will be forced to consider a finite spatial domain

Given the fluid flux J_f (determining the solute flux (3.5)), we can solve the coupled system of oxygen and glucose. Using these we can then solve for the system governing bicarbonate, carbon dioxide and hydrogen ions. Finally we determine the acidity using the relation pH$=-\log_{10}(H)$.

First, we notice that the plateau is still observed in this three-dimensional geometry and as presented in Figure 5.10a the addition of convection has some effect on the pH but does not exhibit a drastic change due to the relatively low magnitude of the interstitial fluid velocity of a single blood vessel (see the inset of Figure 5.10a) indicating that diffusion is the dominant form of transport for such small molecules on the microscale.

As mentioned in Chapter 2, the acidic microenvironment is caused by upregulated glycolysis. In this model the ratio of oxygen to glucose consumption is determined by the parameter R where $R = 6$ corresponds to purely respiration (where 6 oxygen are consumed and 1 glucose molecule) or all the way down to 1 which indicates that far more glycolysis is occurring than respiration. If cells performed only respiration, the plateau in pH would be even more pronounced since all of the oxygen is being consumed close to the vessel leading to a sudden switch to glycolysis close to the vessel (see Figure 5.10b). As R decreases

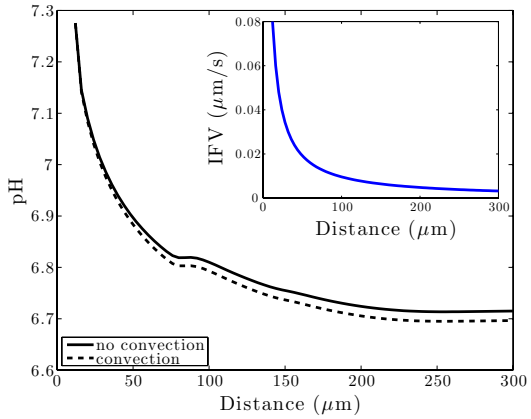

(a) The effect of adding convection to the model. Inset: IFV, u, outside the vessel.

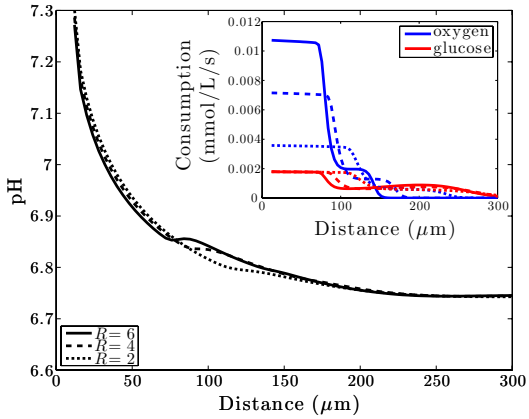

(b) The effect of altering the metabolism ratio R. Inset: Consumption rates.

Figure 5.10: pH profiles.

the transition is less pronounced as cells near the vessel do not consume all of the limited oxygen supply leaving some for cells at intermediary distances.

Vessel permeability varies drastically from normal vessels to tumour vessels and as it increases the convective and diffusive transport of molecules are enhanced. As shown in Figure 5.11a, high permeabilities (the tumour base case μ_0) have enough oxygen crossing the vessel wall to ensure that glycolysis does not have to take over close to the vessel while for low values (e.g. $\mu_0/50$), there is no plateau observed since the anoxic environment causes glycolysis to take over immediately outside the vessel. Note, that despite this latter case corresponding to a permeability closer to a normal vessel than a tumour vessel, we are still dealing with a tumour vessel with a *very* limited oxygen supply. This is reflected by the consumption rates that decrease to the repressed metabolic phase due to intermediate oxygen concentrations right outside the vessel wall.

Finally, we observe the effects of hypoxia and anoxia by varying the vessel concentration of oxygen. For very low values of oxygen (e.g. $V_O/10$), we observe the same phenomenon as when we considered low permeability. The switch to glycolysis happens very near the vessel whereas for our base case oxygen concentration we observe the plateau; this is shown in Figure 5.11b. For a high oxygen concentration found in a normal tissue (e.g. $3V_O$) we notice the smooth pH curve expected from a sufficient oxygen supply since the switch to a glycolysis-dominated metabolism occurs after the steady state of pH is reached.

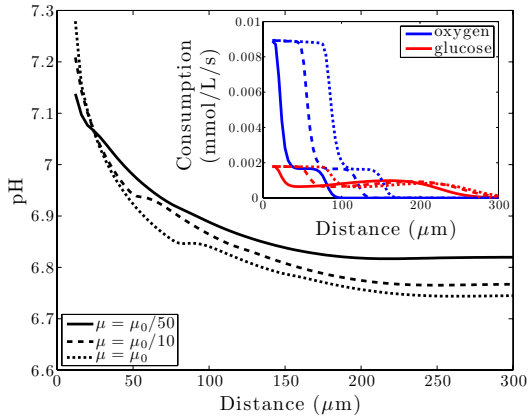

(a) The effect of altering the microvessel permeability, from base case values denoted by μ_0 to lower values corresponding to normal or normalized vessels.

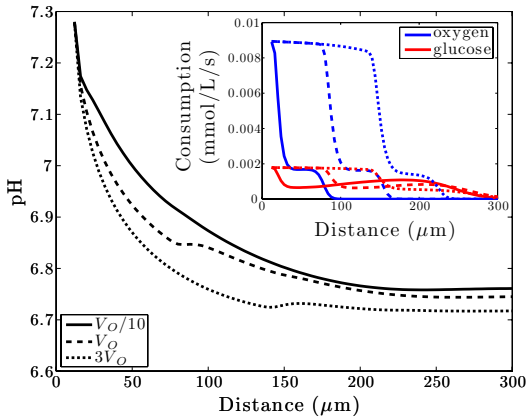

(b) The effect of changing the oxygen concentration in the microvessel from the base case hypoxic value V_O to higher and lower values.

Figure 5.11: pH profiles. Inset: Glucose and oxygen consumption rates.

5.6 Conclusions

The mathematical models formulated and analyzed above can give insight into the metabolic behaviours of cancer cells on the microscale. The tumour microenvironment characterized by hypoxia and nutrient depravation leads to the utilization of highly unregulated glycolytic pathways and the consumption by respiring cells of the lactate produced by these cells. These metabolic scenarios are encompassed by the functional forms proposed for glucose, lactate and oxygen consumption.

To consider the effect of altering parameters in the model to the efficiency of energy production we must also consider the rate of ATP turnover in the tissue. To this end a detailed biochemical summary was performed in order to calculate novel estimates for ATP yields. These energetic landscapes were considered in tissues that utilize anaerobic glycolysis, thus keeping more cells alive, and those that experience the Warburg effect, performing glycolysis in oxygenated areas. The analysis shows that the latter does confer a proliferative advantage by producing more ATP.

The effects of metabolic inhibition was taken into account by knocking out the pathways considered in our model. Glycolytic inhibition blocked glycolysis and glucose-fuelled

respiration, LDH inhibition blocked glycolysis and lactate-fuelled respiration while respiration inhibition blocked both forms of respiration. Both strategies that block glycolysis lead to significant decreases in total ATP production while those that block respiration still allow sufficient ATP for cell survival.

Of the many biochemical reactions stated above, some are tissue-dependent, pH-dependent or are not well established in the literature. Tissue-dependency of these models has been considered in [90], while the coupling of buffering and reactions has been considered on the microscale and temporal models [25, 155]. The uncertainty with the reactions above is primarily associated with the transmembrane transport of glucose across the cell membrane of glucose (C.12), pyruvate and phosphate transport into the mitochondria (C.18) and other processes that consume the electrochemical gradient in the mitochondrion. These transport processes may be very important to accurately modelling the efficiency of tumour metabolism.

Model extensions, including the addition of acidity and buffering mechanisms along with convective transport in the interstitial space and across the blood vessel wall have also been indicated. The work presented here should lead to a reconsideration of the biochemical reactions that constitute metabolic mathematical models and provide a minimally parameterized and straightforward basis for future metabolite consumption models.

Chapter 6

Mathematical Model for the Sequential Application of a Cytotoxic Nanoparticle and a PI3K Inhibitor

The previous two chapters detailed models of a solid tumour's macroscale angiogenic response to hypoxia and the subsequent microscale metabolism that a tumour performs. Treatment effects were analyzed by parameter variations that corresponded to treatments. Here, we address treatment concentrations and combinations in a specific type of solid tumour, breast cancer. This chapter details a mathematical model that describes drug concentrations, subsequent effects on protein expression and finally cell viability. The model was formulated based on data obtained via close collaboration with experimentalists at Dr. S. Sengupta's Laboratory for Nanomedicine at Havard Medical School. This experimental work was the first time that the combination of nanomedicine and a molecular targeted therapy was tested *in vivo*. The primarily goal of the mathematical model was to establish the optimal schedule of these two therapies which was determined by minimizing cell viability. The majority of the results contained in this chapter were published in Cancer Research [8].

Before launching into the layers of the mathematical models, we will summarize the necessary medical background and specifics of the study that were not already addressed in Chapter 2.

6.1 Medical motivation

Paralleling the question of optimal scheduling of chemotherapy and antiangiogenic agents to optimize treatment effects [35, 59] is the problem of optimal scheduling chemotherapy and molecular inhibitors. In both cases the complementary therapy is attempting to maximize the cytotoxic effects of chemotherapy. In the work considered here, a mathematical model was developed for a novel combination of anticancer treatments: a chemotherapy drug encapsulated in a nanoparticle delivery vehicle and a molecular inhibitor. Combinations of cytotoxic agents and molecular inhibitors have been previously considered in leukaemia and breast cancer [156, 157] but never with the effective delivery rendered by a nanodelivery device. These nanomedicines have many advantages over traditional delivery including preferential accumulation in the tumour via the enhanced permeability and retention (EPR) effect [46] and their ability to spatially and temporally control their drug release [53].

In this study, the impact of sequencing of a cisplatin-based supramolecular nanoparticle with an inhibitor of phosphoinositide 3-kinase (PI3K) was studied in a cell model that is particularly difficult to treat: triple negative breast cancer (TNBC). TNBC is characterized by the absence of estrogen receptors, progesterone receptors and Her2/neu. These entities are typical targets for hormonal and chemotherapy treatments. Cisplatin has shown some success in treating TNBC [32] but the dosage is highly limited due to toxicity, particularly of the kidneys. To counteract this the group of our collaborators engineered a polymeric cisplatinum (II) nanoparticle, which displayed preferential tumour accumulation, bypassed the kidney, and exhibited an enhanced antitumour efficacy compared to free cisplatin [158]. However, cisplatin has another drawback, it can upregulate PI3K signalling, which reduces the apoptotic response of cells [43]. This outcome suggests that a rational combination of PI3K inhibitor and cisplatin nanoparticles could further improve treatment efficacy. Indeed, experiments showed that treatment with a novel (self-assembling) cisplatin nanoparticle (SACN) results in activation of PI3K signalling. The motivation now is to use a mathematical model to predict the optimal treatment scheduling of SACNs combined with a PI3K inhibitor called PI8282. The model will be outlined below before showing and the validation of the results were obtained both *in vitro* and *in vivo*. Our results reveal the treatment with SACNs followed by the administration of PI828 results in better results than pre-treatment with PI8282 or simultaneous administration. These results indicate the appropriate sequencing of this cytotoxic nanomedicine and a

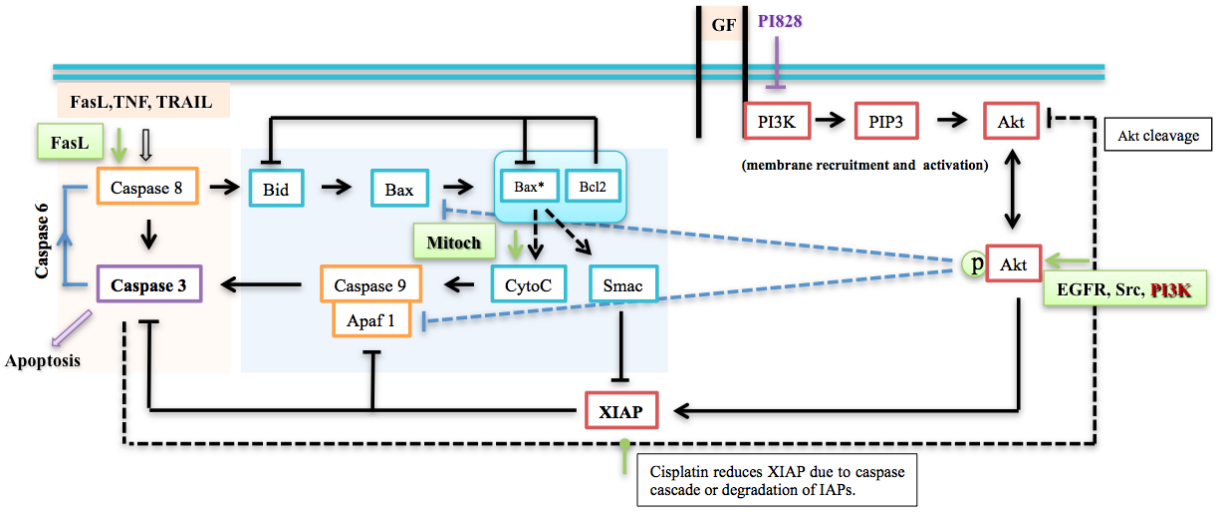

Figure 6.1: A detailed pathway of cell apoptosis showing the interactions between the major players in this process. Image courtesy of Dr. M. Kohandel.

molecular targeted therapeutic to achieve optimal therapeutic efficiency.

6.2 Mathematical model

The mathematical model developed here is broken up into three parts. The first part will describe the protein expression levels of pAkt, caspase-3 and XIAP. The next will include the treatment effects of cisplatin-NP and PI828 on protein expression. Then a nanoparticle release model will be used to describe the release profile of the nanoparticles measured in this study. Finally, we will propose a simple model for predicting cell viability. The consideration of parameter estimation will come in the next section.

In addition to the three proteins mentioned above, there are many more proteins and cell signalling pathways that encourage cell survival or cell apoptosis, summarized succinctly in Figure 6.1. Among all of them, we only consider a select few that are critical indicators of cell viability: pAkt, caspase-3 and XIAP. pAkt and XIAP are key cell survival factor while caspase-3 is widely considered to be the primary indicator of imminent cell apoptosis. The expression of these proteins can be determined experimentally by Western blotting techniques.

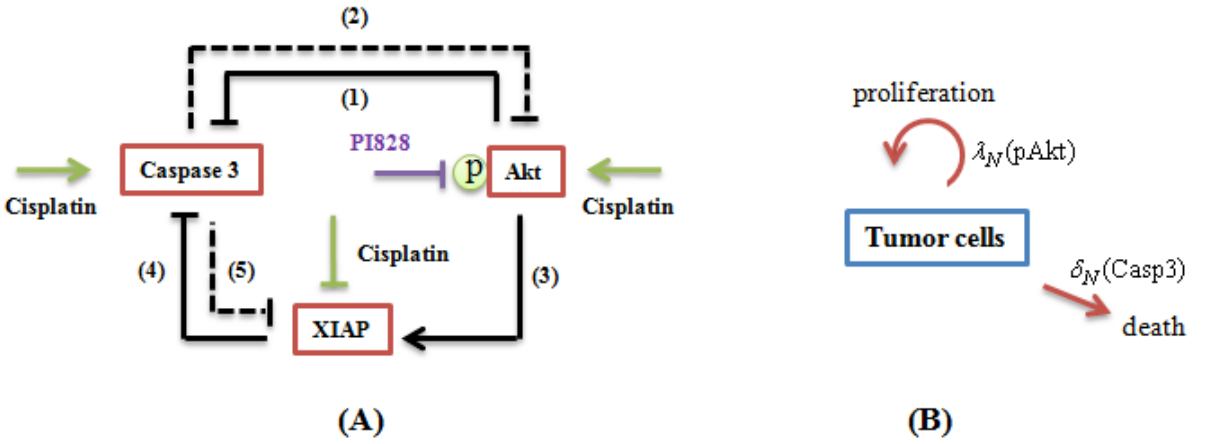

Figure 6.2: A diagram summary of the protein expression and cell viability model. (A) The simplified apoptosis pathway including the interactions of pAkt, XIAP and caspase-3. (B) The cell viability model where tumour cells proliferate at a rate proportional to pAkt concentration and the death rate is proportional to caspase-3 concentration. Image courtesy of Dr. M. Kohandel.

6.2.1 Protein expression model

Several mathematical models of varying complexity have been developed to study intrinsic and extrinsic apoptosis [159, 160, 161]; see [162] for a review. Here, we consider a simple model containing three critical proteins: pAkt, XIAP, and capsase-3. The effects of combinations of liposomal cisplatin and PI828 treatments are investigated. The basic reaction pathways are shown in Figure 6.2.

Akt phosphorylation is induced by activated PI3K. Once activated, Akt negatively regulates apoptotic pathways at a pre-mitochondrial level by blocking the actions of proteins such as Bad and Bax, which in turn inhibits the release of cytochrome c into the cytosol. It has also been reported that Akt directly phosphorylates and inactivates cell death protease caspase-9 [163]. For simplicity and to keep the number of parameters manageable, these multiple pro-survival initiatives are considered to have the net effect of inhibiting capsase-3 production, see (1) in Figure 6.2.

It has been also reported that active caspase-3 cleaves Akt in vitro, and inhibiting caspase-3 can block this effect [164]. Thus, a negative feedback is assumed to represent the cleavage of Akt by caspase-3, (2) in Figure 6.2. In addition, activated Akt interacts with

and phosphorylates XIAP, protecting it from autoubiquitination [165], (3) in Figure 6.2.

XIAP inhibits caspase-3 by the degradation of caspase-3 ((4) in Figure 6.2), and caspase-3 inhibits XIAP through ubiquitination and degradation [166, 159, 160, 167], (5) in Figure 6.2(A). Caspase-3 can also inhibit XIAP by inactivating XIAP through formation of a complex [159].

To include the effect of treatment, we first note that based on our experimental data and other studies [164, 168], cisplatin increases the production of pAkt. This activation might be mediated through EGFR and PI3K. Similar to previous studies [164], our data shows an increase in caspase-3 due to cisplatin. This increase could be due to activation of FasL, which in turn activates caspase-8 and subsequently caspase-3 [169, 170]. Another possible pathway is the release of cytochrome c, which subsequently activates caspase-9 and caspase-3 [171, 170].

In addition, phosphorylation of XIAP by Akt protects ubiquitination and degradation of XIAP in response to cisplatin. Since we have only considered the active form of XIAP in our model, we assume that cisplatin reduces XIAP, as observed in the experimental data. The reduction in XIAP could be also due to increase in caspase-3. Finally, we assume that PI828 inhibits phosphorylation of Akt by binding to P13K.

Here, we will consider the effects of the chemotherapy agent cisplatin in nanoparticles in combination with the P13K inhibitor PI828. Cisplatin is known to increase concentrations of caspase-3 triggering cell death but unfortunately, it simultaneously increases pAkt which commonly leads to anti-apoptotic effects and thus lowered efficacy of cisplatin treatment and overall chemoresistance. To counter this resistance, PI828 can be administered which inhibits PI3K, rapidly preventing the production of pAkt. The primary goal of this modelling is to determine the optimal combination of these two drugs to minimize cell viability for appropriate ranges of treatment dosages.

We consider the effects of the aforementioned treatments, liposomal cisplatin and PI828 along with their combinations, on the select group of proteins critical to apoptosis described above: pAkt, caspase-3 and XIAP. Denoting the dimensionless concentrations of the proteins by P=[pAkt]/P_0, C=[caspase-3]/C_0 and X=[XIAP]/X_0, where P_0, C_0 and X_0 are experiment-dependent scaling factors. The system of equations for the protein expression that we will use includes the indirect mutual inhibition of pAkt and caspase-3, the direct mutual inhibition of caspase-3 and XIAP, along with production, natural decay and

treatment effects, and is given by:

$$\frac{dP}{dt} = \frac{k_p + \lambda_p f_p(t)}{1 + \alpha_p C + \gamma_p g_i(t)} - \delta_p P \tag{6.1}$$

$$\frac{dC}{dt} = \frac{k_c + \lambda_c f_c(t)}{1 + \alpha_c P} - \beta_c X C - \delta_c C \tag{6.2}$$

$$\frac{dX}{dt} = k_x + \lambda_x P X - \beta_c C X - \delta_x X, \tag{6.3}$$

where the concentration of PI828 is denoted by $g(t)$ and the effects of cisplatin on pAkt and caspase-3 production are denoted by $f_p(t)$ and $f_c(t)$ respectively. The models for these treatment effects will be addressed below.

6.2.2 Treatment effects

We will first consider the effect of PI828, a potent inhibitor of Akt phosphorylation. It performs this inhibition by blocking the activity of the enzyme P13K which is responsible for phosphorylating Akt, creating pAkt. There are no release kinetics to consider for this treatment. A reasonable approach would be to consider extracellular and intracellular concentrations, denoted by g_e and g_i respectively, that follow mass transport and exponential decay of the effect giving

$$\frac{dg_e}{dt} = -r_g g_e$$
$$\frac{dg_i}{dt} = r_g g_e - d_g g_i.$$

However, even this simplistic approach introduces an unnecessary parameter and variable since the effect of PI828 is very rapid (compared to the time scale of the experiments: hours). Thus, it is sufficient to simply take

$$\frac{dg}{dt} = -d_g g. \tag{6.4}$$

The treatment effects of cisplatin on pAkt and caspase-3 are modeled by

$$\frac{df_p}{dt} = r_c c_i(t - T_i) - d_p f_p(t), \tag{6.5}$$

$$\frac{df_c}{dt} = r_c c_i(t - T_i) - d_c f_c(t), \tag{6.6}$$

where $c_i(t)$ is the intracellular cisplatin concentration which will be modelled below. Since protein expression increase occurs on a similar time scale, and in the interest of parameter reduction, we assume that the effect of the drug has the same activation constant r_c and time delay T_i, after the release of cisplatin nanoparticles, that accounts for intracellular diffusion to active sites and the delayed impact of cisplatin on the apoptosis pathway. This delay is attributed to the translational and transcriptional events that occur prior to changes in the expression of the proteins of interest. However, to facilitate the fitting to follow this model development, the delay in the equations above is not a strict time delay. Instead, a linear chain of reactions is used where the delay of a signal is approximated by N steps with equal reaction rates k [172]. Thus, the value of T_i is not explicitly included in parameter fitting and can be shown to have mean $\bar{T} = N/k$ and standard deviation $\sigma_T = \bar{T}/\sqrt{N}$ [173]. The number of intermediary reactions, N, which is suggested to be set somewhere between 5 and 15, is set to 10 here since anything larger would promote stiffness in the system and impede the proficiency of the fitting algorithms. The treatment effects do exhibit different decay rates d_p and d_c since the cisplatin-induced production of pAkt is sustained longer than the increased production of caspase (i.e. $d_p < d_c$).

6.2.3 Nanoparticle release

For nanoparticle release, many models were investigated. Preliminary data suggested that out of all the candidates, a biexponential (or a biexponential with decay) release profile was appropriate while a monoexponential yielded an unsatisfactory fit. Subsequent experiments showed a simple erosion model fit well while even the simplest monoexponential model was sufficient. Here we will only present the final published results utilizing the monoexponential decay model while unpublished release profile results are found in D.

To determine the rate of cisplatin release from the liposome nanoparticles, release experiments were performed over 120 hours in acidic and neutral conditions. In an acidic environment these release profiles can be accurately determined by a one-parameter ex-

ponential release profile. We can motivate the functional form by considering a simple ordinary differential equation (ODE) that includes both the constant and sustained release of drug due to encapsulation in the liposome. To facilitate this, we assume that the administered liposomes initially consists of a fixed fraction of cisplatin, θ_u, that will be subsequently released upon administration at rate r_u and a fixed fraction of cisplatin, $\theta_i = 1 - \theta_u$, that remains inert and is omitted from the modelling that follows. The fraction of the total amount of contained cisplatin that is released depends primarily on the acidity of the environment. In an acidic environment, just over 60% of the cisplatin is eventually released from the liposome, as opposed to the approximately 40% that is released in a neutral environment (this can be seen in Figure 6.5). This helps to preferentially target tissues exhibiting an acidic microenvironment as found in solid tumours. The concentration of the cisplatin that is released from the nanoparticle is denoted by $c(t)$ while the unreleased cisplatin concentration remains to be released is denoted by $u(t)$. The initial conditions are $u(t_0) = \theta_u c_T$ and $c(t_0) = 0$ where t_0 is the time of administration and c_T is the administered dosage (μM). The system of ODEs is then:

$$\frac{du}{dt} = -r_u u(t), \tag{6.7}$$

$$\frac{dc}{dt} = r_u u(t), \tag{6.8}$$

with the solution of interest being $c(t)$.

6.2.4 Cellular chemotherapy concentrations

The model given above for the release profile experiments must be extended for the *in vitro* experiments where expression of proteins are measured. The previous model will now correspond to extracellular concentrations of cisplatin (denoted with subscript e) that will now be transported inside the cell where the intracellular concentration (denoted with subscript i) can then have an effect on the protein pathways. To facilitate this we add a term to these extracellular concentrations to include the mass transport of cisplatin into the cells, a process with some rate constant r_c and time delay T_e. This time delay accounts for the effects of extracellular diffusion and transmembrane transport. In the interest of avoiding extraneous parameters, and since the computational process to include delay parameters introduces significant stiffness, we will make the assumption that this transport delay (and the rate constant) is the same for nanoparticles and free cisplatin. Similar to

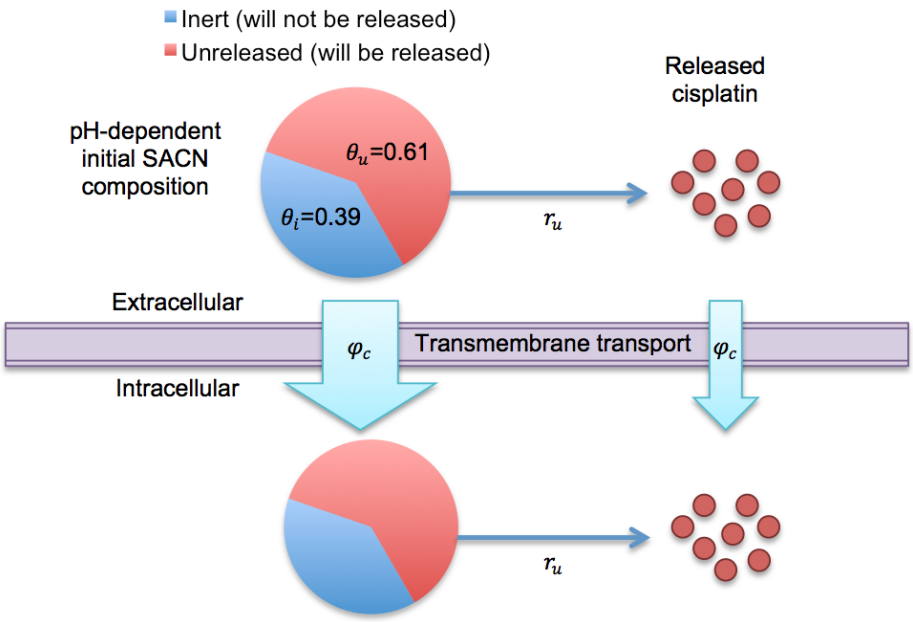

Figure 6.3: Depiction of the drug model in Equations (6.9)–(6.12) for nanoparticle release and delayed transmembrane transport of self-assembling cis-platinum nanoparticles (SACNs) and free cisplatin in an acidic environment.

the time delay T_i in the treatment effects equations, we assume a linear chain of reactions to obtain a distributed delay for the data fitting procedure. These drug-related reactions are shown schematically in Figure 6.3. This leads to the extended system:

$$\frac{du_e}{dt} = -r_u u_e(t) - \phi_c u_e(t), \tag{6.9}$$

$$\frac{dc_e}{dt} = r_u u_e(t) - \phi_c c_e(t), \tag{6.10}$$

$$\frac{du_i}{dt} = -r_u u_i(t) + \phi_c u_e(t - T_e), \tag{6.11}$$

$$\frac{dc_i}{dt} = r_u u_i(t) + \phi_c c_e(t - T_e). \tag{6.12}$$

6.2.5 Cell viability

With the model for protein expression and therapeutic concentrations established, we now propose a model to predict cell viability. Making the simple assumptions that cell survival is proportional to pAkt expression and cell death is proportional to caspase-3 expression proves to be a sufficient model for this prediction (see Figure 6.9a). The resulting differential equation for cell viability is then given by

$$\frac{dN}{dt} = (\lambda_N P - \delta_N C)N. \tag{6.13}$$

6.3 Parameter estimation

All of the parameter estimation to follow was performed using the MATLAB toolbox PottersWheel (http://www.potterswheel.de) [139, 173]. This toolbox is capable of loading multiple experimental data files and then estimating local and global parameters in the ODE model. The parameter values were not determined simultaneously. The data fitting process was done step-by-step as shown schematically in Figure 6.4. While the best fit for release parameters is likely the unique global minimum of the chi-square error, those determined for protein expression are not guaranteed to be a global minimum due to the lack of experimental estimates of most of the parameters (aside from the decay rates) and

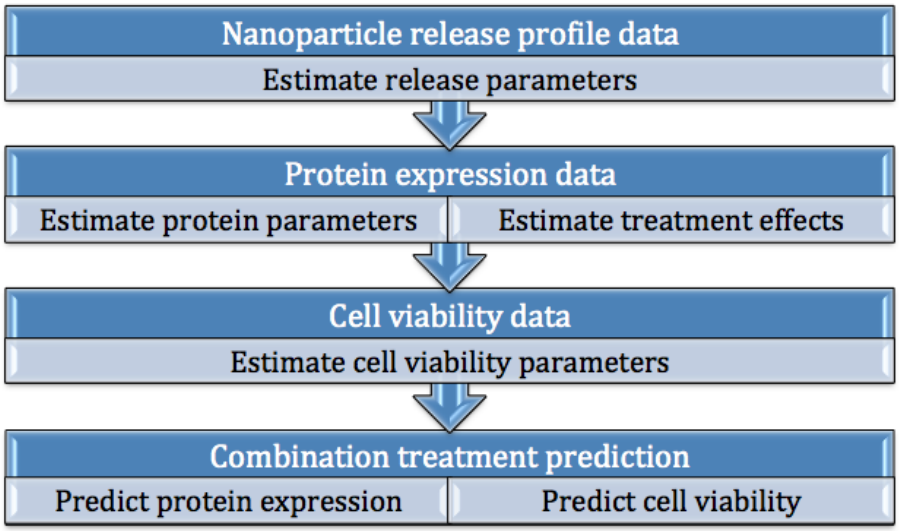

Figure 6.4: Flowchart showing the computational algorithm used to fit parameters in the mathematical model.

the sheer number of parameters to be estimated. The cell viability parameters are likely the best estimate based on the given set of protein expression parameters.

6.4 Results

6.4.1 Cisplatin nanoparticle release

Fitting the parameters of the nanoparticle release model in Equations (6.7)–(6.8) to the release profile data yields a suitable fit for the acidic environment ($\chi^2_{red} = 0.54$, $N = 15$, $p = 2$) and a mediocre one for the neutral environment ($\chi^2_{red} = 1.66$, $N = 15$, $p = 2$), see Figure 6.5 for these profiles and D for discussion of the reduced chi-squared statistic χ^2_{red}. The release parameters for these fits are given in Table 6.1. Only those determined for acidic environments are utilized in the calculations to follow so we will not present a detailed model for neutral release properties; however, the release profile for a neutral environment could be suitably fit by the addition of a single parameter that accounts for liposomal erosion ($\chi^2_{red} = 0.61$, $N = 15$, $p = 3$); this would have negligible effect on the acidic release ($\chi^2_{red} = 0.58$, $N = 15$, $p = 3$).

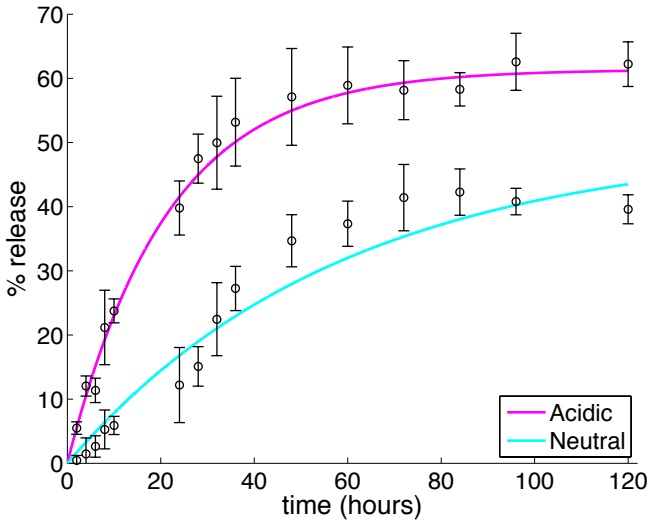

Figure 6.5: (Data points) The release profile of cisplatin liposomes was evaluated at 37°C in neutral and acidic (tumour-like) pH in triplicates. 500 mwco dialysis bags packed with 16198665 ng liposome were stirred in 30 mL of acidic and neutral pH. 500 μL samples were taken out at predetermined time points from the outer chamber and analyzed by AAS by serial dilution. (Solid lines) Release profiles of cisplatin nanoparticles in acidic (χ^2_{red}=0.54, N=15, p=2) and neutral (χ^2_{red}=1.66, N=15, p=2) microenvironments determined by fitting solutions of Equations (6.7)–(6.8).

Parameter	Neutral	Acidic
r_u	0.0471 [1/h]	0.0171 [1/h]
θ_u	0.499	0.614

Table 6.1: Nanoparticle release parameters in (6.7)–(6.8).

6.4.2 Protein expression

The data from the in vitro protein expression experiments in 4T1 breast cancer cells are used to determine the parameters in the model above; these parameters are given in Table 6.2. The only parameters present in the literature are those that determine decay rates of the proteins [159]. Each experiment is considered to have a scaling factor for each protein which are given in Table 6.3. This takes into account that the value used to non-dimensionalize the protein concentrations is different for each experiment.

Parameter	Value	Parameter	Value	Parameter	Value
k_p	1.86 [1/h]	α_p	0.13	d_g	0.001* [1/h]
k_c	11.56 [1/h]	α_c	0.56	γ_p	6.42 [1/μM]
k_x	0.29 [1/h]	λ_x	0.01 [1/h]	ϕ_c	0.26 [1/h]
δ_p	0.36 [1/h]	β_c	2.30 [1/h]	r_c	0.47 [1/h]
δ_c	0.48 [1/h]	β_x	0.040 [1/h]	d_p	0.030 [1/h]
δ_x	0.57 [1/h]	λ_p	0.34 [1/h·nM]	d_c	0.28 [1/h]
		λ_c	11.9 [1/h·nM]		

Table 6.2: Protein expression parameters in (6.1)–(6.3).
*Parameter reached minimum allowable value. Indicates PI828 decay is not detected in experiments on this time scale. This is evident from the continued inhibition exhibited in Figure 6.7b.

Figure(s)	P_0	C_0	X_0
Figure 6.6a–6.6c (3 μM)	0.514	1.18	1.06
Figure 6.6a–6.6c (5 M)	0.381	1.36	0.770
Figure 6.7b	0.812	1.32	0.1*
Figure 6.8a-6.8b (Post)	0.510	0.834	1.29
Figure 6.8a-6.8b (Control)	0.511	0.529	1.29

Table 6.3: Experimental scaling factors for protein expression in (6.7)–(6.8).

6.4.3 Cell viability

Finally, with the release parameters and protein expression parameters approximated from the data, we can introduce two parameters that predict cell viability. For this step of the fitting we must have the same scaling parameters for each experiment. Fitting to the existing

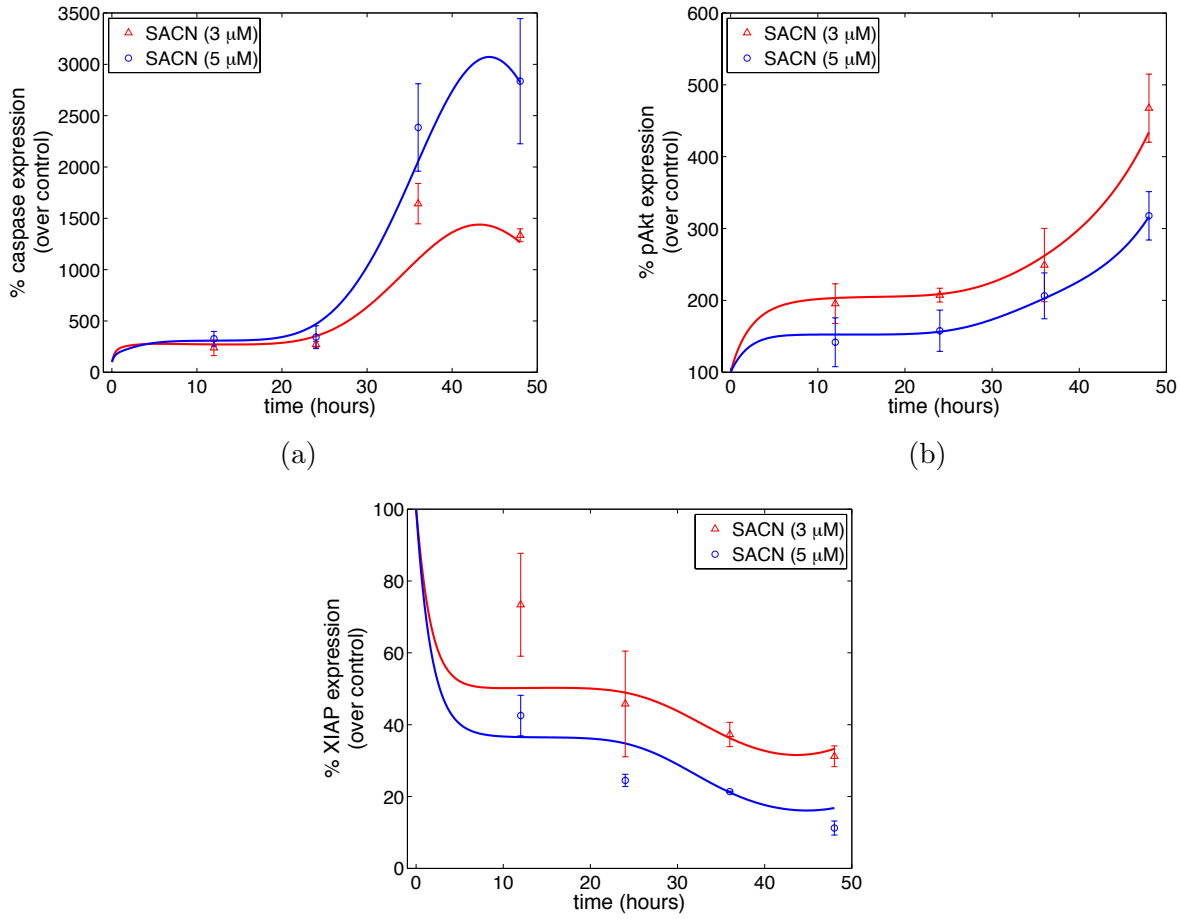

Figure 6.6: Mathematical predicted expression of caspase 6.6a, pAkt 6.6b and XIAP 6.6c in the presence of different concentrations of SACN alone.

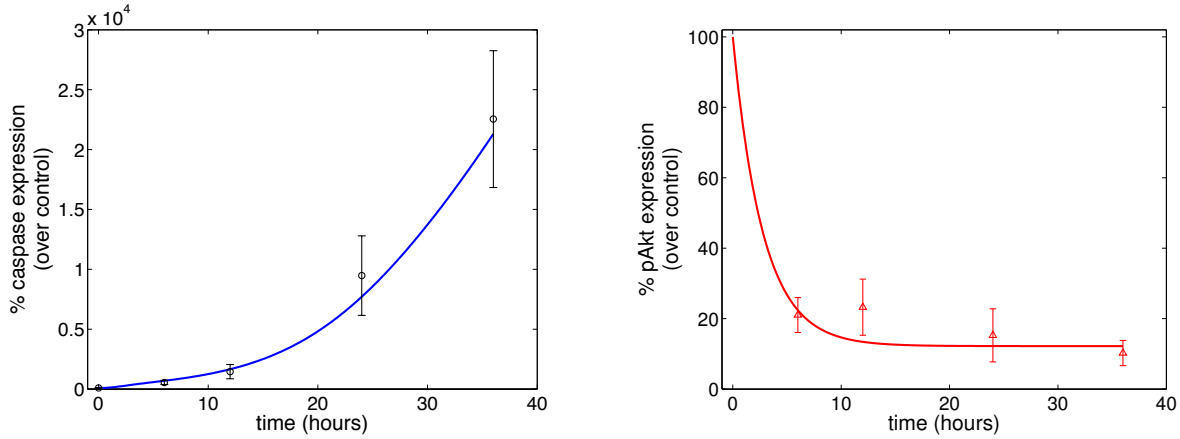

(a) (b)

Figure 6.7: The inhibition of pAkt and increase of caspase by PI828 alone 6.7b.

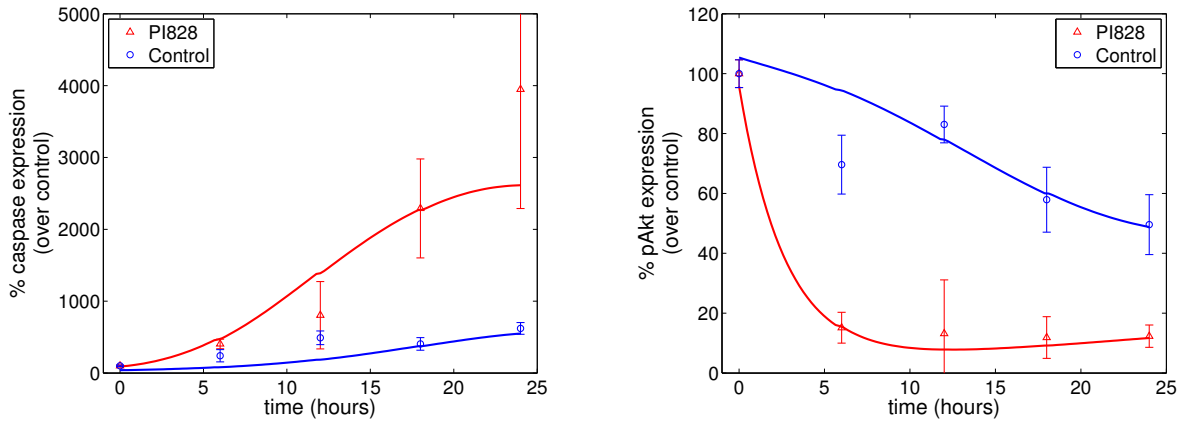

(a) (b)

Figure 6.8: The inhibition of pAkt by PI828 post treatment with SACN 6.8b and the synergistic increase in caspase expression as compared to SACN alone-treated controls 6.8a.

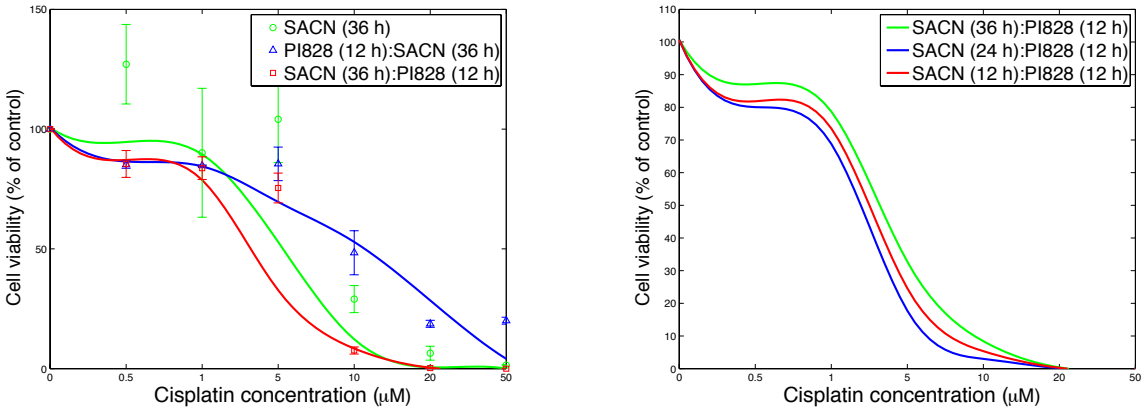

(a) (b)

Figure 6.9: (a) Mathematical model-based prediction of cell viability using different dosing schedules of SACNs and PI828. (Data points) *In vitro* measurements where the effect of different drug combinations on 4T1 cell viability was quantified using MTS assay. SACN-treated: cells were incubated with SACN containing media in an increasing concentration gradient (0.5–50 μM) for 36 hours, after which it was replaced with control media for 12 hours. PI828 pretreatment: cells were pretreated with 5 μM PI828 for 12 hours, after which the culture media were removed and cells were incubated with SACN in an increasing concentration gradient (0.5–50 μM) for 36 hours. PI828 posttreatment: cells were incubated with SACN-containing media in increasing concentration gradient (0.5–50 μM) for 36 hours, after which it was replaced with PI828-containing media at 5 μM concentration for 12 hours. All readings were taken at 48 hours (data shown are mean $\pm$ SEM, $n = 3$). (Lines) The cell viability data was used to fit (6.13) for increasing SACN concentrations yielding the parameters in Table 6.4. For the purpose of plotting, the model predictions at each SACN concentration were interpolated using cubic splines. (b) The mathematical model solution for cell viability for various post-SACN PI828 treatments: 36 hours of SACN followed by 12 hours of PI828, 24 hours of SACN followed by 12 hours of PI828, and 12 hours of SACN followed by 12 hours of PI828. Minimal cell viability was exhibited in the case where PI828 was administered 24 hours after SACN. Once again each cell viability prediction was taken at 48 hours and the prediction for each SACN concentration was interpolated with a cubic spline.

cell viability data at the 48 hour time point, (data points in Figure 6.9a) gives the parameters in Table 6.4 and the model fit at the 48 hour time point shown in Figure 6.9a. Using these parameters in the model, the cell viability associated with other treatment combinations can now be determined. Since the data already displays that PI828 posttreatment outperforming pretreatment, we will only investigate the posttreatment scenario. The cell viability associated with administering PI828 12, 24 and 36 hours after SACN treatment is shown in Figure 6.9b where once again the cell viability prediction is after 48 hours have elapsed since the start of treatment. The 24 hour mark represents a superior treatment option to both the earlier and later dosing regimens of molecular inhibitor, as in the early administration (12 hours) the cisplatin has not had enough time to take effect whilst in the later administration (36 hours) the treatment effects have begun to wear off by the time PI828 is administered. This reinforces the importance of precise timing, on the order of hours, in order to maximize the synergistic effects of these drugs and minimize cell viability.

Parameter	Value
λ_N	2.7×10^{-3} [1/h]
δ_N	1.5×10^{-3} [1/h]

Table 6.4: Cell viability parameters in (6.13).

6.5 Conclusions

Our mathematical model captured the rising cleaved caspase-3 and p-Akt levels, as can be seen by the accurate fits in Figures 6.6a and 6.6b along with decreasing XIAP levels after treatment with cisplatin nanoparticle (Figure 6.6c). The potent inhibition of pAkt after PI828 administration was also facilitated by the model (Figure 6.7b). On the basis of our assumptions and the above data, the model predicted the desired synergistic effects of the combination treatments. Relative to the control case, the mathematical model predicted synergistic increase in caspase-3 due to treatment with SACNs along with the p-Akt inhibition provided by PI828 (Figures 6.8a and 4H respectively). In addition, as shown in Figure 6.9a, PI828 administered after SACN treatment was predicted to result in lower cell viability compared with pretreatment with PI828 followed by SACNs treatment or with SACNs alone. We then sought to find the most efficient time for the administration

of PI828 after cisplatin nanoparticle treatment. It was determined that administration of PI828 approximately 24 hours after cisplatin would yield lower cell viability as compared to 36 hours or earlier times (Figure 6.9b).

Chapter 7

Contributions and Future Work

In this concluding chapter, I will first outline the minor contributions to research that I have made during my Ph.D., which do not comprise the bulk of my thesis in Chapters 4–6. These include collaborative projects and unpublished results. This will be followed by brief summaries of the major contributions made to the field of mathematical oncology including evidence of scientific impact in the literature. Finally, a selection of future directions that these mathematicals could take will be suggested.

7.1 Minor contributions

I will briefly outline a couple minor contributions that pertain to the material disseminated in Chapter 5 along with a collaborative research project on antioxidant systems that has led to a number of co-authored manuscripts.

A minor contribution that has some potential of evolving into substantially more is a reconsideration of phosphate transport's effect on ATP yield. The effects of this preliminary parameter alteration was included in the supplementary material of the metabolic symbiosis study in C.6. Phosphate transport, among other mitochondrial transport processes, remains relatively unestablished in the literature. The role of the pH differences between the cytosol, intermembrane space and mitochondrial matrix could be significant to modelling the proton gradient across the mitochondrial membrane. In fact, if one makes strong simplifying assumptions, the ATP yield from a single glucose molecule may be reduced from approximately 29 [20], to approximately 24. The truth may lie somewhere

in between these two values, or even below that threshold, if pyruvate transport or other molecular transport reduces the proton gradient further. Regardless, it remains pertinent that these transport processes, along with ATP transport and subsequent utilization should be compensated for in any model that makes steady state, or flux balance, assumptions.

An incremental generalization of the single vessel results in Chapter 5 is the two vessel model equivalent that is a more appropriate simplified model of tissue and has been used in previous models e.g. [83]. This introduces a well-defined parameter of intercapillary distance and can be used to analyze asymmetrical situations as well. This still represents a highly constrained geometry but represents the first generalization to a multi-vessel system.

Another project, which relates to the metabolism models is the development of models for antioxidant systems including the glutathione peroxide system. These counteract reactive oxygen species (ROS) that are produced by cellular respiration and by growth factors in tumours, among other processes. While essential to cell metabolism, at high concentrations ROS become detrimental to normal cell function and in extreme conditions can trigger apoptosis (cell death). To safeguard cells from ROS, there are various antioxidant enzymes that remove ROS or render them harmless. The ROS that is produced at the highest rate is typically hydrogen peroxide (H_2O_2), a molecule that can be reduced by various enzymes including catalase and those in the glutathione peroxides (GPx) family. A mathematical model that considers the effects of these antioxidants in detoxifying hydrogen peroxidase is summarized in E. Interestingly we discovered that there is a synergy between catalase and glutathione-peroxidase-1 which amplifies the detoxification power of glutathione peroxidase-1. Hence any change (upregulation or downregulation) in the catalase concentration has a direct affect on the glutathione peroxidase-1 activity and has to be included in understanding any related phenomena. Also we propose that the activity of glutathione peroxidase-1 could be regulated by changing the concentration of catalase. The synergistic relationship between these antioxidants is reported in [174]. This work was expanded to include the effects of cell permeability, especially the role of aquaporin expression. This has important consequences for the efficacy of ascorbic acid for cancer treatment and has also been submitted [175].

7.2 Major contributions

The major contributions to the field of mathematical oncology include the following:

(i) **Establishing the role of convective transport in angiogenesis signalling**: This model could be used in tumour growth models or to predict the effects of various treatments. The alteration of biochemical signalling by convection could be generalizable to other cell signalling pathways in tumours, and has been investigated in the context of tumour invasion [176].This model has been used in the literature as inspiration for including convective transport of AGFs in a tumour growth model [177] and has been quoted in [178] for the observation that, "Angiogenic behaviours were suppressed when closer to the core of the tumour and maximal angiogenic stimulation was detected towards the [outer] rim of the tumor." It has also been cited as an example of convection-based models [179, 180]. The angiogenic effect of altering physiological parameters in tumours is the focus of Chapter 4.

(ii) **Mathematical model for metabolic symbiosis in solid tumours**: This metabolism model includes lactate-fuelled and glucose-fuelled respiration along with oxygen-repressible glycolysis. This was the first model to spatially consider the optimal ATP production strategy in a tumour on the microscale and could be used to analyze metabolic inhibitors. This may lead to a significant contribution to the study of metabolism in biochemistry. This forms the majority of Chapter 5.

(iii) **The link between metabolism and acidity**: Using acidity models in tumours, the effects of blood vessel permeability (antiangiogenic agents), hypoxia and metabolic behaviour on acidosis are investigated. This research is contained in the latter half of Chapter 5.

(iv) **The optimal sequence of chemotherapy nanoparticles and molecular inhibitors**: Utilizing nanoparticle release models in conjunction with protein expression models can yield cell viability estimates for treatment optimization. The experimentally confirmed prediction of inhibitor application after chemotherapy nanoparticles could guide optimal scheduling models in this context. This contribution has the most medical and clinical relevance and is outlined in Chapter 6.

7.3 Future work

Each of these aforementioned models could be extended or utilized in alternate systems. I will indicate a sample of what I estimate to be the most fruitful endeavours.

For Chapter 4, the most obvious extension is to a non-symmetrical geometry that could model more complex tumour shapes than the spherical one considered. However,

this extension only warrants consideration if relevant experimental data is generated that confirms the role of convection in angiogenic signalling. In terms of qualitative modelling of angiogenesis, the distinct roles of various AGFs could be included by introducing separate equations for the different factors and explicitly including the inhibitory effects of antiangiogenic factors and the stimulatory effects of proangiogenic factors via appropriate terms in differential equations. The appeal of the model considered here is the utilization of effective parameters for the two groups of AGFs that dramatically reduce the number of parameters. By expanding the model to include multiple factors, diffusion coefficients, degradation and production rates must also be estimated. A less dramatic model improvement would be including continuous parameter values over the spatial domain of interest, rather than the piecewise constant parameters considered, i.e. instead of of having one value inside the tumour and one value outside the tumour (for diffusion, production and decay) these values could be smoothly interpolated. The same could be said for the pressure parameters as well, since the effective pressures, hydraulic conductivities, vessel permeabilities, etc. are all considered to be piecewise constant as well. This model also holds promise for inclusion in more complicated models, including tumour growth models (I have some preliminary results in this area), and more directly, models of tumour angiogenesis.

In Chapter 5 there are many possible areas for expansion include radially-dependent parameters (diffusion coefficients, cell densities that modify metabolic parameters), axially-dependent parameters (vessel concentrations, vessel permeability) and more generalized functional forms for the consumption rates (e.g. ATP-dependent or pH-dependent). Additional details of cellular metabolic pathways including other glycolytic and respiratory intermediaries within the pathways or alternative metabolic pathways such as glutaminolysis, could be adapted on a tumour-dependent basis. The most significant extension would be to include non-symmetrical three-dimensional geometries. While relatively straightforward to formalize and even solve numerically, a complicated spatial domain would only be clinically relevant once pertinent clinical data is generated. The details of the metabolic reactions that are used to derive the summary metabolic reactions given by (5.1), (5.2) and (5.3) are contained in C.4. An inherent assumption of these reactions is that all ATP produced in these processes are subsequently consumed at the same rate. While not tightly coupled, in steady state this is not an overly strict simplifying assumption. However if there is significant overcompensation or underconsumption of ATP, it may be worth adding ATP (and therefore ADP, phosphate and possible AMP) concentrations to a time-dependent model.

The model developed in Chapter 6 has multiple layers including nanoparticle release, protein expression and cell viability. The most rudimentary of the three is the cell viability model, which was proposed to be as simple as possible, in an attempt to predict cell viability from only the expression of two proteins. Since this endeavour achieved the research purpose, it was deemed inappropriate to propose a more complicated model for this application, however a more comprehensive protein expression model could lead to a more accurate cell viability model. The protein expression model could also be significantly extended to include more of the apoptotic signalling pathways, however, we limited ourselves to the inclusion of only those proteins for which expression was measured by our experimental collaborators. There are many nanoparticle release models that exist in the literature, and model selection here was motivated primarily by parameter minimization and satisfactory fit to data.

These models could also be coalesced into a single entity that includes many microenvironmental features including IFP, AGFs, metabolites, acidity and multiple treatments (and ROS). Certainly each of these processes are connected, as demonstrated in Chapter 2 and graphically summarized in Figure 2.8. While mathematically and computationally attractive this would rely heavily on experimental verification that simultaneously measures many different quantities. Mathematical modelling of the many interconnected processes and phenomena in solid tumours will continue to progress in terms of biological, chemical and physical relevance but most importantly in clinical and medical impact. This field is a rich area for collaboration between multiple disciplines and I hope that this thesis can serve as a launching point for others who want to investigate these fertile areas of mathematical oncology.

APPENDICES

Appendix A

Mixture Theory

The derivation of the equations for IFP and IFV in Section 3.1 consider a highly simplified derivation of a tissue treated as a fluid. However, the resulting equations are identical to those obtained through more rigorous and complicated formulations. As an example, we will present a brief argument for a biphasic tissue, adapted from [71] that considers the tissue as a mixture of solid and fluid phases. The preliminary details of mixture theory, not contained in [71], are adapted from unpublished notes from Dr. G. Tenti (provided in personal communication) whose origins lie in the work of Biot [181].

Considering a biphasic material, for concreteness assume that there is a fluid phase and a solid phase, which comprise volumes ΔV_f and ΔV_s respectively, in the volume element ΔV, where we assume saturation, so $\Delta V_f + \Delta V_s = \Delta V$. Within ΔV_f there is only fluid with mass ΔM_f and within ΔV_s there is only solid with mass ΔM_s. We have two notions of mass density that we could use, the apparent (partial, or bulk) mass density $\tilde{\rho}_i = \Delta M_i / \Delta V$, $i = f, m$ or the true (realistic, or material) mass density $\rho_i = \Delta M_i / \Delta V_i$, $i = f, m$. The proportionality between these two mass densities is the volume fraction $\phi_i = \Delta V_i / \Delta V$, $i = f, m$, so that $\tilde{\rho}_i = \rho_i \phi_i$, $i = f, m$. Since $\phi_f + \phi_s = 1$ due to the saturation condition, we will take $\phi_f = \epsilon$, and thus $\phi_s = 1 - \epsilon$.

By considering the conservation of mass, with no sources or sinks, we have the continuity

equations

$$\frac{\partial \tilde{\rho}_f}{\partial t} + \nabla \cdot (\tilde{\rho}_f \mathbf{v}_f) = 0,$$
$$\frac{\partial \tilde{\rho}_s}{\partial t} + \nabla \cdot (\tilde{\rho}_s \mathbf{v}_s) = 0,$$

where $\mathbf{v}_f$ and $\mathbf{v}_s$ are the velocities of the fluid and solid phases respectively. These equations can be rewritten in terms of their true mass densities by using the relations $\tilde{\rho}_f = \epsilon \rho_f$ and $\tilde{\rho}_s = (1-\epsilon)\rho_s$ to give

$$\frac{\partial \epsilon \rho_f}{\partial t} + \nabla \cdot (\epsilon \rho_f \mathbf{v}_f) = 0,$$
$$\frac{\partial (1-\epsilon)\rho_s}{\partial t} + \nabla \cdot ((1-\epsilon)\rho_s \mathbf{v}_s) = 0.$$

Expanding these expressions give

$$\epsilon \frac{D\rho_f}{Dt} + \rho_f \left(\nabla \cdot (\epsilon\, \mathbf{v}_f) + \frac{\partial \epsilon}{\partial t} \right) = 0,$$
$$(1-\epsilon)\frac{D\rho_s}{Dt} + \rho_s \left(\nabla \cdot ((1-\epsilon)\mathbf{v}_s) + \frac{\partial (1-\epsilon)}{\partial t} \right) = 0,$$

where the material derivative $D\rho_i/Dt$ is given by

$$\frac{D\rho_i}{Dt} = \frac{\partial \rho_i}{\partial t} + \nabla \rho_i \cdot \mathbf{v}_i, \qquad i = f, m.$$

Assuming the fluid and solid phases are undergoing incompressible flow (or even stronger that the solid, and possibly the fluid, is incompressible) sets this material derivative to zero and gives

$$\nabla \cdot (\epsilon\, \mathbf{v}_f) + \frac{\partial \epsilon}{\partial t} = 0,$$
$$\nabla \cdot ((1-\epsilon)\mathbf{v}_s) + \frac{\partial (1-\epsilon)}{\partial t} = 0.$$

Adding these two equations gives

$$\nabla \cdot (\epsilon\, \mathbf{v}_f + (1-\epsilon)\mathbf{v}_s) = 0. \tag{A.1}$$

The expression that relates these velocities to the interstitial fluid pressure p is given by a generalized Darcy's Law

$$\epsilon(\mathbf{v}_f - \mathbf{v}_s) = -K\nabla p,$$

where K is the average tissue hydraulic conductivity; the derivation will be omitted, see [182] for a clear generalized derivation of this equation in soft tissues. Substituting this into (A.1) gives

$$\nabla \cdot (-K\nabla p + \mathbf{v}_s) = 0.$$

Here we will simply assume that $\nabla \cdot \mathbf{v}_s = 0$, equivalent to assuming that the matrix dilatation of the elastic solid is in steady state. This finally gives

$$\nabla^2 p = 0,$$

which in cylindrical coordinates is simply (3.4).

A similar derivation for the macroscopic case with a distributed vessel source, mirroring that given in Section 3.1.2, also leads to the same result in (3.12).

Appendix B

Parameter values for mathematical models

B.1 Homogeneous AGFs parameters

The angiogenic growth factor parameters given in [1] and used in Section 3.3 to plot the AGFs in Figure 3.2 and the angiogenic activity in Figure 3.3 are given here in Table B.1. These form the basis for the host and tumour parameters used in Chapter 4 and presented in Table 4.2 for adding convection to an angiogenic factor model [81].

Parameter	Units	Host	Tumour
D_p	mm^2/s	4.0×10^{-5}	5.5×10^{-5}
D_a	mm^2/s	3.25×10^{-5}	4.0×10^{-5}
k_p	s^{-1}	2.0×10^{-4}	1.99×10^{-4}
k_a	s^{-1}	1.5×10^{-4}	1.1×10^{-4}
g_p	$\mu/\text{mm}^3/\text{s}$	2.0×10^{-4}	12.0×10^{-4}
g_a	$\mu/\text{mm}^3/\text{s}$	1.5×10^{-4}	7.0×10^{-4}

Table B.1: Angiogenic growth factor parameters from [1]. They use a tumour radius of 2.5 mm.

B.2 Interstitial fluid pressure parameters

The pressure parameters given in [2] and used in Section 3.1.2 to plot the nondimensionalized IFP and IFV are given in Table B.2. These form the basis for host, tumour and normalized tumour parameters used in Chapter 4 and presented in Table 4.2.

Parameter	Units	Host	Tumour
L_p	mm/s/mmHg	3.6×10^{-7}	1.86×10^{-5}
K	$mm^2/s/mmHg$	2.5×10^{-5}	2.5×10^{-5}
S/V	mm^2/mm^3	17.4	16.5
p_v	mmHg	20	20
σ_v	-	0.91	8.7×10^{-5}
π_v	mmHg	20	19.8
π_i	mmHg	10	17.3
p_e	mmHg	10.9	20
α	–	2	14

Table B.2: Pressure parameters from [2].

B.3 Microvessel model for pH

To convert between the notation used by Casciari et al. in their papers [3, 4] to the notation used in this thesis, please consult Table B.3.

The production rates and parameters used in Section 3.4.2 are given in Tables B.4 and B.5 respectively.

i	a	b	c	d	e	f	g	h
X	O	G	L	C	B	Cl^-	H	Na^+

Table B.3: Conversion of concentration notation C_i from [3, 4] to notation standardized in this thesis X. Note that the ions Cl^- and Na^+ are omitted in [25] since they are extraneous charge-maintaining variables when a model does not include charge migration. If these concentrations exhibited interesting spatial patterns outside tumour vessels, then they would be worth including in a simple model.

Compound	X	Q_X (10^{-2}mM/s)
Cl^-	Cl	0
Na^+	Na	-
Glucose	G	$p_G \frac{G}{G+k_G} f_1(O)$
O_2	O	$RP_G \frac{O}{O+k_O} f_2(O)$
$Lactate^-$	L	$-2Q_G + \frac{1}{3}Q_O$
CO_2	C	$-k_r HB + k_f C$
$Bicarbonate^-$	B	$-k_f C + k_r HB - Q_O$
H^+	H	$-k_f C + k_r HB - Q_O + Q_L$

Table B.4: Consumption rates and parameters for acidity-metabolism model from [25], where $f_i(O) = 1 - a_i O^{0.02} \exp(-100(O-0.01)^4)$, $i = 1, 2$ where $a_1 = 2/3$ and $a_2 = 1/2$. Other reaction parameters are $p_G = 1.8 \times 10^{-3}$ mM/s, $k_O = 2 \times 10^{-4}$mM, $k_G = 5 \times 10^{-2}$ mM, $k_r = 58$ /mM/s and $k_f = 7.4 \times 10^{-7}$ /s.

X	D_X (cm^2/s)	μ_X (cm/s)	V_X (mM)	σ_X
Cl	2.26×10^{-7}	1.20×10^{-4}	1.05×10^{2}	0.99
Na	3.14×10^{-7}	1.20×10^{-4}	1.22×10^{2}	0.99
G	1.10×10^{-6}	3.0×10^{-5}	2	0.95
O	1.82×10^{-5}	3.0×10^{-5}	1.43×10^{-2}	0.99
L	1.8×10^{-6}	1.20×10^{-4}	2	0.99
C	8.9×10^{-7}	3.0×10^{-5}	1	0.99
B	2.2×10^{-7}	1.7×10^{-5}	20	0.99
H	1.9×10^{-6}	1.20×10^{-4}	4×10^{-5}	0.99

Table B.5: Molecular parameters for metabolism model from [25]: diffusion coefficients D_X, vessel permeability μ_X, vessel concentration V_X and osmotic reflection coefficient σ_X estimated from [62].

Appendix C

Metabolism model details

This appendix serves as supplementary material for Chapter 5.

C.1 Boundary conditions

The interstitial flux in the interstitial space of the tissue is assumed to be given by Fick's Law $J_X = -D_X \nabla X$, where D_X is an effective diffusion coefficient in the tissue. This form assumes that diffusion is the dominant transport mechanism for oxygen, glucose and lactate on the microscale. This expression could be generalized to include convective transport and charge migration effects.

In this case the transvascular transport is also assumed to be diffusion-dominated and is given by $J_s = \mu_X S(V_X - X)$, where μ_X is the vessel permeability to solute X, V_X is the blood vessel concentration and $X_1 = X(\omega^+)$ is the perivascular concentration; the superscript '+' denotes the exterior surface of the vessel. Once again this diffusive expression could be extended to include convective transport (e.g. the Patlak equation [80]).

At the vessel wall the solute flux in the interstitium should be equal to the solute flux across the vessel wall. Equating the above expressions for J_X and J_s gives the appropriate boundary condition:

$$-D_X \frac{dX}{dr}\bigg|_{r=\omega^+} = \mu_X(V_X - X_1). \tag{C.1}$$

This would me appropriate for any blood vessel that exhibits a difference in concentration between the blood inside and the tissue outside. In many tumour blood vessels, the vessel walls are poorly constructed, exhibiting large fenestrations and thus highly elevated permeability. In the limit of large μ_X, we obtain the simplified version of the boundary condition $X(\omega^+) = V_X$, which assumes that the perivascular concentration and vessel concentration are equal. This is the one we have used in our analysis.

We also require the concentrations to reach a steady state as we move away from the vessel and take

$$\frac{dX}{dr} = 0 \quad \text{at } r = \Omega, \tag{C.2}$$

where Ω is the penetration depth [71], a distance far enough from the microvessel to justify the assumption that the system has reached steady state but close enough to ensure minimal contributions from other nearby vessels.

C.2 Generalized analytical derivation

In this paper the system was integrated twice in cylindrical co-ordinates to replace one of the differential equations with a formula. Here we will generalize that result by showing the calculation in Cartesian coordinates with the more widely applicable boundary condition given in (C.1). The dimensional system is given by:

$$D_X \frac{d^2X}{dr^2} = Q_X, \qquad X = O, L, G, \tag{C.3}$$

where Q_X are the consumption rates of species X (given by (5.10)–(5.12)) and they satisfy the relation $Q_G = Q_O/6 - Q_L/2$.

The nondimensional system is given by

$$\frac{d^2o}{dr^2} = Q_o, \tag{C.4}$$

$$\frac{d^2\ell}{dr^2} = Q_\ell, \tag{C.5}$$

$$\frac{d^2g}{dr^2} - \frac{\alpha_o}{6}\frac{d^2o}{dr^2} + \frac{\alpha_\ell}{2}\frac{d^2\ell}{dr^2} = 0, \tag{C.6}$$

where $\alpha_x = d_x v_x$ ($d_x = D_X/D_G$, $v_x = V_X/V_G$), and $Q_x = Q_X/(D_X V_X)$. These are subject to the nondimensional boundary conditions

$$-\left.\frac{dx}{dr}\right|_{r=\rho} = \mu_x(1 - x_1), \tag{C.7}$$

where $x_1 = x(\rho)$ and $\mu_x = \mu_X/D_X$; the far-field boundary condition is

$$\left.\frac{dx}{dr}\right|_{r=P} = 0. \tag{C.8}$$

First, integrating (C.6) over (r, P) and enforcing the far-field boundary condition (C.8) gives

$$\frac{dg}{dr} - \frac{\alpha_o}{6}\frac{do}{dr} + \frac{\alpha_\ell}{2}\frac{d\ell}{dr} = 0, \tag{C.9}$$

the identical expression to that found in cylindrical coordinates (5.17). Before integrating again, it is worth noting that by applying the more general vessel boundary condition (C.7) and rearranging the previous equality at $r = \rho$ yields

$$g_1 = 1 - \frac{\beta_o}{6}(1 - o_1) + \frac{\beta_\ell}{2}(1 - \ell_1), \tag{C.10}$$

where $\beta_x = \mu_x v_x$ ($\mu_x = \mu_X/\mu_G$). Now integrating the equation (C.9) once more, this time over (ρ, r), gives

$$g(r) = g_1 - \frac{\alpha_o}{6}\big(o_1 - o(r)\big) + \frac{\alpha_\ell}{2}\big(\ell_1 - \ell(r)\big), \tag{C.11}$$

an analogous expression to (5.18) with modified perivascular concentrations.

C.3 Numerical methods

For estimation of the maximum consumption rate of oxygen p_O (mM/s), we use parameter fitting and boundary value problem (BVP) solving functions in MATLAB[139]. This algorithm imposes a constraint on the system that limits the rate of ATP production by lactate or glucose fuelled respiration, proportional to the rate of oxygen consumption. The data we use to fit the model are from experiments performed by [5] that represent the first micrometer scale measurements of the partial pressure of oxygen (pO_2) and interstitial

pH adjacent to tumour blood vessels. We will utilize their measurements of average pO_2 provided as a function of distance from a single blood vessel to estimate this oxygen consumption rate in the model. In their experiment the individual measurements were taken from multiple blood vessels in 7 tumours. When averaged, these measurements were only considered up to a distance D/3 from the vessel, where D is the distance to the nearest neighbouring vessel, in order to ensure that the contribution was predominantly from the local effects of a single vessel. These tumours were grown in window chambers, and so are appropriately modelled in Cartesian coordinates [25, 83].

To reduce the number of parameters and to discourage overfitting the problem, we will fix the half-maximal concentration $K_O = 2 \times 10^{-4}$, a value previously estimated on the microscale [25]; this is lower than 4.640×10^{-3} mM measured in EMT6/Ro tumour spheroid [105] and commonly used for macroscopic models (e.g. [64, 65, 63, 89]). The simplified boundary value problem is given by the Cartesian equation (C.3) ($X = O$), with

$$Q_O = p_O \frac{O}{O + K_O},$$

or in nondimensional terms by (C.4) with

$$Q_o = p_o \frac{o}{o + \kappa_o},$$

where $p_o = p_O/(D_O V_O)$, along with boundary conditions $o(\rho) = 1$ and $dx/dr|_{r=P} = 0$. To solve the BVP the MATLAB function 'bvp5c' was used; this function utilizes the four-stage Lobatto Illa formula (implemented as an implicit Runge-Kutta formula) and ensures fifth-order accuracy. Analytical Jacobian matrices were specified for the boundary conditions and the BVP once it was converted to a first order differential equation system. The absolute and relative residual tolerances are set to 10^{-7}. Starting at $p_o = 1 \times 10^{-5}$, the function 'fminsearch', which utilizes the Nelder-Mead algorithm, was used to find the minimum residual sum of squares, i.e. $RSS = \sum_{i=1}^{N} (y_i - o(x_i))^2$, where the points (x_i, y_i) are the spatial variable and the oxygen concentration data means from [5] and $o(x_i)$ are the solutions to the BVP interpolated at the same points as the observations. After 11 iterations, the algorithm converges to a value of $RSS = 0.0184$ with $p_o = 5.35 \times 10^{-5}$. The algorithm terminates since the difference between the estimated parameter value (p_O) and other points in the simplex is less than a tolerance of 10^{-4} and the corresponding function values (RSS) are also less than this tolerance. This solution for $o(r)$ with corresponding

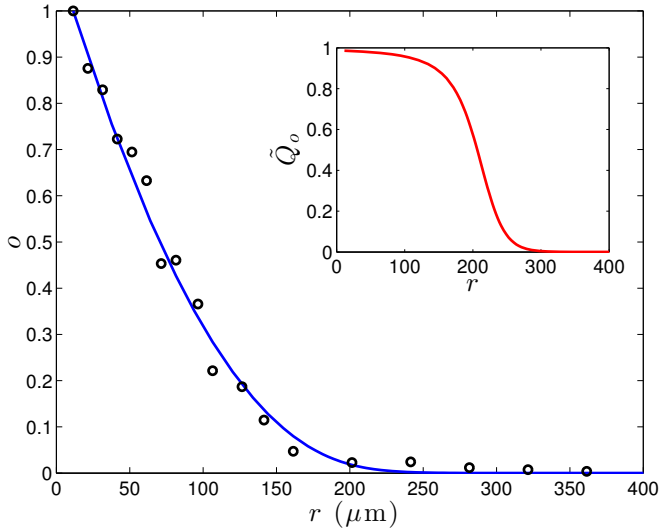

Figure C.1: Solution to oxygen boundary value problem fit to radial oxygen profile data from [5]. Inset: scaled oxygen consumption rate.

scaled consumption rate $\tilde{Q}_o = Q_o/p_o$ is shown in Figure C.1. In dimensional terms, using the values for D_O and V_O in Table 5.1, this corresponds to $p_O = 1.39 \times 10^{-3}$ mM/s. This value is one order of magnitude lower than the value used in [64], which was based off [4]. This sets a maximum value for the total oxygen consumption rate of both lactate-fuelled and glucose-fuelled respiration, i.e. $p_O = 6B_O = 3B_L$. This can be justified by noting that $Q_O \leq \max(6B_O, 3B_L)$.

To show the effect of changing geometries, from the Cartesian system used in [25] to the cylindrical one used here, we have found the solution to the simple oxygen BVP in Cartesian and cylindrical coordinates using the parameters determined above. The solutions and the corresponding consumption rates are shown in Figure C.2. This demonstrates the significant difference between modelling the experimental setup of a window chamber, e.g. the pO_2 and pH measurements by Helmlinger et al. [5], using a flat vessel wall [25, 83], and using a rounded wall which corresponds to the *in vivo* situation of an isolated microvessel [183].

For the full system we fix all parameters at specified values and use the MATLAB solver 'bvp5c' to numerically solve the couple ODE system given by (5.13)–(5.14). Once

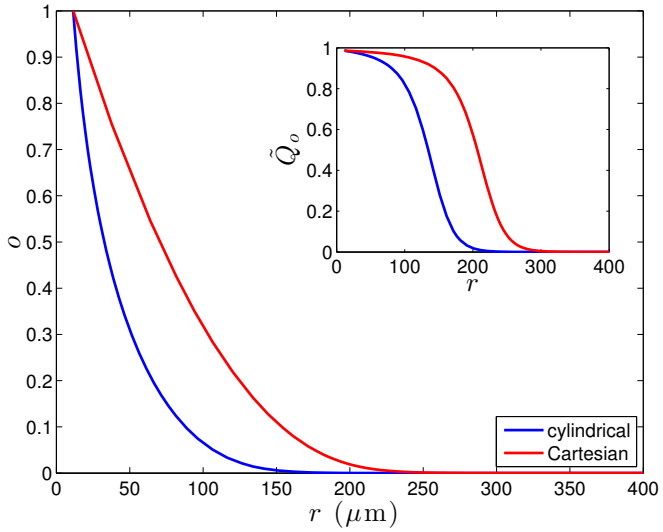

Figure C.2: The Cartesian solution to oxygen boundary value problem fit to radial oxygen profile data from [5] is the same as that in Figure C.1. The cylindrical solution utilizes the same parameters as the Cartesian solution. This visualizes the effect of changing geometries (Cartesian: flat wall; cylindrical: rounded wall). Inset: Corresponding scaled oxygen consumption rate.

again the Jacobian matrices for the boundary conditions and the corresponding first order system are specified and the absolute and relative residual tolerances are set to 10^{-7}. The formula 5.15 is used to determine the resulting glucose concentration. The ATP production is then determined by the formula (5.19).

C.4 Biochemical Summary

Preliminaries

The direction of the arrows in the reactions to follow are taken to be in the direction that is predominantly exhibited in the environment that is being considered; they do not imply irreversibility of the reaction. The reactions presented below are sometimes the sum of many reactions in which case the Enzyme Commission (EC) number(s) will be

stated. These reactions are protonated to a physiological pH of 7.3, to remain consistent with the pathways in the HumanCyc database [184]. The reactions presented below hold at physiological pH $6.9 \leq$ pH ≤ 7.4. In many cases, the nomenclature is simplified to promote readability (e.g. the name D-glucopyranose which encompasses both $\alpha-$D and $\beta-$D glucose will be referred to simply as 'glucose'). Molecular formulae are given in Tables C.1. The primary purpose of the following biochemical summary is to determine the relation between oxygen consumption, glucose consumption and ATP turnover in various simplified metabolic regimes. The ATP yield will be emphasized by boxing the number of ATP produced (and subsequently consumed) under a reaction and in summary equations. This is the key to translating the biochemical reactions into ATP yields that will be used in the mathematical model.

Transport across cell membrane

Glucose transport: We will simply write glucose transport across the cell membrane as one molecule transported from extracellular space (subscript e) to the cytosol (subscript c). The stoichiometry of this transmembrane transport is tissue-dependent and humans express sodium-dependent transporters [185] and glucose/H^+ symporters but predominantly utilize uniporters [186]:

$$\mathrm{G}_e \rightarrow \mathrm{G}_c. \tag{C.12}$$

Cystolic processes: Glycolysis

The molecules involved in the reactions presented in this section all occur in the cytosol; the subscript c on the molecules will be omitted in this subsection for simplicity.

Glycolysis: The conversion of glucose to pyruvate is the first step of cellular respiration that will be used for the glucose-fuelled summary reactions to follow. The process of glycolysis includes ten reactions catalyzed by the following enzymes in the given order: (i) glucokinase/hexokinase (EC 2.7.1.1/2.7.1.2), (ii) glucose-6-phosphate isomerase (EC 5.3.1.9), (iii) 6-phosphofructokinase (EC 2.7.1.11), (iv) fructose-biphosphate aldolase (EC 4.1.2.13), (v) triosephosphate isomerase (EC 5.3.1.1), (vi) glyceraldehyde-3-phosphate dehydrogenase (EC 1.2.1.12), (vii) phosphoglycerate kinase (EC 2.7.2.3), (viii) phosphoglycerate mutase (EC 5.4.2.11/5.4.2.12), (ix) phosphoglycerate enolase (EC 4.2.1.11), and

(x) pyruvate kinase (EC 2.7.1.40). The summary reaction for glycolysis is:

$$\mathrm{G} + 2\mathrm{ADP} + 2\mathrm{P_i} + 2\mathrm{NAD^+} \rightarrow 2\mathrm{P} + 2\mathrm{ATP} + 2\mathrm{NADH} + 2\mathrm{H^+} + 2\mathrm{H_2O} \tag{C.13}$$

ATP hydrolysis: We assume ATP is consumed at the same rate that it is produced. Reactions that have utilized this reaction will have the number of ATP consumed in a box underneath the reaction arrow. This cellular energy consumption is given below and is the stoichiometric proton source [187]. Due to the pKa of phosphate, it may buffer a significant proportion of these protons, or other buffers may diminish this effect. They will appear in summary equations as cytosolic protons H_c^+.

$$\mathrm{ATP} + \mathrm{H_2O} \rightarrow \mathrm{ADP} + \mathrm{P_i} + \mathrm{H^+} \tag{C.14}$$

Lactate dehydrogenase (LDH): This enzyme (EC 1.1.1.27) facilitates the conversion between pyruvate and lactate. This is necessary for NADH regeneration (oxidation) without oxygen.

$$\mathrm{P} + \mathrm{NADH} + \mathrm{H^+} \rightleftharpoons \mathrm{L^-} + \mathrm{NAD^+} \tag{C.15}$$

Glucose to Lactate:=(C.13)+$\boxed{2}$×(C.14)+2×(C.15). This is the net fermentation reaction given in (5.1) that characterizes glycolytic cell population.

$$\mathrm{G} \xrightarrow[\boxed{2}]{k_G} 2\mathrm{L^-} + 2\mathrm{H^+}. \tag{C.16}$$

Note: Cytosolic $\mathrm{H^+}$ production during conversion of glucose to lactate is a result of ATP consumption, not the release of $\mathrm{H^+}$ from the neutral lactic acid.

Transport into mitochondria

The subscript m denotes molecules inside the mitochondrial matrix. We will omit consideration of transport across the outer mitochondrial membrane since the molecules that must subsequently cross the inner mitochondrial matrix can easily traverse the large porins of the outer membrane, expect in the case of phosphate transport due to the necessity of

protonation. We will differentiate the intermembrane space (with the subscript i) when considering the proton gradient across the inner mitochondrial matrix.

A key consideration for these reactions that involve molecules passing from one cell compartment to another is that any charge differences induced by transport must be compensated for with the corresponding cost to the proton gradient. While the reactions are all charge balanced with respect to the total reaction, if they are not electroneutral with respect to each cell compartment (each subscript) on both sides of the reaction, then the equivalent proton transport must be included. This ensures the critical maintenance of the electrochemical gradient across the inner mitochondrial membrane.

Malate-aspartate shuttle: This shuttle effectively delivers NADH from the cytosol into the matrix to be utilized by ETC. We will take this to be the dominant shuttle mechanism and thus consider the glycerol phosphate shuttle to be negligible (it is less efficient). Sum of reactions/transport: (i) malate dehydrogenase (cytosol, EC 1.1.1.37), (ii) malate import (iii) malate oxoglutarate antiporter, (iv) malate dehydrogenase (matrix), (v) aspartate aminotransferase (matrix, EC 2.6.1.1), (vi) glutamate-aspartate antiporter, (vii) aspartate aminotransferase (intermembrane space), (viii) oxaloacetate export. This shuttle is electroneutral but does diminish the proton gradient:

$$\mathrm{NADH}_c + \mathrm{H}_c^+ + \mathrm{NAD}_m^+ \rightarrow \mathrm{NAD}_c^+ + \mathrm{NADH}_m + \mathrm{H}_m^+ \tag{C.17}$$

Pyruvate transport: The mitochondrial pyruvate carrier has been identified [188, 189] but the exact stoichiometry remains unclear. Here we will assume the transport is symport with H^+. If this is not the case it would have minimal effect on the system since it only accounts for a one proton reduction in the gradient per pyruvate.

$$\mathrm{P}_c + \mathrm{H}_i^+ \rightarrow \mathrm{P}_m + \mathrm{H}_m^+ \tag{C.18}$$

Glycolysis + Transport:=(C.12)+(C.13)+2×(C.17)+2×(C.18)

$$\mathrm{G}_e + 2\mathrm{ADP} + 2\mathrm{P_i} + 2\mathrm{NAD}_m^+ + 2\mathrm{H}_i^+ \rightarrow 2\mathrm{P}_m + 2\mathrm{ATP} + 2\mathrm{NADH}_m + 4\mathrm{H}_m^+ + 2\mathrm{H_2O} \tag{C.19}$$

The subscript on extracellular glucose will be omitted in what follows.

ATP-ADP translocase: This is required for ATP produced in mitochondria to reach

the cytosol and ADP in cytosol to be recycled into mitochondria.

$$\mathrm{ADP}_c + \mathrm{ATP}_m \rightarrow \mathrm{ADP}_m + \mathrm{ATP}_c \tag{C.20}$$

This diminishes the electrochemical gradient by one charge and must be compensated for with the opposite and equal charge transfer.

Phosphate carrier: The transport of phosphate is taken to be antiport with OH^- [190]. However the net reaction is complicated by the multiple protonations of phosphate at physiological pH. The pKa of phosphate in cells is 6.82, lower than the typical pH of the cytosol and mitochondrial matrix and approximately equal to the intermembrane space pH [191]. To fully model this process a multi compartment intracellular buffering model would have to be constructed. Under the restriction that $\mathrm{P_i}$ exists predominantly as a hydrogen phosphate ion ($\mathrm{HPO_4^{2-}}$) in the cytosol and mitochondrial matrix, and can be sufficiently converted to dihydrogen phosphate ion ($\mathrm{H_2PO_4^-}$) in the intermembrane space, the form required for transport [190]. The neutral summary reaction is:

$$\mathrm{P_{i},}_c + 2\mathrm{H}_i^+ \rightarrow \mathrm{P_{i},}_m + 2\mathrm{H}_m^+. \tag{C.21}$$

To derive this we will briefly distinguish between $\mathrm{P_i^{2-}}$:=$\mathrm{HPO_4^{2-}}$ and $\mathrm{P_i^-}$:=$\mathrm{H_2PO_4^-}$. It is the sum of the following processes:

1. outer membrane transport: $\mathrm{P_{i},}_c^{2-} \rightarrow \mathrm{P_{i},}_i^{2-}$,
2. intermembrane protonation: $\mathrm{P_{i},}_i^{2-} + \mathrm{H}_i^+ \rightarrow \mathrm{P_{i},}_i^-$,
3. hydroxide antiport: $\mathrm{P_{i},}_i^- + \mathrm{OH}_m^- \rightarrow \mathrm{P_{i},}_m^- + \mathrm{OH}_i^-$,
4. mitochondrial disassociation: $\mathrm{P_{i},}_m^- \rightarrow \mathrm{P_{i},}_m^{2-} + \mathrm{H}_m^+$,
5. hydroxide balance: $\mathrm{H}_i^+ + \mathrm{OH}_i^- \rightarrow \mathrm{H_2O}_i$, $\mathrm{H}_m^+ + \mathrm{OH}_m^- \rightarrow \mathrm{H_2O}_m$,
6. water exchange: $\mathrm{H_2O}_i \rightarrow \mathrm{H_2O}_m$.

ATP transport:=(C.20)+(C.21). The transport of ATP into the cytosol, and reimport of phosphate and ADP is summarized by:

$$\mathrm{ADP}_c + \mathrm{P_{i},}_c + 2\mathrm{H}_i^+ + \mathrm{ATP}_m \rightarrow \mathrm{ADP}_m + \mathrm{P_{i},}_m + 2\mathrm{H}_m^+ + \mathrm{ATP}_c \tag{C.22}$$

Mitochondrial matrix processes

The molecules in this section without subscripts are all present in the mitochondrial matrix (typically denoted with subscript m).

Pyruvate dehydrogenase complex: The link between glycolysis and the citric acid cycle.

$$\mathrm{P} + \mathrm{CoA} + \mathrm{NAD}^+ \rightarrow \mathrm{Ac\text{-}CoA} + \mathrm{NADH} + \mathrm{CO_2} \tag{C.23}$$

Citric acid cycle: The summary of reactions catalyzed by: (i) citrate synthase (EC 2.3.3.1), (ii) aconitase hydratase (EC 4.2.1.3), (iii) isocitrate dehydrogenase (EC 1.1.1.41), (iv) oxoglutarate dehydrogenase (EC 1.2.4.2), (v) succinyl-CoA synthetase (EC 6.2.1.4), (vi) succinate dehydrogenase (EC 1.3.5.1), (vii) fumarase (EC 4.2.1.2), (viii) malate dehydrogenase (EC 1.1.1.37). We also include phosphate exchange for conversion of energy output of pathways from GTP to ATP yield alone via nucleoside-diphosphate kinase (EC 2.7.4.6).

$$\mathrm{Ac\text{-}CoA} + 3\mathrm{NAD}^+ + \mathrm{Q} + \mathrm{ADP} + \mathrm{P_i} + 2\mathrm{H_2O} \rightarrow \\ \mathrm{CoA} + 3\mathrm{NADH} + \mathrm{QH_2} + \mathrm{ATP} + 2\mathrm{H}^+_m + 2\mathrm{CO_2} \tag{C.24}$$

Pyruvate cofactor yield:=(C.23)+(C.24)+(C.22)

$$\mathrm{P} + 4\mathrm{NAD}^+ + \mathrm{Q} + \mathrm{ADP}_c + \mathrm{P}_{\mathrm{i},c} + 2\mathrm{H}^+_i + 2\mathrm{H_2O} \rightarrow 4\mathrm{NADH} + \mathrm{QH_2} + \mathrm{ATP}_c + 4\mathrm{H}^+_m + 3\mathrm{CO_2} \tag{C.25}$$

Electron transport chain (ETC)

NADH oxidation: The complete ETC is the sum of Complex I, Complex III and Complex IV. Used to calculate the number of intermembrane protons generated per NADH.

$$\mathrm{NADH} + \frac{1}{2}\mathrm{O_2} + 11\mathrm{H}^+_m \rightarrow \mathrm{NAD}^+ + 10\mathrm{H}^+_i + \mathrm{H_2O} \tag{C.26}$$

$\mathrm{QH_2}$ oxidation: Partial ETC (from Q) is the sum of Complex III and Complex IV. Used to calculate the number of intermembrane protons generated per $\mathrm{QH_2}$.

$$\mathrm{QH_2} + \frac{1}{2}\mathrm{O_2} + 6\mathrm{H}^+_m \rightarrow \mathrm{Q} + 6\mathrm{H}^+_i + \mathrm{H_2O} \tag{C.27}$$

ATP synthase: It requires the transport of ten protons from the intermembrane space across the inner membrane into the mitochondrial matrix to drive a single revolution of the 10 subunits of ATP synthase [21]. This enables the production of 3 ATP molecules.

$$3\mathrm{ADP} + 3\mathrm{P_i} + 10\mathrm{H}_i^+ \rightarrow 3\mathrm{ATP} + 7\mathrm{H}_m^+ + 3\mathrm{H_2O} \tag{C.28}$$

ATP production by ETC:=(C.28)+3×(C.22). The net movement of 16 protons results in 3 ATP in the cytosol.

$$3\mathrm{ADP}_c + 3\mathrm{P}_{\mathrm{i},c} + 16\mathrm{H}_i^+ \rightarrow 3\mathrm{ATP}_c + 3\mathrm{H_2O} + 13\mathrm{H}_m^+ \tag{C.29}$$

Respiration summaries

Pyruvate and ETC:=(C.25)+4×(C.26)+(C.27)

$$\mathrm{P} + 2.5\mathrm{O_2} + \mathrm{ADP}_c + \mathrm{P}_{\mathrm{i},c} + 46\mathrm{H}_m^+ \rightarrow \mathrm{ATP}_c + 3\mathrm{CO_2} + 44\mathrm{H}_i^+ + 3\mathrm{H_2O} \tag{C.30}$$

Glucose and ETC:=(C.19)+2×(C.30)+2×(C.26)

$$\mathrm{G} + 6\mathrm{O_2} + 4\mathrm{ADP}_c + 4\mathrm{P}_{\mathrm{i},c} + 110\mathrm{H}_m^+ \rightarrow 4\mathrm{ATP}_c + 6\mathrm{CO_2} + 106\mathrm{H}_i^+ + 10\mathrm{H_2O} \tag{C.31}$$

Glucose-fuelled ATP yield:=(C.31)+106/16=6.625×(C.29). A total of $6.625 \times 3 = 19.875$ ATP are generated by the ETC per glucose molecule bringing the total to $\phi_g = 19.875 + 4 = 23.875$ ATP per glucose.

$$\mathrm{G} + 6\mathrm{O_2} + \phi_g\mathrm{ADP}_c + \phi_g\mathrm{P}_{\mathrm{i},c} + \phi_g\mathrm{H}_m^+ \rightarrow 6\mathrm{CO_2} + (\phi_g + 6)\mathrm{H_2O} + \phi_g\mathrm{ATP}_c \tag{C.32}$$

Glucose-fuelled respiration:=(C.32)+$\boxed{\phi_g}$×(C.14)

$$\mathrm{G} + 6\mathrm{O_2} + \phi_g\mathrm{H}_m^+ \xrightarrow[\boxed{23.875}]{} 6\mathrm{CO_2} + 6\mathrm{H_2O} + \phi_g\mathrm{H}_c^+ \tag{C.33}$$

In order for this summary reaction to balance we must assume that the proton load induced by ATP consumption in the cytosol is then transferred to the intermembrane space. We can then dismiss these protons by assuming they are lost to proton leak, i.e.

$H_i^+ \rightarrow H_m^+$, or we could have them be used as fuel for sustained ATP production. For simplicity, to remain consistent in this respect to previous ATP yield estimates and since proton leak is a significant factor in loss of energy metabolism efficiency, we will assume the former approach yielding:

$$\underset{\boxed{23.875}}{G + 6O_2 \xrightarrow{k_O} 6CO_2 + 6H_2O} \tag{C.34}$$

Lactate and ETC:=Reverse reaction of (C.15)+(C.18)+(C.17)+(C.26)+(C.30)

$$L^- + 3O_2 + ADP_c + P_{i,c} + 55H_m^+ \rightarrow 3CO_2 + 53H_i^+ + 4H_2O \tag{C.35}$$

Lactate-fuelled ATP yield:=(C.35)+53/16=3.3125×(C.29). A total of $\phi_\ell = 3.3125 \times 3 + 1 = 10.9375 \approx 11$ ATP are generated per lactate molecule.

$$L^- + 3O_2 + \phi_\ell ADP_c + \phi_\ell P_{i,c} + (\phi_\ell + 1)H_m^+ \rightarrow 3CO_2 + (\phi_e ll + 3)H_2O + \phi_\ell ATP_c \tag{C.36}$$

Lactate-fuelled respiration:=(C.36)+ϕ_ℓ×(C.14).

$$\underset{\boxed{11}}{L^- + 3O_2 + (\phi_\ell + 1)H_m^+ \longrightarrow 3CO_2 + 3H_2O + \phi_\ell H_c^+} \tag{C.37}$$

Once again, if we desire to eliminate protons, we will assume $H_c^+ \rightarrow H_i^+ \rightarrow H_m^+$. Thus ending at:

Lactate-fuelled respiration:=(C.36)+$\boxed{\phi_\ell}$×(C.14).

$$\underset{\boxed{11}}{L^- + 3O_2 + H_m^+ \xrightarrow{k_L} 3CO_2 + 3H_2O} \tag{C.38}$$

C.5 Metabolism reaction details

Presented below are the constituent steps of metabolic processes including glycolysis, malate-aspartate shuttle, citric acid cycle and electron transport chain. In some cases the

Molecule	Symbol	Formula
Metabolites in mathematical model		
oxgen	O_2	O_2
lactate	L^-	$C_3H_5O_3^-$
glucose	G	$C_6H_{12}O_6$
Coenzymes		
adenosine monophosphate	AMP	$C_{10}H_{12}N_5O_4$-PO_3^{2-}
adenosine diphosphate	ADP	AMP-PO_3^{3-}
adenosine triphosphate	ATP	ADP-PO_3^{4-}
nicotinamide adenine dinucleotide	NAD^+	$C_{21}H_{26}N_7O_{14}P_2^-$
reduced NAD^+	NADH	NAD^+-H^{2-}
coenzyme Q_{10}	Q	$C_{59}H_{90}O_4$
ubiquinol	QH_2	$C_{59}H_{92}O_4$
coenzyme A	CoA	$C_{21}H_{32}N_7O_{16}P_3S^{4-}$
acetyl CoA	Ac-CoA	CoA-$C_2H_2O^{4-}$
Other molecules		
proton[a]	H^+	H^+
water	H_2O	H_2O
carbon dioxide	CO_2	CO_2
phosphate[b]	P_i	HPO_4^{2-}
pyruvate	P	$C_3H_3O_3^-$

Table C.1: Molecular formulae for the central molecules presented in metabolic reactions considered in (C.12)–(C.38). The formulae presented are those that predominantly exist at physiological pH $6.9 \leq \text{pH} \leq 7.4$ and in this range the reactions are balanced in mass and charge.

[a] The proton typically exists as hydronium H_3O^+ in water.

[b] A pK_a value for phosphate is 6.82 so $H_2PO_4^-$ exists at significant concentrations, especially in acidic environments found in cancer cells and in the intermembrane space of most cells, where pH values are low.

reactions have been simplified, especially those that comprise the ETC. It should be noted that all reactions are balanced in mass and charge at physiological pH, $6.6 \leq \text{pH} \leq 7.4$, based on the p$K_a$ values of the molecules.

Glycolysis

These are the ten enzyme-catalysed steps of glycolysis including enzyme commission (EC) numbers. Glycolytic intermediary formulae at physiological pH are given in Table C.2 while other molecules are given in Table C.4.

1. Glucokinase/hexokinase (EC 2.7.1.1/2.7.1.2)

$$\text{G} + \text{ATP} \rightarrow \text{G6P} + \text{ADP} + \text{H}^+ \tag{C.39}$$

2. glucose-6-phosphate isomerase (EC 5.3.1.9)

$$\text{G6P} \rightarrow \text{F6P} \tag{C.40}$$

3. 6-phosphofructokinase (EC 2.7.1.11)

$$\text{F6P} + \text{ATP} \rightarrow \text{FBP} + \text{ADP} + \text{H}^+ \tag{C.41}$$

4. fructose-biphosphate aldolase (EC 4.1.2.13)

$$\text{FBP} \rightarrow \text{G3P} + \text{DHAP} \tag{C.42}$$

5. triosephosphate isomerase (EC 5.3.1.1)

$$\text{DHAP} \rightarrow \text{G3P} \tag{C.43}$$

6. glyceraldehyde-3-phosphate dehydrogenase (EC 1.2.1.12)

$$\text{G3P} + \text{NAD}^+ + \text{P}_\text{i} \rightarrow \text{BPG} + \text{NADH} + \text{H}^+ \tag{C.44}$$

Molecule	Symbol	Formula	Reactions
glucose	G	$C_6H_{12}O_6$	(C.39)
glucose 6-phosphate	G6P	$C_6H_{11}O_9P^{2-}$	(C.39),(C.40)
fructose 6-phosphate	F6P	$C_6H_{11}O_9P^{2-}$	(C.40),(C.41)
fructose-1, 6-biphosphate	FBP	$C_6H_{10}O_{12}P_2^{4-}$	(C.41),(C.42)
glyceraldehyde 3- phosphate	G3P	$C_3H_5O_6P^{2-}$	(C.42),(C.43),(C.44)
dihydroxyacetone phosphate	DHAP	$C_3H_5O_6P^{2-}$	(C.42),(C.43)
1,3-biphosphoglycerate	BPG	$C_3H_4O_{10}P_2^{4-}$	(C.44),(C.45)
3-phosphoglycerate	PG3	$C_3H_4O_7P^{3-}$	(C.45),(C.46)
2-phosphoglycerate	PG2	$C_3H_4O_7P^{3-}$	(C.46),(C.47)
phosphoenolpyruvate	PEP	$C_3H_2O_6P^{3-}$	(C.47),(C.48)
pyruvate	P	$C_3H_3O_3^-$	(C.48)

Table C.2: Molecular formulae for glycolytic intermediaries involved in the metabolic reactions (C.39)–(C.48). Chemical formulas presented are those that predominantly exist at physiological pH 6.6 $\leq$ pH $\leq$ 7.4 based on the pK_a values of the molecules, and in this range the reactions are balanced in mass and charge.

7. phosphoglycerate kinase (EC 2.7.2.3)

$$\mathrm{BPG} + \mathrm{ADP} \rightarrow \mathrm{PG3} + \mathrm{ATP} \tag{C.45}$$

8. phosphoglycerate mutase (EC 5.4.2.11/5.4.2.12)

$$\mathrm{PG3} \rightarrow \mathrm{PG2} \tag{C.46}$$

9. phosphoglycerate enolase (EC 4.2.1.11)

$$\mathrm{PG2} \rightarrow \mathrm{PEP} + \mathrm{H_2O} \tag{C.47}$$

10. pyruvate kinase (EC 2.7.1.40)

$$\mathrm{PEP} + \mathrm{ADP} + \mathrm{H^+} \rightarrow \mathrm{P} + \mathrm{ATP} \tag{C.48}$$

Malate-aspartate shuttle

Most treatments of this shuttle present it as a two-compartment system, but here we will explicitly consider the cytosol, inter membrane space and mitochondrial matrix. While always occurring in the mitochondrial matrix, depending on the source, malate dehydrogenase and aspartate aminotransferase are presented as occurring in either the cytosol or intermembrane space. We will assume malate dehydrogenase is predominantly cytosolic and that aspartate aminotransferase predominantly occurs in the intermembrance space. The former is justified because if this occurred in the intermembrane space it would require the transport of the relatively large coenzyme NADH across the outer mitochondrial membrane rather than import of malate and export oxaloacetate. The latter is less consequential since if aspartate aminotransferase was cystolic it would require the export of two molecules and import of one molecule, however these molecules would all cancel out in either case. Below are the six steps of the malate-aspartate shuttle, responsible for effectively transferring a reduced NADH from the cytosol into the mitochondrion. The formulae for molecules that are also CAC intermediaries are provided in Table C.3, namely, malate (M), oxaloacetate (OAA) and 2-oxoglutarate (α), while those that are not are provided in Table C.4.

1. malate dehydrogenase (cytosol, EC 1.1.1.37)

$$\mathrm{OAA}_c + \mathrm{NADH}_c + \mathrm{H}_c^+ \rightarrow \mathrm{M}_c + \mathrm{NAD}_c^+ \tag{C.49}$$

2. outer mitochondrial membrane transport of malate

$$\mathrm{M}_c \rightarrow \mathrm{M}_i \tag{C.50}$$

3. malate-oxoglutarate antiporter

$$\mathrm{M}_i + \alpha_m \rightarrow \mathrm{M}_m + \alpha_i \tag{C.51}$$

4. malate dehydrogenase (matrix, EC 1.1.1.37)

$$\mathrm{M}_m + \mathrm{NAD}_m^+ \rightarrow \mathrm{OAA}_m + \mathrm{NADH}_m + \mathrm{H}_m^+ \tag{C.52}$$

5. aspartate aminotransferase (matrix, EC 2.6.1.1)

$$\mathrm{OAA}_m + \mathrm{Glut}_m^- \rightarrow \mathrm{Asp}_m + \alpha_m \tag{C.53}$$

6. glutamate-aspartate antiporter

$$\mathrm{Asp}_m + \mathrm{Glut}_i^- \rightarrow \mathrm{Asp}_i + \mathrm{Glut}_m^- \tag{C.54}$$

7. aspartate aminotransferase (intermembrane space, EC 2.6.1.1)

$$\mathrm{Asp}_i + \alpha_i \rightarrow \mathrm{OAA}_i + \mathrm{Glut}_i^- \tag{C.55}$$

8. OAA export

$$\mathrm{OAA}_i \rightarrow \mathrm{OAA}_c \tag{C.56}$$

Citric acid cycle

The ten constituent reactions of the CAC are provided below. The formulae for CAC intermediaries are given in Table C.3 while all others are given in Table C.4.

1. Citrate synthase (EC 2.3.3.1)

$$\mathrm{OAA} + \mathrm{Ac\text{-}CoA} + \mathrm{H_2O} \rightarrow \mathrm{Cit} + \mathrm{CoA} + \mathrm{H^+} \tag{C.57}$$

2. Aconitase hydratase (EC 4.2.1.3)

$$\mathrm{Cit} \rightarrow \mathrm{cis\text{-}Acon} + \mathrm{H_2O} \tag{C.58}$$

$$\mathrm{cis\text{-}Acon} + \mathrm{H_2O} \rightarrow \mathrm{Iso} \tag{C.59}$$

3. Isocitrate dehydrogenase (EC 1.1.1.41)

$$\mathrm{Iso} + \mathrm{NAD^+} \rightarrow \mathrm{OAS} + \mathrm{NADH} + \mathrm{H^+} \tag{C.60}$$

$$\mathrm{OAS} + \mathrm{H^+} \rightarrow \alpha + \mathrm{CO_2} \tag{C.61}$$

Molecule	Symbol	Formula	Reactions
oxaloacetate	OAA	$C_4H_2O_5^{2-}$	(C.49),(C.52),(C.53),(C.55), (C.56),(C.57),(C.66)
citrate	Cit	$C_6H_5O_7^{3-}$	(C.57),(C.58)
cis-aconitate	cis-Acon	$C_6H_3O_6^{3-}$	(C.58),(C.59)
isocitrate	Iso	$C_6H_5O_7^{3-}$	(C.59),(C.60)
oxalosuccinate	OAS	$C_6H_3O_7^{3-}$	(C.60),(C.61)
2-oxoglutarate	α	$C_5H_4O_5^{2-}$	(C.51),(C.53),(C.55),(C.61),(C.62)
succinyl-CoA	s-CoA	CoA-$C_4H_3O_3^{5-}$	(C.62),(C.63)
succinate	Suc	$C_4H_4O_4^{2-}$	(C.63),(C.64)
fumarate	F	$C_4H_2O_4^{2-}$	(C.64),(C.65)
malate	M	$C_4H_4O_5^{2-}$	(C.49),(C.51),(C.52),(C.65),(C.66)

Table C.3: Molecular formulae for citric acid cycle intermediates involved in the metabolic reactions (C.57)–(C.66). Chemical formulas presented are those that predominantly exist at physiological pH $6.6 \leq \text{pH} \leq 7.4$ based on the pK_a values of the molecules, and in this range the reactions are balanced in mass and charge.

4. oxoglutarate dehydrogenase (EC 1.2.4.2)

$$\alpha + \text{NAD}^+ + \text{CoA} \rightarrow \text{S-CoA} + \text{NADH} + \text{CO}_2 \tag{C.62}$$

5. succinyl-CoA synthetase (EC 6.2.1.4)

$$\text{S-CoA} + \text{GDP} + \text{P}_\text{i} \rightarrow \text{Suc} + \text{CoA} + \text{GTP} \tag{C.63}$$

6. succinate dehydrogenase (EC 1.3.5.1)

$$\text{Suc} + \text{Q} \rightarrow \text{F} + \text{QH}_2 \tag{C.64}$$

7. fumarase (EC 4.2.1.2)

$$\text{F} + \text{H}_2\text{O} \rightarrow \text{M} \tag{C.65}$$

8. malate dehydrogenase (EC 1.1.1.37)

$$\text{M} + \text{NAD}^+ \rightarrow \text{OAA} + \text{NADH} + \text{H}^+ \tag{C.66}$$

Nucleoside-diphosphate kinase (NDK, EC 2.7.4.6): Phosphate exchange for conversion of energy output of pathways to ATP yield alone.

$$\mathrm{GTP} + \mathrm{ADP} \rightarrow \mathrm{GDP} + \mathrm{ATP} \tag{C.67}$$

Electron transport chain

The net reactions of the complexes that make up the electron transport chain (ETC) are presented below in a simplified form.

Complex I:

$$\mathrm{NADH} + \mathrm{Q} + 5\mathrm{H}_m^+ \rightarrow \mathrm{NAD}^+ + \mathrm{QH}_2 + 4\mathrm{H}_i^+ \tag{C.68}$$

Complex III:

$$\mathrm{QH}_2 + 2\mathrm{H}_m^+ + 2\mathrm{Cyt}c^{3+} \rightarrow \mathrm{Q} + 4\mathrm{H}_i^+ + 2\mathrm{Cyt}c^{2+} \tag{C.69}$$

Complex IV:

$$2\mathrm{Cyt}c^{2+} + 4\mathrm{H}_m^+ + \frac{1}{2}\mathrm{O}_2 \rightarrow \mathrm{H}_2\mathrm{O} + 2\mathrm{Cyt}c^{3+} + 2\mathrm{H}_i^+ \tag{C.70}$$

Liver functions

Processes that maintain vessel concentrations:

Alanine deamination (alanine to pyruvate): Consumes 4 ATP.

Gluconeogenesis (pyruvate to glucose): Consumes 6 ATP.

C.6 The effect of respiratory ATP yield on the results

The calculations contained in Chapter 5 consider a respiratory ATP yield of 28.9 [20]. This corresponds to the traditional system where ATP yield does not include the costs associated with ATP consumption and phosphate transport. Preliminary considerations, that admittedly use strong assumptions, suggest that the ATP yield may be as low as 24 ATP per glucose molecules. The recalibrated results, using this lower ATP yield, are presented in Figures C.3, C.4, C.5 are analogous to Figures 5.5, 5.6, 5.8. The difference in results is that the contribution of respiratory processes is diminished relative to glycolytic ATP

Molecule	Symbol	Formula	Reactions
Coenzymes			
adenosine monophosphate	AMP	$C_{10}H_{12}N_5O_7P^{2-}$	
adenosine diphosphate	ADP	AMP-PO_3^{3-}	(C.39),(C.41),(C.45), (C.48),(C.67)
adenosine triphosphate	ATP	ADP-PO_3^{4-}	(C.39),(C.41),(C.45), (C.48),(C.67)
nicotinamide adenine dinucleotide	NAD^+	$C_{21}H_{26}N_7O_{14}P_2^-$	(C.44),(C.49),(C.52), (C.60),(C.62),(C.68)
reduced NAD^+	NADH	NAD^+-H^{2-}	(C.44),(C.49),(C.52), (C.60),(C.62),(C.68)
coenzyme Q_{10}	Q	$C_{59}H_{90}O_4$	(C.68),(C.69)
ubiquinol	QH_2	$C_{59}H_{92}O_4$	(C.68),(C.69)
coenzyme A	CoA	$C_{21}H_{32}N_7O_{16}P_3S^{4-}$	(C.57),(C.62),(C.63)
acetyl CoA	Ac-CoA	CoA-$C_2H_2O^{4-}$	(C.57)
guanosine monophosphate	GMP	$C_{10}H_{12}N_5O_8P^{2-}$	
guanosine diphosphate	GDP	GMP-PO_3^{3-}	(C.63),(C.67)
guanosine triphosphate	GTP	GDP-PO_3^{4-}	(C.63),(C.67)
Other molecules			
proton[a]	H^+	H^+	(C.39),(C.41),(C.44), (C.48),(C.49),(C.52), (C.57),(C.60)–(C.61), (C.68)–(C.70)
oxgen	O_2	O_2	(C.70)
water	H_2O	H_2O	(C.47),(C.57),(C.58), (C.59),(C.70)
carbon dioxide	CO_2	CO_2	(C.61),(C.62)
phosphate	P_i	$H_2PO_4^-/HPO_4^{2-}$	(C.44),(C.63)
glutamine	Glut	$C_5H_{10}N_2O_3$	
glutamate	$Glut^-$	$C_5H_8NO_4^-$	(C.53),(C.54),(C.55)
aspartate	Asp	$C_4H_6NO_4^-$	(C.53),(C.54),(C.55)

Table C.4: Molecular formulae for other molecules involved in the metabolic reactions (C.39)–(C.70). Chemical formulas presented are those that predominantly exist at physiological pH $6.6 \leq \text{pH} \leq 7.4$ based on the pK_a values of the molecules, and in this range the reactions are balanced in mass and charge.

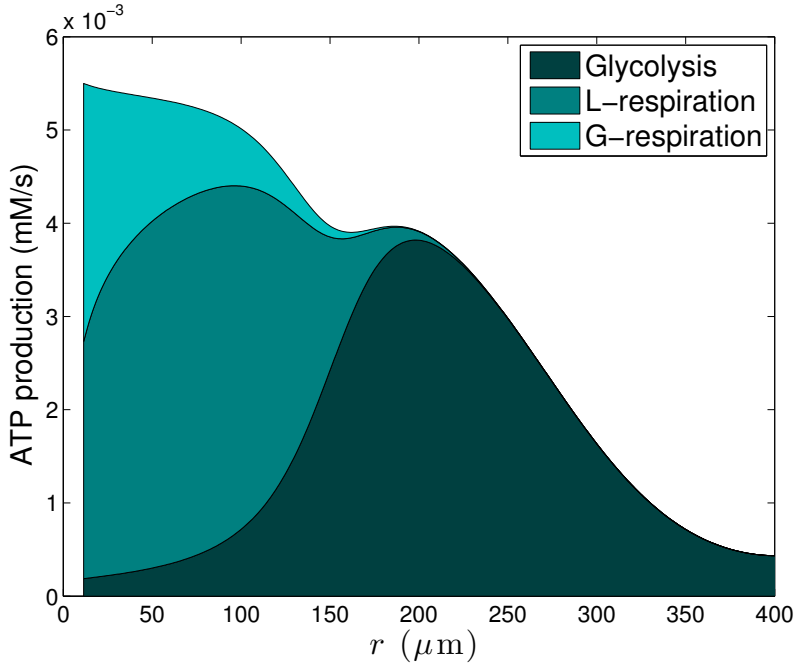

Figure C.3: The base case for ATP turnover (consumption/production) rates corresponding to consumption rates given in Figure 5.4 with altered respiratory ATP parameters. The contributions of the pathways are bounded by the total ATP turnover rate P_{ATP}. Glycolysis dominates in hypoxic/anoxic regions while glucose-fuelled respiration occurs sparingly near the blood vessel. Lactate-fuelled cells are consuming the byproduct of the glycolytic cells where there is oxygen present.

production, and thus the share of the total ATP yield due to oxygen-fuelled metabolism is lessened.

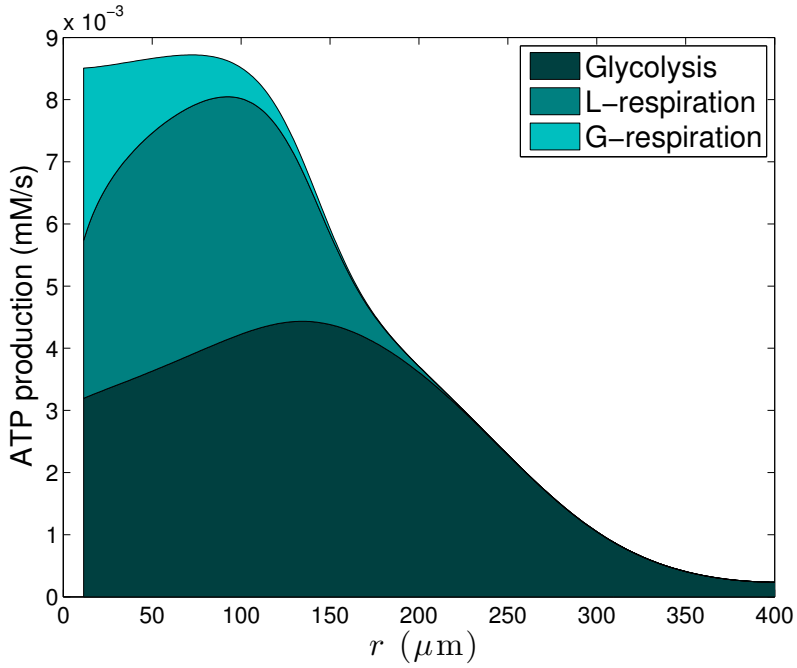

Figure C.4: ATP turnover (consumption/production) rates for cells exhibiting the Warburg effect with altered respiratory ATP parameters (differs from base case because Λ_O decreased from 4000 to 100). The contributions of the pathways are bounded by the total ATP turnover rate P_{ATP}. Glycolysis is dominant in all regions of the tumour. Glucose-fuelled respiration occurs sparingly near the blood vessel. Lactate-fuelled cells are consuming the byproduct of the glycolytic cells where there is oxygen present.

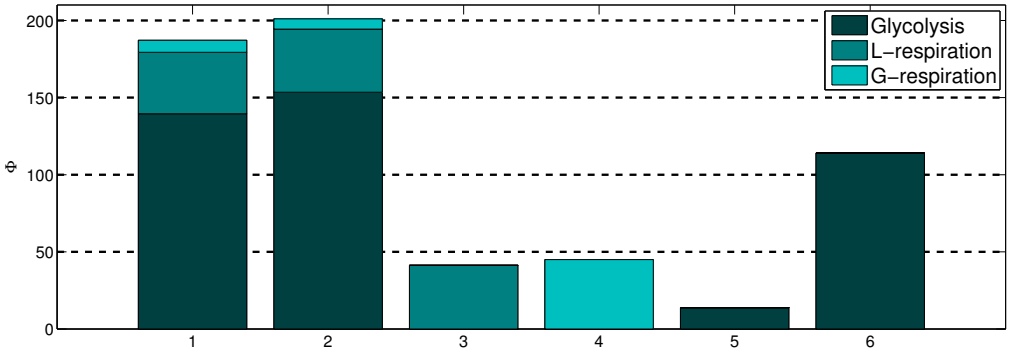

	1. base	2. W	3. Glyc	4. LDH	5. Resp	6. R-W
Λ_O	4000	100	N/A	N/A	4000	100
B_G	1	1	0	0	1	1
B_L	1	1	1	0	0	0
B_O	1	1	0	1	0	0

Figure C.5: The contributions of the pathways are bounded by the total ATP turnover rate Φ in a unit annulus of tissue. This more accurately represents the total contribution of each cell population to metabolism. From left to right the bars denote the following cell populations: 1. **Base case**: Tissue that exhibits lactate consumption in hypoxic conditions with parameters in Table 5.1. 2. **Warburg effect**: Tissue utilizing aerobic glycolysis. 3. **Glycolytic knockdown**: Tissue experiencing complete glycolytic inhibition. 4. **LDH inhibitor**: Tissue experiencing complete LDH inhibition. 5. **Respiration knockdown**: Tissue experiencing mitochondrial inhibition with glycolysis repression by oxygen. 6. **Respiration knockdown and Warburg effect**: Mitochondrial inhibition with aerobic glycolysis. The dashed red line shows a threshold of $\Phi = 100$. If either of the reactions which block glycolysis are knocked out (glycolysis or LDH inhibitors) the total ATP produced is less than half the threshold. If on the other hand respiration is inhibited then either (i) if oxygen represses glycolysis there is minimal ATP production, or (ii) if glycolysis is independent of oxygen concentration there is more ATP produced than the threshold.

Appendix D

Additional nanoparticle release and protein expression work

This appendix serves as supplementary material for Chapter 6. The preliminary nanoparticle release profile fitting with definitions for the goodness of fit measure χ^2 and additional protein expression experiments that went unpublished is outlined here.

D.1 Preliminary nanoparticle models

Preliminary nanoparticle release experiments suggested a biexponential release with decay was an appropriate model. Here we will outline this result while noting that a simpler decay equation was sufficient for fitting in Chapter 6.

For cisplatin released from liposomes, a biexponential release is assumed. Biexponential processes are common in pharmocokinetics to describe various phenomenon (e.g. the clearance of doxorubicin from plasma [192]) where two similar yet separate processes occur with differing rate constants. This biexponential release profile is characterized by an initial burst followed by a slower sustained release. We can motivate the functional form by considering a simple system of ordinary differential equations (ODEs) that includes both the initial rapid release of some cisplatin and the sustained release due to encapsulation in the liposome. To facilitate this, we assume that the administered liposomes consists of cisplatin that is rapidly released at rate r_b and slowly released at rate r_s. The concentrations

of rapidly and slowly released cisplatin are denoted by c_b and c_s respectively, and the liposomes are initially comprised of a fixed amount of quick release and prolonged release given by c_{b0} and c_{s0} respectively (see Figure D.1). For both release processes, only a fraction, ϕ, of the total amount of contained cisplatin is released, an amount that depends primarily on the acidity of the environment. Even in an acidic environment, our data shows that 55% of the cisplatin is never released from the liposome. The total amount of administered cisplatin, denoted c_T, satisfies the relation $c_T = c_{b0} + c_{s0}$ where the total amount of released cisplatin is given by ϕc_T. In addition to the two types of release, we must also consider the natural decay of released cisplatin at a rate d_L. The system of ODEs is then:

$$\frac{dc_b}{dt} = -r_b c_b \tag{D.1}$$

$$\frac{dc_s}{dt} = -r_s c_s \tag{D.2}$$

$$\frac{dc_e}{dt} = r_b c_b + r_s c_s - d_L c_e \tag{D.3}$$

with the solution of interest being the released cisplatin

$$c_e(t) = A_b \exp(-r_b t) + A_f \exp(-r_f t) - (A_b + A_f) exp(-d_L t),$$

where

$$A_b = \frac{\phi c_{b0} r_b}{d_L - r_b}, \qquad A_f = \frac{\phi c_{f0} r_f}{d_L - r_f}.$$

We use equations (D.1)–(D.3) to obtain parameters to describe the release profile data in neutral and acidic environments. The pH-dependent parameters that differ between environments will be the fraction of released cisplatin ϕ and the decay rate of the cisplatin d_L; the release parameters remain constant between both environments. We will quantify the goodness of fit for a model f with p parameters to N observations y_i with the reduced chi-squared statistic $\chi^2_{red} = \chi^2/\nu$, where ν is the degrees of freedom, typically set to $\nu = N - p - 1$ and

$$\chi^2 = \sum_{i=1}^{N} \frac{y_i - f(x_i)}{\sigma_i^2},$$

where σ_i^2 is the variance of the ith observation. It is typically assumed that $\chi^2_{red} < 1$ is overfitting and $\chi^2_{red} > 1$ is an inadequate model with the goal being to get χ^2_{red} as close as possible to one. Fitting the parameters to the release profile data yields a very accurate

Parameter	Units	Fit Value
r_b	h^{-1}	0.5737
r_s	h^{-1}	0.05352
$d_L^{(n)}$	h^{-1}	0.0009932
$d_L^{(a)}$	h^{-1}	0.001703
c_{b0}	μM	0.4099
c_{f0}	μM	0.5901
$\phi^{(n)}$	-	0.2300
$\phi^{(a)}$	-	0.3790

Table D.1: Parameters for the preliminary release profile experiments.

(over)fit as can be seen in Figure D.2 ($\chi^2_{red} = 0.1032$, $N = 18$, $p = 8$). The parameters are given in Table D.1.

It is worth noting that a single exponential fit does not provide an accurate prediction for liposome release in these experiments, although monoexponential fits are commonly sufficient. The model in this case would be (D.1) and $\frac{dc_e}{dt} = r_b c_b - d_L c_e$. Attempting to fit our release profiles with this model leads to fits that overestimate the release at times immediately following the initial burst (e. g. t=6, 7 hours) and then underestimates values for later times, as can be seen in Figure D.3. The reason for this is that the relatively small standard deviations for early times are causing the rate of release to be large enough to fit the burst while driving the decay rate d_L to zero in an attempt to fit the underestimated later time points with larger standard deviations. In fact, setting the value $d_L = 0$ improves the fit slightly with $\chi^2_{red} = 3.799$ ($N = 18$, $p = 5$); this is the result shown in Figure D.3. Allowing the release rate r_b to be locally fitted to each experiment does not improve the fitting statistic ($\chi^2_{red} = 4.1102$, $N = 18$, $p = 6$; results not shown).

D.1.1 Liposomal model

As mentioned in Chapter 6, the unsatisfactory fit in the neutral microenvironment to the final nanoparticle release experiments could be fit by the addition of a single additional parameter accounting for liposomal erosion. The fit to this model is given in Figure D.4 ($\chi^2_{red} = 0.61$, $N = 15$, $p = 3$); this would have negligible effect on the acidic release ($\chi^2_{red} = 0.58$, $N = 15$, $p = 3$).

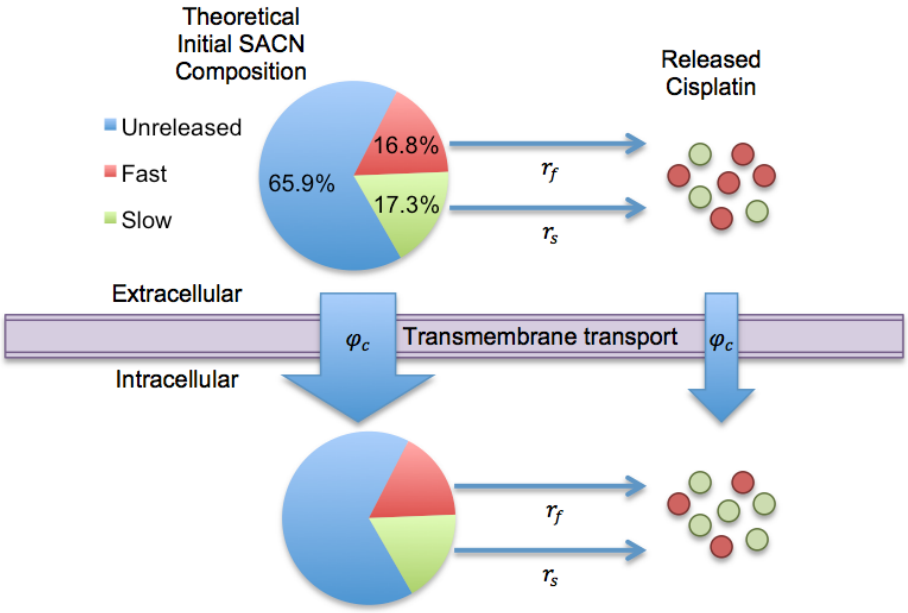

Figure D.1: Depiction of biexponential drug model corresponding to the extension of (D.1)–(D.3) to cellular concentrations for nanoparticle release and delayed transmembrane transport of self-assembling cis-platinum nanoparticles (SACNs) and free cisplatin in an acidic environment.

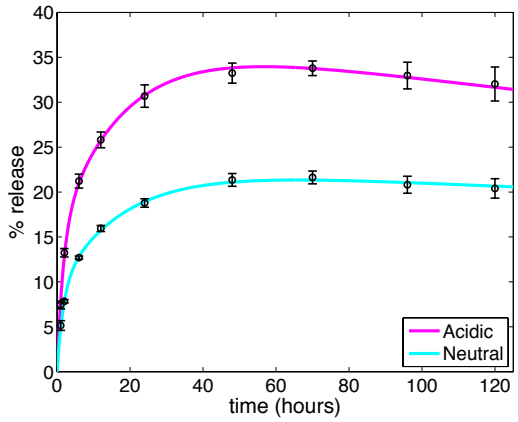

(a) Release profile of cisplatin from liposomes in acidic and neutral environments. For this project, we use the acidic release profile that is typical in the tumour microenvironment.

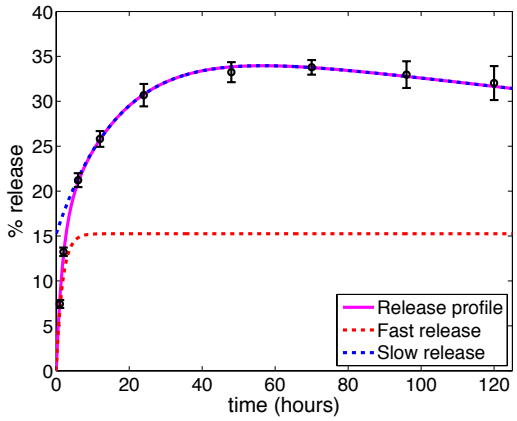

(b) Showing the acidic release profile as a sum of the fast dynamics and slow dynamics of the liposomal release.

Figure D.2: Release profile kinetics.

D.2 Additional protein expression experiments

Initially, the PI828 post-treatment experiment was performed without a control. This data was used in the parameter fitting algorithm but remained unpublished since this experiment with controls is contained in Figure 6.8. The model fit to this data is shown in Figure D.5.

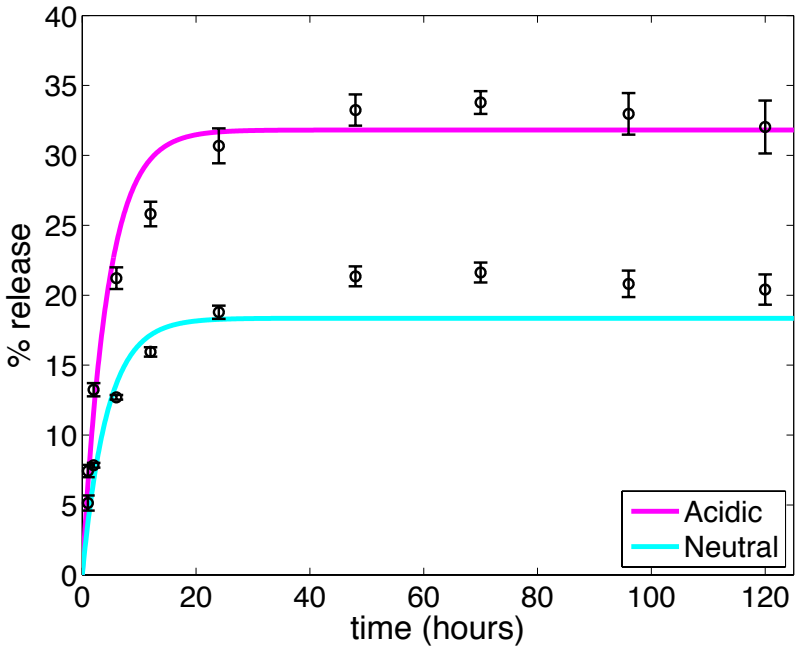

Figure D.3: Attempting to fit the release profile of cisplatin from liposomes in acidic and neutral environments using a single exponential.

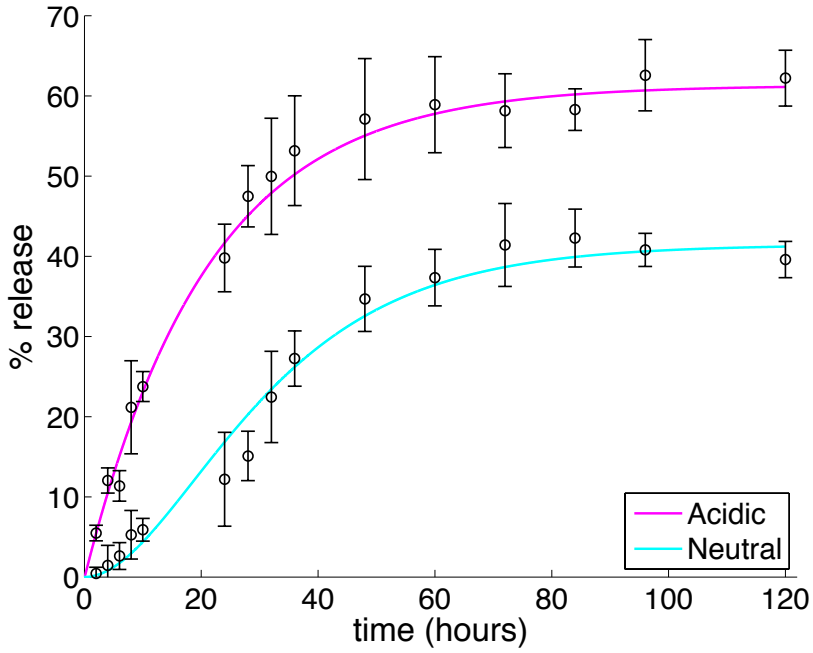

Figure D.4: Fitting the release profile of cisplatin from liposomes in acidic and neutral environments using a liposomal release model.

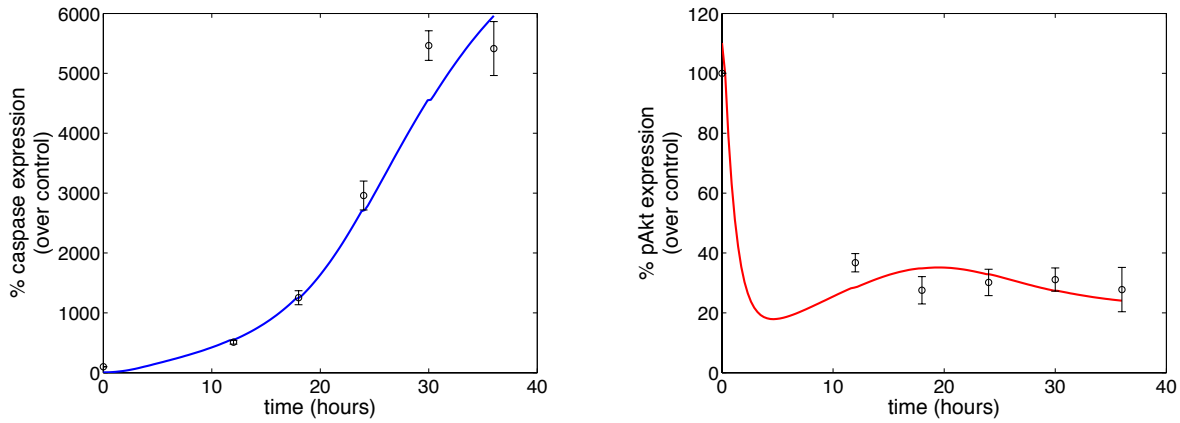

(a) (b)

Figure D.5: The inhibition of pAkt by PI828 post treatment with SACN D.5b and the synergistic increase in caspase expression as compared to SACN alone-treated controls D.5a.

Appendix E

Reactive oxygen species and antioxidant model

A collaborative work that I made both analytical and numerical contributions to, is briefly outlined below with a focus on those aspects which I was directly involved in.

E.1 Introduction

H_2O_2 is produced in eukaryotes during metabolic processes [193, 194] and by other external and internal sources such as growth factors [195, 196]. The concentration level of H_2O_2 plays a role in the initiation progression and treatment efficacy of major diseases such as cancer, diabetes, Alzheimers disease and Parkinsons disease [197, 198, 199, 200, 201, 202, 203]. H_2O_2 is also involved in critical cell signalling processes such as cell growth and apoptosis [204, 205, 206, 207].

H_2O_2 is highly reactive and can directly and indirectly damage cell compartments, hence cells must employ detoxifying mechanisms to remove excess H_2O_2 [208, 209, 210]. One of the principal mechanisms for detoxification is glutathione peroxidase, which along with other detoxifying agents such as catalase remove H_2O_2 [211, 212]. Whether or not these antioxidants work independently or they have evolved symbiotically to assist each other with H_2O_2 detoxification is not clear. To unravel this we derive a relationship between the concentration of H_2O_2, the production rate of H_2O_2 and the concentrations of antioxidants

based on the kinetic equations which govern the detoxification of H_2O_2 by glutathione peroxidase-1 and catalase. We use this relationship to show that catalase and glutathione peroxide-1 behaves in a synergetic way. This synergy could help in understanding many pathological cases, the efficacy of therapies and the design of new drugs or therapies.

E.2 Mathematical model

The three major families of antioxidants that exist in cells, which help to regulate and detoxify H_2O_2, are the glutathione peroxidase family, the peroxiredoxin family and catalase. In our model we assume that catalase and glutathione peroxidases are the major antioxidants in the system to avoid the extraneous complexity of the full problem. We also utilize the fact that glutathione peroxidase-1 is the predominant member of the glutathione peroxidase family in removing H_2O_2 and thus only consider its effect in our model [213]. We also assume that catalase, which is sequestered in the peroxisomes, is exposed to the same concentration levels of H_2O_2. We will discuss the affect of these assumptions in the discussion section and argue that these assumptions do not affect the main conclusion of this paper. We use chemical reaction equations to derive corresponding kinetic equations for the concentrations of involved species and thus obtain a relationship between the concentrations of these species at steady state.

The detoxification of H_2O_2 by catalase is given by the chemical reaction

$$H_2O_2 \xrightarrow{k_{cat}} O_2 + 2H_2O. \tag{E.1}$$

In this process H_2O_2 is converted to harmless oxygen and water in the presence of catalase.

GPx has been the subject of previous mathematical models [214] and its mechanism is well established [215, 216]. The action of these enzymes rely on the presence of a specific cofactor: glutathione (GSH) which is responsible for converting GPx_0 to [GS-GPx] and then [GS-GPx] back to its reduced form GPx_r. These reduced forms can now once again eliminate H_2O_2 from the environment. The generally accepted molecular reactions that occur in the conversion of H_2O_2 to H_2O, in dilute solutions, is represented by the following

three reactions [216]:

$$\mathrm{GPx_r} + \mathrm{H_2O_2} + \mathrm{H^+} \xrightarrow{k_1} \mathrm{GPx_0} + \mathrm{H_2O}, \tag{E.2}$$

$$\mathrm{GPx_0} + \mathrm{GSH} \xrightarrow{k_2} [\mathrm{GS\text{-}GPx}] + \mathrm{H_2O}, \tag{E.3}$$

$$[\mathrm{GS\text{-}GPx}] + \mathrm{GSH} \xrightarrow{k_3} \mathrm{GPx_r} + \mathrm{GSSG} + \mathrm{H^+}, \tag{E.4}$$

where k_1, k_2 and k_3 are the reaction rates calculated by Antunes et al. [215] and given in Table E.1. These reactions are commonly summarized as

$$\mathrm{H_2O_2} + 2\mathrm{GSH} \xrightarrow{\mathrm{GPx}} \mathrm{GSSG} + 2\mathrm{H_2O}. \tag{E.5}$$

Table E.1: Rate constants for the GPx system from [215].

Rate	$(\mu\mathrm{M}^{-1}\mathrm{s}^{-1})$
k_1	21
k_2	0.04
k_3	10

We will now write down a system of equations that correspond to the reactions (E.1)–(E.4). An equation that tracks $\mathrm{H^+}$ and $\mathrm{H_2O}$ concentrations are not included, under the assumption that reactions are independent of pH and water content. The two major assumptions are: (i) spatial independence, this leads to a system of ODEs, and (ii) the concentration of catalase remains constant. We will denote this constant catalase concentration by C. Letting $x_1 = [\mathrm{GPx_r}]$, $x_2 = [\mathrm{GPx_0}]$, $x_3 = [[\mathrm{GS\text{-}GPx}]]$ denote the concentrations of GPx and its intermediate forms during recycling, $x_4 = [\mathrm{H_2O_2}]$ the concentration

of hydrogen peroxide, and $x_5 = [\text{GSH}]$ gives the following system of ODEs:

$$\dot{x_1} = k_3 x_3 x_5 - k_1 x_1 x_4, \tag{E.6}$$
$$\dot{x_2} = k_1 x_1 x_4 - k_2 x_2 x_5, \tag{E.7}$$
$$\dot{x_3} = k_2 x_2 x_5 - k_3 x_3 x_5, \tag{E.8}$$
$$\dot{x_4} = -k_1 x_1 x_4 - k_{cat} C x_4 + p_4, \tag{E.9}$$
$$\dot{x_5} = -k_3 x_3 x_5 - k_2 x_2 x_5 + p_5, \tag{E.10}$$
$$\tag{E.11}$$

where p_4 and p_5 are the constant production rates of H_2O_2 and GSH respectively. Note than an equation for GSSG is omitted since it only plays the role of a waste product.

We are interested in finding the steady state solution to (E.6)–(E.10) and will now derive the concentration of H_2O_2 as a function of x_1, x_2, x_5 and C. Equations (E.6)–(E.8) sum to zero, so the total concentration of GPx is fixed at some total value e_T satisfying $x_1 + x_2 + x_3 = e_T$. This relationship is only valid because there are no sources or sinks more any of these species. Furthermore, the concentration of [GS-GPx] is negligible since $k_2 \ll k_1$ and $k_2 \ll k_3$, so we will use the approximation $x_1 + x_2 = e_T$. Using these assumptions, the steady state concentrations can be found, or we could look at temporal behaviour.

E.3 Results

I have analyzed the aforementioned system in multiple scenarios. Along with performing numerical analytical analysis of this system, I have also proven stability results. We have also used the model to quantify the synergy between catalase and glutathione-peroxidase-1 which amplifies the detoxification power of glutathione peroxidase-1. Hence any change (upregulation or downregulation) in the catalase concentration has a direct affect on the glutathione peroxidase-1 activity and has to be included in understanding any related phenomena. Also we propose that the activity of glutathione peroxidase-1 could be regulated by changing the concentration of catalase. The synergistic relationship between these antioxidants is reported in [174]. This work was expanded to include the effects of cell permeability, especially the role of aquaporin expression. This has important consequences for the efficacy of ascorbic acid for cancer treatment [175]. While I was involved in model

development and calculating system solutions, I am not the first author of these results, so they are omitted.

References

[1] S. Ramanujan, G. C. Koenig, T. P. Padera, B. R. Stoll, and R. K. Jain, "Local imbalance of proangiogenic and antiangiogenic factors: a potential mechanism of focal necrosis and dormancy in tumors," *Cancer Res.*, vol. 60, pp. 1442–1448, 2000.

[2] R. K. Jain, R. T. Tong, and L. L. Munn, "Effect of vascular normalization by antiangiogenic therapy on interstitial hypertension, peritumor edema, and lymphatic metastasis: insights from a mathematical model," *Cancer Res.*, vol. 67, pp. 2729–2735, 2007.

[3] J. J. Casciari, S. V. Sotirchos, and R. M. Sutherland, "Mathematical modelling of microenvironment and growth in EMT6/Ro multicellular tumour spheroids," *Cell Prolif.*, vol. 25, pp. 1–22, 1992.

[4] J. J. Casciari, S. V. Sotirchos, and R. M. Sutherland, "Variations in tumor cell growth rates and metabolism with oxygen concentration, glucose concentration, and extracellular pH," *J. Cell. Physiol.*, vol. 151, pp. 386–394, 1992.

[5] G. Helmlinger, F. Yuan, M. Dellian, and R. K. Jain, "Interstitial pH and pO_2 gradients in solid tumors in vivo: high-resolution measurements reveal a lack of correlation," *Nat. Med.*, vol. 3, pp. 177–182, Feb 1997.

[6] R. A. Gatenby and P. K. Maini, "Mathematical oncology: cancer summed up," *Nature*, vol. 421, no. 6921, pp. 321–321, 2003.

[7] A. R. Anderson and V. Quaranta, "Integrative mathematical oncology," *Nature Reviews Cancer*, vol. 8, no. 3, pp. 227–234, 2008.

[8] A. Pandey, A. Kulkarni, B. Roy, A. Goldman, S. Sarangi, P. Sengupta, C. Phipps, J. Kopparam, M. Oh, S. Basu, *et al.*, "Sequential application of a cytotoxic nanoparticle and a PI3K inhibitor enhances antitumor efficacy," *Cancer research*, 2013.

[9] N. Bellomo, N. Li, and P. K. Maini, "On the foundations of cancer modelling: selected topics, speculations, and perspectives," *Mathematical Models and Methods in Applied Sciences*, vol. 18, no. 04, pp. 593–646, 2008.

[10] T. S. Deisboeck, Z. Wang, P. Macklin, and V. Cristini, "Multiscale cancer modeling," *Annual review of biomedical engineering*, vol. 13, 2011.

[11] T. Roose, S. J. Chapman, and P. K. Maini, "Mathematical models of avascular tumor growth," *Siam Review*, vol. 49, no. 2, pp. 179–208, 2007.

[12] B. Ribba, T. Alarcón, K. Marron, P. K. Maini, and Z. Agur, "The use of hybrid cellular automaton models for improving cancer therapy," in *Cellular Automata*, pp. 444–453, Springer, 2004.

[13] J. Ferlay, H.-R. Shin, F. Bray, D. Forman, C. Mathers, and D. M. Parkin, "Estimates of worldwide burden of cancer in 2008: GLOBOCAN 2008," *International journal of cancer*, vol. 127, no. 12, pp. 2893–2917, 2010.

[14] L. Kachuri, P. De, L. Ellison, and R. Semenciw, "Cancer incidence, mortality and survival trends in Canada, 1970–2007," *Chronic diseases and injuries in Canada*, vol. 33, no. 2, pp. 69–80, 2013.

[15] D. Hanahan and R. A. Weinberg, "The hallmarks of cancer," *Cell*, vol. 100, pp. 57–70, 2000.

[16] J. Folkman, "Tumor angiogenesis: therapeutic implications," *N. Engl. J. Med.*, vol. 285, pp. 1182–1186, 1971.

[17] D. Hanahan and R. A. Weinberg, "Hallmarks of cancer: The next generation," *Cell*, vol. 144, no. 5, pp. 646 – 674, 2011.

[18] D. Hanahan and J. Folkman, "Patterns and emerging mechanisms of the angiogenic switch during tumorigenesis," *Cell*, vol. 86, pp. 353–364, 1996.

[19] R. K. Jain, "Transport of molecules across tumor vasculature," *Cancer Metastasis Rev.*, vol. 6, pp. 559–593, 1987.

[20] M. D. Brand, "The efficiency and plasticity of mitochondrial energy transduction," *Biochemical Society Transactions*, vol. 33, no. 5, pp. 897–904, 2005.

[21] P. R. Rich, "The molecular machinery of Keilin's respiratory chain," *Biochemical Society Transactions*, vol. 31, no. 6, pp. 1095–1106, 2003.

[22] O. Warburg, "On the origin of cancer cells," *Science*, vol. 123, pp. 309–314, 1956.

[23] M. G. Vander Heiden, L. C. Cantley, and C. B. Thompson, "Understanding the Warburg effect: the metabolic requirements of cell proliferation," *science*, vol. 324, no. 5930, pp. 1029–1033, 2009.

[24] K. Smallbone, D. J. Gavaghan, R. A. Gatenby, and P. K. Maini, "The role of acidity in solid tumour growth and invasion," *Journal of Theoretical Biology*, vol. 235, no. 4, pp. 476–484, 2005.

[25] H. R. Molavian, M. Kohandel, M. Milosevic, and S. Sivaloganathan, "Fingerprint of cell metabolism in the experimentally observed interstitial pH and pO_2 in solid tumors," *Cancer Res.*, vol. 69, pp. 9141–9147, 2009.

[26] L. A. Sauer, J. W. Stayman, and R. T. Dauchy, "Amino acid, glucose, and lactic acid utilization in vivo by rat tumors," *Cancer research*, vol. 42, no. 10, pp. 4090–4097, 1982.

[27] P. Sonveaux, F. Végran, T. Schroeder, M. C. Wergin, J. Verrax, Z. N. Rabbani, C. J. De Saedeleer, K. M. Kennedy, C. Diepart, B. F. Jordan, *et al.*, "Targeting lactate-fueled respiration selectively kills hypoxic tumor cells in mice," *The Journal of clinical investigation*, vol. 118, no. 12, p. 3930, 2008.

[28] A. Di Marco, M. Gaetani, and B. Scarpinato, "Adriamycin (NSC-123,127): a new antibiotic with antitumor activity.," *Cancer chemotherapy reports. Part 1*, vol. 53, no. 1, p. 33, 1969.

[29] B. Rosenberg and L. Vancamp, "Platinum compounds: a new class of potent anti-tumour agents," *Nature*, vol. 222, pp. 385–386, 1969.

[30] A. Lorch, A. Kleinhans, A. Kramar, C. K. Kollmannsberger, J. T. Hartmann, C. Bokemeyer, O. Rick, and J. Beyer, "Sequential versus single high-dose chemotherapy in patients with relapsed or refractory germ cell tumors: long-term results of a

prospective randomized trial," *Journal of Clinical Oncology*, vol. 30, no. 8, pp. 800–805, 2012.

[31] A. Ardizzoni, L. Boni, M. Tiseo, F. V. Fossella, J. H. Schiller, M. Paesmans, D. Radosavljevic, A. Paccagnella, P. Zatloukal, P. Mazzanti, *et al.*, "Cisplatin-versus carboplatin-based chemotherapy in first-line treatment of advanced non–small-cell lung cancer: an individual patient data meta-analysis," *Journal of the National Cancer Institute*, vol. 99, no. 11, pp. 847–857, 2007.

[32] B. Sirohi, M. Arnedos, S. Popat, S. Ashley, A. Nerurkar, G. Walsh, S. Johnston, and I. Smith, "Platinum-based chemotherapy in triple-negative breast cancer," *Annals of oncology*, vol. 19, no. 11, pp. 1847–1852, 2008.

[33] G. M. Tozer, "Measuring tumour vascular response to antivascular and antiangiogenic drugs," *Br. J. Radiol.*, vol. 76 Spec No 1, pp. 23–35, 2003.

[34] A. A. Van der Veldt, M. Lubberink, I. Bahce, M. Walraven, M. P. de Boer, H. N. Greuter, N. H. Hendrikse, J. Eriksson, A. D. Windhorst, P. E. Postmus, *et al.*, "Rapid decrease in delivery of chemotherapy to tumors after anti-VEGF therapy: implications for scheduling of anti-angiogenic drugs," *Cancer cell*, vol. 21, no. 1, pp. 82–91, 2012.

[35] R. K. Jain, "Normalization of tumor vasculature: an emerging concept in antiangiogenic treatment," *Science*, vol. 307, pp. 58–62, 2005.

[36] T. T. Batchelor, A. G. Sorensen, E. di Tomaso, W.-T. Zhang, D. G. Duda, K. S. Cohen, K. R. Kozak, D. P. Cahill, P.-J. Chen, M. Zhu, *et al.*, "AZD2171, a pan-VEGF receptor tyrosine kinase inhibitor, normalizes tumor vasculature and alleviates edema in glioblastoma patients," *Cancer cell*, vol. 11, no. 1, pp. 83–95, 2007.

[37] J. Folkman, "Angiogenesis and apoptosis," *Seminars in Cancer Biology*, vol. 13, no. 2, pp. 159 – 167, 2003.

[38] G. M. Tozer, C. Kanthou, C. S. Parkins, and S. A. Hill, "The biology of the combretastatins as tumour vascular targeting agents," *Int. J. Exp. Pathol.*, vol. 83, pp. 21–38, 2002.

[39] H. Hurwitz, L. Fehrenbacher, W. Novotny, T. Cartwright, J. Hainsworth, W. Heim, J. Berlin, A. Baron, S. Griffing, E. Holmgren, N. Ferrara, G. Fyfe, B. Rogers, R. Ross,

and F. Kabbinavar, "Bevacizumab plus irinotecan, fluorouracil, and leucovorin for metastatic colorectal cancer," *N. Engl. J. Med.*, vol. 350, no. 23, pp. 2335–2342, 2004.

[40] A. Sandler, R. Gray, M. C. Perry, J. Brahmer, J. H. Schiller, A. Dowlati, R. Lilenbaum, and D. H. Johnson, "Paclitaxel–carboplatin alone or with bevacizumab for non–small-cell lung cancer," *New England Journal of Medicine*, vol. 355, no. 24, pp. 2542–2550, 2006.

[41] F. M. Gabhann and A. S. Popel, "Targeting neuropilin-1 to inhibit VEGF signaling in cancer; comparison of therapeutic approaches," *PLoS Comput. Biol.*, vol. 2, 2006.

[42] S. Wu and R. Singh, "Resistance to chemotherapy and molecularly targeted therapies: rationale for combination therapy in malignant melanoma," *Current molecular medicine*, vol. 11, no. 7, pp. 553–563, 2011.

[43] L. L. Belyanskaya, S. Hopkins-Donaldson, S. Kurtz, A. P. Simões-Wüst, S. Yousefi, H.-U. Simon, R. Stahel, and U. Zangemeister-Wittke, "Cisplatin activates Akt in small cell lung cancer cells and attenuates apoptosis by survivin upregulation," *International journal of cancer*, vol. 117, no. 5, pp. 755–763, 2005.

[44] A. V. Rao, G. Akabani, and D. A. Rizzieri, "Radioimmunotherapy for non-Hodgkin's lymphoma," *Clin. Med. Res.*, vol. 3, pp. 157–165, 2005.

[45] S. M. Moghimi, A. C. Hunter, and J. C. Murray, "Long-circulating and target-specific nanoparticles: theory to practice," *Pharmacol. Rev.*, vol. 53, pp. 283–318, 2001.

[46] Y. Matsamura and H. Maeda, "A new concept for macromolecular therapeutics in cancer chemotherapy: mechanisms of tumoritropic accumulation of protein and the antitumor agent smancs," *Cancer Res.*, vol. 46, pp. 6387–6392, 1986.

[47] J. Fang, H. Nakamura, and H. Maeda, "The EPR effect: unique features of tumor blood vessels for drug delivery, factors involved, and limitations and augmentation of the effect," *Advanced drug delivery reviews*, vol. 63, no. 3, pp. 136–151, 2011.

[48] Y. Lu and P. S. Low, "Folate-mediated delivery of macromolecular anticancer therapeutic agents," *Adv. Drug Deliv. Rev.*, vol. 54, pp. 675–693, 2002.

[49] J. F. Ross, P. K. Chaudhuri, and M. Ratnam, "Differential regulation of folate receptor isoforms in normal and malignant tissues in vivo and in established cell lines. Physiologic and clinical implications," *Cancer*, vol. 73, pp. 2432–2443, 1994.

[50] R. J. Lee and P. S. Low, "Folate-mediated tumor cell targeting of liposome-entrapped doxorubicin in vitro," *Biochim. Biophys. Acta*, vol. 1233, pp. 134–144, 1995.

[51] J. Sudimack and R. J. Lee, "Targeted drug delivery via the folate receptor," *Adv. Drug Deliv. Rev.*, vol. 41, pp. 147–162, 2000.

[52] P. C. Brooks, A. M. Montgomery, M. Rosenfeld, R. A. Reisfeld, T. Hu, G. Klier, and D. A. Cheresh, "Integrin $\alpha_v\beta_3$ antagonists promote tumor regression by inducing apoptosis of angiogenic blood vessels," *Cell*, vol. 79, pp. 1157–1164, 1994.

[53] S. Sengupta, D. Eavarone, I. Capila, G. Zhao, N. Watson, T. Kiziltepe, and R. Sasisekharan, "Temporal targeting of tumour cells and neovasculature with a nanoscale delivery system," *Nature*, vol. 436, pp. 568–572, 2005.

[54] S. Awasthi, "A dendrimer-based prodrug for use in an anti-cancer nanocell," Master's thesis, Massachusetts Institute of Technology, 2007.

[55] M. Kohandel, C. A. Haselwandter, M. Kardar, S. Sengupta, and S. Sivaloganathan, "Quantitative model for efficient temporal targeting of tumor cells and neovasculature," *Computational and Mathematical Methods in Medicine*, vol. 2011, 2011.

[56] D. Hanahan, G. Bergers, and E. Bergsland, "Less is more, regularly: metronomic dosing of cytotoxic drugs can target tumor angiogenesis in mice," *J. Clin. Invest.*, vol. 105, pp. 1045–1047, 2000.

[57] R. S. Kerbel and B. A. Kamen, "The anti-angiogenic basis of metronomic chemotherapy," *Cancer Rev.*, vol. 4, pp. 423–436, 2004.

[58] S. Man, G. Bocci, G. Francia, S. K. Green, S. Jothy, D. Hanahan, P. Bohlen, D. J. Hicklin, G. Bergers, and R. S. Kerbel, "Antitumor effects in mice of low-dose (metronomic) cyclophosphamide administered continuously through the drinking water," *Cancer Research*, vol. 62, pp. 2731–2735, 2002.

[59] C. Phipps, "Combination of chemotherapy and anitangiogenic therapies: A mathematical modelling approach," Master's thesis, University of Waterloo, 2010.

[60] T. Alarcón, H. M. Byrne, and P. K. Maini, "A cellular automaton model for tumour growth in inhomogeneous environment," *Journal of Theoretical Biology*, vol. 225, no. 2, pp. 257–274, 2003.

[61] K. Smallbone, R. A. Gatenby, R. J. Gillies, P. K. Maini, and D. J. Gavaghan, "Metabolic changes during carcinogenesis: potential impact on invasiveness," *Journal of Theoretical Biology*, vol. 244, no. 4, pp. 703–713, 2007.

[62] R. K. Jain and L. T. Baxter, "Mechanisms of heterogeneous distribution of monoclonal antibodies and other macromolecules in tumors: Significance of elevated interstitial pressure," *Cancer Res.*, vol. 48, pp. 7022–7032, 1988.

[63] A. Bertuzzi, A. Fasano, A. Gandolfi, and C. Sinisgalli, "ATP production and necrosis formation in a tumour spheroid model," *Math. Model. Nat. Phenom*, vol. 2, no. 3, pp. 30–46, 2007.

[64] K. L. Kiran, D. Jayachandran, and S. Lakshminarayanan, "Mathematical modelling of avascular tumour growth based on diffusion of nutrients and its validation," *The Canadian Journal of Chemical Engineering*, vol. 87, no. 5, pp. 732–740, 2009.

[65] R. Venkatasubramanian, M. A. Henson, and N. S. Forbes, "Incorporating energy metabolism into a growth model of multicellular tumor spheroids," *Journal of theoretical biology*, vol. 242, no. 2, pp. 440–453, 2006.

[66] R. K. Jain, "Transport of molecules in the tumor interstitium: a review," *Cancer Res.*, vol. 47, pp. 3039–3051, 1987.

[67] L. T. Baxter and R. K. Jain, "Transport of fluid and macromolecules in tumors. I. Role of interstitial pressure and convection," *Microvasc. Res.*, vol. 37, pp. 77–104, 1989.

[68] L. T. Baxter and R. K. Jain, "Transport of fluid and macromolecules in tumors. II. Role of heterogeneous perfusion and lymphatics," *Microvasc. Res.*, vol. 40, pp. 246–263, 1990.

[69] L. T. Baxter and R. K. Jain, "Transport of fluid and macromolecules in tumors. III. Role of binding and metabolism," *Microvasc. Res.*, vol. 41, pp. 5–23, 1991.

[70] L. T. Baxter and R. K. Jain, "Transport of fluid and macromolecules in tumors. IV. A microscopic model of the perivascular distribution," *Microvasc. Res.*, vol. 41, pp. 252–272, 1991.

[71] P. A. Netti, L. T. Baxter, Y. Boucher, R. Skalak, and R. K. Jain, "Macro- and microscopic fluid transport in living tissues: Application to solid tumors," *AIChE Journal*, vol. 43, no. 3, pp. 818–834, 1997.

[72] S. Whitaker, "Flow in porous media I: A theoretical derivation of Darcy's law," *Transport in porous media*, vol. 1, no. 1, pp. 3–25, 1986.

[73] C. Breward, H. Byrne, and C. Lewis, "The role of cell-cell interactions in a two-phase model for avascular tumour growth," *Journal of Mathematical Biology*, vol. 45, no. 2, pp. 125–152, 2002.

[74] C. J. Breward, H. M. Byrne, and C. E. Lewis, "A multiphase model describing vascular tumour growth," *Bulletin of mathematical biology*, vol. 65, no. 4, pp. 609–640, 2003.

[75] E. A. Swabb, J. Wei, and P. M. Gullino, "Diffusion and convection in normal and neoplastic tissues," *Cancer Res.*, vol. 34, pp. 2814–2822, 1974.

[76] E. H. Starling, "The influence of mechanical factors on lymph production," *The Journal of physiology*, vol. 16, no. 3-4, p. 224, 1894.

[77] O. t. Kedem and A. Katchalsky, "Thermodynamic analysis of the permeability of biological membranes to non-electrolytes," *Biochimica et biophysica Acta*, vol. 27, pp. 229–246, 1958.

[78] P. Hahnfeldt, D. Panigrahy, J. Folkman, and L. Hlatky, "Tumor development under angiogenic signaling: A dynamical theory of tumor growth, treatment response and postvascular dormancy," *Cancer Res.*, vol. 59, pp. 4770–4775, 1999.

[79] Y. Boucher, L. T. Baxter, and R. K. Jain, "Interstitial pressure gradients in tissue-isolated and subcutaneous tumors: implications for therapy," *Cancer research*, vol. 50, no. 15, pp. 4478–4484, 1990.

[80] C. S. Patlak, D. A. Goldstein, and J. F. Hoffman, "The flow of solute and solvent across a two-membrane system," *J. Theor. Biol.*, vol. 5, pp. 426–442, 1963.

[81] C. Phipps and M. Kohandel, "The effect of interstitial fluid pressure on angiogenic behavior in solid tumors," *Computational and Mathematical Methods in Medicine*, vol. 2011, 2011.

[82] B. R. Stoll, C. Migliorini, A. Kadambi, L. L. Munn, and R. K. Jain, "A mathematical model of the contribution of endothelial progenitor cells to angiogenesis in tumors: implications for antiangiogenic therapy," *Blood*, vol. 102, pp. 2555–2561, 2003.

[83] J. R. Griffiths, D. J. McIntyre, F. A. Howe, and M. Stubbs, "Why are cancers acidic? A carrier-mediated diffusion model for H^+ transport in the interstitial fluid," *Novartis Found. Symp.*, vol. 240, pp. 46–62, 2001.

[84] L. C. Garg and T. H. Maren, "The rates of hydration of carbon dioxide and dehydration of carbonic acid at 37," *Biochimica et Biophysica Acta (BBA)-General Subjects*, vol. 261, no. 1, pp. 70–76, 1972.

[85] J. P. Kirkpatrick, D. M. Brizel, and M. W. Dewhirst, "A mathematical model of tumor oxygen and glucose mass transport and metabolism with complex reaction kinetics," *Radiat. Res.*, vol. 159, pp. 336–344, 2003.

[86] A. Krogh, "The number and distribution of capillaries in muscles with calculations of the oxygen pressure head necessary for supplying the tissue," *The Journal of physiology*, vol. 52, no. 6, pp. 409–415, 1919.

[87] J. J. Blum, "Concentration profiles in and around capillaries," *American Journal of Physiology–Legacy Content*, vol. 198, no. 5, pp. 991–998, 1960.

[88] E. P. Salathé and T.-C. Wang, "Substrate concentrations in tissue surrounding single capillaries," *Mathematical Biosciences*, vol. 49, no. 3, pp. 235–247, 1980.

[89] A. Bertuzzi, A. Fasano, A. Gandolfi, and C. Sinisgalli, "Necrotic core in EMT6/Ro tumour spheroids: Is it caused by an ATP deficit?," *Journal of theoretical biology*, vol. 262, no. 1, pp. 142–150, 2010.

[90] B. Mendoza-Juez, A. Martínez-González, G. F. Calvo, and V. M. Pérez-García, "A mathematical model for the glucose-lactate metabolism of in vitro cancer cells," *Bulletin of mathematical biology*, pp. 1–18, 2012.

[91] R. E. Zeebe, "On the molecular diffusion coefficients of dissolved CO_2, HCO_3^-, CO_3^{2-} and and their dependence on isotopic mass," *Geochimica et Cosmochimica Acta*, vol. 75, no. 9, pp. 2483–2498, 2011.

[92] A. Tamimi, E. B. Rinker, and O. C. Sandall, "Diffusion coefficients for hydrogen sulfide, carbon dioxide, and nitrous oxide in water over the temperature range 293-368 K," *Journal of Chemical and Engineering Data*, vol. 39, no. 2, pp. 330–332, 1994.

[93] D. M. Himmelblau, "Diffusion of dissolved gases in liquids," *Chemical Reviews*, vol. 64, no. 5, pp. 527–550, 1964.

[94] K. Kigoshi and T. Hashitani, "The self-diffusion coefficients of carbon dioxide, hydrogen carbonate ions and carbonate ions in aqueous solutions," *Bulletin of the Chemical Society of Japan*, vol. 36, no. 10, pp. 1372–1372, 1963.

[95] L. Yuan-Hui and S. Gregory, "Diffusion of ions in sea water and in deep-sea sediments," *Geochimica et cosmochimica acta*, vol. 38, no. 5, pp. 703–714, 1974.

[96] S. A. Feig, G. S. Shaber, G. F. Schwartz, A. Patchefsky, H. I. Libshitz, J. Edeiken, R. Nerlinger, R. F. Curley, and J. D. Wallace, "Thermography, mammography, and clinical examination in breast cancer screening review of 16,000 studies," *Radiology*, vol. 122, no. 1, pp. 123–127, 1977.

[97] Q. Zhao, J. Zhang, R. Wang, and W. Cong, "Use of a thermocouple for malignant tumor detection," *Engineering in Medicine and Biology Magazine, IEEE*, vol. 27, no. 1, pp. 64–66, 2008.

[98] A. C. F. Ribeiro, O. Ortona, S. M. N. Simoes, C. I. A. V. Santos, P. M. R. A. Prazeres, A. J. M. Valente, V. M. M. Lobo, and H. D. Burrows, "Binary mutual diffusion coefficients of aqueous solutions of sucrose, lactose, glucose, and fructose in the temperature range from (298.15 to 328.15) K," *Journal of Chemical & Engineering Data*, vol. 51, no. 5, pp. 1836–1840, 2006.

[99] C. K. N. Li, "The glucose distribution in 9l rat brain multicell tumor spheroids and its effect on cell necrosis," *Cancer*, vol. 50, no. 10, pp. 2066–2073, 1982.

[100] L. Hlatky, R. K. Sachs, and E. L. Alpen, "Joint oxygen-glucose deprivation as the cause of necrosis in a tumor analog," *Journal of cellular physiology*, vol. 134, no. 2, pp. 167–178, 1988.

[101] L. A. M. Van der Wielen, M. Zomerdijk, J. Houwers, and K. Luyben, "Diffusivities of organic electrolytes in water," *Chemical Engineering Journal*, vol. 66, no. 2, pp. 111–121, 1997.

[102] K. Groebe and W. Mueller-Klieser, "Distributions of oxygen, nutrient, and metabolic waste concentrations in multicellular spheroids and their dependence on spheroid parameters," *European biophysics journal*, vol. 19, no. 4, pp. 169–181, 1991.

[103] R. T. Ferrell and D. M. Himmelblau, "Diffusion coefficients of nitrogen and oxygen in water," *Journal of Chemical and Engineering Data*, vol. 12, no. 1, pp. 111–115, 1967.

[104] J. Freyer and R. Sutherland, "Determination of diffusion constants for metabolites in multicell tumor spheroids," in *Oxygen Transport to TissueIV*, pp. 463–475, Springer, 1983.

[105] J. J. Casciari, S. V. Sotirchos, and R. M. Sutherland, "Glucose diffusivity in multicellular tumor spheroids," *Cancer research*, vol. 48, no. 14, pp. 3905–3909, 1988.

[106] C. Kelly, K. Smallbone, and M. Brady, "Tumour glycolysis: the many faces of HIF," *Journal of theoretical biology*, vol. 254, no. 2, pp. 508–513, 2008.

[107] Y. Jiang, J. Pjesivac-Grbovic, C. Cantrell, and J. P. Freyer, "A multiscale model for avascular tumor growth," *Biophysical journal*, vol. 89, no. 6, pp. 3884–3894, 2005.

[108] G. Schaller and M. Meyer-Hermann, "Multicellular tumor spheroid in an off-lattice Voronoi-Delaunay cell model," *Physical Review E*, vol. 71, no. 5, p. 051910, 2005.

[109] G. Schaller and M. Meyer-Hermann, "Continuum versus discrete model: a comparison for multicellular tumour spheroids," *Philosophical Transactions of the Royal Society A: Mathematical, Physical and Engineering Sciences*, vol. 364, no. 1843, pp. 1443–1464, 2006.

[110] J. Pfeuffer, I. Tkáč, and R. Gruetter, "Extracellular-intracellular distribution of glucose and lactate in the rat brain assessed noninvasively by diffusion-weighted 1H

nuclear magnetic resonance spectroscopy in vivo," *Journal of Cerebral Blood Flow & Metabolism*, vol. 20, no. 4, pp. 736–746, 2000.

[111] K. Groebe, S. Erz, and W. Mueller-Klieser, "Glucose diffusion coefficients determined from concentration profiles in EMT6 tumor spheroids incubated in radioactively labeled L-glucose," in *Oxygen Transport to Tissue XVI*, pp. 619–625, Springer, 1994.

[112] I. Tannock, "The relation between cell proliferation and the vascular system in a transplanted mouse mammary tumour," *British Journal of Cancer*, vol. 22, no. 2, p. 258, 1968.

[113] X. Zhang, C. G. Li, C. H. Ye, and M. L. Liu, "Determination of molecular self-diffusion coefficient using multiple spin-echo NMR spectroscopy with removal of convection and background gradient artifacts," *Analytical chemistry*, vol. 73, no. 15, pp. 3528–3534, 2001.

[114] M. Liu, J. K. Nicholson, A. John, and J. C. Lindon, "Measurement of biomolecular diffusion coefficients in blood plasma using two-dimensional ^{1}H-^{1}H diffusion-edited total-correlation NMR spectroscopy," *Analytical chemistry*, vol. 69, no. 8, pp. 1504–1509, 1997.

[115] M. G. Nichols and T. H. Foster, "Oxygen diffusion and reaction kinetics in the photodynamic therapy of multicell tumour spheroids," *Physics in medicine and biology*, vol. 39, no. 12, p. 2161, 1999.

[116] W. F. Mueller-Klieser and R. M. Sutherland, "Oxygen consumption and oxygen diffusion properties of multicellular spheroids from two different cell lines," in *Oxygen Transport to TissueVI*, pp. 311–321, Springer, 1984.

[117] J. Grote, R. Süsskind, and P. Vaupel, "Oxygen diffusivity in tumor tissue (DS-carcinosarcoma) under temperature conditions within the range of 20–40°C," *Pflügers Archiv*, vol. 372, no. 1, pp. 37–42, 1977.

[118] I. F. Tannock, "Oxygen diffusion and the distribution of cellular radiosensitivity in tumours," *British Journal of Radiology*, vol. 45, no. 535, pp. 515–524, 1972.

[119] B. W. Pogue, J. A. O'Hara, C. M. Wilmot, K. D. Paulsen, and H. M. Swartz, "Estimation of oxygen distribution in RIF-1 tumors by diffusion model-based interpre-

tation of pimonidazole hypoxia and Eppendorf measurements," *Radiation Research*, vol. 155, no. 1, pp. 15–25, 2001.

[120] A. Daşu, I. Toma-Daşu, and M. Karlsson, "Theoretical simulation of tumour oxygenation and results from acute and chronic hypoxia," *Physics in medicine and biology*, vol. 48, no. 17, p. 2829, 2003.

[121] D. R. Grimes, C. Kelly, K. Bloch, and M. Partridge, "A method for estimating the oxygen consumption rate in multicellular tumour spheroids," *Journal of The Royal Society Interface*, vol. 11, no. 92, p. 20131124, 2014.

[122] I. Fatt, C. J. Giasson, and T. D. Mueller, "Non-steady-state diffusion in a multilayered tissue initiated by manipulation of chemical activity at the boundaries," *Biophysical journal*, vol. 74, no. 1, pp. 475–486, 1998.

[123] K. Uchida, M. Mochizuki, and K. Niizeki, "Diffusion coefficients of co2 molecule and bicarbonate ion in hemoglobin solution measured by fluorescence technique," *Jpn. J. Physiol*, vol. 33, pp. 619–634, 1983.

[124] P. Carmeliet and R. K. Jain, "Angiogenesis in cancer and other diseases," *Nature*, vol. 407, pp. 249–257, 2000.

[125] D. Fukumura and R. K. Jain, "Tumor microenvironment abnormalities: causes, consequences, and strategies to normalize," *J. Cell. Biochem.*, vol. 101, pp. 937–949, 2007.

[126] D. Fukumura, L. Xu, Y. Chen, T. Gohongi, B. Seed, and R. K. Jain, "Hypoxia and acidosis independently up-regulate vascular endothelial growth factor transcription in brain tumors in vivo," *Cancer Res.*, vol. 61, pp. 6020–6024, 2001.

[127] D. D'Arcangelo, F. Facchiano, L. M. Barlucchi, G. Melillo, B. Illi, L. Testolin, C. Gaetano, and M. C. Capogrossi, "Acidosis inhibits endothelial cell apoptosis and function and induces basic fibroblast growth factor and vascular endothelial growth factor expression," *Circ. Res.*, vol. 86, pp. 312–318, 2000.

[128] A. Bellocq, S. Suberville, C. Philippe, F. Bertrand, J. Perez, B. Fouqueray, G. Cherqui, and L. Baud, "Low environmental pH is responsible for the induction of nitric-oxide synthase in macrophages. Evidence for involvement of nuclear factor-kappaB activation," *J. Biol. Chem.*, vol. 273, pp. 5086–5092, 1998.

[129] C. H. Heldin, K. Rubin, K. Pietras, and A. Ostman, "High interstitial fluid pressure - an obstacle in cancer therapy," *Nat. Rev. Cancer*, vol. 4, pp. 806–813, 2004.

[130] R. T. Tong, Y. Boucher, S. V. Kozin, F. Winkler, D. J. Hicklin, and R. K. Jain, "Vascular normalization by vascular endothelial growth factor receptor 2 blockade induces a pressure gradient across the vasculature and improves drug penetration in tumors," *Cancer Res.*, vol. 64, pp. 3731–3736, Jun 2004.

[131] C.-L. E. Helm, M. E. Fleury, A. H. Zisch, F. Boschetti, and M. A. Swartz, "Synergy between interstitial flow and VEGF directs capillary morphogenesis in vitro through a gradient amplification mechanism," *Proceedings of the National Academy of Sciences of the United States of America*, vol. 102, no. 44, pp. 15779–15784, 2005.

[132] N. Ferrara and W. J. Henzel, "Pituitary follicular cells secrete a novel heparin-binding growth factor specific for vascular endothelial cells," *Biochemical and biophysical research communications*, vol. 161, no. 2, pp. 851–858, 1989.

[133] D. M. Ornitz and N. Itoh, "Fibroblast growth factors," *Genome Biol*, vol. 2, no. 3, pp. 1–12, 2001.

[134] F. Rastinejad, P. J. Polverini, and N. P. Bouck, "Regulation of the activity of a new inhibitor of angiogenesis by a cancer suppressor gene," *Cell*, vol. 56, no. 3, pp. 345–355, 1989.

[135] M. S. O'Reilly, L. Holmgren, Y. Shing, C. Chen, R. A. Rosenthal, M. Moses, W. S. Lane, Y. Cao, E. H. Sage, and J. Folkman, "Angiostatin: a novel angiogenesis inhibitor that mediates the suppression of metastases by a Lewis lung carcinoma," *cell*, vol. 79, no. 2, pp. 315–328, 1994.

[136] M. S. O'Reilly, T. Boehm, Y. Shing, N. Fukai, G. Vasios, W. S. Lane, E. Flynn, J. R. Birkhead, B. R. Olsen, and J. Folkman, "Endostatin: an endogenous inhibitor of angiogenesis and tumor growth," *cell*, vol. 88, no. 2, pp. 277–285, 1997.

[137] G. A. Truskey, F. Yuan, and D. F. Katz, *Transport phenomena in biological systems*. Pearson Prentice Hall, 2004.

[138] R. K. Jain, "Determinants of tumor blood flow: a review," *Cancer research*, vol. 48, no. 10, pp. 2641–2658, 1988.

[139] MATLAB, *R2013a*. Natick, Massachusetts, United States: The MathWorks Inc., 2013.

[140] B. Endrich, H. S. Reinhold, J. F. Gross, and M. Intaglietta, "Tissue perfusion inhomogeneity during early tumor growth in rats," *J. Natl. Cancer Inst.*, vol. 62, pp. 387–393, 1979.

[141] D. S. Izyumov, A. V. Avetisyan, O. Y. Pletjushkina, D. V. Sakharov, K. W. Wirtz, B. V. Chernyak, and V. P. Skulachev, "Wages of fear: transient threefold decrease in intracellular ATP level imposes apoptosis," *Biochimica et Biophysica Acta (BBA)-Bioenergetics*, vol. 1658, no. 1, pp. 141–147, 2004.

[142] O. Feron, "Pyruvate into lactate and back: from the Warburg effect to symbiotic energy fuel exchange in cancer cells," *Radiotherapy and Oncology*, vol. 92, no. 3, pp. 329–333, 2009.

[143] E. C. Nakajima and B. Van Houten, "Metabolic symbiosis in cancer: Refocusing the Warburg lens," *Molecular carcinogenesis*, 2012.

[144] A. K. Bouzier, P. Voisin, R. Goodwin, P. Canioni, and M. Merle, "Glucose and lactate metabolism in C6 glioma cells: evidence for the preferential utilization of lactate for cell oxidative metabolism," *Developmental neuroscience*, vol. 20, no. 4-5, pp. 331–338, 1998.

[145] J. Katz, K. Brand, S. Golden, and D. Rubinstein, "Lactate and pyruvate metabolism and reducing equivalent transfer in Ehrlich ascites tumor," *Cancer Research*, vol. 34, no. 4, pp. 872–877, 1974.

[146] H. Pelicano, D. S. Martin, R. H. Xu, and P. Huang, "Glycolysis inhibition for anticancer treatment," *Oncogene*, vol. 25, no. 34, pp. 4633–4646, 2006.

[147] R. A. Gatenby and R. J. Gillies, "Glycolysis in cancer: a potential target for therapy," *The international journal of biochemistry & cell biology*, vol. 39, no. 7, pp. 1358–1366, 2007.

[148] C. Granchi and F. Minutolo, "Anticancer agents that counteract tumor glycolysis," *ChemMedChem*, vol. 7, no. 8, pp. 1318–1350, 2012.

[149] M. Dellian, G. Helmlinger, F. Yuan, and R. K. Jain, "Fluorescence ratio imaging of interstitial pH in solid tumours: effect of glucose on spatial and temporal gradients," *British journal of cancer*, vol. 74, no. 8, p. 1206, 1996.

[150] P. Voisin, V. Bouchaud, M. Merle, P. Diolez, L. Duffy, K. Klint, J.-M. Franconi, and A.-K. Bouzier-Sore, "Microglia in close vicinity of glioma cells: correlation between phenotype and metabolic alterations," *Frontiers in neuroenergetics*, vol. 2, p. 131, 2010.

[151] R. L. Elstrom, D. E. Bauer, M. Buzzai, R. Karnauskas, M. H. Harris, D. R. Plas, H. Zhuang, R. M. Cinalli, A. Alavi, C. M. Rudin, *et al.*, "Akt stimulates aerobic glycolysis in cancer cells," *Cancer research*, vol. 64, no. 11, pp. 3892–3899, 2004.

[152] A. Le, C. R. Cooper, A. M. Gouw, R. Dinavahi, A. Maitra, L. M. Deck, R. E. Royer, D. L. Vander Jagt, G. L. Semenza, and C. V. Dang, "Inhibition of lactate dehydrogenase A induces oxidative stress and inhibits tumor progression," *Proceedings of the National Academy of Sciences*, vol. 107, no. 5, pp. 2037–2042, 2010.

[153] P. Costantini, E. Jacotot, D. Decaudin, and G. Kroemer, "Mitochondrion as a novel target of anticancer chemotherapy," *Journal of the National Cancer Institute*, vol. 92, no. 13, pp. 1042–1053, 2000.

[154] R. W. Putnam and A. Roos, "Which value for the first dissociation constant of carbonic acid should be used in biological work," *Am J Physiol*, vol. 260, no. 5 Pt 1, pp. C1113–C1116, 1991.

[155] N. Martin, I. Robey, E. Gaffney, R. Gillies, R. Gatenby, and P. Maini, "Predicting the safety and efficacy of buffer therapy to raise tumour pHe: an integrative modelling study," *British journal of cancer*, vol. 106, no. 7, pp. 1280–1287, 2012.

[156] F. Ravandi, J. E. Cortes, D. Jones, S. Faderl, G. Garcia-Manero, M. Y. Konopleva, S. O'Brien, Z. Estrov, G. Borthakur, D. Thomas, *et al.*, "Phase I/II study of combination therapy with sorafenib, idarubicin, and cytarabine in younger patients with acute myeloid leukemia," *Journal of Clinical Oncology*, vol. 28, no. 11, pp. 1856–1862, 2010.

[157] D. Takabatake, T. Fujita, T. Shien, K. Kawasaki, N. Taira, S. Yoshitomi, H. Takahashi, Y. Ishibe, Y. Ogasawara, and H. Doihara, "Tumor inhibitory effect of gefitinib

(ZD1839, iressa) and taxane combination therapy in EGFR-overexpressing breast cancer cell lines (MCF7/ADR, MDA-MB-231)," *International journal of cancer*, vol. 120, no. 1, pp. 181–188, 2007.

[158] P. Sengupta, S. Basu, S. Soni, A. Pandey, B. Roy, M. S. Oh, K. T. Chin, A. S. Paraskar, S. Sarangi, Y. Connor, *et al.*, "Cholesterol-tethered platinum II-based supramolecular nanoparticle increases antitumor efficacy and reduces nephrotoxicity," *Proceedings of the National Academy of Sciences*, vol. 109, no. 28, pp. 11294–11299, 2012.

[159] T. Eissing, H. Conzelmann, E. D. Gilles, F. Allgower, E. Bullinger, and P. Scheurich, "Bistability analyses of a caspase activation model for receptor-induced apoptosis," *J. Biol. Chem.*, vol. 279, pp. 36892–36897, Aug 2004.

[160] H. S. Choi, S. Han, H. Yokota, and K. H. Cho, "Coupled positive feedbacks provoke slow induction plus fast switching in apoptosis," *FEBS Lett.*, vol. 581, pp. 2684–2690, Jun 2007.

[161] J. G. Albeck, J. M. Burke, S. L. Spencer, D. A. Lauffenburger, and P. K. Sorger, "Modeling a snap-action, variable-delay switch controlling extrinsic cell death," *PLoS Biol.*, vol. 6, pp. 2831–2852, Dec 2008.

[162] S. L. Spencer and P. K. Sorger, "Measuring and modeling apoptosis in single cells," *Cell*, vol. 144, pp. 926–939, Mar 2011.

[163] M. H. Cardone, N. Roy, H. R. Stennicke, G. S. Salvesen, T. F. Franke, E. Stanbridge, S. Frisch, and J. C. Reed, "Regulation of cell death protease caspase-9 by phosphorylation," *Science*, vol. 282, pp. 1318–1321, Nov 1998.

[164] E. Asselin, G. B. Mills, and B. K. Tsang, "XIAP regulates Akt activity and caspase-3-dependent cleavage during cisplatin-induced apoptosis in human ovarian epithelial cancer cells," *Cancer Res.*, vol. 61, pp. 1862–1868, Mar 2001.

[165] H. C. Dan, M. Sun, S. Kaneko, R. I. Feldman, S. V. Nicosia, H. G. Wang, B. K. Tsang, and J. Q. Cheng, "Akt phosphorylation and stabilization of X-linked inhibitor of apoptosis protein (XIAP)," *J. Biol. Chem.*, vol. 279, pp. 5405–5412, Feb 2004.

[166] Q. L. Deveraux, E. Leo, H. R. Stennicke, K. Welsh, G. S. Salvesen, and J. C. Reed, "Cleavage of human inhibitor of apoptosis protein XIAP results in fragments with distinct specificities for caspases," *EMBO J.*, vol. 18, pp. 5242–5251, Oct 1999.

[167] M. Hornle, N. Peters, B. Thayaparasingham, H. Vorsmann, H. Kashkar, and D. Kulms, "Caspase-3 cleaves XIAP in a positive feedback loop to sensitize melanoma cells to TRAIL-induced apoptosis," *Oncogene*, vol. 30, pp. 575–587, Feb 2011.

[168] S. E. Winograd-Katz and A. Levitzki, "Cisplatin induces PKB/Akt activation and p38(MAPK) phosphorylation of the EGF receptor," *Oncogene*, vol. 25, pp. 7381–7390, Nov 2006.

[169] M. Muzio, B. R. Stockwell, H. R. Stennicke, G. S. Salvesen, and V. M. Dixit, "An induced proximity model for caspase-8 activation," *J. Biol. Chem.*, vol. 273, pp. 2926–2930, Jan 1998.

[170] V. M. Gonzalez, M. A. Fuertes, C. Alonso, and J. M. Perez, "Is cisplatin-induced cell death always produced by apoptosis?," *Mol. Pharmacol.*, vol. 59, pp. 657–663, Apr 2001.

[171] P. Li, D. Nijhawan, I. Budihardjo, S. M. Srinivasula, M. Ahmad, E. S. Alnemri, and X. Wang, "Cytochrome c and dATP-dependent formation of Apaf-1/caspase-9 complex initiates an apoptotic protease cascade," *Cell*, vol. 91, pp. 479–489, Nov 1997.

[172] N. MacDonald, "Time delay in simple chemostat models," *Biotechnology and bioengineering*, vol. 18, no. 6, pp. 805–812, 1976.

[173] T. Maiwald and J. Timmer, "Dynamical modeling and multi-experiment fitting with PottersWheel," *Bioinformatics*, vol. 24, no. 18, pp. 2037–2043, 2008.

[174] H. Molavian, C. Phipps, M. Kohandel, B. G. Wouters, and S. Sivaloganathan, "Observation of a synergy between catalase and peroxidase-1 and its effect on the concentration of H_2O_2." submitted, 2014.

[175] H. Molavian, C. Phipps, M. Kohandel, B. G. Wouters, and S. Sivaloganathan, "Catalase activity and cell permeability to hydrogen peroxide; the central players in the efficacy of pharmacological concentrations of ascorbic acid for cancer treatment." submitted, 2014.

[176] A. C. Shieh and M. A. Swartz, "Regulation of tumor invasion by interstitial fluid flow," *Physical biology*, vol. 8, no. 1, p. 015012, 2011.

[177] M. Wu, H. B. Frieboes, S. R. McDougall, M. A. Chaplain, V. Cristini, and J. Lowengrub, "The effect of interstitial pressure on tumor growth: coupling with the blood and lymphatic vascular systems," *Journal of theoretical biology*, vol. 320, pp. 131–151, 2013.

[178] S. A. Mousa and L. H. Anwar, "Anti-angiogenesis therapy as an adjunct to chemotherapy in oncology," in *Angiogenesis Modulations in Health and Disease*, pp. 143–155, Springer, 2013.

[179] A. Ozcelikkale, S. Ghosh, and B. Han, "Multifaceted transport characteristics of nanomedicine: Needs for characterization in dynamic environment," *Molecular pharmaceutics*, vol. 10, no. 6, pp. 2111–2126, 2013.

[180] B. Abdollahi, N. Dunlap, and H. B. Frieboes, "Bridging the gap between modeling of tumor growth and clinical imaging," in *Abdomen and Thoracic Imaging*, pp. 463–487, Springer, 2014.

[181] M. A. Biot, "Theory of elasticity and consolidation for a porous anisotropic solid," *Journal of Applied Physics*, vol. 26, no. 2, pp. 182–185, 1955.

[182] W. Ehlers and B. Markert, "A linear viscoelastic biphasic model for soft tissues based on the theory of porous media," *Journal of biomechanical engineering*, vol. 123, no. 5, pp. 418–424, 2001.

[183] C. Phipps, H. Molavian, and M. Kohandel, "A microscale mathematical model for metabolic symbiosis." submitted, 2014.

[184] P. Romero, J. Wagg, M. L. Green, D. Kaiser, M. Krummenacker, and P. D. Karp, "Computational prediction of human metabolic pathways from the complete human genome," *Genome biology*, vol. 6, no. 1, p. R2, 2004.

[185] R. K. Crane, D. Miller, and I. Bihler, "The restrictions on possible mechanisms of intestinal active transport of sugars," *Membrane transport and metabolism*, vol. 439, 1961.

[186] C. V. Iancu, J. Zamoon, S. B. Woo, A. Aleshin, and J.-y. Choe, "Crystal structure of a glucose/H^+ symporter and its mechanism of action," *Proceedings of the National Academy of Sciences*, vol. 110, no. 44, pp. 17862–17867, 2013.

[187] R. A. Robergs, F. Ghiasvand, and D. Parker, "Biochemistry of exercise-induced metabolic acidosis," *American Journal of Physiology-Regulatory, Integrative and Comparative Physiology*, vol. 287, no. 3, pp. R502–R516, 2004.

[188] S. Herzig, E. Raemy, S. Montessuit, J.-L. Veuthey, N. Zamboni, B. Westermann, E. R. Kunji, and J.-C. Martinou, "Identification and functional expression of the mitochondrial pyruvate carrier," *Science*, vol. 337, no. 6090, pp. 93–96, 2012.

[189] D. K. Bricker, E. B. Taylor, J. C. Schell, T. Orsak, A. Boutron, Y.-C. Chen, J. E. Cox, C. M. Cardon, J. G. Van Vranken, and N. Dephoure, "A mitochondrial pyruvate carrier required for pyruvate uptake in yeast, drosophila, and humans," *Science*, vol. 337, no. 6090, pp. 96–100, 2012.

[190] R. Stappen and R. Krämer, "Kinetic mechanism of phosphate/phosphate and phosphate/OH-antiports catalyzed by reconstituted phosphate carrier from beef heart mitochondria," *Journal of Biological Chemistry*, vol. 269, no. 15, pp. 11240–11246, 1994.

[191] A. M. Porcelli, A. Ghelli, C. Zanna, P. Pinton, R. Rizzuto, and M. Rugolo, "pH difference across the outer mitochondrial membrane measured with a green fluorescent protein mutant," *Biochemical and biophysical research communications*, vol. 326, no. 4, pp. 799–804, 2005.

[192] A. Gabizon, R. Catane, B. Uziely, B. Kaufman, T. Safra, R. Cohen, F. Martin, A. Huang, and Y. Barenholz, "Prolonged circulation time and enhanced accumulation in malignant exudates of doxorubicin encapsulated in polyethylene-glycol coated liposomes," *Cancer Res.*, vol. 54, pp. 987–992, 1994.

[193] B. Halliwell and J. M. Gutteridge, "Free radicals in biology and medicine," 1989.

[194] W. Dröge, "Free radicals in the physiological control of cell function," *Physiological reviews*, vol. 82, no. 1, pp. 47–95, 2002.

[195] M. Ohba, M. Shibanuma, T. Kuroki, and K. Nose, "Production of hydrogen peroxide by transforming growth factor-beta 1 and its involvement in induction of egr-1 in

mouse osteoblastic cells," *The Journal of Cell Biology*, vol. 126, no. 4, pp. 1079–1088, 1994.

[196] V. J. Thannickal and B. L. Fanburg, "Activation of an H_2O_2-generating NADH oxidase in human lung fibroblasts by transforming growth factor β_1," *Journal of Biological Chemistry*, vol. 270, no. 51, pp. 30334–30338, 1995.

[197] B. Halliwell, "Oxidative stress and cancer: have we moved forward?," *Biochem. j*, vol. 401, pp. 1–11, 2007.

[198] M. B. Spina and G. Cohen, "Dopamine turnover and glutathione oxidation: implications for Parkinson disease," *Proceedings of the National Academy of Sciences*, vol. 86, no. 4, pp. 1398–1400, 1989.

[199] S. Fahn and G. Cohen, "The oxidant stress hypothesis in Parkinson's disease: evidence supporting it," *Annals of neurology*, vol. 32, no. 6, pp. 804–812, 1992.

[200] B. Halliwell, "Role of free radicals in the neurodegenerative diseases," *Drugs & aging*, vol. 18, no. 9, pp. 685–716, 2001.

[201] H. Wiseman and B. Halliwell, "Damage to DNA by reactive oxygen and nitrogen species: role in inflammatory disease and progression to cancer," *Biochem. J*, vol. 313, pp. 17–29, 1996.

[202] S. P. Hussain, L. J. Hofseth, and C. C. Harris, "Radical causes of cancer," *Nature Reviews Cancer*, vol. 3, no. 4, pp. 276–285, 2003.

[203] J. L. Evans, I. D. Goldfine, B. A. Maddux, and G. M. Grodsky, "Oxidative stress and stress-activated signaling pathways: a unifying hypothesis of type 2 diabetes," *Endocrine reviews*, vol. 23, no. 5, pp. 599–622, 2002.

[204] Y. Y. Lo and T. F. Cruz, "Involvement of reactive oxygen species in cytokine and growth factor induction of c-fos expression in chondrocytes," *Journal of Biological Chemistry*, vol. 270, no. 20, pp. 11727–11730, 1995.

[205] M. Sundaresan, Z.-X. Yu, V. J. Ferrans, K. Irani, and T. Finkel, "Requirement for generation of H_2O_2 for platelet-derived growth factor signal transduction," *Science*, vol. 270, no. 5234, pp. 296–299, 1995.

[206] H. Sauer, M. Wartenberg, and J. Hescheler, "Reactive oxygen species as intracellular messengers during cell growth and differentiation," *Cellular Physiology and Biochemistry*, vol. 11, no. 4, pp. 173–186, 2001.

[207] A. Dumont, S. P. Hehner, T. G. Hofmann, M. Ueffing, W. Dröge, and M. L. Schmitz, "Hydrogen peroxide-induced apoptosis is CD95-independent, requires the release of mitochondria-derived reactive oxygen species and the activation of NF-κB," *Oncogene*, vol. 18, no. 3, 1999.

[208] J. A. Imlay, "Pathways of oxidative damage," *Annual Reviews in Microbiology*, vol. 57, no. 1, pp. 395–418, 2003.

[209] J. A. Imlay, S. M. Chin, and S. Linn, "Toxic DNA damage by hydrogen peroxide through the Fenton reaction in vivo and in vitro," *Science*, vol. 240, no. 4852, pp. 640–642, 1988.

[210] B. Gonzalez-Flecha, J. C. Cutrin, and A. Boveris, "Time course and mechanism of oxidative stress and tissue damage in rat liver subjected to in vivo ischemia-reperfusion," *Journal of Clinical Investigation*, vol. 91, no. 2, p. 456, 1993.

[211] G. Cohen and P. Hochstein, "Glutathione peroxidase: The primary agent for the elimination of hydrogen peroxide in erythrocytes*," *Biochemistry*, vol. 2, no. 6, pp. 1420–1428, 1963.

[212] H. Sies, "Glutathione and its role in cellular functions," *Free Radical Biology and Medicine*, vol. 27, no. 9, pp. 916–921, 1999.

[213] S. Toppo, L. Flohé, F. Ursini, S. Vanin, and M. Maiorino, "Catalytic mechanisms and specificities of glutathione peroxidases: variations of a basic scheme," *Biochimica et Biophysica Acta (BBA)-General Subjects*, vol. 1790, no. 11, pp. 1486–1500, 2009.

[214] C. F. Ng, F. Q. Schafer, G. R. Buettner, and V. G. J. Rodgers, "The rate of cellular hydrogen peroxide removal shows dependency on GSH: mathematical insight into in vivo H_2O_2 and GPx concentrations," *Free radical research*, vol. 41, no. 11, pp. 1201–1211, 2007.

[215] F. Antunes, A. Salvador, and R. E. Pinto, "PHGPx and phospholipase A_2/GPx: Comparative importance on the reduction of hydroperoxides in rat liver mitochondria," *Free Radical Biology and Medicine*, vol. 19, no. 5, pp. 669–677, 1995.

[216] L. Flohé and I. Brand, "Kinetics of glutathione peroxidase," *Biochimica et Biophysica Acta (BBA)-Enzymology*, vol. 191, no. 3, pp. 541–549, 1969.